CRANFIELD UNIVERSITY

On Scaling and System Identification of Flexible Aircraft Dynamics

SEZSY YUNIORRITA YUSUF

School of Aerospace, Transport and Manufacturing
Dynamics, Simulation & Control Group
Department of Aerospace Engineering

PhD THESIS

This page is intentionally left blank.

CRANFIELD UNIVERSITY

SCHOOL OF AEROSPACE, TRANSPORT AND MANUFACTURING

PhD THESIS

ACADEMIC YEAR 2018-19

SEZSY YUNIORRITA YUSUF

ON SCALING AND SYSTEM IDENTIFICATION OF FLEXIBLE AIRCRAFT DYNAMICS

SUPERVISOR :
DR MUDASSIR LONE & DR ALASTAIR COOKE

October 2019

This page is intentionally left blank.

Abstract

The use of subscale models has been common practice in the industry and has helped engineers gain more confidence in their design processes. However, each subscale model is developed for a specific test, and consequently, different types of models are needed for observing aerodynamic, structural and aeroelastic characteristics of a full-scale aircraft. Yet, traditional aircraft design methods face serious challenges when a novel aircraft design emerges and a proof-of-concept is needed for investigating this multi-disciplinary problem. An example of such a problem is the development of aircraft configurations with high aspect ratio wings for which the disciplines of aeroelastic and flight mechanics are strongly interconnected. Moreover, if the prediction of dynamic behaviour is of interest, a method that utilises system identification for analysing experimental data is of importance. Therefore, this thesis aims to develop a methodology to investigate the complex flight dynamic behaviour of flexible aircraft by combining techniques for developing subscale models and methods with the field of system identification. This aim is achieved through three objectives: 1) assessment of system identification methods for subscale flexible aircraft, 2) theoretical development of subscale modelling in terms of scaling laws and aeroelastic simulation framework and, 3) wind tunnel testing of the subscale model. Aspects of System Identification have been explored through use-cases where experimental data for a rigid aircraft both in full-scale and subscale configuration is used. The results highlight the fact that in testing a subscale model, dynamics are more prone to exhibit non-linear behaviour when compared to the full-scale model. It followed by the application of system identification for a flexible aircraft based on a simulation framework. This study emphasised the need for non-linear identification methods, such as an output error method, to characterise a flexible aircraft system. The work continues with the exploration of scaling laws applied to a simple aerofoil that is free to pitch and plunge. These results build the foundation for the development of a subscale high aspect ratio wing for wind tunnel experiments. The work highlights the trade-offs and compromises faced during the development of a dynamically subscaled model and the practice of system identification. The main contribution lies in the development of a low-cost methodology in building a subscale model that allows the use of dynamically scaled models at the early design stages. This practice provides the designer with a means to de-risk novel aircraft concepts as early as possible and in doing so, reduce overall development costs.

Keywords: system identification, dynamic scaling, wind tunnel testing, aeroelastic

This page is intentionally left blank.

Acknowledgments

Alhamdulillah, this too shall pass...
However, the knowledge that I gain will always remain. Its not about the degree, its the experience.

And it would be harder without the two amazing men of my life, Adi and Kean. Thanks for all the understanding and patient to face me in my ups and downs, Kang Adi. The '*go and hug, Bubu*' always makes my day. Thanks for the unconditional love, Kean. Bubu is always busy, eh?

I also would like to express my sincere gratitude to my supervisor Dr Mudassir Lone for his trust and continuing support in the past years, also for always challenging me and pushing me outside my comfort zone. Not to forget, Dr Alastair Cooke for the valuable feedback on the thesis structure. And Dr James Whidborne for answering my questions during the tea break, which (most of the time) ended up with a new exciting problem. Many thanks to Dr. Luca Zanotti for the introduction to the subspace identification methods.

For my sponsor, the Indonesian endowment fund for education (LPDP) for the funding in the last four years.

Thanks a lot for all my fellow colleagues, which makes this journey exciting and full of stories: Simone Weber for all the late (girlish) night discussion and God knows how many feedbacks. *I'm glad our path crossed!*. Alessandro Pontillo for always being excited, *yes, mas.. we will be famous!*. Martin Carrizales for the bottomless coffee, doughnuts and of course **chilli sauce!!**. Raheeg Alamin, my sista', now that I'm submitting, you can distract me as much as you wish. Matt Story, thanks for all the emotionally supported .gif. *You can do it!*. Shun He, `Hello, Table number one`! Thanks for all of the discussion on I_{yy} ('ai-way-way'). And Estela Bragado, be prepared.. *Look, a sailor!*. For the newly doctors: Dr David Hayes, my exergetic birthday friend, *any Muslim news today?*. Dr Vilius Portapas, thanks for being so kind in your own way, *banana pancake?*, and Dr Gaetan Dussart *wow..nice plots!*.

Many thanks for the Indonesian society for making me feel home far away from home. The Lubis family, Bang Alex dan Ka Mona, thanks for helping me feed my family, don't forget the *elasticity factor!*. Ibrahim's family and the Rahadyans, thanks for always be the supporting system and taking care of Kean every time needed. Also to Katia and Aprizal, for always being ready to help. To all the Indonesian society member since 2015, which have been graduated. I met lots of new families in the past years.

Last but not least, my biggest gratitude for both Jusuf's families. Thanks for all the support through the video call, mah-pah, bu-aya, lytha. Special thanks to Fajar for the surprise visit. Sorry to be away for so long, you can play with Kean now again.

This page is intentionally left blank.

Contents

This page is intentionally left blank.

List of Figures

This page is intentionally left blank.

List of Tables

Nomenclature

A	State matrix	
A_i	Amplitude of the i^{th} sinusoidal input	
B	Input matrix	
$\mathcal{B}$	Rigid body translational and angular velocity	
C	Output matrix	
$\mathbf{C}$	Structural damping matrix	
$C(k)$	Theodorsen function	
C_D	Drag coefficient	
C_L	Lift coefficient	
C_M	Pitching moment coefficient	
C_l	Rolling moment coefficient	
C_{L_α}	Slope of $C_L - \alpha$ plot	
C_{M_α}	Slope of $C_M - \alpha$ plot	
$C_{M_{\delta_e}}$	Elevator effectiveness coefficient	
C_{M_q}	Pitch damping coefficient	
D	Drag force	(N)
F	External forces	(N)
Fr	Froude number	
I_{xx}	Moment of inertia in roll direction	(kg.m^2)
I_{xy}	Product of inertia in ox- and oy- axis	(kg.m^2)
I_{yy}	Moment of inertia in pitch direction	(kg.m^2)
$J(\ )$	Cost function	
$\mathbf{K}$	Structural stiffness matrix	
$\mathcal{L}$	Dimension of length	
$\bar{L}_{()}$	Rolling moment	(N.m^2)

$\bar{L}_p$	Roll damping	(N.m^2)
$L_{[]}$	Lift force	(N)
$\bar{L}_{\delta_a}$	Aileron effectiveness	(N.m^2)
$\mathbf{M}$	Structural mass matrix	
$\mathcal{M}$	Dimension of mass	
$M_{[]}$	Pitching moment	(N.m)
Ma	Mach number	
N	Number of data points	
Q_i	Generalised external forces	
$\mathbb{R}$	Real number	
$\mathbf{R}$	Covariance matrix	
Re	Reynolds number	
S	Wing area	(m^2)
$\tilde{S}_G$	Torsional stiffness scaling factor	
$\tilde{S}_I$	Inertia scaling factor	
$\tilde{S}_K$	Structural stiffness scaling factor	
$\tilde{S}_T$	Time scaling factor	
S_U	Velocity scaling factor	
$\tilde{S}_m$	Mass scaling factor	
$\tilde{S}_\lambda$	Structural damping scaling factor	
S_ρ	Air density scaling factor	
St	Strouhal number	
T	Time length	(s)
$\mathcal{T}$	Dimension of time	
U	Free stream velocity	(m/s)
$\mathbf{X}$	Regressor matrix	
a	Acceleration	(m/s^2)
b	Wing semi-span	(m)
$\bar{c}$	Mean aerodynamic chord	(m)

$c_{1/2}$	Semi-chord length	(m)
$\mathbf{d}$	Generalised (6 DoF) structural node displacement	
g	Gravitational acceleration	9.8 (m/s^2)
h	Altitude	(m)
i_α	Incidence angle	(deg)
l	Characteristic length	(m)
m	Mass	(kg)
p	Aircraft roll rate	(rad/s)
q	Aircraft pitch rate	(rad/s)
$\bar{q}$	Dynamic pressure	(N/m^2)
r	Aircraft yaw rate	(rad/s)
t	Time	(s)
u	Translational velocity in the x-direction	(m/s)
$\mathbf{u}$	Vector of input	
v	Translational velocity in the y-direction	(m/s)
w	Translational velocity in the z-direction	(m/s)
x	Displacement in the x-direction	(m)
$\mathbf{x}$	State vector	
y	Displacement in the y-direction	(m)
$\mathbf{y}$	Model output / dependent variables	
z	Displacement in the z-direction	(m)
$\mathbf{z}$	Vector of output measurement	

Greek Alphabet

α	Angle of attack	(rad) or (deg)
χ	Right eigenvector	
δ_a	Aileron deflection	(rad) or (deg)
δ_e	Elevator deflection	(rad) or (deg)
δ_r	Rudder deflection	(rad) or (deg)
$\dot{\eta}_i$	i^{th} Generalised velocity	

$\ddot{\eta}_i$	i^{th} Generalised acceleration	
η_i	i^{th} Generalised displacement	
γ	Flight path angle	
λ	Wing static stall characteristics	
λ_i	Eigenvalue	
μ	Dynamic viscosity	(Pa.s)
ν	Measurement noise	
ω	Natural frequency	(rad/s)
ω_f	Filter bandwidth	(Hz)
ω_N	Nyquist frequency	(Hz)
ω_s	Sampling frequency	(Hz)
ω_{max}	Maximum frequency of interest	(Hz)
Φ	Structural mode shape	
ϕ	Rotation around x-axis	(deg)
Π_i	Non-dimensional relation	
Ψ	Eigen vector	
ψ	Rotation around z-axis	(deg)
ρ	Air density	(kg/m^3)
ρ_0	Air density at sea level	(kg/m^3)
σ	Standard deviation	
τ	Time constant	
τ	Time shift parameter	
Θ	Parameter vector	
θ	Rotation around y-axis	(deg)
$\hat{\Theta}$	Estimated parameter	
Υ	Wingtip deflection	
υ	Kinematic viscosity	(m^2/s)
φ_i	Phase angle i^{th} harmonic components	(rad)
ς	Size of the wingtip device with respect to semispan	

ξ Vector of regressors

ζ Damping ratio

Subscript

c Corrected data

FS Full-scale

k Discrete system

m Measured data

sc Subscale model

as Symmetric aileron deflection

0 Bias

Superscript

$\ddot{}$ Second derivatives with respect to time

$\dot{}$ First derivatives with respect to time

$\tilde{}$ Normalised

This page is intentionally left blank.

Abbreviation

BEARDS	BEAm Reduction and Dynamic Scaling
BEARDS^{TM}	BEAm Reduction and Dynamic Scaling Theoretical Framework
CA^{2}LM	Cranfield Accelerated Aircraft Loads Model
CFD	Computational Fluid Dynamics
CG	Centre of Gravity
DoF	Degree-of-Freedom
EGI	Embedded GPS/INS
ERA	Eigenvalue Realisation Algorithm
FE	Finite Element
FFT	Fast Fourier Transform
GPS/INS	Global Positioning System/Inertial Navigation System
GVT	Ground Vibration Testing
HAR	High Aspect Ratio
IMU	Inertial Measurement Unit
ISA	International Standard Atmosphere
MAC	Modal Assurance Criteria
MOF	Multivariate Orthogonal Function
MSFE	Mean-Square Fit Error
MTOW	Maximum Take-Off Weight
N4SID	Numerical algorithms for Subspace State Space System Identification
OE	Output Error
OFP	OverFit Penalty
OLS	Ordinary Least Square
PE	Parameter Estimation
PF	Peak Factor
PSE	Predicted Squared Error
RoR	Random on Random
RPF	Relative Peak Factor
SID	System Identification
SIDPAC	System IDentification Programs for AirCraft
SPPO	Short Period Pitching Oscillation
SSM	Spar, Skin and lumped Masses configuration of the xb-2 Wing
SVD	Singular Value Decomposition
TAS	True Air Speed
UAV	Unmanned Aerial Vehicle
XB-2	eXperimental BEARDS 2, refer to the full-scale model configuration
xb-2	Experimental BEARDS 2, refer to the subscale model configuration

This page is intentionally left blank.

CHAPTER 1

Introduction

The aircraft design cycle, as presented in Figure 1.1, is an iterative activity which traditionally takes a long period of time, involves numerous risks and requires expertise in various disciplines [1, 2]. Nowadays, the aerospace industry is aiming to make the design cycle leaner while at the same time develop highly efficient more integrated aircraft. Moreover, de-risking the design as early as possible and validating design methods and tools are also critical [3, 4]. Many studies have been conducted to reduce the design cycle time using various optimisation methods [5–7] that mostly focus on conceptual design and only utilise computational approaches. This context has motivated this study looking to integrate dynamic scaling and system identification (SID) and pathways for introducing these disciplines as early as possible [8, 9].

Scaled models have been used extensively in the past to understand the flight dynamic phenomena and at the same time, enable a designer to predict and analyse the characteristics of a system [10]. Despite the rapid advancements in computational ability, wind tunnel testing still has a significant impact on aircraft design validation [11]. On the other hand, the field of SID has been critical for providing a means of validating design methods and tools using flight test data [12, 13]. Therefore, SID has always been used right at the end of a design cycle. Furthermore, the majority of SID practice has focused on the estimation of parameters found in rigid body flight dynamic models, where often the non-linear, unsteady and aeroelastic effects are either highly simplified or completely ignored.

Typically dynamic scaling is conducted at the preliminary design stages and only focuses on steady and static problems, such as early-stage wind tunnel testing [14]. Moreover, past dynamic scaling work was carried out in a way that allowed the inertial, aerodynamic and structural problems to be treated in isolation. For example, wind tunnel testing is conducted to obtain the aerodynamic data [15], the spin test is done to observe the inertia effect [16], and Ground Vibration Tests (GVT) are utilised to characterise the structural behaviour. The only area where all these three factors are combined into a complete aeroelastic problem is where the designers are concerned with flutter, which is also observable through subscale models [17]. However, the aeroelastic problems are usually addressed at a much later design stage where the key components such as wing

configuration are fixed.

The trends of air transport nowadays are moving towards high capacity long-range aircraft characterised by highly flexible wing structures [18]. Such concepts bring significant interference between the rigid body and the structural dynamics. As an implication, rigid body dynamics no longer dominates the flight dynamics characteristics of the aircraft and the structural dynamics are now affecting the flight dynamics characteristics [19, 20]. This coupling can change the stability and control characteristics of the aircraft and can affect the aircraft's handling qualities. Here, experimented programme using subscale models can be a useful approach that gives the designer insight into potential problems. By conducting the experiments in the earlier design stage, it can de-risk the design process and provide higher confidence at later design stages. At the same time, the subscale model can provide a high fidelity mathematical model [21, 22]. As emphasised by Chambers [10], "*The most critical contributions of models are to provide confidence and risk reduction for new design and to enhance the safety and efficiency of existing configuration*".

Figure 1.2 provides the framework for utilising the subscale model as part of the design process, which emphasises the two main focus areas of this thesis: **Dynamic Scaling** and **System Identification**. The process starts with a definition of the full-scale concept model, which consists of the aircraft configuration and flight condition. Then dynamic scaling is aimed for building the subscale model. This process is essential to make sure that the sub-scale model can represent the similitude dynamic behaviour of the full-scale model. Lastly, experimental testing is carried out to observe the dynamic behaviour of the subscale model. System identification methods are then applied to the experimental data to quantify the dynamic behaviour of interest, which will be used to evaluate the design.

Current research on sub-scale aeroelastic systems mainly focuses on the scaling methodology and their results compared to the theoretical scaled models. This research takes the work further by utilising system identification methods to estimate the flight dynamic characteristics of the subscale model. It also fills the gap in linking the subscale experimental results with the full-scale theoretical model using system identification methods, providing further insight into the flight dynamic characteristics.

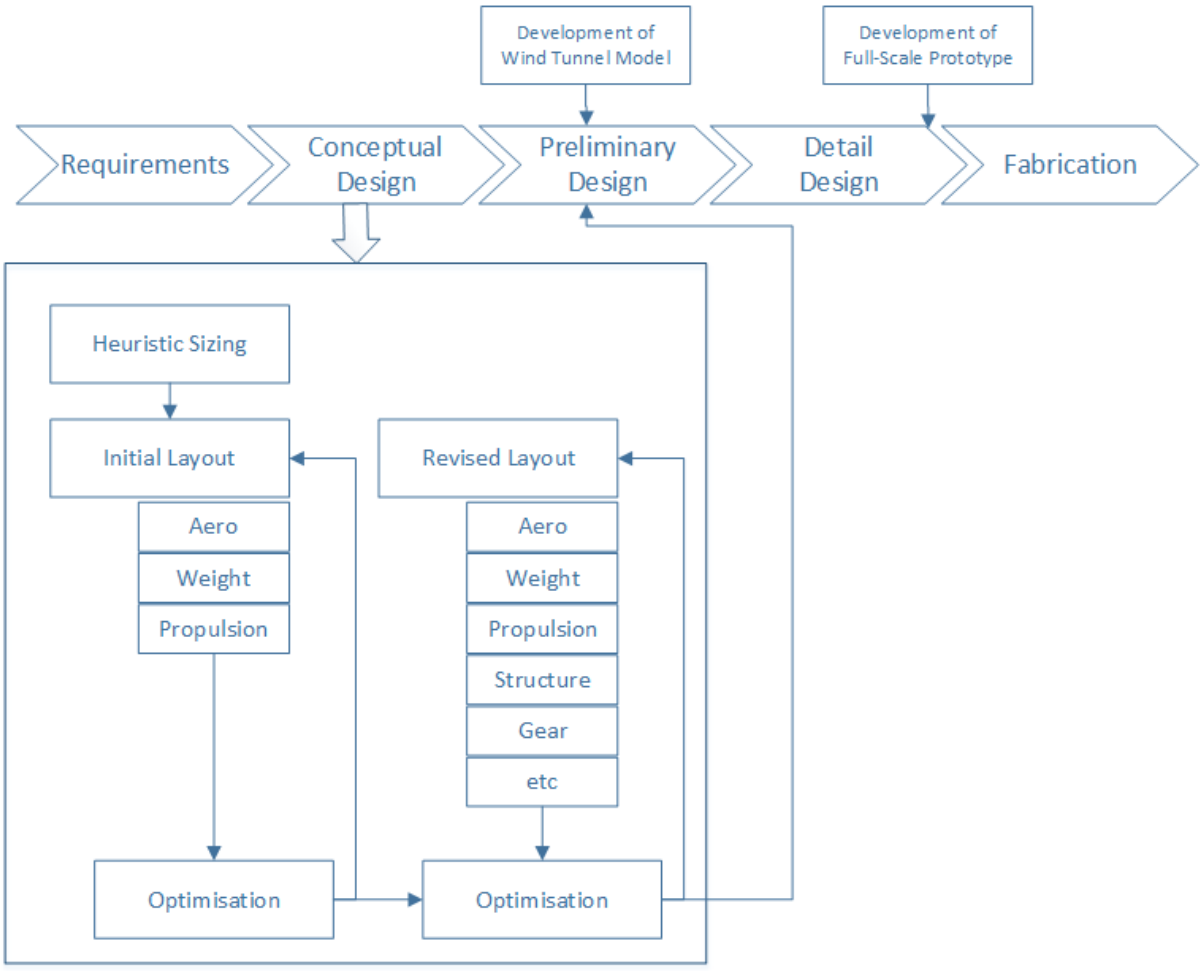

Figure 1.1: Aircraft design process (Reproduced from Reference [1]).

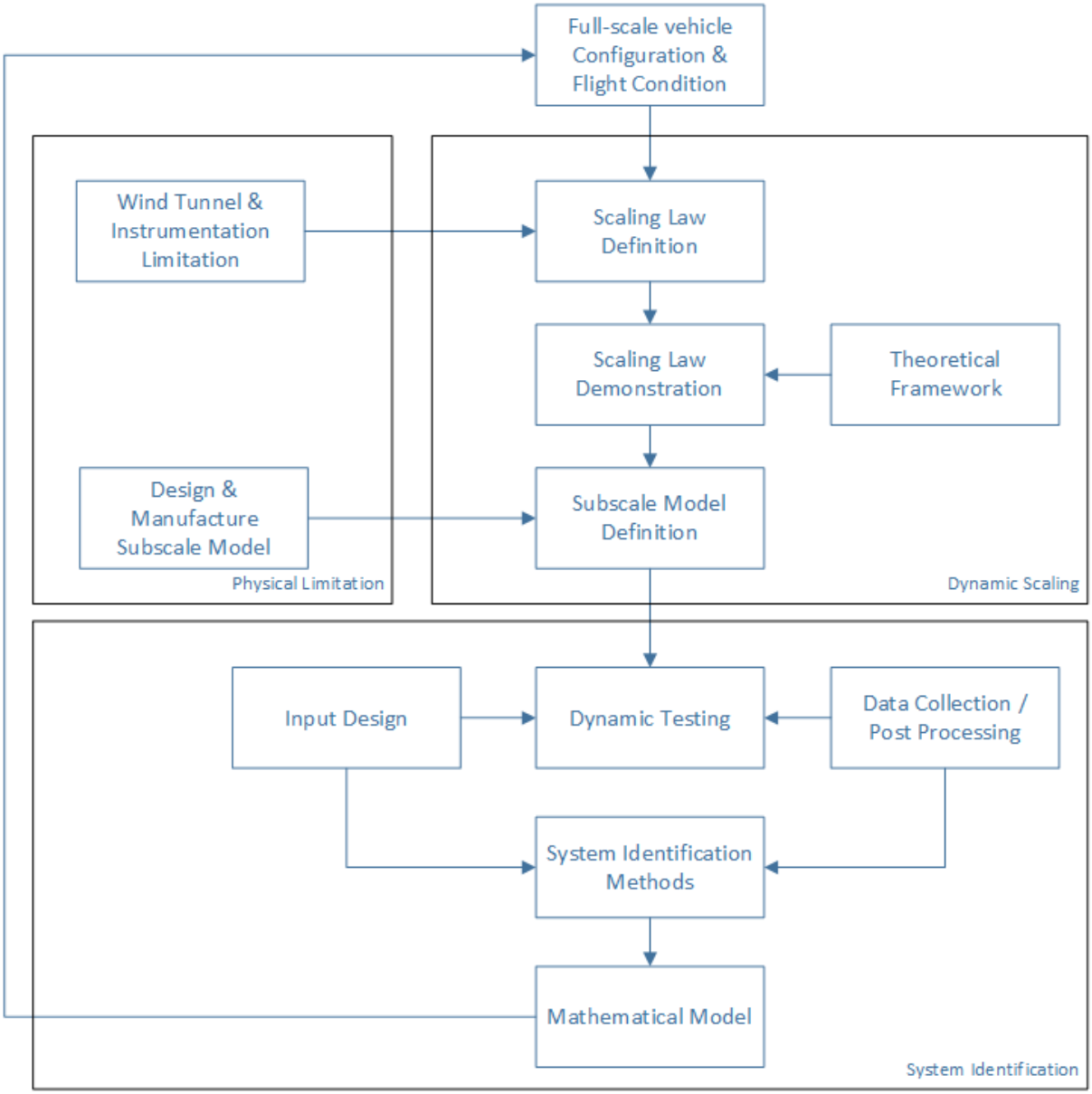

Figure 1.2: Research framework.

1.1 Aim and Objectives

The aim of this research project is to develop a methodology that enables the investigation of the complex flight dynamic behaviour of flexible aircraft by combining techniques for developing subscale models and methods within the field of system identification. To achieve this aim, the objectives of this research are defined effectively as exploratory studies, theoretical development and experimental testing.

Within the field of system identification, the exploration of time-domain system identification methods was conducted by:

- Assessing the limitations of time-domain identification methods.
- Reviewing the challenges in parameter estimation on experimental data.
- Understanding the differences in the identification methods when considering full-scale aircraft and subscale models, as well as the corresponding dynamics.
- Reviewing the various approaches in parameter estimation for flexible aircraft.

Theoretical development of subscale modelling for wind tunnel testing was done through:

- Review of scaling parameters and respective implications.
- Definition of scaling laws that relate the full-scale vehicle behaviour to subscale model dynamics.
- Development of a theoretical framework for assessing the scaling laws.

Experimental testing of the subscale model in a wind tunnel environment implies that the following requirements to be met:

- Assessing the limitations in manufacturing aeroelastic subscale model .
- Validation of the theoretical structural model.
- Validation of the theoretical aeroelastic framework based on wind tunnel experimental results.

1.2 Contributions to Knowledge

In practice a dynamically scaled model is valid for one flight condition only, mainly due to the interconnected relation between the scaling laws that force compromises in model design. In the past, this posed a significant difficulty in the use of subscale models, worsened by the fact that the cost of developing subscale models can be quite high. The work detailed in this thesis was conducted as part of a program aiming to develop a cheap, low cost approach to manufacture a dynamically scaled model [23, 24]. The key contribution

of this thesis is the development of a methodology to build and test dynamically scaled wind-tunnel models. As a case study, a flexible wing has been put through the scaling process and then manufactured (through PolyJet printing technology). Therefore, a cost-effective, dynamically scaled flexible model can be used at earlier design stages to mitigate risks. Also, the low cost manufacturing process allows the development of multiple subscale models, each aimed towards a particular flight condition.

The secondary contributions resulting from the application of the methods developed to achieve the overall aim can be listed as follows:

- Development of a regressor time-shifting method for identifying the rigid body dynamics, where measurements from two sensors in separate locations with different filtering and sampling rate exist [25].
- Suggest a model for identification method to observe the flight dynamic characteristics of a subscale aircraft inside a wind tunnel environment, where dynamic stall occurs [26].
- A method is proposed for the development of a reduced order flight dynamic model that takes into account structural flexibility as well as morphing wingtip effects [27, 28]. The application of this model in a real-time pilot-in-the-loop simulation has provided insight into the handling qualities of the vehicle [29].
- Adopted an approach based on non-dimensional equation of motion to highlight the scaling laws trade-offs when trying to satisfy scaling laws. This has added to the limited amount of literature available on this topic.
- Development of a theoretical simulation framework under the incompressible flow assumption, that has been used as a basis for the development of an aeroleastic subscale model.

1.3 Document Structure

This thesis consists of seven chapters that help build the research framework given in Figure 1.2. The thesis starts with the introduction of the work in Chapter 1, followed by a brief literature review in Chapter 2. The literature review focuses on existing work regarding dynamic scaling, aeroelastic systems, and system identification. The exploration of the System IDentification (SID)/Parameter Estimation (PE) methods are presented in Chapters 3 and 4. Chapter 3 focuses on the application of parameter identification techniques to a full-scale, subscale and structural problem using experimental data, while Chapter 4 explores the application of the SID/PE methods for aero-structural problems where aerodynamics, structure and inertial components are all coupled. This chapter is followed by the exploration of dynamic scaling trade-offs, which is demonstrated through the application of the similitude principles to a 2 Dimensional pitch-plunge aerofoil system in Chapter 5. Chapter 6 brings together all the concepts and lessons from the exploratory studies in the previous chapters and demonstrates application to a current problem: *development and identification of subscale high aspect ratio wing at the early stage design.* Finally, Chapter 7 concludes the thesis with a brief list of key findings and recommends areas of further work.

CHAPTER 2

Literature Review

The three important factors to be considered in aeroelasticity and flight dynamics are aerodynamic forces, inertial forces and elastic forces as presented by the Collar's triangle [30] in Figure 2.1. Understanding the interaction between these three factors is necessary to mitigate risks and ensure performance in aircraft development. For instance, the interactions between aerodynamics and inertial forces lead to the traditional view of flight mechanics, such as aircraft stability and control or aircraft response to atmospheric disturbances. On the other hand, the interaction between elastic and aerodynamic forces covers issues related to static aeroelasticity, such as divergence and control reversals. In the extreme case, the coupling between all three factors can lead to self-excited aeroelastic instabilities known as flutter. Traditionally, in the conceptual design stage, these fields are treated separately and individually optimised. This is reflected in the practice of design verification through proof-of-concept studies at the early stage. The usual practice is to carry out subscale model testing, which allows a practical means of focusing on a specific set of the aforementioned interactions [10, 31, 32].

This chapter starts with an elaboration of past studies that discuss experiments using a subscale model to address aerodynamics and flight dynamics problems, as well as aeroelastic problems. These experiments focused on dynamic testing. In this case, system identification plays a vital role in the interpretation of results from such dynamic testing. As a result, this chapter then continues with an overview of the important components

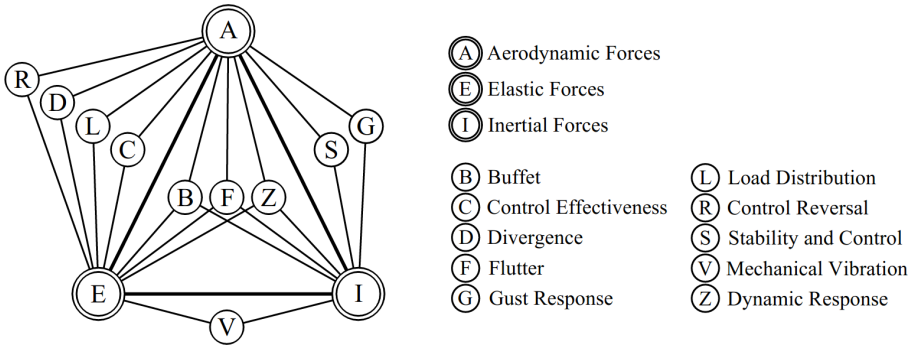

Figure 2.1: Collar's triangle (Reproduced from Reference [33]).

of System Identification. Discussed some past studies regarding the identification of the aeroelastic system. This is followed by a brief discussion on the interpretation of results from scaled tests (such as wind tunnel tests) and the impact on full-scale vehicle design.

2.1 Subscale Modelling

For ages, people have always relied on experimental testing to understand the characteristics of a system. Within aerodynamics wind tunnel testing become common practice. The first wind tunnel was designed by Francis Wenham in 1871 [34]. Although it turned out to provide little or no help in answering the aerodynamic challenges of that time, it highlighted the importance of lift-to-drag ratio, albeit at small angles of attack through direct lift and drag measurement [34]. Then in the 1910s, Eiffel successfully addressed the validity of the principle behind wind tunnel testing: *"The same force as is made by the thing against air, is made by air against the thing"*. He compared the aerodynamic force on a flat plate using wind tunnel and drop test, and found them to be the same [34]. Furthermore, Eiffel pioneered a complete aircraft wind tunnel test to show the correspondence between a model and its performance in actual flight.

Since then, testing a subscale model has become a widely accepted and valuable design and scientific tool, as mentioned by Chambers *"Progress in the technology associated with model testing in worldwide applications has firmly established model aircraft as a key element in new aerospace research and development programs"* [10]. The statement was also emphasised by Friedmann, who underlined the importance of wind tunnel tests using subscale models as a demonstrator for various methods [35].

One of the significant elements to utilising subscale models is that one can experiment with the condition which is dangerous/risky. For example, spin was a major aircraft safety concern in the early days of aircraft development, which triggered NASA to build a spin tunnel facility in 1920 [36]. The example of a subscale model for spin testing is presented in Figure 2.2 and it shows the variation of aircraft size for spin testing application in comparison with the full-scale aircraft.

Two different subscale models are commonly used for observing the flight dynamic characteristics during the aircraft design process: static and dynamic models. The 'static model' is specifically built for static wind tunnel tests. It is built to imitate the geometrical features and it focuses on extracting detailed aerodynamic data at a particular flight condition and configuration. The challenge in developing such static models is to reproduce the full-scale aerodynamic features, such as flow separation points and boundary layer conditions [10]. However, static testing only provides static aerodynamic data and ignores the dynamic effects. Thus, dynamic testing is introduced to fill the knowledge gap in observing flow physics due to aircraft motion. The practice of dynamic testing can be tracked back to as early as 1924, where Munk tested several airplanes with different weights and sizes to compare their performance [37].

Nowadays, for flight dynamics analyses, dynamic testing can be further divided into several categories such as: forced oscillation, single/multiple Degree-of-Freedom (DoF) wind tunnel tests, wind tunnel free-flight models and scaled technology demonstrators [16]. Each test tends to focus on a specific set of dynamics. For instance forced oscillation

Figure 2.2: Example of different test model used for spin testing. Left to right: full-scale aircaft, radio-controlled model, and spin tunnel model (Reproduced from Reference [10]).

tests are conducted to observe the dynamic derivatives related to angular rates, while the single DoF test is used to characterise the unsteady aerodynamics associated with phenomena such as wing rock [38]. The differences in the focus of such tests underlines the fact that each test needs a dedicated subscale model. For example, it is crucial for the free-flight model to be heavily instrumented, which is not essential for the forced oscillation test. A more comprehensive study on dynamic testing is available in References [10, 16, 38].

Another type of dynamic test that utilises subscale models is aeroelastic testing. An aeroelastic subscale model is designed to reproduce scaled static deflections and modal behaviour of the full-scale aircraft [30, 39]. The concept of scaling for both flight dynamics and aeroelastic testing is similar. However, the development of the subscale model focuses on different similarity issues. In contrast with the subscale model for flight physics development which is assumed to be rigid, the aeroelastic subscale model needs to consider structural flexibility. This is characterised by matching the structural stiffness and the distribution of mass [30]. Aeroelastic tests aim to evaluate phenomena related to flutter, gust response, divergence, as well as limit cycle oscillations [40–42] . The problem can also be extended to an aeroservoelastic problem in which the control surface is free to move and the response of the free-play control surfaces is observed through experimental tests.

2.1.1 Similitude Requirements

As discussed in the previous section, the development of a subscale model is heavily dependent on the technical domain and phenomena that is of interest. In particular

Scale Factor	Incompressible Flow	Compressible Flow
Linear dimension	n	n
Relative density ($m/\rho l^3$)	1	1
Mach number	-	1
Froude number ($U/\sqrt{lg}$)	1	1
Linear Acceleration	1	1
Weight, mass	$n^3/\left(\rho/\rho_0\right)$	$n^3/\left(\rho/\rho_0\right)$
Moment of inertia	$n^5/\left(\rho/\rho_0\right)$	$n^5/\left(\rho/\rho_0\right)$
Linear velocity (U)	$n^{1/2}$	$n^{1/2}$
Angular velocity	$n^{-1/2}$	$n^{-1/2}$
Time	$n^{1/2}$	$n^{1/2}$
Reynolds number (Ul/υ)	$n^{3/2}\upsilon/\upsilon_0$	$n^{3/2}\upsilon/\upsilon_0$

n is the linear scaling factor, ρ_0 representing the air density at sea level, υ representing kinematic viscosity, $\upsilon = \frac{\mu}{\rho}$, and υ_0 representing kinematic viscosity at sea level.

Table 2.1: Scale factor for a rigid subscale model (Reproduced from Reference [10]).

for examining dynamic behaviour through *dynamic testing*, the subscale model needs to satisfy the dynamic similarity requirements relative to the full-scale model. Table 2.1 is an example of the required scale factors for developing a rigid subscale model. A dynamic model that is not dynamically scaled will not allow the observation to be related with the real full-scale vehicle [16]. In general experimental testing using subscale models must satisfy the following similitude requirements [10, 32]:

- **Geometric Similarity**: the basic necessary similitude requirement [43], where the subscale model must have the geometrical representation of the full-scale model. The practice of matching the geometric similarities can be traced back to one of the earliest dynamic testing experiment, where Munk matched the shape and diameter of the propeller for the subscale aircraft development [37]. This requirement forms the basis for other similitude requirements especially when considering Froude number similarity.

- **Froude Number**: a ratio of flow inertia to the external force. This criteria is a necessary condition for similarity in mechanical phenomena [43]. Froude number does not consider the viscosity and compressibility of the fluid, but a "free surface" at constant pressure; when the fluid is a gas, this law applies due to the effect of gravitational force [44]. It relates the velocity components of a model corresponding to body forces. The Froude number is defined as:

$$\mathrm{Fr} = \frac{U}{\sqrt{\bar{c}g}} \tag{2.1.1}$$

  where U is the free stream velocity, $\bar{c}$ is the characteristic length, and g is gravitational acceleration. The Froude number similarity in a subscale aircraft test is essential when the force due to gravity is being considered since gravitational acceleration is not scalable. For a flight dynamic test, Froude number is an essential

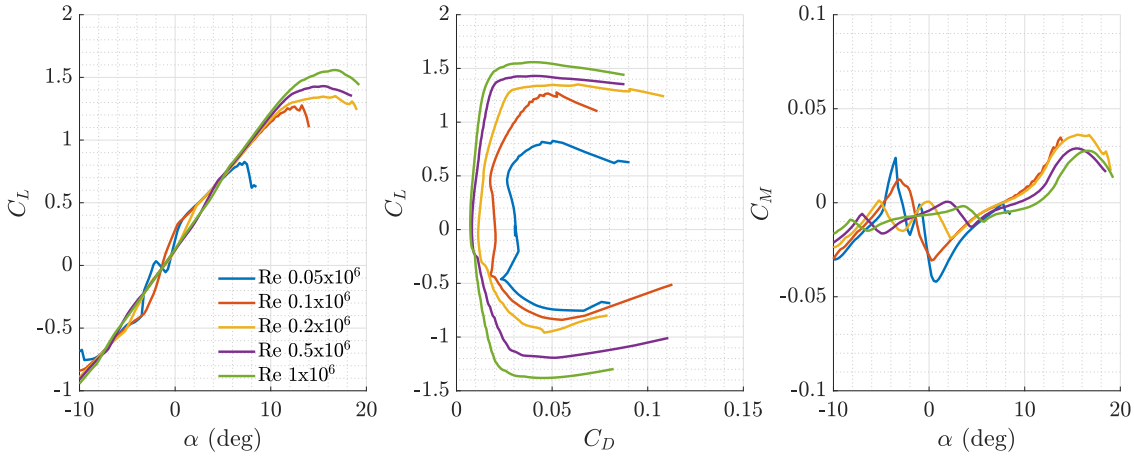

Figure 2.3: Reynolds number effects on force and moment characteristics (Data are generated from Reference [45]).

parameter to observe the manoeuvring vehicle, for example during coordinated turn or level flight [32] where the lift force counteracts the gravitational force.

- **Reynolds Number**: the ratio between inertia forces of the fluid and the viscous force. One of the crucial properties that affects the Reynolds number is viscosity [43] and this non-dimensional parameter is define as:

$$\mathrm{Re} = \frac{\rho U \bar{c}}{\mu} \tag{2.1.2}$$

in which ρ is the air density, U is the aircraft velocity, $\bar{c}$ is the characteristic length and μ is the dynamic viscosity. Viscosity, or the stickiness of the gas, affects the boundary layer development which in turn influences the aerodynamic forces acting on the object. Figure 2.3 presents the effect of Reynolds number variation on the aerodynamic characteristics of a NACA-23015[1] [45]. The figure shows that at lower Reynolds numbers the aerofoil stalls at a lower angle-of-attack while experiencing a higher drag coefficient. The difference in the Reynold number also affects the trends in the pitching moment coefficient as a function of angle of attack. Due to its effect on the flow pattern, Reynolds number similarity is generally essential for all types of fluid dynamic problems [46]. However, Reynolds number is often compromised and considered as a secondary parameter for many dynamic tests highlighting the difficulties in satisfying this similarity requirement [47].

- **Mach Number**: this captures the compressibility effects within a fluid medium. It is the ratio between the inertial and the compressibility force and it is an essential criterion for scenarios where compresibility effects cannot be ignored. For an object that operates above Mach > 1, a shock wave formed in the nose area provides a mechanism for drag generation that is not present in subsonic flow [46]. For the development of a subscale model, there is a trade-off between Mach number matching and Froude number matching, as both of them are functions of velocity. Froude number is given in Equation 2.1.1, while Mach number is expressed as

[1]The data given here is based on Xfoil where the calculation, neglected the compressibility effect (Mach number), and also considered a common wind tunnel distrubance level.

follows:

$$\mathrm{Ma} = \frac{U}{a} \tag{2.1.3}$$

where a is the speed of sound, and U is the airspeed. It is almost impossible to match both Froude and Mach number simultaneously, and often one of the similarity requirements needs to be sacrificed. For flight dynamic tests, the model data based on Mach number scaling may not be able to represent the flight dynamics characteristics [32, 47], which consequently leads to ignoring the Mach number similarity criteria. However, Mach number affect the Coefficient of Lift (C_L), especially when comparing an atmospheric free-flying subscale model with high-speed full-scale aircraft. Thus, to maintain the C_L similarity, the test has to be conducted in a different flight condition than that of the full-scale aircraft [47]. For a more detailed discussion on the similitude investigation at full-scale Mach numbers and its trade-off with Froude number similarity, the reader is referred to Reference [31].

- **Strouhal Number**: this is related to the oscillatory dynamics of the aircraft. It is the ratio between local and convective inertia forces [46], and it is an important consideration when unsteady, nonlinear flow conditions are dominant such as during a spin testing [16, 32]. Strouhal number is defined as:

$$\mathrm{St} = \frac{\omega \bar{c}}{U} \tag{2.1.4}$$

where, ω is the frequency, $\bar{c}$ is the characteristic length, and U is the velocity. The Strouhal number has a similar form with reduced angular velocity, although the latter applies to different parameters. Reduced angular frequency is related to angular rates and control surface rates, while the Strouhal number is related to unsteady flow effects caused by the oscillatory perturbations of the aircraft. In the application of the aeroelastic system, the reduced frequency parameter is of importance [30, 48] because the aerodynamic derivatives (especially lift coefficient) may be significantly affected by the unsteadiness of the flow. As an example, in flutter testing the Strouhal number is used to relate the flutter frequency of the full-scale aircraft and subscale model [32].

- **Relative Mass Properties**: an essential parameter for a subscale model where inertial forces are considered. Included in this category are relative density and relative mass moment of inertia. The importance of matching relative mass and inertia for dynamic testing for flight dynamics application goes back to the 1920s when Scherberg developed a methodology to match the scaled inertia, mass and the position of the centre of gravity for rigid body spinning tests. This was accomplished by building a lighter model that was loaded with the mass for a specific distribution [49]. For a flexible aircraft, similitude in mass distribution is required to ensure the similitude in the loading distribution and the elastic deformations [32]. Moreover, relative mass properties is an important factor for subscale model studies of flutter.

- **Relative Structural Properties**: essential for a subscale model where structural properties must be considered, such as the study of flutter or an aircraft flexible body modes. Included in this requirement are both similarity in the structural bending and torsional stiffness parameters. These parameters are related to mate-

rial properties and geometrical shape of the subscale model [48, 50]. For a static aeroelastic test, the similitude of these parameters are of primary concern, while mass scaling is considered not to be as critical [32].

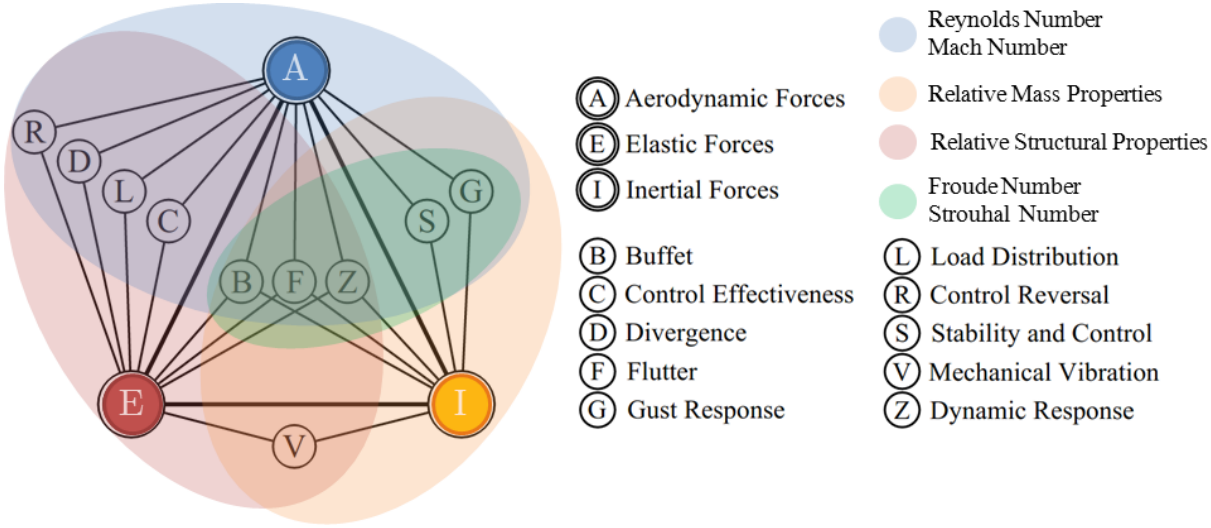

Figure 2.4: Similitude requirements in the Collar's triangle (Modified from Reference [33]).

The relation between the similitude requirements and the dynamics of interest is highlighted in the Collar's triangle shown in Figure 2.4. Although often compromises, Mach number and Reynolds number are crucial factors for ensuring aerodynamic similarity. Likewise, the similarity in the relative structural properties is essential for testing that includes elastic forces, while relative mass and inertia scaling are crucial for testing that includes inertial forces. In the case of two forces interacting, matching the similitude requirements that are related for both forces is also crucial. As an example, for mechanical vibration problem, the subscale model should be scaled according to the mass and inertia distribution, as well as the structural characteristics (specific bending and torsion parameters). However, in the case of all three forces interacting, such as buffet, flutter or dynamic response, both Froude number and Strouhal number similarity have to be matched as well.

Ideally, a subscale model should entirely represent the full-scale model. However, it is rarely possible to scale down all dynamic similitudes simultaneously [51]. One needs to focus on the parameter which is the most important for a particular dynamic of interest [16, 32]. For example, it is only possible to have a subscale model that matches both Froude and Mach number, if the subscale model is flying in a different medium or tested at different flight conditions (e.g. angle of attack setting) [32]. Consequently, the scaling laws when designing a wind tunnel subscale model should be carefully chosen based on (1) similitude requirements, (2) dynamics of interest and, (3) wind tunnel capabilities [52].

2.1.2 Similitude of Aeroelastic System

Flutter is considered to be one of the most critical aeroelastic engineering problems that can result in catastrophic structural failure, and even today, its prediction poses an

engineering challenge. Nevertheless, due to the design process and culture of today's aerospace industry, where design problems are addressed separately, flutter instability conditions can appear late in the aircraft development cycle [48, 53]. Figure 2.5 illustrates the rough order in terms of modal frequencies of the natural modes for the various design problems of interest. In this diagram, the aerodynamics model also represents the flight-dynamic model placed in a low frequency dynamics, the finite element model represents the structural dynamics at higher frequency dynamics, while the aeroservoelastic model covers a much wider spectrum of dynamics as it requires the coupling of the aerodynamics and the structural dynamics. The figure also illustrates experimental testing as part of the design process. Wind tunnel testing conducted to evaluate the low frequency dynamics, while the ground vibration test is conducted to validate the finite element model. Furthermore, flutter tests are conducted to understand the aeroelastic behaviour.

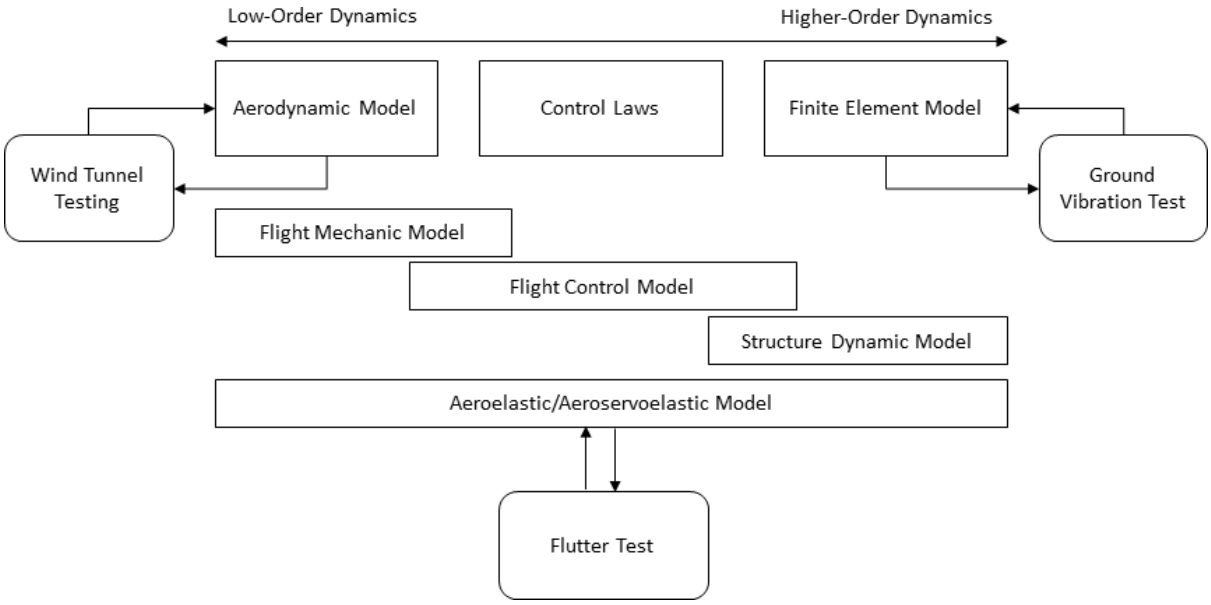

Figure 2.5: Model and experiments in aircraft design (Reproduced from References [48, 54]).

Assessing for flutter instability at a later design stage is possible for a conventional aircraft because the frequencies between the flight dynamics and aeroelastic modes are well separated. The rigid body mode frequency is usually less than 1 Hz, and the elastic frequency of a conventional aircraft is around 2-3 Hz [55], although the elastic frequency can be as low as 1 Hz in some advanced supersonic aircraft [55]. The same problem also arises when the aircraft has high aspect ratio, lightweight wings. Structural flexibility can move the aeroelastic frequencies closer to the rigid body dynamics and consequently result in undesirable and complex non-linear aeroservoelastic coupling [55–58], and possibly more critical flutter issues [59–62].

With the advent of high aspect ratio wings, the issue of structural flexibility and its coupling with flight dynamics has become more and more critical. The similitude requirements need to be revisited if scaled technology demonstrators are to be used. Friedmann [35] describes twelve classical scaling parameters that must be considered to scale down a 2-Dimensional aerofoil in incompressible flow. However, this classical aeroelastic scaling is inadequate to deal with the problem where the system such as control system actuation is also involved. Pototzky [63] developed an aeroservoelastic analytical model by incorpo-

rating the aeroelastic equations of motion with gust and control surfaces, which was only valid for a structure with small deformations. In developing the scaling law, the common scaling factor being used to relate the full-scale and subscale model are the comparison between the geometrical length (S_g), speed (S_U) and air density (S_ρ), as follows:

$$S_g = \frac{\bar{c}_{FS}}{\bar{c}_{SC}} \tag{2.1.5}$$

$$S_U = \frac{U_{FS}}{U_{SC}} \tag{2.1.6}$$

$$S_\rho = \frac{\rho_{FS}}{\rho_{SC}} \tag{2.1.7}$$

Here, FS represents the full-scale aircraft while SC represents the subscale model, and the geometrical scaling is done via the mean aerodynamic chord ($\bar{c}$). These common scaling factors also work for scaling gust response [64, 65]. Furthermore, Wan and Cesnik also found that these common scaling factors for linear structures is also applicable for non-linear structures that exhibit large deformations [66].

Nevertheless, Froude number similarity can dictate the relationship between the geometrical and speed scaling laws of the subscale model and the full-scale aircraft [65]. Although the importance of the Froude number for an aeroelastic system is still debatable. For a small subscale UAV (Unmanned Aerial Vehicle), Oulette [67] found that the effect of Froude number is less significant if the dynamics are only restricted to the short period mode and certain structural dynamics. In contrast, Wan and Cesnik [66] emphasise that Froude number plays a vital role to guarantee the matching of nonlinear stiffness properties between models. Froude number is important for wind tunnel experiments in which gravity provides one of the loads, such as for side wall mounted models [65]. Mounting a subscale model on the floor can eliminate the need of matching the Froude number, as in this configuration, the gravity does not affect the wing load distribution.

Another similitude requirement to be considered is Mach number similarity. This requirement is vital for rotary wing applications but not very critical where the flow can be assumed to be incompressible [35]. Ting et al. [68] suggested that the change in Mach number affected the lift curve slope of the aircraft and considered this effect by aiming for a similar C_L value, obtained through a higher angle-of-attack setting for the subscale model [68]. For the use of aeroelastic subscale models, especially to observe flutter or limit-cycle oscillations, it is also essential to match the reduced frequency [65]. Furthermore, French and Eastep [39] also emphasise the need to match both frequency and structural mode shapes simultaneously [69, 70]. To verify the scaling process between the fullscale and the wind tunnel subscale model, Pototzky utilised root locus patterns [63]. The root locus is used to show the pole position of each aeroelastic mode. Furthermore, root-locus pattern is also used to predict the change in the aeroelastic mode of the subscale model for various dynamic pressures. If the patterns are scaled correctly, it reassures the fact that flutter frequencies and flutter dynamic pressures of the subscale model are scaled accordingly [63].

On the other hand, Ricciardi et al. [69, 71] have developed the non-dimensional aeroelastic equations of motion and used it as the basis of the non-linear optimisation routine for developing a subscale model. Here, one of the criteria is to match the modal properties (frequency, mode shape and modal masses) for a truncated number of modes which fall

within the frequency range of interest. Another optimisation method proposed by Spada et al. [72] is based on two optimisation loops. Here, the first loop aims to match the static deformation while the second loop targets the natural frequencies and mode shapes. Nonetheless, none of the previous studies discuss the damping characteristics of either the subscale or full-scale, except in Reference [70] where a cost function is proposed to directly scale the aeroelastic equation and to match aeroelastic reduced frequency and damping. However, this method is computationally expensive because it requires aeroelastic analysis for each optimisation cycle.

2.1.3 Development of Subscale Model

The subscale model is developed based on the scaling laws and dictated by the similitude requirements. However, the consequence of applying scaling laws to build a subscale prototype is that the sub-scale model cannot be manufactured in a similar way to the full-size aircraft [71]. This shows the importance of choosing appropriate design and material properties for the subscale model.

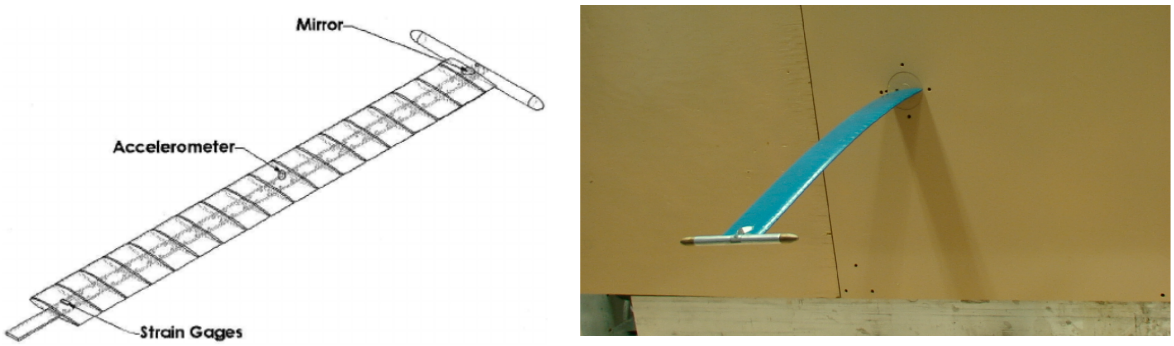

Figure 2.6: Example of aeroelastic wind tunnel model (Reproduced from References [42] and [73]).

A common method for building an aeroelastic model for wind tunnel testing is by designing a spar that represents the stiffness of the wing coupled with the aerodynamic external shape using light balsa pods [17]. Usually, concentrated lumped masses need to be placed carefully in order to match both modal frequencies and mode shapes [39]. To study the aeroelasticity of high-aspect-ratio wings, Tang and Dowell [42, 73] used a flat steel spar with multiple thin flanges to reduce torsional stiffness and make it more flexible. The aerodynamic profile was made of 18 aerofoil pieces glued to the spar with spaces between plates filled with light wood (basswood), as presented in Figure 2.6. This wood resulted in additional mass which contributes towards a small increment of bending and torsional stiffness [73]. It is worth mentioning that this wing is not a representation of a full-scale system, meaning that no scaling laws has been applied here.

For a dynamically scaled wing design, the internal structure should be designed to match both the bending and torsional stiffnesses. In fact, these dictate the choice of material property for the subscale model. Previous work on building the subscale model includes the use of ladder configurations [71], spar and stinger configurations [41] as well as conventional rib and spar configurations [72, 74]. Other variations include flange spar

configurations [75]. Figure 2.7 presents examples of the different structural design that can be used for the development of a subscale model. The reader is referred to Reference [30] for a more detailed explanation on different spar configuration and its consequences to the structural properties of a model.

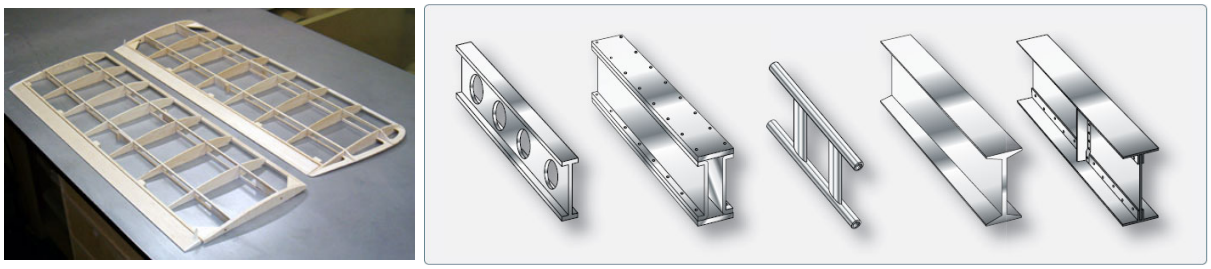

Figure 2.7: Example of the internal structural design for subscale model, left: rib and spar configuration, and right: various spar configuration (Reproduced from References [76, 77]).

The spar design is not only determined by the choice of material but also depends on the method used to attach the aerodynamic profile to the spar. For a rib and spar configuration, a thin layer of skin can be used to cover and form the aerodynamic shape. For this type of design the skin can be made using fibreglass or composites [41, 74]. Alternatively, polyethylene can be used to introduce the aerodynamic shape while balsa may be used as local support for a ladder configuration as discussed in Reference [71]. It is often assumed that the chosen material for manufacturing the aerodynamic shape introduces negligible stiffness to the subscale model. And hence, requires designers to focus on optimising the spar design to match the target stiffness properties [71]. Appropriate mass/inertia distributions can be achieved using balsa wood with stainless steel/aluminium ribs [74], foam/PVS core [41], carbon fibre [78], or aluminium [71].

Alternatively, 3-D printing technology is available today and provides a quick, cheap and simple way to build subscale models. This technology allows the accurate manufacturing of thin but solid models [79]. The idea to utilise 'replica-type plastic model' is not new, and in the past, the manufacturing tolerance, changes in material properties and the cost of fabrication were the challenges that limited the wide spread use of this method [17]. It is arguable that the manufacturing precision is lower when compared to traditional metal models. However, for an initial design test, a 3-D printed subscale model is sufficient as a proof-of-concept, especially considering the lower cost and manufacturing time [80]. Although the wind tunnel model being discussed in Reference [80] is a simple model of a missile's nose cone, and not a wing configuration. Nowadays, the cost of 3-D printing is economically acceptable and at the same time allows a more complicated design to be easily manufactured. The use of 3-D printing for developing a subscale model is becoming increasingly popular and is suitable for the development of the subscale models, for instance a scaled wing-box structure [81], or a flexible half-wing designs [82]. However, even with this available technology, the problems for developing highly flexible subscale wings are still addressed conventionally by designing the aerodynamic profile in sections and leaving a small gap between each section [68, 73, 82]. The latter often leads to undesirable aerodynamic flow around the gap regions [24].

To overcome this issue, Pankonien and Reich [83] built a wind-tunnel flutter model using multi-material 3-D printing techniques. This multi-material printing allows stiffness

control along the span with elastomeric breaks to maintain a continuous aerodynamic surface [83]. The results show that the printed subscale model achieves a predictable response with flutter speed within 15% of the predicted value and a modal assurance criterion of greater than 0.89 for the first three mode shapes. This novel 3-D printing technique uses Polyjet technology that allows printing multi-material components in a similar manner to the inkjet printer which prints using multicolour ink [84]. The Polyjet 3-D printer uses jets to layer a photopolymer curable resin onto the printers build bay [84]. The careful combination of multiple materials in this technology allows printing both rigid and flexible (elastomeric) components within the same build. Therefore, 3-D PolyJet printing can be a rapid and inexpensive solution for developing subscale wind tunnel models, especially where structural deformation is of interest. However, literature regarding the use of multi-material printing for developing dynamically scaled models is still limited. The reader is referred to Reference [84] for a detailed description of this manufacturing method and Reference [85] for reviews on the additive manufacturing processes

2.2 System Identification

The subject of system identification is a part of systems theory that deals with an inverse problem, as referred by Iliff [86]: "*Given the answer, what was the question?*". However, a more comprehensive definition of system identification is given by Zadeh [87] as "*determination, on the basis of observation of input and output, of a system within a specified class of systems to which the system under test is equivalent*". This subject deals with not only theoretical aspect but also practical components. As highlighted by Ljung [88], system identification is "*[an] 'art' and science to construct a mathematical model of a dynamic system based on observed input-output data*". Here, the 'science part' is related to the techniques for parameter estimation and model structures determination, while the 'art' deals with the practical application in defining and addressing the problem.

The origins of system identification can be traced back to statistical theory and curve-fitting. The early stages of system identification occured through analogue matching, and as digital computers emerged, more advanced estimation techniques subsequently evolved. References [89–92] present the surveys and recent applications of system identification over the last few decades highlighting the challenges of system identification. These can be categorised in the four essential components referred to as **Quad-M** [54]: **Manoeuvre**, **Measurement**, **Models**, and **Methods** as given in Figure 2.8. Each of these components will be described in the following section.

2.2.1 Manoeuvre

As explained earlier, system identification is an inverse problem in which accurate observations are of high importance. As mentioned by Jategaonkar [54] "*If it is not in the data, it cannot be modelled*" meaning that the manoeuvre for identification purposes should be able to capture the dynamics of interest. In other words, it is important to design the experiments such that relevant dynamics of the vehicle are sufficiently excited

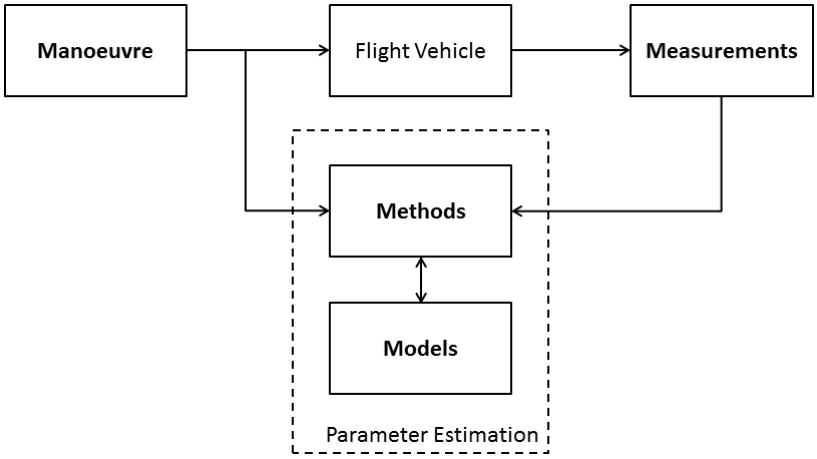

Figure 2.8: Four essential components of system identification (adopted from Reference [54]).

for system identification purposes. One of the ways in desiging the experiment is through input design, which requires the consideration of the following [93]:

- The input must be able to excite the modes and corresponding parameters appropriately (Sensitivity).
- The input signals (amplitude, bandwidth, and rates) are realisable by the specific actuators (Realisability).
- The input should restrict the motion of the aircraft within the identified flight region of interest (Model limitation).

For a conventional aircraft, system identification can be used to obtain the key parameters corresponding to the aircraft dynamics such as the short-period, phugoid and dutch roll modes. Each components of each observed dynamics acts over a different frequency band characterised by the eigenfrequency. For example, the phugoid mode has a slower dynamic compared to the short-period mode. Furthermore, when considering flexible aircraft, the resonance frequency of each structural mode needs to be considered as well. Hence, for identification purposes, the input must have enough energy to excite the frequencies around the eigenfrequency of interest. In that case, experiments can be designed to capture a wide range of frequencies or repeated multiple times while targeting different frequencies of interest.

In general, the classical input designs for aircraft identification are: step, doublet, 3-2-1-1 and frequency sweep. The step, doublet and 3-2-1-1 are classified as square input, while the frequency sweep input belongs to the category of sinusoidal input [54, 94]. Each input design has a different bandwidth and magnitude of excitation energy. An illustration of the different input design methods in the time domain and the energy spectra in frequency domain are presented in Figure 2.9. The frequency sweep input in Figure 2.9 is designed to cover the range of 0.2 to 1 Hz. The figure shows that 3-2-1-1 input and frequency sweep input have a wide frequency band (in terms of energy spectrum) compared to the step and doublet input. These inputs are able to excite more of the system dynamics and it is worth noting that the increase in the frequency bandwidth is proportionally inverse

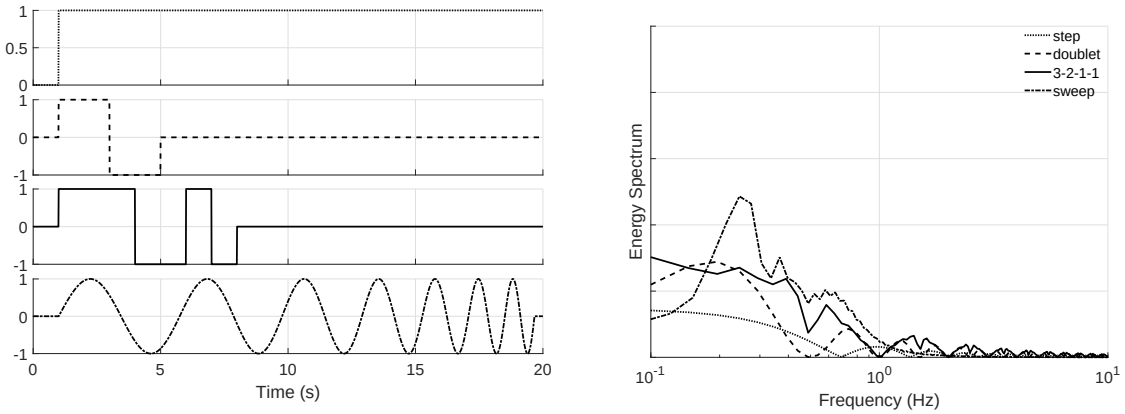

Figure 2.9: Time and frequency domain comparison of various inputs.

to the change in the energy content [54]. A low magnitude energy content means that the input might not be able to excite the system adequately.

For time domain identification, the 3-2-1-1 input is preferable due to the higher bandwidth and a more uniform energy content compared to other square input. On the other hand frequency-sweep input should be used for the identification methods in frequency domain [95]. However, both 3-2-1-1 and frequency sweeps inputs tend to drive the aircraft away from the test flight conditions due to the low-frequency content at the beginning of the frequency sweep and the first three pulse input in the case of 3-2-1-1 [94]. Thus, the challenge in designing an input for identification purposes lies in maximising the data content in the most efficient way. Furthermore, it is preferable that the input only results in small deviations to keep the vehicle around the trim condition. By doing so, small perturbation assumption can be used for identification purposes allowing the more straightforward identification of linear models.

Several ongoing works on the development of optimal input in short duration flight are available in References [96–98]. Amongst those, an optimal input design is the orthogonal multi-sine input. One of the examples of the multi-sine input is for identification of a hypersonic aircraft [99]. This input design approach is an extension of Schroeder sweep input design [98] which is optimised and then used simultaneously for more than one control surface to excite the different modes in an orthogonal sense. The idea behind multi-sine input is similar to the frequency sweep input: to excite the specific modes in the frequency region of interest. Instead of continuously applying a sinusoidal input with increasing frequency, a sum of sinusoids over various frequencies, amplitudes and phases are used. This results in a shorter signal duration compared to the traditional frequency sweeps and higher frequency bandwidths compared to the standard 3-2-1-1 input. It should be noted that this requires at least some a-priori knowledge of where the dynamics of interest lie in the frequency domain. The multi-sine input[2] takes the following form [94]:

$$u(t) = \sum_{i=1}^{n} A_i \cos\left(\frac{2\pi i t}{T} + \varphi_i\right) \tag{2.2.1}$$

where n is the total number of harmonic frequencies, T is the time length of the excitation,

[2]The multisine input design is generated through the `mkmsswp.m` function within the SIDPAC (System IDentification Programs for AirCraft) library [94]

and φ_i is the phase of each harmonic components. The latter is chosen to produce a low peak factor (PF) defined as [94]:

$$\mathrm{PF}(\mathbf{u}) \equiv \frac{[\max(\mathbf{u}) - \min(\mathbf{u})]/2}{\sqrt{(\mathbf{u}^T\mathbf{u})/N}} \tag{2.2.2}$$

A single sinusoid has a PF of $\sqrt{2}$ and relative peak factor (RPF) is thus defined as:

$$\mathrm{RPF}(\mathbf{u}) = \frac{PF(\mathbf{u})}{\sqrt{2}} \tag{2.2.3}$$

RPF is a way to measure the efficiency of the input for identification purposes. A single sinusoid has RPF equal to 1. For parameter estimation purposes, a low RPF is preferable because in this case the input has sufficient energy with low amplitude for a wide range of frequencies. Low amplitude input also implies that the excitation did not drive the aircraft away from the nominal operating point. An in-depth mathematical view on optimising the multisine excitation is given in Reference [100].

For aircraft identification, input design is usually performed through the use of the control surfaces such as elevators, ailerons and rudder, depending on the dynamics of interest (or using all the control surfaces orthogonally for multi-sine orthogonal input). It is uncommon to use the flap to excite the dynamics because the flap actuators usually do not provide sufficient bandwidth. However, in the case of identifying the wing bending dynamics of a sailplane, de Silva and Mönnich [101] argued that flaps are suitable for dynamic inputs as it provides direct influence on wing lift rather than the elevator. By having a direct change of the wing force, it is more efficient in exciting the wing bending modes compared to the elevator deflection. This is because the lift developed from the variation in the angle of attack has a delay response from the aircraft pitching dynamics. Furthermore, in the case of identifying flexible transport aircraft, Najmabadi [102] found that the frequency sweep input through rudder does not adequately excite any modes. For a shorter input duration, Grauer et al [103] utilised multi-sine input for extracting models of an aeroelastic joined-wing wind tunnel model. However, unlike the square or frequency sweep input, it is impossible for the pilot to produced multi-sine command input. Thus, this input can only be performed through the use of a computer controlled flight control system.

2.2.2 Measurement

The purpose of system identification is to find a suitable model based on the measured dynamics. Although the manoeuvre should be designed to capture the dynamics of interest, if the measurement was not able to capture the dynamics, the identification results cannot be trusted. Thus, the problem of measurement in system identification focuses on data gathering activities, such as accurate data acquisition and instrumentation systems.

Data acquisition deals with data collection: the records of time series data of input and output variables. Here, the discussion of the problem related to data acquisition is limited to the sampling rate of the sensor. According to Nyquist frequency, a sampling rate of

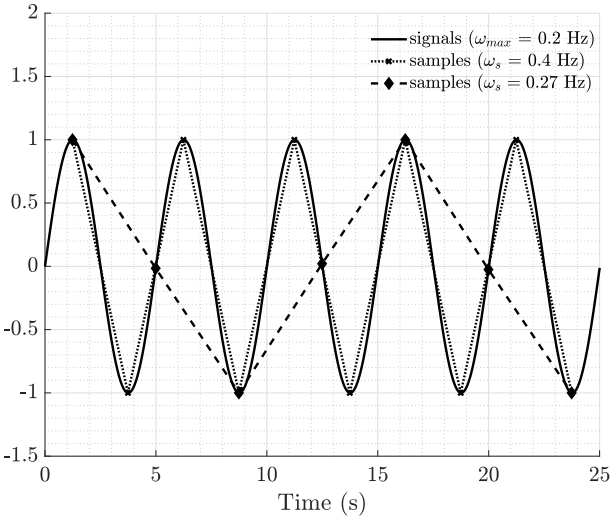

Figure 2.10: Nyquist frequency and aliasing problem.

ω_N can capture frequency content up to $\omega_s/2$.

$$\omega_N = \omega_s/2 \tag{2.2.4}$$

This means that the sampling rate according to Nyquist frequency needs to be at least twice the maximum frequency of interest (ω_{max}) [104]. Figure 2.10 presents the comparison of the signals with the frequency of interest of 0.2 Hz and the sampling frequency of 0.4 Hz. Here, the sampling frequency of 0.4 Hz means that frequencies as low as 0.2 Hz can be captured. Furthermore, the figure also illustrates the pre-sampling data problem known as aliasing. For this illustration, the sampling frequency of 0.27 Hz is chosen, resulting in a Nyquist frequency of 0.135 Hz. By doing so, rather than capturing the signals at 0.2 Hz, this rate is capturing at a much lower frequency of 0.07 Hz. A falsely attributed high-frequency signal to lower frequencies due to the sampling process is known as the aliasing problem [94].

The aliasing problem as well as noise and atmospheric disturbances suggest a higher sampling rate for accurate estimation near the maximum frequency of interest [94, 95]. In fact, Tischler [95] stated that the rule of thumb is to select filter bandwidth (ω_f) at least five times the maximum frequency of interest, and the minimum sampling rates of five times higher of the filter bandwidth.

$$\omega_s \geq 5 \cdot \omega_f \tag{2.2.5}$$

$$\omega_f \geq 5 \cdot \omega_{max} \tag{2.2.6}$$

combining both equations results in

$$\omega_s \geq 25 \cdot \omega_{max} \tag{2.2.7}$$

This means that to identify a system that has maximum frequency of interest of 2 Hz, the minimum sampling rate of the sensor should be 50 Hz.

Regardless of the sampling rate, a proper instrumentation system is needed and that has to be located appropriately within the airframe. A standard instrumentation system for

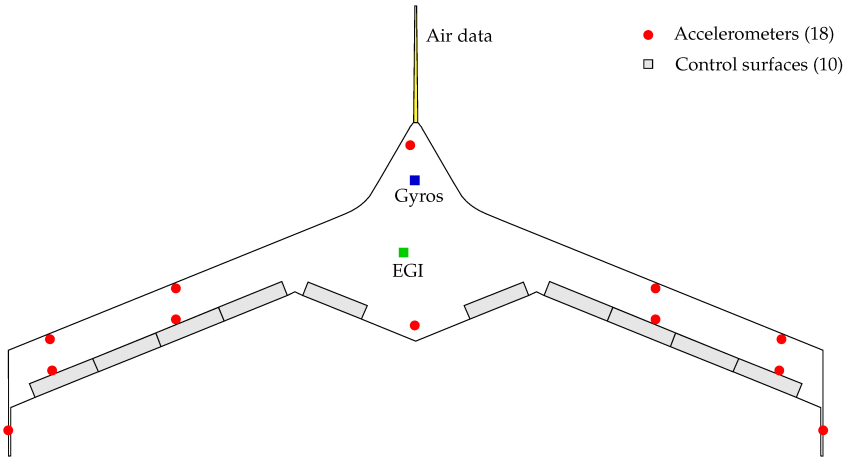

Figure 2.11: Example of sensor location for aeroelastic identification (Reproduced from Reference [105]).

rigid body aircraft identification from flight data includes [94]:

- the use of vanes (air-relative velocity) to measure the angle of attack, sideslip angle and airspeed.
- the use of accelerometers and gyroscopes to measure the translational accelerations and angular velocities respectively. Both sensors are positioned to align with the body axes of the aircraft.
- the use of potentiometers to measure control surfaces deflection and pilot inputs.

For aeroelastic identification, such as flutter, more sensors have to be deployed to identify the structural behaviour. An example of sensor locations of a subscale aeroelastic research aircraft is given in Figure 2.11, and it consists of: potentiometers at control surfaces (grey area)[3], 18 distributed accelerometers (red dots), embeded GPS/INS (EGI) system (green square), gyroscopes (blue dot) and air data vanes (yellow) [105]. A more in-depth discussion on the type, number and location of the sensors for aeroelastic testing (flutter test in particular) can be found in Reference [106]. Moreover, Reference [101] presents practical comparative results of aeroelastic aircraft identification from various sensors including accelerometers and strain gauges. A more in-depth discussion on the use of strain measurement to identify structural behaviour can be found in Reference [107].

In practice, each measurement device has systematic and random errors. Given the numbers of the sensor for aircraft identification, a method to check the consistency of the measurement is needed. This approach is also known as data compatibility analysis, which is based on the kinematic relationships. The compatibility analysis is needed to ensure that the measured data is consistent and free from systematic errors, such as time lag, scale factor, and zero shift biases. For further elaboration on data compatibility check the reader is referred to References [54, 94].

[3]The exact location of the potentiometers in the control surfaces are not exactly specified in Reference [105]

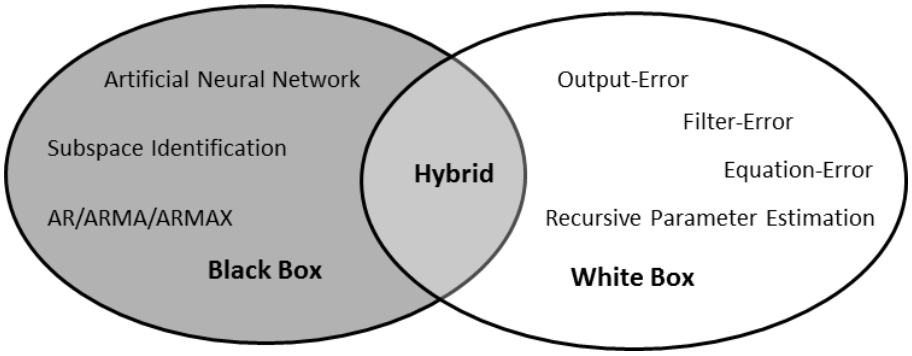

Figure 2.12: Example of methods used for aircraft identification.

2.2.3 Methods

System Identification is applicable in both time and frequency domains. The basis for frequency domain identification method is the Fast Fourier Transform (FFT) which transforms the time domain data into frequency domain data [108]. It is arguable that the frequency domain has advantages when compared to the time domain. Frequency domain allows direct estimation of the control input through transfer functions and, most importantly, it does not require numerical integration, so there is no risk of divergence in the parameter estimation algorithms [95, 108]. Thus, these methods can be used to identify unstable systems. On the other hand, by applying a Fourier Transform the transformation from time to frequency domain data is prone to leakage errors [109] [4]. However, for a linear time-invariant system, both time and frequency domain identification are effectively equivalent [109]. This emphasises the fact that time domain methods are more capable of identifying a non-linear system. More importantly, Jategaonkar [54] emphasises that the state-space representation in the time domain is closer to physical reality than frequency-domain techniques. A brief summary from Reference [95] of the comparison between time and frequency domain identification is presented in Table 2.2.

Furthermore, in the application of time domain estimation for the aeroelastic system, problems lie in the number of estimated parameters as well as the wide range of identified frequencies. This manifests in the large-sized matrices and large number of ordinary differential equations [110]. The typical approach for aeroelastic system estimation is the output error [101, 111–113]. However, given the complexity of aeroelastic systems, often those studied are limited to the analyses of either longitudinal dynamics only [111], limited to the first elastic mode [112], or using the step-by-step method in which the number of estimated parameters taken into account is gradually increasing [101]. Identification of an aeroelastic system can also target the prediction of the damping and frequency at a particular flight condition that can be used to identify flutter margins [114, 115].

Another approach in dealing with estimation of aeroelastic characteristics can be done by only looking at it as a structural problem at the beginning through methods such as Eigenvalue Realisation Algorithm (ERA) [116, 117]. This method starts by estimating the eigenvalue characteristics of the system, which consist of natural frequencies, mode shapes and damping ratios. Eigenvalue estimation is a common approach in civil engineering

[4]Note that leakage error is different from aliasing. Aliasing is caused by the improper sampling of the signal, while leakage error is caused by the length of the measurement signal. However, a random signal will always have leakage.

	Frequency Domain	Time Domain
Measurement	Small number of data points Data in frequency domain (derived from time history data)	Large number of data points Data in time history, maybe some filtering is needed
Algorithm	Matching frequency response No integration occurs, can be used for unstable system	Matching time history data Integration is usually involved in the process, special techniques are required to identify unstable systems
Identified Model	Linear model, special technique needed for non-linear model Time delay can be directly identified No biases identified	Linear and non-linear model can be directly identified Time delay cannot be directly identified Bias must be identified and the model can be correlated
Manoeuvre input	Frequency sweep	Multi-step input (such as 3-2-1-1)
Confidence intervals	Accurate	Optimistic (factor of 5-10 is needed)

Table 2.2: Comparison of frequency and time domain identification methods.

and also known as modal analysis [118, 119]. Bucharles and Vacher [120] are using ERA methodology in determining the initial aeroelastic model. The results are then combined with the rigid body model and optimised through the output error method. A similar approach is also applied for the identification of an aeroelastic system based on wind tunnel test results [121, 122]. In comparison to other algorithms, the use of ERA method in identification of an aeroelastic wind tunnel model has been shown to have a higher success rate with reasonable computational cost [123]. More recent algorithms used to identify the eigenvalue characteristics of a discrete model are the subspace identification methods which are discussed in References [124–127].

2.2.4 Model

The aircraft's dynamics in system identification is captured through a mathematical model which can either be behavioural or phenomenological. The phenomenological model, also known as "white-box" models, are often derived from Newtonian mechanics in which the parameters have a physical meaning yet these can be complex and difficult to simulate. On the other hand, the behavioural models (or "black-box" models), are easier to implement and quicker to simulate with limited interpretive or predictive capabilities of the physical model [54]. An illustration of identification algorithms for aircraft identification in time domain is shown in Figure 2.12. Here, the term hybrid refers to "gray-box" models, that attempt to combine the "black-box" and "white-box" modelling approaches.

For flight dynamic analysis, models that have a parameter with physical meaning are preferable, while for structural identification the black-box model is more favourable. However, when the aircraft is treated as a *flying flexible machine* [128], the model is a combination of flight dynamics (represented by aerodynamics coefficient) and structural dynamics. The flight dynamics model represented by the conventional 6 DoF equation of motion in the aircraft's centre of gravity, while the structural dynamics are represented through n number of nodes with $n \times 6$ DoF. Figure 2.13 gives an illustration of the beam element model of a flexible aircraft and its coordinate system. Point O represents the 6 DoF of the rigid body motion of the aircraft in a reference frame. Typically for conventional aircraft this reference frame is attached to the centre of gravity. Point P represents the axes system and the degree of freedom of P^{th} structural node and the strips on each node represent the aerodynamic contributions.

By considering the rigid and structural DoF, the general linearised equations of motion for aeroelastic aircraft is given by [129]:

$$M(\eta)\begin{Bmatrix} \ddot{\eta} \\ \dot{\mathcal{B}} \end{Bmatrix} + C(\eta, \mathcal{B})\begin{Bmatrix} \dot{\eta} \\ \mathcal{B} \end{Bmatrix} + K(\eta, \mathcal{B})\begin{Bmatrix} \eta \\ 0 \end{Bmatrix} = Q_{ext}(\eta, \dot{\eta}, \mathcal{B}, \Omega) \tag{2.2.8}$$

in which η consists of nodal displacements and rotations, while $\mathcal{B}$ contains the rigid body translational and angular velocity in the body frame $\begin{Bmatrix} u & v & w & p & q & r \end{Bmatrix}^T$. M is the mass matrix that takes into account the coupling between the rigid body and structural dynamics of the aircraft. C and K represent the damping and stiffness matrices respectively, while Q_{ext} is the external forcing term as a function of η, $\dot{\eta}$, $\mathcal{B}$, and rigid body orientation Ω, which define as $\begin{Bmatrix} x & y & z & \phi & \theta & \psi \end{Bmatrix}^T$. External forces include

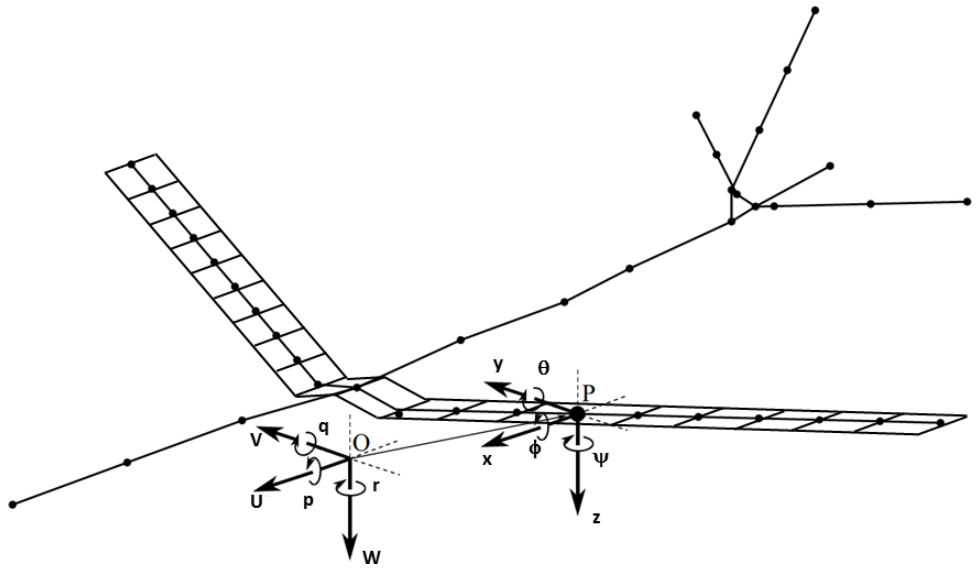

Figure 2.13: Example of axes system and the structure node of the aircraft.

engine thrust, gravitational loading and aerodynamic loading.

A simplified approximation of the aeroelastic system is usually based on the use of the mean axes system [130]. These axes are defined as orthogonal axes, in which the orientation of the axis is chosen so that the linear and angular momenta of the relative motion to the body axes are zero. Therefore, the inertial coupling between the overall and relative deformation is reduced. Schwanz and Wells [110] grouped the aeroelastic analysis for flight dynamics in six categories; Exact, Quasi-Static, Modal Substitution, Residual Stiffness, Residual Flexibility and Modal Truncation. For more details on the approximations and assumptions the reader is referred to Reference [131].

In the aeroelastic aircraft identification problem, a more generalised approach (similar to the modal truncation model) is preferable as it gives more insight into the system. One of the standard theories used for the generalised approach was developed by Waszak and Schmidt [132], assuming large amplitude in the body coordinate system but small structural deformations. The generalised forces are introduced to couple the rigid-body and elastic degrees-of-freedom. The generalised equation of motion has been used in several studies to characterise the stability of aeroelastic vehicles [19, 20, 55, 133].

2.3 Validation and Interpretation

Once the subscale model has been through experiments and its characteristics has been identified, the problem of relating these results to predict the full-scale behaviour is of interest. As aforementioned in Section 2.1.1, the subscale model must satisfy the similitude requirements that are manifested in the set of scaling factors presented in Table 2.1. These scaling factors illustrate the fact that the dynamics of the subscale model which is n times the size of the full-scale model will have a dynamic response $n^{1/2}$ of the full-scale aircraft. Therefore, both models cannot be compared directly in the time domain. Instead, by converting time response into a non-dimensional time τ, the non-dimensional time response is then comparable [35]. The non-dimensional time τ

defined as:

$$\tau = \frac{U}{l}t \tag{2.3.1}$$

where U is the velocity, l is the characteristic length, and t is the response in the time domain.

The same concept of non-dimensional similarity also applies when relating wind-tunnel data to flight test data; a common example is the use of aerodynamic coefficients. The use of such aerodynamic coefficients is common practice in the area of fluid mechanics [46]. As an example the Lift (C_L) can be defined as:

$$C_L = \frac{L}{\frac{1}{2}\rho U^2 S} \tag{2.3.2}$$

where L is the lift force, $\frac{1}{2}\rho U^2$ is the dynamic pressure and, S is the wing area. Table 2.3 illustrates two different models that have different geometrical size and flight conditions and corresponding lift forces. The lift force acting on both models are different, but their C_L values are similar, meaning that considering the size and flight conditions both models have comparable aerodynamic forces. The same value of the aerodynamic coefficient ensures the similitude of aerodynamic characteristics.

Parameter		Full-Scale	Subscale
Altitude	ft	35,000	0
Air Density (ρ)	kg/m^3	0.38	1.225
Velocity (U)	m/s	190	47.5
Dynamic Pressure ($\bar{q}$)	kg/ms^2	6859	1381.95
Wing Area (S)	m^2	122.4	0.478
Lift Force (L)	kN	503	0.396
Lift Coefficient (C_L)	-	0.6	0.6

Table 2.3: Ilustration of the aerodynamic coefficient.

In developing a subscale model, these aerodynamic coefficients are one of the main considerations. Also, depending on the aim of the experiments, one can look at these subjects differently. For example, to validate an aircraft design, one is focused on matching the geometrical properties, while to observe dynamic behaviour one can focus on matching some of the aerodynamic coefficients and can ignore some of the geometrical properties [51]. Either way, the results from the subscale model testing needs to be relatable to the full-scale aircraft.

Kulkarni et al [51] identified four types of errors in the response of different models, as presented in Figure 2.14. These errors consist of full-scale computational error, subscale computational error, numerical scaling error and physical scaling error. Understanding these errors helps quantify the relation between the experimental results using the subscale model and full-scale model.

The use of non-dimensional parameters help in relating the wind-tunnel subscale experiment with the full-scale flight test. Nevertheless, dynamic pressure and the size of the scale model are not the only sources of the aerodynamic coefficients. As mentioned

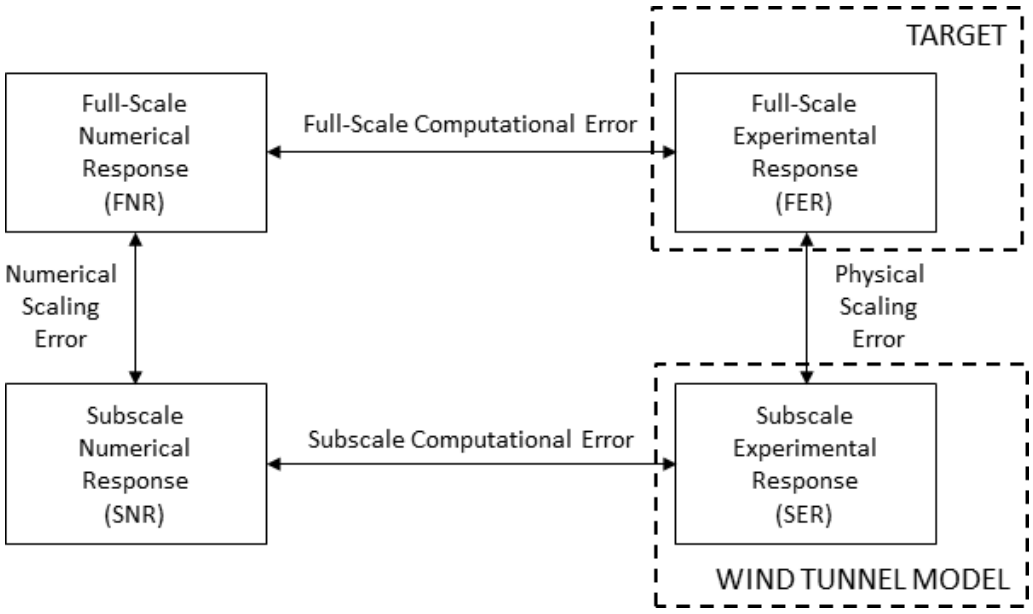

Figure 2.14: Overview of experimental error when using subscale model (Reproduced from Reference [51]).

earlier, the difference in Reynolds and Mach numbers can affect the aerodynamic coefficient. In practice, the correction and extrapolation procedures are the 'secret recipe' of the aircraft industry because these provide the competitive advantage [134]. However, literature regarding wind-tunnel testing and correction schemes that focus on static wind tunnel testing are available in References [135–137]. Furthermore, discussions related to scaling effects are available in References [138, 139].

Some of the identified problems in the extrapolation of wind tunnel results compared to the free flight data are the mounting interference, wall correction, geometric fidelity, and mismatches in Reynold number. Petterson and Rizzi [137] utilised Computational Fluid Dynamics (CFD) for extrapolation of wind tunnel results to the real-flight, which focuses on understanding the effect of the wing mounting and Reynolds number. Traub [140] uses a more straightforward stitching method to extrapolate the drag value from wind tunnel test at a lower Reynolds number to real flight at a higher Reynolds number. For aeroelastic aircraft, Hegg et al. [52] present a methodology of mapping the full-scale dynamics to the aeroelastic subscale model in a controlled wind tunnel environment using different air properties.

Extrapolation of wind tunnel results to the real flight can also be used to give an insight into the handling qualities of the aircraft. Nguyen et al. [141] use Mach and Reynolds number correction to relate wind tunnel data and free flight data for aircraft certification purpose. For an aeroelastic aircraft, this is of interest because previous studies show that introducing flexibility effects in the flight simulator result in worse Cooper-Harper rating than the rigid body aircraft simulation model [55, 142].

2.4 Summary

Based on this review and considering the aim and objectives of this research the following key points can be made:

- The majority of research done so far emphasise the importance of matching Froude and Strouhal numbers for dynamic testing using subscale models. Mach and Reynolds numbers remain critical for static testing of subscale models in wind tunnels.
- For manufacturing aeroelastic subscale models the recent development of 3-D Polyjet printing is a key enabler. However, there is limited research in the application of this method.
- In the identification of aeroelastic behaviour, ERA and output error methods are the most common. These algorithms must be combined with careful model instrumentation to provide high quality measurements as well as dedicated experimental design which leads to optimal inputs for identification.

The interpretation of results from experiments that combine subscale modelling and system identification in the conceptual and early design stages still poses a significant engineering challenge. On the one hand, the lack of a full-scale aircraft at this stage forces engineers to be dependent on computationally expensive numerical methods to predict aeroelastic effects while on the other hand, assumptions and compromises when developing a subscale model and scaling up test results lead to significant uncertainties.

The review has not addressed discussion regarding the development of simulation models either for scaling, simulation or validation purposes. The reader is referred to References [142, 143] for detailed simulation model development of a flexible aircraft. However, a brief introduction on flexible aircraft modelling is presented in Chapter 4.1.

CHAPTER 3

System Identification Methods

The simple block diagram shown in Figure 3.1 presents the problems associated with control, identification and model at a top level. It consist of control input u, dynamic output y, aircraft system S, and external disturbance w. This figure can concisely present the generalised system identification problem, which attempts to find the system S, with stochastic assumptions for the external disturbance w, from measurements of the output y and carefully designed input u. For an established system with an established model structure, the system identification problem simplifies to a parameter estimation problem.

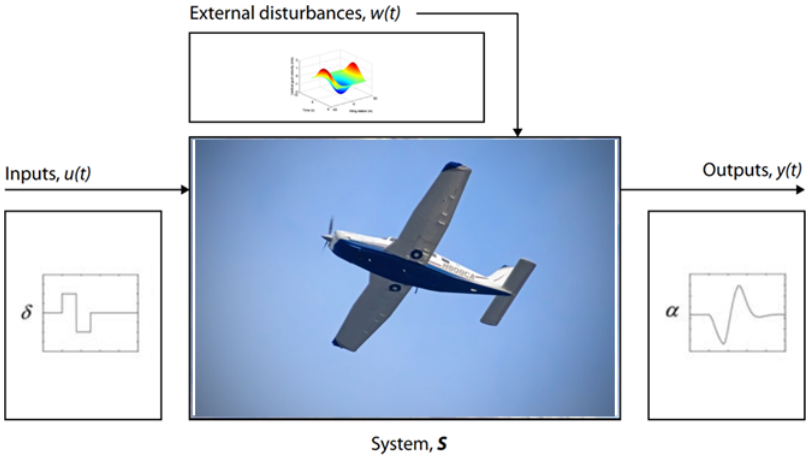

Figure 3.1: Aircraft from a system perspectives.

The following aspects must be clearly specified to solve the parameter estimation problem [94]:

1. a model structure with unknown parameter $\boldsymbol{\Theta}$ to be estimated,
2. a set of observations or measurements, $\mathbf{z}$,
3. mathematical model for the measurement process, and
4. assumptions about the uncertainty in the model parameter $\boldsymbol{\Theta}$ and measurement noise ν.

In general, the measurement equation is defined as:

$$z = h(\Theta) + \nu \tag{3.0.1}$$

Depending on the assumptions, the parameter and measurement can be designated as [144]:

1. Least-squares Model: where parameter $\boldsymbol{\Theta}$ is vector of unknown constant parameters and measurement noise ν is a random vector of measurement noise.
2. Output-error Model: where the parameter vector $\boldsymbol{\Theta}$ can be either a random variable (Bayesian Model) or a vector of unknown constant parameters (Fisher Model) and measurement noise ν is a random variable with probability density $p(\nu)$.

This chapter elaborates on the least-squares approach through regression methods and the Fisher model through output-error methods for parameter estimation of aircraft dynamics. Both least-squares and output-error methods are standard identification procedure for rigid body aircraft identification. However, these methods are not practical to identify structural properties. Therefore, the last section in this chapter covers subspace identification approach, which is a common methodology applied to the problem of structural model identification.

3.1 Regression Method

The regression method falls within the equation-error approach because it aims to minimise a cost function defined directly from the input-output equation [54]. Consider the following linear aerodynamic model:

$$C_M = C_{M_0} + C_{M_\alpha}\alpha + C_{M_q}q + C_{M_{\delta_e}}\delta_e + \nu \tag{3.1.1}$$

This is an example of a regression model for a typical pitching moment dynamics. Here α, q, and δ_e are the independent variables, while C_M is the dependent variable or response variable. Assuming that the dependent and independent variables are measurable, Equation 3.1.1 is left with C_{M_0}, C_{M_α}, C_{M_q}, and $C_{M_{\delta_e}}$ as the constant parameters to be determined.

In general, Equation 3.1.1 can be written as:

$$\begin{aligned} y &= \Theta_0 + \sum_{j=1}^{n} \Theta_j \xi_j \\ z(i) &= \Theta_0 + \sum_{j=1}^{n} \Theta_j \xi_j(i) + \nu(i), \quad i = 1, 2, \ldots, N \end{aligned} \tag{3.1.2}$$

where y is the dependent variable, ξ contains the regressor vectors which are the functions of the independent variables, Θ_j contains the model parameters, $z(i)$ are the output measurements for N number of data points, and ν is the measurement error.

For the Ordinary Least Squares (OLS) approach, Equation 3.1.2 is reformulated as follows:

$$y = \mathbf{X}\Theta \tag{3.1.3}$$

with the following measurement equation:

$$z = \mathbf{X}\Theta + \nu \tag{3.1.4}$$

where $z \in \mathbb{R}^{N\times 1}$, $\Theta \in \mathbb{R}^{n_p\times 1}$, $\mathbf{X} \in \mathbb{R}^{N\times n_p}$, $\nu \in \mathbb{R}^{N\times 1}$, and n_p is the number of parameters to be estimate. The parameter vector Θ is obtained by minimising the following cost function:

$$J(\Theta) = \frac{1}{2}\left[z - \mathbf{X}\Theta\right]^T \left[z - \mathbf{X}\Theta\right] \tag{3.1.5}$$

The estimated parameter Θ that minimises the cost function must satisfy:

$$\frac{\partial J}{\partial \mathbf{\Theta}} = -\mathbf{X}^T z + \mathbf{X}^T\mathbf{X}\mathbf{\Theta} = 0 \tag{3.1.6}$$

and some algebraic rearrangement leads to:

$$\hat{\Theta} = (\mathbf{X}^T\mathbf{X})^{-1}\mathbf{X}^T z \tag{3.1.7}$$

Therefore, under the assumptions of zero mean Gaussian noise the estimate covariance matrix can be calculated as follows:

$$\mathrm{E}\left[(\hat{\Theta} - \Theta)(\hat{\Theta} - \Theta)^T\right] = \sigma^2(\mathbf{X}^T\mathbf{X})^{-1} \tag{3.1.8}$$

such that the real parameter value Θ are within $\hat{\Theta} \pm 2\sigma\sqrt{(\mathbf{X}^T\mathbf{X})^{-1}}$ [94]. [1]

3.1.1 Unmeasured Variables

One of the major problems in utilising the OLS approach is when the dependent variables cannot be measured directly. For example, consider the pitching moment model as presented in Equation 3.1.1. In this case the dependent variables can be computed from standard moment equation [145]:

$$C_M = \frac{I_{yy}}{\bar{q}S\bar{c}}\dot{q} \tag{3.1.9}$$

However, the pitch rate derivatives $\dot{q}$ is typically not a direct measurement. This variable should be calculated from the measurement of dependent variables, linear acceleration and angular rates [54]. Thus, $\dot{q}$ is obtained by differentiating the q variable. Nevertheless, flight test data is often noisy, and to compute the derivatives of measured data from neighbouring values can amplify the noise [94]. One of the solutions to tackle this issue is by calculating the derivatives using local smoothing techniques [146].

The following smoothing approach is based on a second-order polynomial model. It

[1] OLS function can be obtained by utilising `lesq` function from SIDPAC library.

assumes that the local data points lie on a parabola with the local model identified as:

$$y = a_0 + a_1 t + \frac{1}{2} a_2 t^2 \tag{3.1.10}$$

Given $z(i)$ as the ith measured data at $i\Delta t$, the equations used for the local fit are:

$$\begin{aligned} z(i-2) &= a_0 + a_1(-2\Delta t) + \frac{1}{2} a_2(-2\Delta t)^2 \\ z(i-1) &= a_0 + a_1(-\Delta t) + \frac{1}{2} a_2(-\Delta t)^2 \\ z(i) &= a_0 \\ z(i+1) &= a_0 + a_1(\Delta t) + \frac{1}{2} a_2(\Delta t)^2 \\ z(i+2) &= a_0 + a_1(2\Delta t) + \frac{1}{2} a_2(2\Delta t)^2 \end{aligned} \tag{3.1.11}$$

The equation above can be rearrange into matrix form as follows:

$$\begin{bmatrix} 1 & -2\Delta t & 4\Delta^2 t \\ 1 & -\Delta t & \Delta^2 t \\ 1 & 0 & 0 \\ 1 & \Delta t & \Delta^2 t \\ 1 & 2\Delta t & 4\Delta^2 t \end{bmatrix} \begin{bmatrix} a_0 \\ a_1 \\ a_2 \end{bmatrix} = \begin{bmatrix} z(i-2) \\ z(i-1) \\ z(i) \\ z(i+1) \\ z(i+2) \end{bmatrix} \tag{3.1.12}$$

From the Equation 3.1.12, the unknown variables, a_0, a_1, a_2, can be estimated using least-squares solution (see Equation 3.1.4) as:

$$\begin{aligned} \hat{a}_0(i) &= \frac{1}{35}[-3z(i-2) + 12z(i-1) + 17z(i) + 12z(i+1) - 3z(i+2)] \\ \hat{a}_1(i) &= \frac{1}{10\Delta t}[-2z(i-2) - z(i-1) + z(i+1) + 2z(i+2)] \\ \hat{a}_2(i) &= \frac{1}{14\Delta^2 t}[2z(i-2) - z(i-1) - 2z(i) - z(i+1) + 2z(i+2)] \end{aligned} \tag{3.1.13}$$

in which $\hat{a}_0$ is the estimation of smoothed value of z at i, and $\hat{a}_1$ is the estimation of smoothed value of $\dot{z}$ at i, by considering $\dot{y} = a_1 + a_2 t$ [94]. [2]

3.1.2 Identification of a Full-Scale Rigid Body Aircraft

In this example, linear regression is applied to aircraft flight-test data to estimate the non-dimensional longitudinal stability and control derivatives. The test aircraft is the Jetstream 3102 (Figure 3.2). Flight test data was collected for several short-period manoeuvres at different flight configurations. Figure 3.3 presents the measurement data

[2] `deriv.m` function from SIDPAC library can be used to calculate the differential using local smoothing.

from 1 data point of the flight test, which consists of angle-of-attack, pitch-rate, and elevator deflection. It is worth noting that: (1) pitch-rate and angle-of-attack have different filtering and sampling rates and the sensors are physically at different locations, and (2) sensor measurement for pitch-rate is non-collocated with the aircraft's centre of gravity (CG) and the body axes centre used for flight dynamic analysis.

Figure 3.2: Cranfield's Jetstream 31 G-NFLA and reference data.

The aircraft mass and geometry characteristics and test flight conditions are specified as follows [147]:

$$\begin{array}{llll} \bar{c} & = 1.72 \text{ m} & S & = 25.08 \text{ m}^2 \\ m & = 6551 \text{ kg} & U_{TAS} & = 164 \text{ kts} \\ h & = 6210 \text{ ft} & I_{yy} & = 36{,}765 \text{ kg m}^2 \end{array}$$

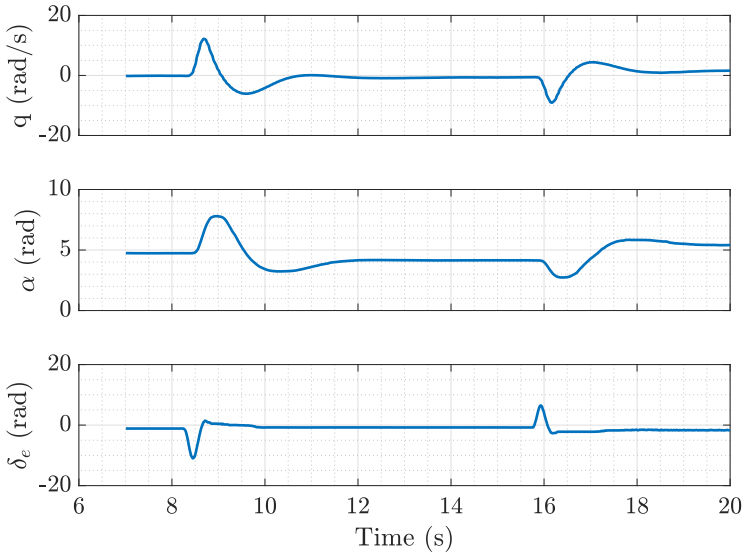

Figure 3.3: Measured input and output variables for short period manoeuvre.

The equations of motion that represent the longitudinal short period motion in state-space form are as follows [145, 148]:

$$\begin{bmatrix} \dot{q} \\ \dot{\alpha} \end{bmatrix} = \begin{bmatrix} \frac{\bar{q}S\bar{c}}{I_{yy}} \frac{\bar{c}}{2U_{TAS}} C_{M_q} & \frac{\bar{q}S\bar{c}}{I_{yy}} C_{M_\alpha} \\ 1 & \frac{\bar{q}S}{mU_{TAS}} C_{L_\alpha} \end{bmatrix} \begin{bmatrix} q \\ \alpha \end{bmatrix} + \begin{bmatrix} \frac{\bar{q}S\bar{c}}{I_{yy}} C_{M_{\delta_e}} \\ \frac{\bar{q}S}{mU_{TAS}} C_{L_{\delta_e}} \end{bmatrix} \begin{bmatrix} \delta_e \end{bmatrix} \quad (3.1.14)$$

The symbols $\bar{q}$, S, $\bar{c}$, m and I_{yy} represent dynamic pressure, reference area, mean aerodynamic chord, aircraft mass and pitch inertia respectively. The identification of derivatives such as C_{M_α}, C_{L_α}, $C_{L_{\delta_e}}$ and $C_{M_{\delta_e}}$ is of specific interest here. For application of OLS method the model equation define as follow:

$$\dot{q} = \frac{\bar{q}S\bar{c}^2}{2I_{yy}U_{TAS}}C_{M_q}q + \frac{\bar{q}S\bar{c}}{I_{yy}}C_{M_\alpha}\alpha + \frac{\bar{q}S\bar{c}}{I_{yy}}C_{M_{\delta_e}}\delta_e \tag{3.1.15}$$

$$\dot{\alpha} - q = \frac{\bar{q}S}{mU_{TAS}}C_{L_\alpha}\alpha + \frac{\bar{q}S}{mU_{TAS}}C_{L_{\delta_e}}\delta_e \tag{3.1.16}$$

Here $\dot{\alpha}$ and $\dot{q}$ are the dependent variables obtained by differentiating the sensor measurements using smoothed numerical derivatives. Furthermore, due to the issues mentioned earlier regarding sensor measurements, it was found that the measured pitch rate (q_m) must be shifted in time to provide more accurate identification of the SPPO (Short Period Pitching Oscillation) dynamics [25]. The issue of measurement time shifting has also been discussed by Tischler [95] and Jategaonkar [54]. By defining time shift parameter (τ) as a function of distance between the angle of attack vane and the Inertial Measurement Unit (IMU) (x_m), $\tau = x_m/U$. The corrected pitch rate and angle of attack are defined as:

$$\begin{aligned} q_c &= q_m(t+\tau) \\ \alpha_c &= \alpha_m + \frac{q_c x_m}{U_{TAS}} \end{aligned} \tag{3.1.17}$$

The comparison between the measurement and corrected variables for both pitch rate (q_m and q_c) and angle of attack (α_m and α_c) based on Equation 3.1.17 are given in Figures 3.4 and 3.5 respectively.

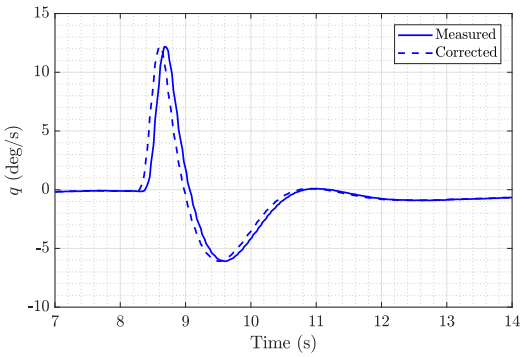

Figure 3.4: Comparison of q_m and q_c.

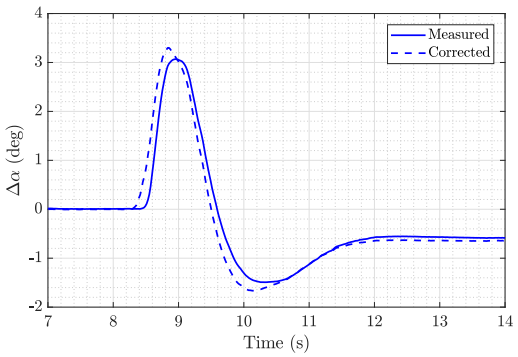

Figure 3.5: Comparison of α_m and α_c.

Figures 3.6 and 3.7 show the results of applying smoothed derivatives to calculate the dependent variables ($\dot{\alpha}$ and $\dot{q}$).

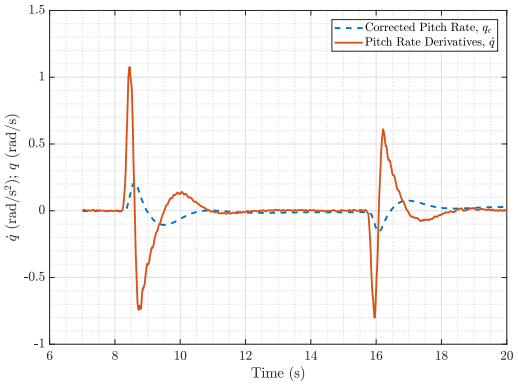

Figure 3.6: Calculation of $\dot{q}$ input.

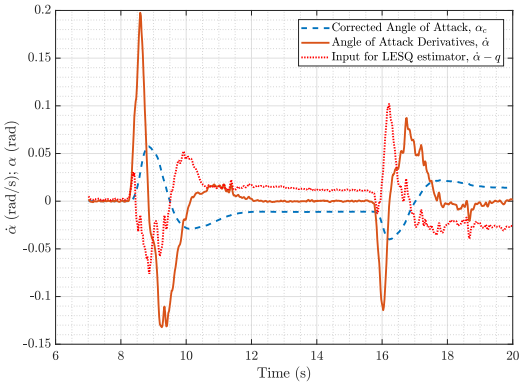

Figure 3.7: Calculation of $\dot{\alpha}$ input.

Applying the least-squares estimation given in Equation 3.1.7 for the pitching moment coefficient as presented in Equation 3.1.16, the following variables need to be defined:

$$\Theta_m = \begin{bmatrix} M_q & M_\alpha & M_{\delta_e} \end{bmatrix}^T$$

$$z_m = \begin{bmatrix} \dot{q}(1) & \dot{q}(2) & \dots & \dot{q}(N) \end{bmatrix}^T$$

$$X_m = \begin{bmatrix} q(1) & \alpha(1) & \delta_e(1) \\ q(2) & \alpha(2) & \delta_e(2) \\ \vdots & \vdots & \vdots \\ q(N) & \alpha(N) & \delta_e(N) \end{bmatrix}$$

where N is the number of data points, and

$$M_q = \frac{\bar{q}S\bar{c}^2}{2I_{yy}U_{TAS}} C_{M_q} \tag{3.1.18}$$

$$M_\alpha = \frac{\bar{q}S\bar{c}}{I_{yy}} C_{M_\alpha} \tag{3.1.19}$$

$$M_{\delta_e} = \frac{\bar{q}S\bar{c}}{I_{yy}} C_{M_{\delta_e}} \tag{3.1.20}$$

A similar approach is also applied to the lift equation, resulting in the identified parameters shown in Table 3.1.

Table 3.1 also allows the comparison of parameter estimated obtained using measured and corrected regressor matrix. The table shows both the identified parameter and its associated variance. The variance is an important parameter to indicate the quality of the parameter estimates obtained. In this case, correcting the measured variable (q) by a slight time shift improves the confidence intervals for almost all parameter estimates as shown in Table 3.1.

On the contrary, the lift coefficient due to elevator deflection ($C_{L_{\delta_e}}$) maintains a high variance. Furthermore, when compared to empirical methods given by Cooke [149], the determined $C_{L_{\delta_e}}$ value is an order of magnitude less. This difference in magnitude emphasises the fact that the short period manoeuvre is not capable of estimating $C_{L_{\delta_e}}$ parameter.

Parameter	Identification using q_m		Identification using q_c	
	$\hat{\Theta}$	$\sigma(\%)$	$\hat{\Theta}$	$\sigma(\%)$
C_{M_q}	9.391	24.8	-19.94	4.51
C_{M_α}	-1.085	5.87	-0.763	2.69
$C_{M_{\delta_e}}$	-0.928	4.40	-1.511	1.03
C_{L_α}	6.524	2.14	6.334	1.85
$C_{L_{\delta_e}}$	-0.3635	27.27	0.3091	29.27
ζ [-]	0.170		0.486	
ω [rad/s]	2.20		2.21	

Table 3.1: Identified parameters and SPPO characteristics using measured and corrected pitch rate.

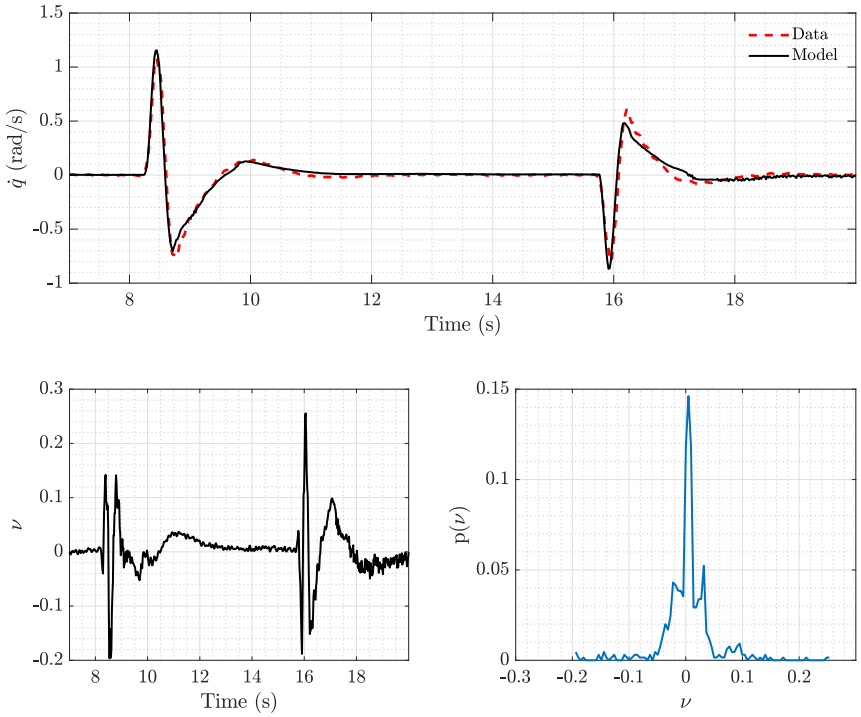

Figure 3.8: Identification of pitching moment coefficient using OLS.

Another way to evaluate the quality of the parameter estimates is by looking at the estimated output. Figure 3.8 shows the comparison of $\dot{q}$ from (derived) measurement and the identification results. The results show a match between the data and the identified model with the residual (ν) being an order of magnitude lower, indicating good quality of identification results.

The reader is referred to Reference [25] for a thorough discussion of this work.

3.1.3 Multivariate Orthogonal Functions

The least squares estimator is a simple and effective identification method. However, some issues can arise with this approach. Firstly, there are possibilities that the polynomial terms are highly correlated. For example, q and $\dot{\alpha}$ are often similar and highly correlated during an aircraft's longitudinal short period motion [150]. These highly correlated regressors can cause a problem in parameter estimation during least squares estimation [94]. Secondly, least-squares regression obliges the use of deterministic regressors, and this means that the model structure should be fixed before conducting the identification procedure. The results from Section 3.1.2 show a large variance in the identified $C_{L_{\delta_e}}$ parameter, which indicates that it is poorly identified.

Multivariate Orthogonal Functions (MOF) are often used to address problems of model structure and highly correlated regressors (data collinearity) while allowing the possibility of having limited non-linear regressors. The issue of the deterministic regressors is addressed by creating multivariate regressors and selecting the regressors order according to their effectiveness in modelling the dependent variable. The goal is to approximate the data efficiently, in a least-squares sense, using a small number of modelling terms [151, 152]. Furthermore, the problem of inter-regressor correlation is addressed by transforming a large pool of dependent variables into a set of orthogonal polynomials [151]. By ensuring orthogonality, the correlation among regressor is expected to vanish or at least be minimised.

As an illustration, suppose that there are two correlated regressors. By orthogonalising the second regressor with respect to the first, the correlated components of the second regressor are effectively removed. As a result, orthogonalisation regressors leads to two orthogonal regressors: the first has no change and the second may have relatively low information content.

The methods for orthogonality can be explained as follows. Consider a linear model equation as:

$$y = \Theta_1\xi_1 + \Theta_2\xi_2 + \cdots + \Theta_n\xi_n \tag{3.1.21}$$

which consists of an output y and regressor ξ. The idea of using MOF for modelling purposes is to convert the regressor ξ into p so that:

$${p_i}^T p_j = 0 \qquad i \neq j, \qquad i, j = 1, 2, \ldots, n \tag{3.1.22}$$

This first regressor used as an orthogonal function is a vector of ones ($p_1 = \mathbf{1}$) which represent a bias term. The next orthogonal function (p_i) is built to be orthogonal based on the previous orthogonal function (p_{i-1}) using the Gram-Schmidt orthogonalisation procedure [94]. Therefore, the jth orthogonal function is defined as:

$$p_j = \xi_j - \sum_{k=1}^{j-1} \gamma_{kj} p_k \qquad j = 2, 3, \ldots, n \tag{3.1.23}$$

in which ξ_j is the jth regressor vector, and γ_{kj} is a scalar vector defined as:

$$\gamma_{kj} = \frac{{p_k}^T \xi_j}{{p_k}^T p_k} \tag{3.1.24}$$

A simple example of orthogonalised vector in two dimensional plane is as follow. Consider $\mathbf{u}$ is a vector of $4\mathbf{i} + 3\mathbf{j}$ and $\mathbf{v}$ is a vector of $2\mathbf{i} + 5\mathbf{j}$. In a two dimensional plane of $\mathbf{i}$ and $\mathbf{j}$ given in Figure 3.9. Using the above methodology, vector $\tilde{\mathbf{v}}$ is built to be orthogonal with $\mathbf{u}$ which satisfies the relationship given in Equation 3.1.23

$$\tilde{\mathbf{v}} = \mathbf{v} - \gamma \mathbf{u} \tag{3.1.25}$$

in which

$$\gamma = \frac{\mathbf{u} \cdot \mathbf{v}}{\mathbf{u} \cdot \mathbf{u}} \tag{3.1.26}$$

The orthogonalised $\tilde{\mathbf{v}}$ is shown in Figure 3.10, and it can be seen that $\tilde{\mathbf{v}}$ is perpendicular with $\mathbf{u}$. Similarly, for three dimensional vectors of $\mathbf{u}$, $\mathbf{v}$, and $\mathbf{w}$ (see Figure 3.11), the orthogonalise vector of $\tilde{\mathbf{v}}$ and $\tilde{\mathbf{w}}$ with respect to $\mathbf{u}$ is given in Figure 3.12. The same concept is also applied in the independent regressor for identification purposes.

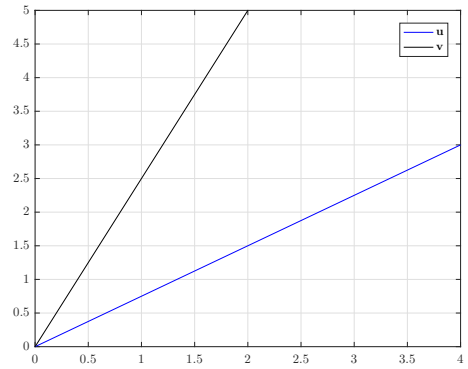

Figure 3.9: Vector $\mathbf{u}$ and $\mathbf{v}$.

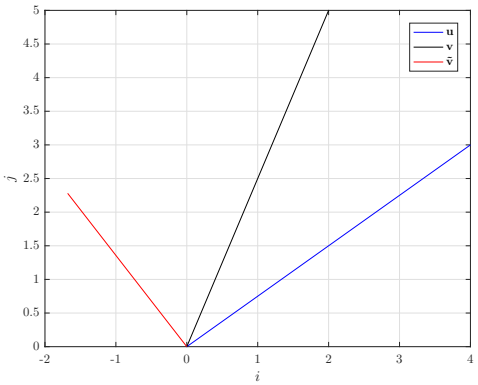

Figure 3.10: Vector $\mathbf{u}$, $\mathbf{v}$, and $\tilde{\mathbf{v}}$.

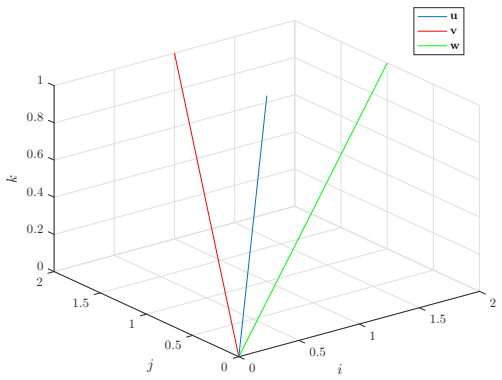

Figure 3.11: Vector $\mathbf{u}$, $\mathbf{v}$, and $\mathbf{w}$.

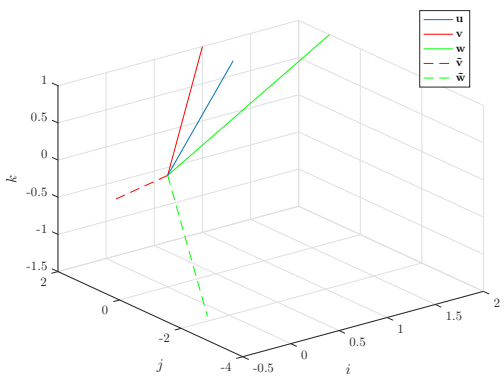

Figure 3.12: Vector $\mathbf{u}$, $\mathbf{v}$, $\mathbf{w}$, $\tilde{\mathbf{v}}$, and $\tilde{\mathbf{w}}$.

In the application of MOF in aircraft identification, the orthogonalization is applied to the original regressor matrix ξ_j resulting in the orthogonal regressors p_i. Therefore, the new orthogonal function can be arranged as follows:

$$\begin{bmatrix} p_1 & p_2 & p_3 & \dots & p_n \end{bmatrix} \begin{bmatrix} 1 & \gamma_{12} & \gamma_{13} & \dots & \gamma_{1n} \\ 0 & 1 & \gamma_{23} & \dots & \gamma_{2n} \\ 0 & 0 & 1 & \dots & \gamma_{3n} \\ \vdots & \vdots & \vdots & \ddots & \vdots \\ 0 & 0 & 0 & 0 & 1 \end{bmatrix} = \begin{bmatrix} 1 & \xi_1 & \xi_2 & \dots & \xi_n \end{bmatrix} \tag{3.1.27}$$

or in concise matrix form:

$$\mathbf{PG} = \mathbf{X} \tag{3.1.28}$$

Therefore, the orthogonal regressor is given by:

$$\mathbf{P} = \mathbf{XG}^{-1} \tag{3.1.29}$$

Now, using the orthogonalised regressor, the least squares identification problem can be rewritten such that the measurement equation is given by:

$$z = Pa + \nu \tag{3.1.30}$$

where z is the dependent variable vector, P is the matrix of orthogonal regressor, a is vector of the unknown parameters and υ is the vector of measurement errors.
Therefore, the parameter estimates is as follows:

$$\hat{a} = (P^T P)^{-1} P^T z \tag{3.1.31}$$

Since the regressor matrix has been orthogonalised, $p_i^T p_j = 0$ for $i \neq j$. Thus

$$\hat{a}_j = (P_j^T P_j)^{-1} {P_j}^T z \tag{3.1.32}$$

This means that the jth parameter only depends on the measured output and the jth regressor.

Due to the nature of the orthogonalisation process which sequentially uses the previous orthogonal regressor, the orthogonal function is heavily dependant on the ordering of the original regressor matrix [94]. Dynamic programming can be utilised to define the sequence of the regressors. The sequence of the regressors is calculated via comparisons to the measured output using the norm value calculated as follows:

$$P_j = \left(\frac{{p_j}^T p_j}{z^T z} \right), \qquad j = 1, 2, ..., n$$

The first regressor is picked from the most significant norm value. And the remaining regressors are orthogonalised based on the subsequent norm of the current regressor. Orthogonal functions with the norm value less than 0.01% are dropped. This small norm value suggests that the function is ill-conditioned or dependent on the other orthogonal functions.

Based on the order of the orthogonal function, the question now is how to determine the most effective number of orthogonal functions to be retained in the final model. On this issue, the concept of predicted squared error (PSE) is utilised [94, 151]. PSE is a combination of mean-square fit error (MSFE) and overfit penalty (OFP), and defined as:

$$PSE = \frac{1}{N}\left(z - \hat{y}\right)^T \left(z - \hat{y}\right) + {\sigma^2}_{max}\frac{n}{N} \tag{3.1.33}$$

in which N is the number of points for each orthogonalised function, n is the number of orthogonal functions, and σ^2 is the maximum model fit error variance known as:

$${\sigma^2}_{max} = \frac{1}{N-1}\sum_{i-1}^{N}\left[z(i) - \bar{z}\right]^2 \tag{3.1.34}$$

MSFE is proportional to the OLS cost function [94], its value will decrease as more orthogonal functions are added to the equation, because this is related to the error prediction of the dependent variable. On the other hand, the OFP value increases as more orthogonal functions are added, because this function is proportional to the number of orthogonal functions n. The PSE is the minimum point of this combination, which is the point at which the modelling terms provide a low fit error as well as good prediction capability. This optimal modelling terms then used as the identified model structure. The flowchart of the multivariate orthogonal function is presented in Figure 3.13[3].

[3]The MOF is utilise using `mof` function from the `SIDPAC` library.

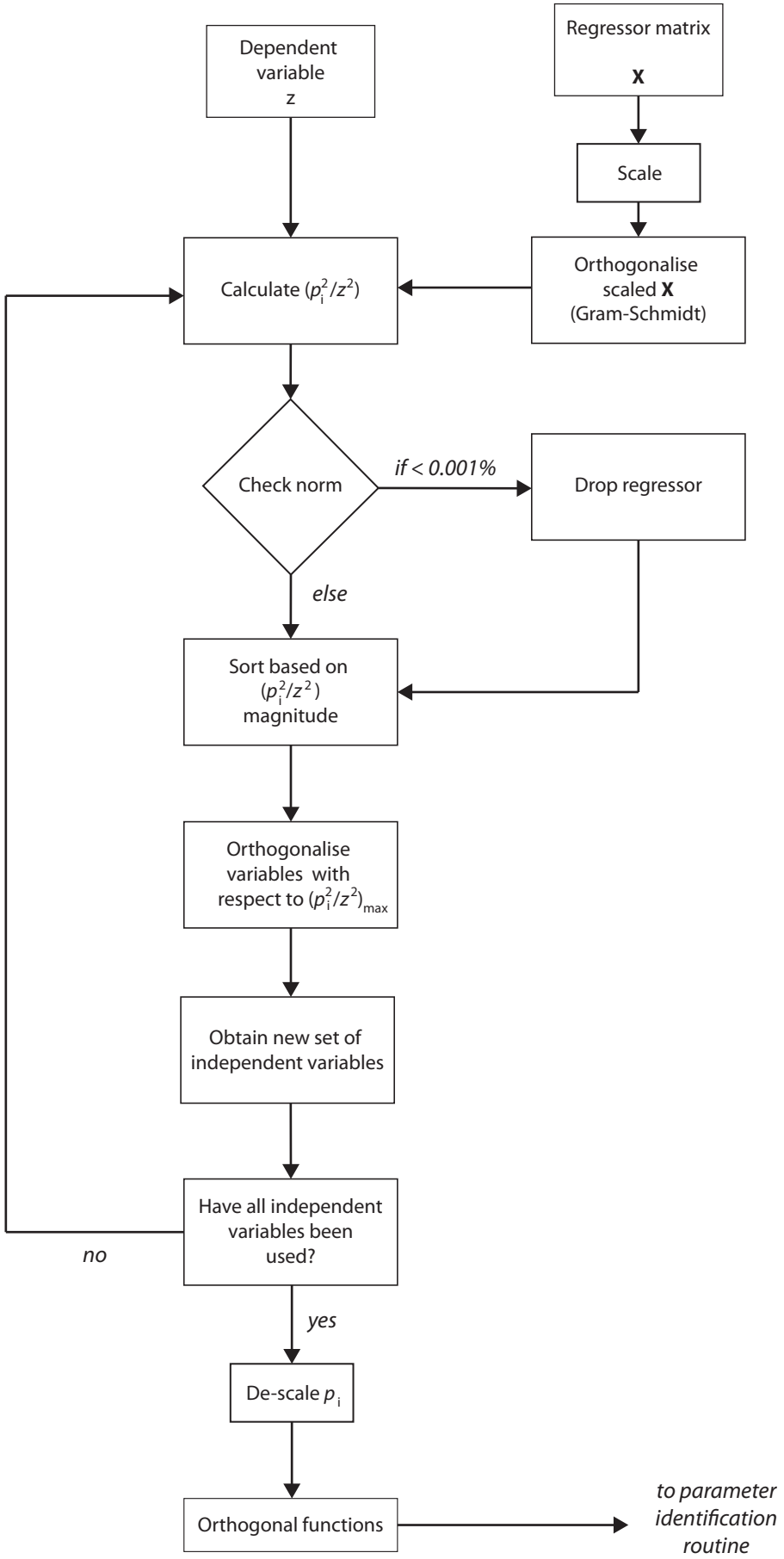

Figure 3.13: Flowchart of MOF function. Reproduce from Reference [153].

Example 3.1.1 ***MOF application in non-linear system identification***
Consider the following 2 DoF non-linear aeroelastic equation of motion [58]:

$$\begin{bmatrix} m & mx_\alpha c_{1/2} \\ mx_\alpha c_{1/2} & I_\alpha \end{bmatrix} \begin{bmatrix} \ddot{h} \\ \ddot{\alpha} \end{bmatrix} + \begin{bmatrix} c_h & 0 \\ 0 & c_\alpha \end{bmatrix} \begin{bmatrix} \dot{h} \\ \dot{\alpha} \end{bmatrix} + \begin{bmatrix} K_h & 0 \\ 0 & K_\alpha(\alpha) \end{bmatrix} \begin{bmatrix} h \\ \alpha \end{bmatrix} = \begin{bmatrix} -L \\ M \end{bmatrix} \tag{3.1.35}$$

In this example, Equation 3.1.35 is simplified by only considering the pitching DoF such that :

$$I_\alpha \ddot{\alpha} + c_\alpha \dot{\alpha} + K_\alpha(\alpha)\alpha = M \tag{3.1.36}$$

The left hand side of the equation represents structural motion, in which the non-linearity is introduced through K_α defined as a fourth-order polynomial (see Figure 3.14):

$$K_\alpha(\alpha) = 2.82\left(1 - 22.1\alpha + 1315.5\alpha^2 - 8580\alpha^3 + 17289.7\alpha^4\right) \tag{3.1.37}$$

and the right hand side of the equation represents the aerodynamic moment M which is modelled as:

$$M = \rho U^2 c_{1/2}^2 C_{M_\alpha}\left[\alpha + \left(\frac{1}{2} - a\right) c_{1/2}\frac{\dot{\alpha}}{U}\right] + \rho U^2 c_{1/2}^2 C_{M_{\delta_e}} \delta_e \tag{3.1.38}$$

Here, δ_e represents the control surface deflection, while C_{M_α} and $C_{M_{\delta_e}}$ representing the non-dimensional pitching moment with respect to the change in the angle of attack and elevator deflection respectively. The system parameters and its definition are presented in Table 3.2.

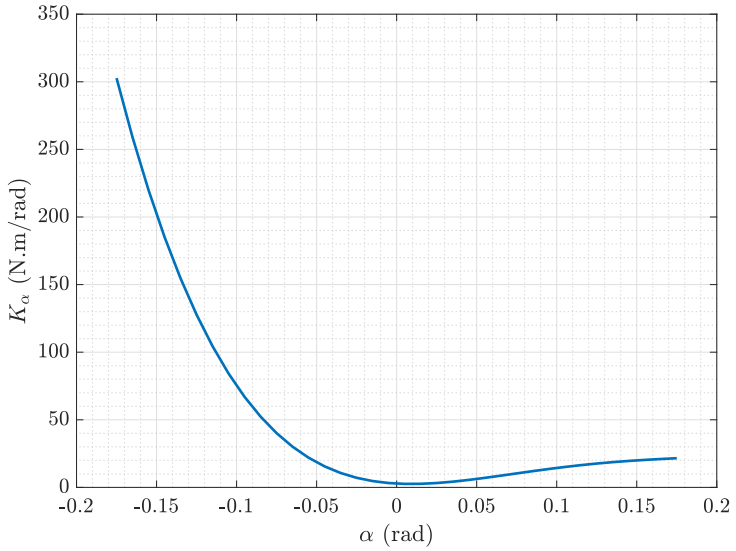

Figure 3.14: Non-linearity of K_α as a function of α.

Parameter	Value	Units	Description
I_α	0.065	kg.m^2	Mass Moment of Inertia
c_α	0.0360	N.s/rad	Pitch Damping coef.
ρ	1.225	kg/m^3	Air Density
U	20	m/s	Air Speed
$c_{1/2}$	0.135	m	Semi Chord
a	-0.6	-	Constants
C_{M_α}	-0.6280	/rad	Pitch Moment coef.
$C_{M_{\delta_e}}$	-0.6350	/rad	Pitch Moment due to Input

Table 3.2: System parameters and definition.

A doublet input from the control surfaces (5^o amplitude) is used to excite the system. Figure 3.15 shows the system response for this input, which consists of δ_e, $\ddot{\alpha}$, $\dot{\alpha}$, α, and $K(\alpha)$ over time. For identification purposes, it is assumed that $\ddot{\alpha}$, $\dot{\alpha}$, α, and δ_e are direct measurements. The identification procedure is applied by merging Equation 3.1.36 with Equation 3.1.37 and 3.1.38 such that:

$$I_\alpha \ddot{\alpha} = \left(\rho U^2 c_{1/2}^2 C_{M_\alpha} - K_\alpha(\alpha)\right)\alpha + \left(\rho U c_{1/2}^3 C_{M_\alpha}\left(\frac{1}{2} - a\right) - c_\alpha\right)\dot{\alpha} + \rho U^2 c_{1/2}^2 C_{M_{\delta_e}} \delta_e \tag{3.1.39}$$

where the left hand side of the equation isolates the dependent variable. In this case, the regressor matrix is defined as:

$$X = \begin{bmatrix} \alpha_1 & \dot{\alpha}_1 & \delta_{e1} \\ \vdots & \vdots & \vdots \\ \alpha_N & \dot{\alpha}_N & \delta_{eN} \end{bmatrix} \tag{3.1.40}$$

and the parameters to be identified are:

$$\begin{aligned} \Theta_\alpha &= \rho U^2 c_{1/2}^2 C_{M_\alpha} - K_\alpha(\alpha) \\ \Theta_{\dot{\alpha}} &= \left(\rho U c_{1/2}^3 C_{M_\alpha}\left(\frac{1}{2} - a\right) - c_\alpha\right) \\ \Theta_{\delta_e} &= \rho U^2 c_{1/2}^2 C_{M_{\delta_e}} \end{aligned}$$

It is worth mentioning that in this case, Θ_α is expected to be a non-linear fourth-order polynomial function. The maximum order of α needs to be stated, when applying the MOF identification method. In this case, the maximum order of α in any model term is 5, while the maximum model order term is also 5. These choices will allow orthogonalised terms to be based on α^5 to α, or α to $\alpha^4\delta_e$, or in the very extreme, a possibility to have terms such as $\alpha\dot{\alpha}\delta_e$ and $\alpha^3\dot{\alpha}\delta_e$.

Given the maximum allowable model order, there are 19 possible combinations of regressors. By orthogonalising the regressors, the MOF function shows that the minimum

PSE is at the orthogonal function number of 6 with the order of:

$$\hat{\Theta} = \begin{bmatrix} \alpha & \dot{\alpha} & \alpha^3 & \alpha^2 & \alpha^4 & \delta_e \end{bmatrix} \tag{3.1.41}$$

As presented in Figure 3.16, the PSE is at the minimum value on the regressor number six, while the R^2 value is almost 100% at the same number of regressors. This number of regressor results in the following model structure being identified:

$$\Theta_\alpha = -8.3468 + 74.3875\alpha - 3831.4\alpha^2 + 1.9346e4\alpha^3 - 5.6614\dot{\alpha} - 0.0775\delta_e \tag{3.1.42}$$

The comparison of the $I_\alpha\ddot{\alpha}$ from simulation and identification results is presented in Figure 3.18 while the comparison of model and identified Θ_α is shown in Figure 3.17. Figure 3.18 shows a match response between the simulation and identification results with residual that are two orders of magnitude lower. Furthermore, the comparison of Θ_α presented in Figure 3.17 shows that the validity of the identification results is limited for the range of α from -0.06 rad to 0.1 rad, as the system is only excited in this region.

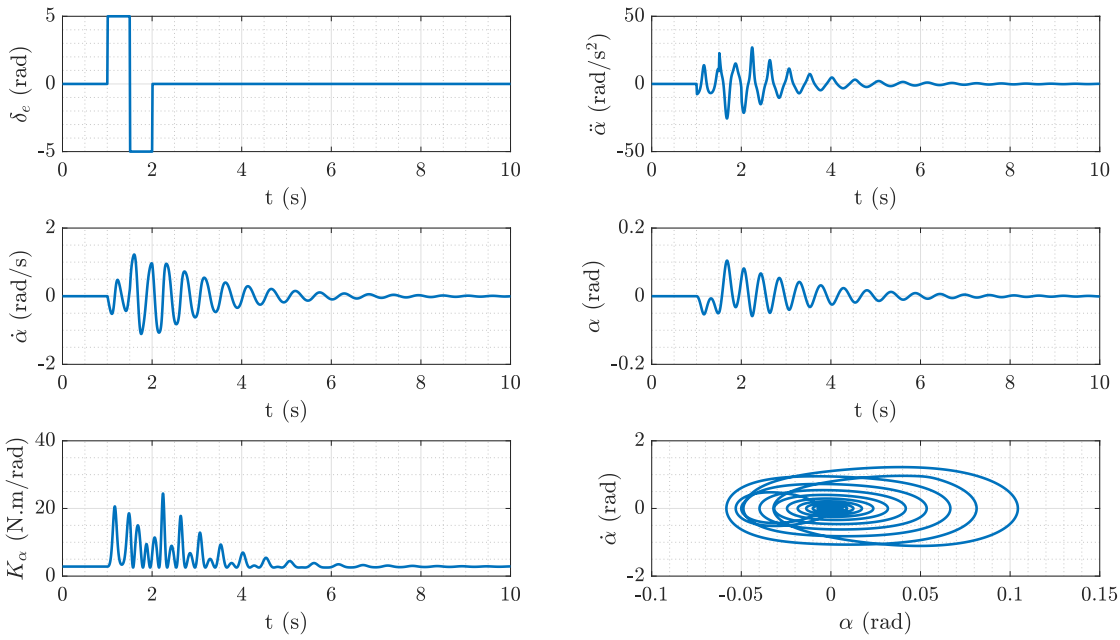

Figure 3.15: System response for a doublet input.

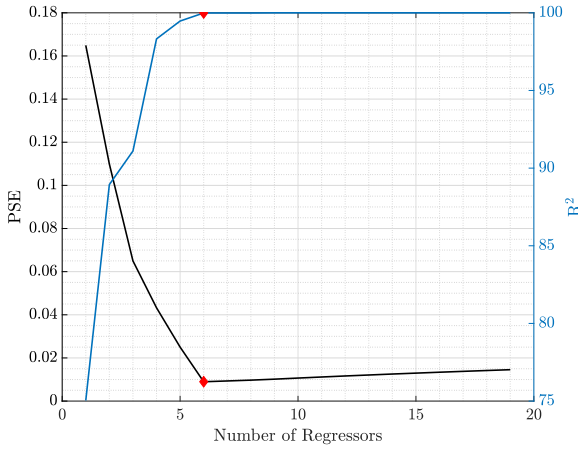

Figure 3.16: PSE and R^2 with respect to the number of regressors.

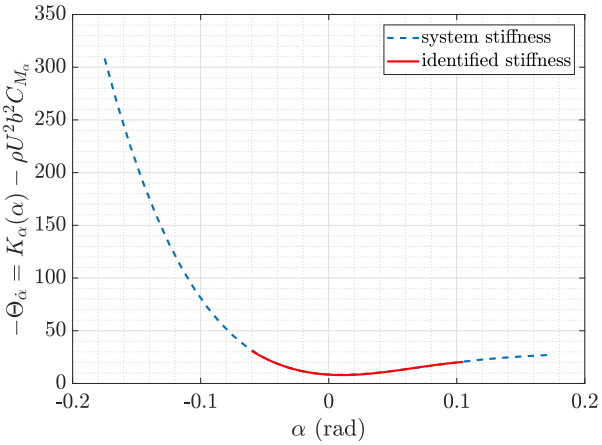

Figure 3.17: Identified Θ_α limited to the α disturbance.

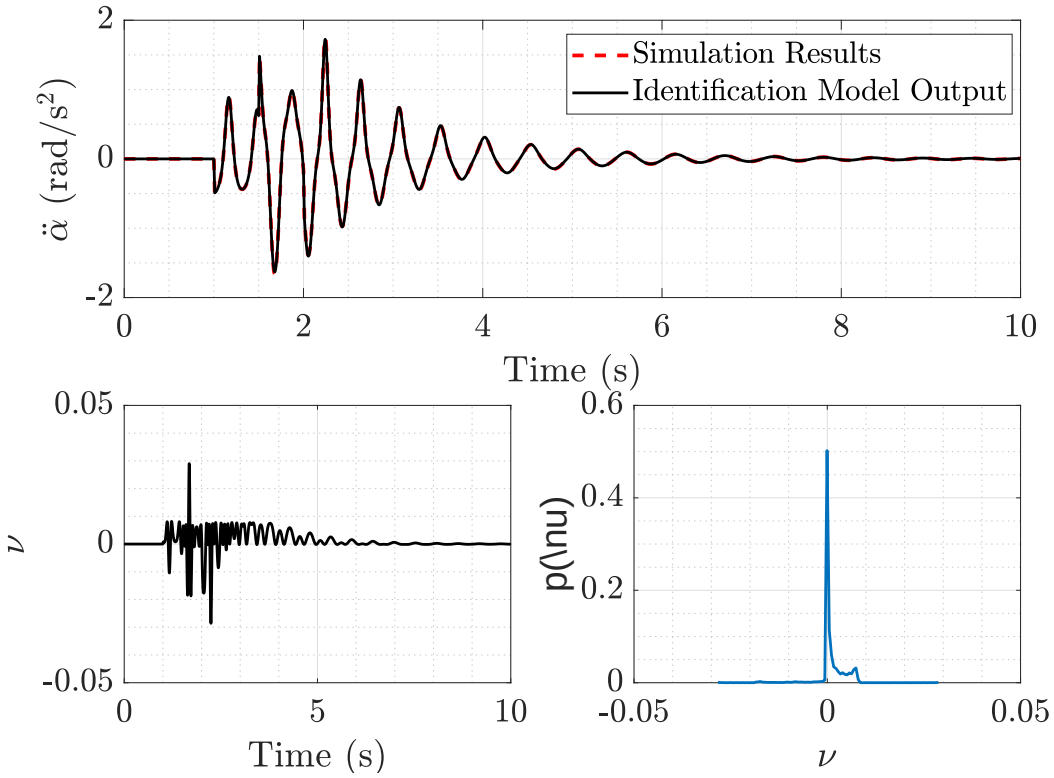

Figure 3.18: Comparison of the identification model and simulation results.

3.2 Output Error Method

The previous regression based method aims to find a suitable mathematical model that matches the dependent variables to the independent variables. Ideally, both of these variables should be obtained through direct measurements. However, it is not possible to measure all variables directly (especially particular states). In practice, a process of integration or differentiation of the measured variables is often needed before the application of the OLS algorithm (see Chapter 3.1.1). This process can lead to inaccuracies in parameter estimates, primarily because the measured data is often noisy and certain systematic errors cannot be avoided (for example errors due to sensor placement) [54].

The unmeasured variables are no longer an issue in the output error method. This method tries to find a suitable model in which the model output is matched directly with the measurement. Integration or differentiation are usually embedded in the model function, and moreover, a non-linear relationship between model parameter Θ and the measurement y is made possible. Furthermore, this method assumes the noise as a random vector with the probability density function $p(\nu)$ and includes this assumption explicitly in the cost function. On the other hand, the OLS approach only uses this noise property after the parameter estimation to quantity parameter covariances.

The Output Error (OE) method is in fact a simplification of the maximum likelihood estimator for deterministic systems, in which the process noise is assumed to be zero and the measurements are only corrupted by measurement noise. Fundamentally the output error method relies on adjusting the model parameter estimates iteratively to minimize the error between measured variables $\mathbf{z}$ and the predicted model output $\mathbf{y}$, as described in the following dynamic system [94]:

$$\dot{\mathbf{x}}(t) = \mathbf{A}\mathbf{x}(t) + \mathbf{B}\mathbf{u}(t) \quad ; \qquad x(0) = x_0 \tag{3.2.1a}$$

$$\mathbf{y}(t) = \mathbf{C}\mathbf{x}(t) + \mathbf{D}\mathbf{u}(t) \tag{3.2.1b}$$

$$\mathbf{z}(i) = \mathbf{y}(i) + \nu(i) \quad ; \qquad i = 1, 2, \ldots, N \tag{3.2.1c}$$

$$\nu \text{ is } \mathbb{N}(\mathbf{0}, \mathbf{R})$$

$$\text{cov}[\nu(i)] = E[\nu(i)\nu^T(j)] = \mathbf{R}\delta_{ij} \tag{3.2.1d}$$

The measurement equation can also be defined as:

$$\mathbf{z} = \mathbf{h}\left(\mathbf{\Theta}\right) + \nu \tag{3.2.2}$$

where $\mathbf{\Theta}$ is a vector of unknown parameters, and ν is a random vector with probability density $p\left(\nu\right)$.

Consider the sequence of measurements $\mathbf{Z}_N = [z(1), z(2), \ldots, z(N)]$ for unknown parameter $\mathbf{\Theta}$, the likelihood function for the measurement is denoted by $\mathbb{L}\left[\mathbf{Z}_N; \mathbf{\Theta}\right]$ such that:

$$\begin{aligned}
\mathbb{L}\left[\mathbf{Z}_N; \mathbf{\Theta}\right] &= \mathbb{L}\left[z(1), z(2), \ldots, z(N); \mathbf{\Theta}\right] \\
&= \mathbb{L}\left[z(N)|\mathbf{Z}(N-1); \mathbf{\Theta}\right] \mathbb{L}\left[z(N-1)|\mathbf{Z}(N-2); \mathbf{\Theta}\right] \ldots \\
&= \prod_{i=1}^{N} \mathbb{L}\left[z(i)|\mathbf{Z}(i-1); \mathbf{\Theta}\right]
\end{aligned} \tag{3.2.3}$$

By considering the measurement error covariance matrix $\mathbf{R}$, the likelihood function as given in Equation 3.2.3 can also be written as [54, 94] :

$$\mathbb{L}\left[\mathbf{Z}_N;\boldsymbol{\Theta},\mathbf{R}\right] = \{(2\pi)^{n_0}|\mathbf{R}|\}^{-N/2}\exp\left[-\frac{1}{2}\sum_{i=1}^{N}[z(i)-y(i)]^T\mathbf{R}^{-1}[z(i)-y(i)]\right] \tag{3.2.4}$$

given n_0 is the number of measured output.

Maximum likelihood estimation effectively searches for parameter $\boldsymbol{\Theta}$ that maximises this likelihood function $\mathbb{L}\left[\mathbf{Z}_N;\boldsymbol{\Theta},\mathbf{R}\right]$. A means of computing the maximum likelihood is by setting first order derivatives of the Equation 3.2.4 with respect to $\boldsymbol{\Theta}$ and $\mathbf{R}$ to zero. However, for computational purposes, it is preferable to minimize the negative logarithm of the likelihood functions rather than maximising the likelihood functions [54, 94]. Therefore, the maximum likelihood estimation problem is often given as:

$$\begin{aligned}\hat{\boldsymbol{\Theta}} &= \max\prod_{i=1}^{N}\mathbb{L}\left[z(i)|\mathbf{Z}(i-1);\boldsymbol{\Theta},\mathbf{R}\right] \\ &= \min\sum_{i=1}^{N}-\ln\left\{\mathbb{L}\left[z(i)|\mathbf{Z}(i-1);\boldsymbol{\Theta},\mathbf{R}\right]\right\} \qquad (3.2.5)\end{aligned}$$

$$J(\boldsymbol{\Theta},\mathbf{R}) = \frac{1}{2}\sum_{i=1}^{N}\nu^T(i)\mathbf{R}^{-1}\nu(i) + \frac{N}{2}\ln|\mathbf{R}| + \frac{Nn_0}{2}\ln(2\pi) \tag{3.2.6}$$

The covariance matrix $\mathbf{R}$ is included in Equation 3.2.6 and it acts as a weighting function for the sum of squares of the response error. When the noise covariance matrix is not known, its value is estimated by differentiating Equation 3.2.6 with respect to $\mathbf{R}$ and setting the result to zero.

$$\frac{\partial J(\boldsymbol{\Theta},\mathbf{R})}{\partial\mathbf{R}} = 0 \tag{3.2.7}$$

This yields:

$$\mathbf{R} = \frac{1}{N}\sum_{i=1}^{N}\nu(i)\nu^T(i) \tag{3.2.8}$$

Equation 3.2.8 highlights the fact that the estimate covariance matrix is dependent on the residual ν, which in turn depends on $\boldsymbol{\Theta}$. At the same time, Equation 3.2.6 shows that the cost function for finding the estimated parameter is dependent on the covariance matrix. Therefore, often relaxation techniques are implemented to calculate the cost function [94]. The relaxation technique is conducted by computing $\mathbf{R}$ for a given fixed $\boldsymbol{\Theta}$, and then minimising the cost function to $\boldsymbol{\Theta}$, and repeating this until a convergence criteria is satisfied.

The problem defined by Equation 3.2.5 and 3.2.6 is effectively an optimisation problem. The following subchapters discuss and compare two search algorithms, namely the modified Newton-Raphson and the Interior Point Algorithm. Both of these algorithms are gradient based methods which needs initial conditions. The initial conditions are usually

calculated through OLS method as given in Figure 3.19.

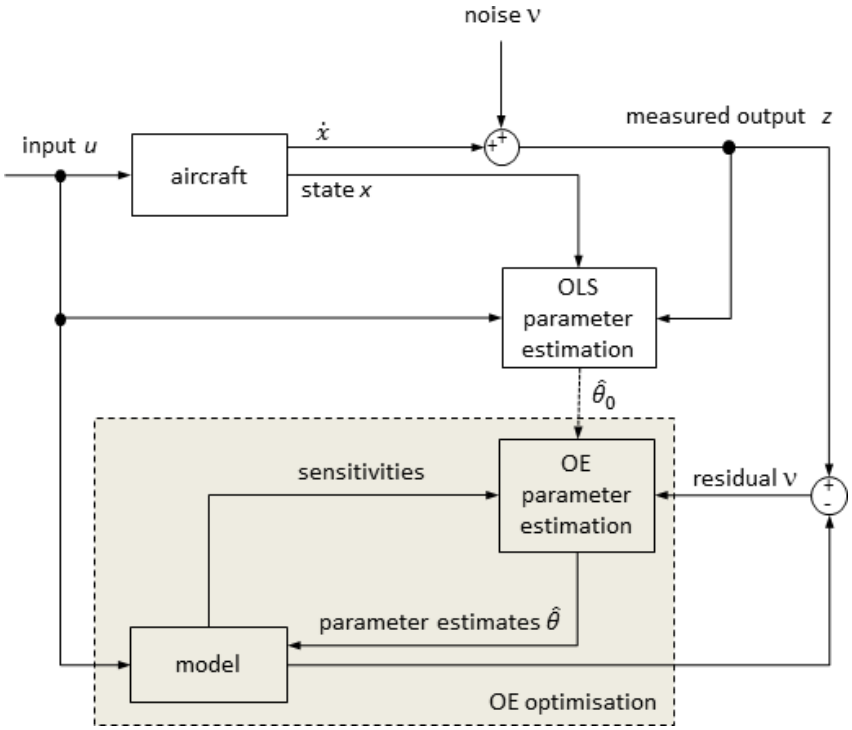

Figure 3.19: Estimation architecture for output error identification.

3.2.1 Modified Newton-Raphson

The Newton-Raphson method is an iterative method aiming to minimise the cost function (or likelihood function in case of MLE) $J(\Theta)$ such that the condition:

$$\frac{\partial J(\Theta)}{\partial \Theta} = 0 \tag{3.2.9}$$

is satisfied. The algorithm relies on small perturbation Taylor series expansion $J(\Theta + \Delta\Theta)$ to define step sizes when searching for optimal parameter estimates. Jategaonkar [54] shows that:

$$\left(\frac{\partial J}{\partial \Theta}\right)_{i+1} \approx \left(\frac{\partial J}{\partial \Theta}\right)_i + \left(\frac{\partial^2 J}{\partial \Theta^2}\right)_i \Delta\Theta \tag{3.2.10}$$

where

$$\Delta\Theta = \Theta_{i+1} - \Theta_i \tag{3.2.11}$$

and $(\partial^2 J/\partial\Theta^2)$ is also often known as the information matrix.

By setting Equation 3.2.10 to zero, $\Delta\Theta$ can be defined as :

$$\Delta\Theta = -\left[\left(\frac{\partial^2 J}{\partial \Theta^2}\right)_i\right]^{-1} \left(\frac{\partial J}{\partial \Theta}\right)_i \tag{3.2.12}$$

In the other words, the basic idea behind this method is to construct a quadratic approximation at each iteration and then take a step in the direction of the minimum of that approximated quadratic function [54]. In the case of the cost function given in Equation 3.2.6, for a given $\widehat{\mathbf{R}}$, the negative log-likelihood function $J(\Theta)$ becomes:

$$\begin{aligned} J(\Theta) &= \frac{1}{2}\sum_{i=1}^{N} \nu^T(i)\widehat{\mathbf{R}}^{-1}\nu(i) \\ &= \frac{1}{2}\sum_{i=1}^{N} [z(i)-y(i)]^T\widehat{\mathbf{R}}^{-1}[z(i)-y(i)] \end{aligned} \tag{3.2.13}$$

The measurement $z(i)$ is independent of the model parameter Θ. Therefore, the partial differential of Equation 3.2.13 with respect to the parameter results in:

$$\frac{\partial \mathbf{J}(\boldsymbol{\Theta})}{\partial \Theta_j} = -\sum_{i=1}^{N} \frac{\partial \mathbf{y}^T(i)}{\partial \Theta_j}\widehat{\mathbf{R}}^{-1}\nu(i) \tag{3.2.14}$$

$$\frac{\partial^2 \mathbf{J}(\boldsymbol{\Theta})}{\partial \Theta_j \partial \Theta_k} = \sum_{i=1}^{N} \frac{\partial \mathbf{y}^T(i)}{\partial \Theta_j}\widehat{\mathbf{R}}^{-1}\frac{\partial \mathbf{y}^T(i)}{\partial \Theta_k} - \sum_{i=1}^{N} \frac{\partial^2 \mathbf{y}(i)}{\partial \Theta_j \partial \Theta_k}\widehat{\mathbf{R}}^{-1}\nu(i) \tag{3.2.15}$$

The computation of the second term of the partial derivative of Equation 3.2.15 can be computationally expensive, complex and time-consuming. Furthermore, since this term is multiplied by the residual ν, this contribution tends to zero as the process converges. In the ideal case of zero mean and independent noise, this term tends to cancel out when summed over a sufficient length of data points [54]. Therefore, the second term of the Equation 3.2.15 is neglected and the optimisation algorithm is usually referred to as the modified Newton-Raphson method. Now substituting Equation 3.2.14, 3.2.15 into Equation 3.2.12 yields:

$$\Delta\widehat{\Theta} = \left[\sum_{i=1}^{N} \frac{\partial \mathbf{y}^T(i)}{\partial \Theta}\widehat{\mathbf{R}}^{-1}\frac{\partial \mathbf{y}(i)}{\partial \Theta}\right]^{-1}_{\Theta=\Theta_0} \left[\sum_{i=1}^{N} \frac{\partial \mathbf{y}^T(i)}{\partial \Theta}\widehat{\mathbf{R}}^{-1}\nu(i)\right]_{\Theta=\Theta_0} \tag{3.2.16}$$

where $\dfrac{\partial \mathbf{y}^T(i)}{\partial \Theta}$ is the system gradient (output sensitivity) and $\sum_{i=1}^{N} \dfrac{\partial \mathbf{y}^T(i)}{\partial \Theta}\widehat{\mathbf{R}}^{-1}\dfrac{\partial \mathbf{y}(i)}{\partial \Theta}$ is known as the Fisher information matrix.

The system gradient is calculated assuming small perturbations through the central differencing scheme. Although more computational time is needed when compared to forwards/backwards differencing methods, the central differencing method is a second order accurate scheme that leads to higher accuracy and sensitivities and helps in reducing the total number of iterations [94]. Furthermore, the inverse of the information matrix is calculated using the rank deficient method implementing through singular value decomposition to reduce the adverse effects of data collinearity.

As mentioned earlier, the relaxation techniques are often used to find the estimated parameter. For example when finding the values for the next iteration, estimates based on Equation 3.2.16, $\widehat{\mathbf{R}}$ and ν are calculated for a fixed $\boldsymbol{\Theta}$. The idea is that given unknown $\boldsymbol{\Theta}$ and $\mathbf{R}$, the optimisation will be well conditioned if $\boldsymbol{\Theta}$ and $\mathbf{R}$ are adjusted alternately

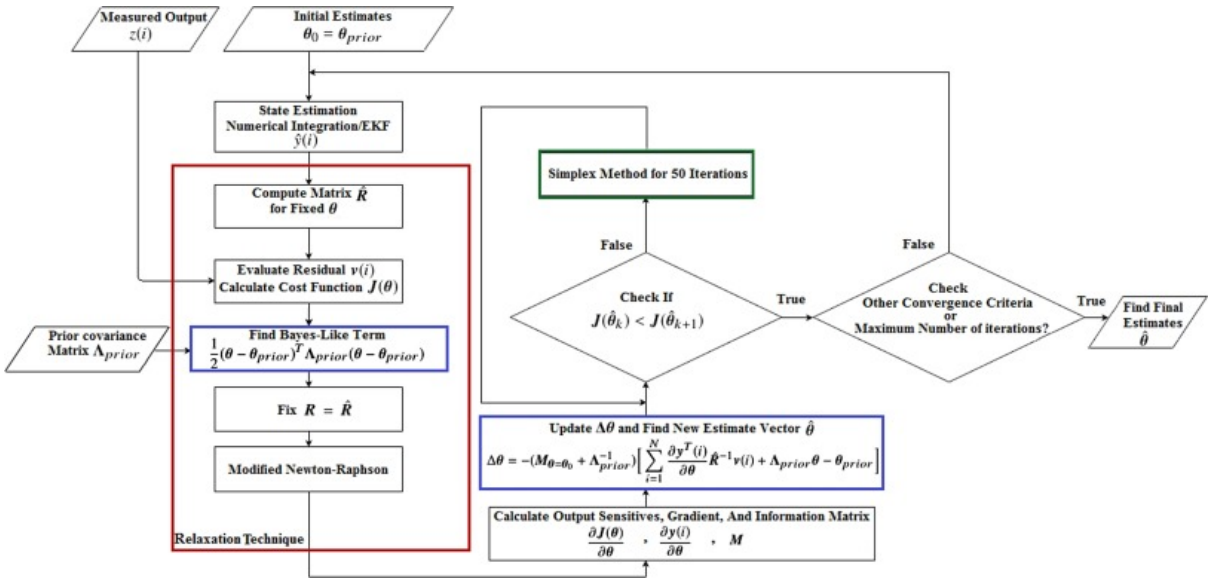

Figure 3.20: The flowchart of the augmented output-error methods (Reproduce from Reference [154]).

[94]. These steps are then repeated until the convergence criteria are satisfied. These criteria can be listed as follows:

1. Absolute value of the change in parameters are small. Klein [94] suggested convergence when change in $\Delta\boldsymbol{\Theta}$ is less than 0.001 Θ_j, while Jategaonkar [54] suggested the value to be less than $10^{-6}\Theta_j$.
2. Change in the cost $J(\widehat{\Theta})$ is small for consecutive iterations:

$$\left|\frac{J(\widehat{\Theta}_k) - J(\widehat{\Theta}_{k-1})}{J(\widehat{\Theta}_{k-1})}\right| < 0.001 \tag{3.2.17}$$

3. Absolute value of the cost gradient are close to zero:

$$\left|\left(\frac{\partial J(\Theta)}{\partial\Theta_j}\right)_{\Theta=\widehat{\Theta}_k}\right| < 0.05 \tag{3.2.18}$$

4. Changes in $\widehat{\mathbf{R}}$ are small:

$$\left|\frac{(\hat{r}_{jj})_k - (\hat{r}_{jj})_{k-1}}{(\hat{r}_{jj})_{k-1}}\right| < 0.05 \tag{3.2.19}$$

In the case of poor optimisation performance where the cost function value increases in relation to the previous iteration, simplex methods are used to estimate the next parameter vector. Simplex method is a direct search method that requires function evaluations and not the gradient [54]. In general this approach is much slower than gradient-based methods but more robust and assures convergence. The flowchart of the `oe` function is presented in Figure 3.20 as presented in Reference [154][4].

[4]The output error method is utilise using `oe` function from SIDPAC library. The `oe` requires a separate MATLAB function to calculate the model dynamics.

3.2.2 Identification of a Subscale Rigid Body Aircraft

In this example, output error method is applied to a subscale model to estimate parameters related to pitching moment stall hysteresis. The subscale model under test is a 1/12 scaled Hawk model which was tested inside the Cranfield University Weybridge tunnel, as shown in Figure 3.21. The subscale model is designed to have 4 DoF (roll, heave, yaw, pitch). However in this test, the model is constrained in roll and heave. It has a mass of 2.52 kg, mass moment of inertia in the pitch direction of 0.101 kg.m^2, and mean aerodynamic chord of 0.16 m. It is important to mention that the subscale model has only been geometrically scaled.

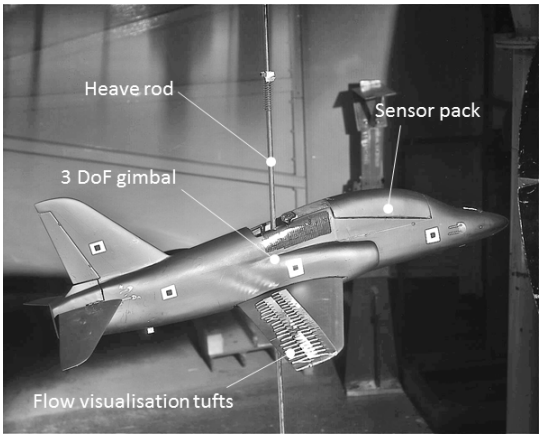

Figure 3.21: 1:12 scale Hawk model installed on dynamic rig. Reproduced from Reference [26].

Wind tunnel test data was collected using a series of doublet inputs at four different wind speeds. In this example, only test condition at 20 m/s and 30 m/s are considered. Figures 3.22 and 3.23 present the measurement data from the dynamic tests. These measurement data are the pitch acceleration (measured from vertical acceleration), the angle-of-attack measurement from the potentiometer at the gimbal and the elevator deflection, which is measured directly from the tailplane actuator.

Pitch acceleration is calculated from the accelerometer positioned at the nose (labelled as the sensor pack) and the gimbal (see Figure 3.21), using the following relationship:

$$\dot{q} = \ddot{\Theta} = \frac{a_1 - a_2}{r} \tag{3.2.20}$$

where a_1 and a_2 are the vertical accelerations measured in two different places, and r is the distance between the accelerometers.

The cross-plot between $\dot{q}$ and α as presented in Figure 3.22 and 3.23 highlight the hysteresis. This is a component of the phenomenon known as dynamic stall [54, 155, 156].

Carnduff et al [157] present a derivation of the linear longitudinal equations of motion for dynamic wind tunnel tests. However, in the appearance of dynamic stall, a dynamic stall model as presented by Goman [158] needs to be adopted and added to the equation. This combination results in the following nonlinear model:

$$\frac{I_{yy}}{\bar{q}S\bar{c}}\dot{q} = C_{M\alpha}\alpha + C_{M_q}q\left(\frac{\bar{c}}{2U}\right) + C_{M\delta_e}\delta_e + \frac{dC_M}{dX}(1-X) \tag{3.2.21}$$

The difference between the linear and non-linear model is the added term $\frac{dC_M}{dX}(1-X)$ which captures the nonlinearity in the pitching moment coefficient. X representes the empirical flow separation point. The general representation of the unsteady flow to characterise this separation point is defined as [158]:

$$\tau_1\frac{dX}{dt} + X = \frac{1}{2}\left[1 - \tanh\left(\lambda\left(\alpha - \tau_2\dot{\alpha} - \alpha^*\right)\right)\right] \tag{3.2.22}$$

Here, the transient and quasi-steady aerodynamic effects are represented by τ_1 and τ_2 respectively, while hysteresis is represented by λ (wing's static stall characteristics) and α^* (the break point corresponding to $X_0 = 0.5$).

As suggested by Jategaonkar [54], a simplified approach was adopted which accounted only for the quasi-steady stall characteristics by neglecting the transient effects. Thus, τ_1 is set to be zero and eliminates the need for modelling the first order dynamics of X. And Equation 3.2.22 becomes:

$$X = \frac{1}{2}\left[1 - \tanh\left(\lambda\left(\alpha - \tau_2\dot{\alpha} - \alpha^*\right)\right)\right] \tag{3.2.23}$$

Therefore, the model equation for output error estimations are defined as:

$$\frac{I_{yy}}{\bar{q}S\bar{c}}\dot{q} = C_{M\alpha}\alpha + C_{M_q}q\left(\frac{\bar{c}}{2U}\right) + C_{M\delta_e}\delta_e + \frac{1}{2}\frac{dC_M}{dX}\left(1 - \tanh\left(\lambda\left(\alpha - \tau_2\dot{\alpha} - \alpha^*\right)\right)\right) \tag{3.2.24}$$

$$q = \dot{\alpha} \tag{3.2.25}$$

and the measurement equations, by considering that a_1 is effectively zero, are defined as:

$$a_2 = r\frac{\bar{q}S\bar{c}}{I_{yy}}\dot{q} \tag{3.2.26}$$

$$\theta = \alpha + b_\alpha \tag{3.2.27}$$

where b_α is the bias α.

The use of output error method requires a set of initial parameter estimates. Here, these are the flight dynamic coefficients and the initial guess is obtained by finding the coefficients for the following linear model:

$$\frac{I_{yy}}{\bar{q}S\bar{c}}\dot{q} = C_{M\alpha}\alpha + C_{M_q}q\left(\frac{\bar{c}}{2U}\right) + C_{M\delta_e}\delta_e \tag{3.2.28}$$

The initial estimates for the non-linear component were selected from the past work conducted by Fischenberg [156]. λ was set to 15 and τ_2 was calculated from the relationship given for VFW-614 ATTAS aircraft and defined as $\tau_2 = 4.45\frac{\bar{c}}{U}$. The α^* value was set to be 5^o as the maximum angle of attack during test never exceeded 15°, and the initial

value for $\frac{dC_M}{dX}$ is set to zero.

The identification results are given in Figures 3.24 and 3.25 and the parameter values are summarised in Table 3.3. These figures show that the non-linear model with the added hysteresis model has a better match with the measurements, especially in angle of attack. It also shows that the residual from the model output and the measurement decreases with the addition of the nonlinear term. It is worth mentioning that here the linear model is also identified using output error method for comparison.

The parameter estimation results presented in Table 3.3 show that the estimated parameters are within the expected order of magnitude with relatively small standard deviations. However, the τ_2 parameter which is related to $\dot{\alpha}$ and represents quasi-steady aerodynamic effects has a significantly large standard deviation. This implies that this parameter is insignificant in the estimation process and needs to be dropped. Hence, the proposed model can be written as follows:

$$C_M = C_{M\alpha}\alpha + C_{M_q} q \left(\frac{\bar{c}}{2U}\right) + C_{M\delta_e}\delta_e + \frac{1}{2}\frac{dC_M}{dX}\left[1 - \tanh\left(\lambda(\alpha - \alpha^*)\right)\right] \tag{3.2.29}$$

Parameter	Linear Model		Nonlinear Models			
	$\hat{\Theta}$	$s(\hat{\Theta})$	$\hat{\Theta}$	$s(\hat{\Theta})$	$\hat{\Theta}$	$s(\hat{\Theta})$
V = 20 m/s (t: 24-34 s)						
$C_{M\alpha}$	-0.186	0.0013	-0.291	0.002	-0.291	0.002
C_{Mq}	-11.14	0.186	-9.628	0.109	-9.845	0.097
$C_{M\delta_e}$	-2.013	0.026	-2.168	0.023	-2.205	0.019
$\frac{dC_M}{dX}$	-	-	0.0262	0.001	0.0260	0.001
b_α (rad)	0.0355	0.0004	0.0324	0.0002	0.0324	0.0002
λ	-	-	46.80	6.536	50.21	7.162
α^*(rad)	-	-	0.115	0.0019	0.115	0.002
τ_2	-	-	-0.0178	0.0061	-	-
V = 30 m/s (t: 6-12 s)						
$C_{M\alpha}$	-0.179	0.003	-0.395	0.007	-0.395	0.007
C_{Mq}	-19.06	0.529	-13.37	0.218	-13.98	0.149
$C_{M\delta_e}$	-2.991	0.071	-2.575	0.029	-2.520	0.024
$\frac{dC_M}{dX}$	-	-	0.0587	0.002	0.059	0.002
b_α	0.007	0.0009	-0.009	0.0011	-0.008	0.001
λ	-	-	17.171	0.816	17.08	0.78
α^*(rad)	-	-	0.0934	0.002	0.095	0.002
τ_2	-	-	0.0151	0.004	-	-

Table 3.3: Parameter identification results.

Table 3.4 presents the correlation between each parameter. Overall, it shows that the term $C_{M\delta_e}$ is highly correlated with C_{Mq} and α^*, while $\frac{dC_M}{dX}$ is highly correlated with $C_{M\alpha}$ and α^*. Furthermore, at the higher velocity the parameter related to the non-linear terms, $\frac{dC_M}{dX}$, α^*, λ, and b_α are highly correlated amongst each other. This indicates high uncertainty at higher velocities and suggests the need for a more comprehensive set of

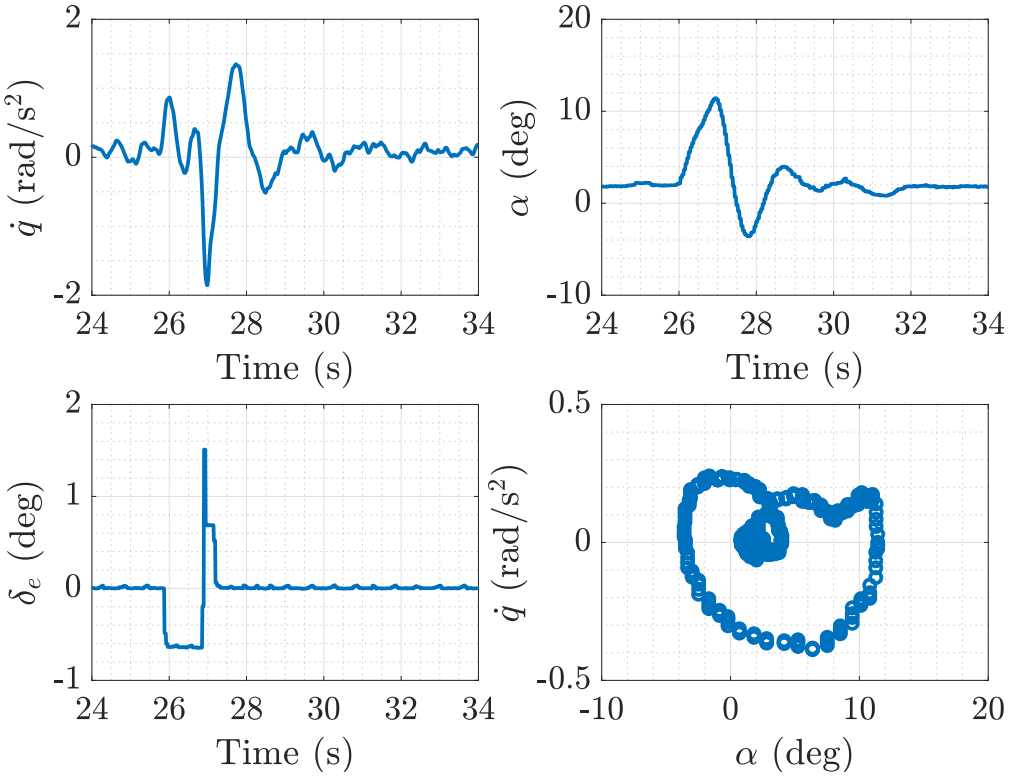

Figure 3.22: Measured input and output for Hawk model at 20 m/s.

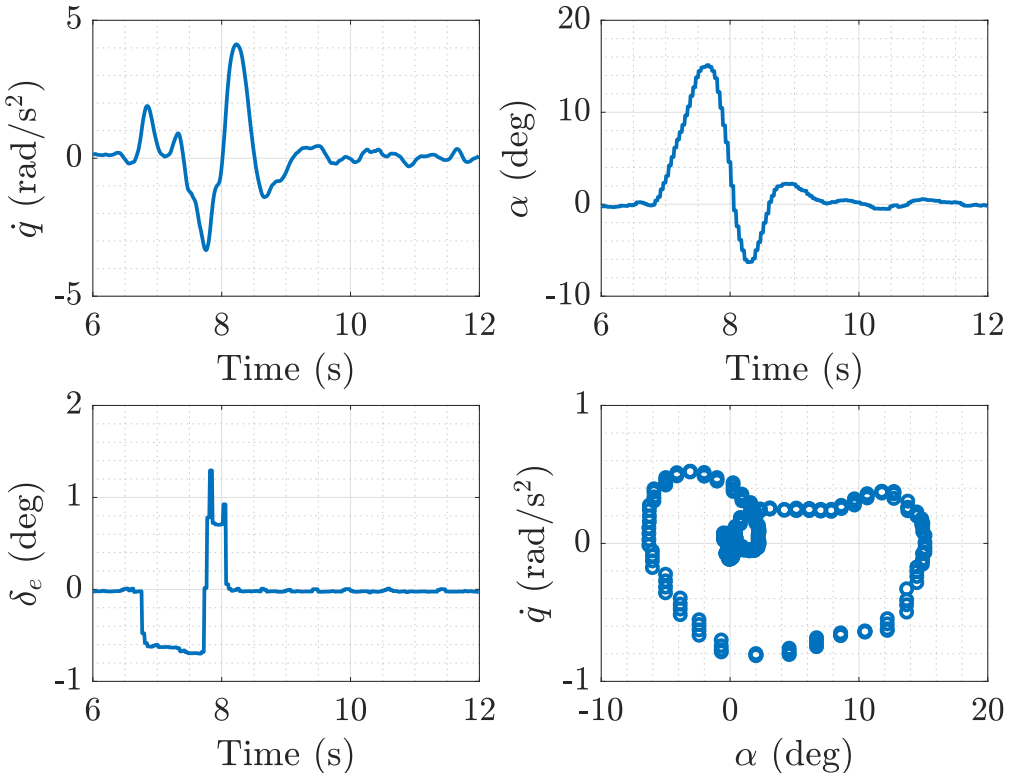

Figure 3.23: Measured input and output for Hawk model at 30 m/s.

tests to be able to identify each parameter at the desired quality. Furthermore, the reader is referred to Reference [26] for a thorough discussion of this work.

Θ	V = 20 m/s							V = 30 m/s						
$C_{M\alpha}$	1	-	-	-	-	-	-	1	-	-	-	-	-	-
C_{Mq}	0.027	1	-	-	-	-	-	0.167	1	-	-	-	-	-
$C_{M\delta_e}$	0.195	0.676	1	-	-	-	-	0.125	0.865	1	-	-	-	-
b_α	0.192	0.100	0.162	1	-	-	-	0.866	0.238	0.225	1	-	-	-
$\frac{dC_M}{dX}$	0.586	0.072	0.351	0.204	1	-	-	0.988	0.154	0.136	0.906	1	-	-
λ	0.210	0.099	0.244	0.111	0.638	1	-	0.850	0.338	0.359	0.928	0.893	1	-
α^*	0.033	0.224	0.583	0.103	0.768	0.394	1	0.764	0.364	0.472	0.808	0.816	0.940	1

Table 3.4: Correlation matrix based on output error method.

3.2.3 Interior Point Algorithm

The modified Newton-Raphson method as explained in the previous section gives the unconstrained solution, which means that the solution of the nonlinear optimisation problem consist of unbounded-variables. In some cases, bounded-variables/constrained parameters might be relevant and especially needed for [54]:

1. Identifying parameters that describe physical effects, such as the Oswald efficiency factor which is typically less than one,
2. Estimating time delays in the measurement that by definition are greater than zero, and/or
3. Estimate parameters that can lead to numerical difficulties.

Given a dynamic system, the interior-point algorithm is developed to find the minimum of a constrained non-linear multivariable function that is specified as[5]:

$$\min_x f(x) \text{ such that } \begin{cases} c(x) \leq 0 \\ c_{eq}(x) = 0 \\ A \cdot x \leq b \\ A_{eq} \cdot x = b_{eq} \\ lb \leq x \leq ub \end{cases} \tag{3.2.30}$$

in which b and b_{eq} are vectors, A and A_{eq} are matrices, $c(x)$ and $c_{eq}(x)$ are functions that return vectors, and $f(x)$ is a function that returns a scalar.

In the case of aircraft system identification, the constrained non-linear multivariable problem can be simplified and formulated as:

$$\min_\Theta J(\Theta), \text{ subject to } \Theta_{\min} \leq \Theta \leq \Theta_{\max} \tag{3.2.31}$$

where $J(\Theta)$ is the cost function as given in Equation 3.2.6 for the dynamic systems defined in Equation 3.2.1.

The basis of this optimisation methodology is a trust-region approach [159], which means to find x that minimises $f(x)$, the function value is evaluated at the initial condition, then

[5]The interior point algorithm is utilised within the embedded MATLAB `fmincon` function.

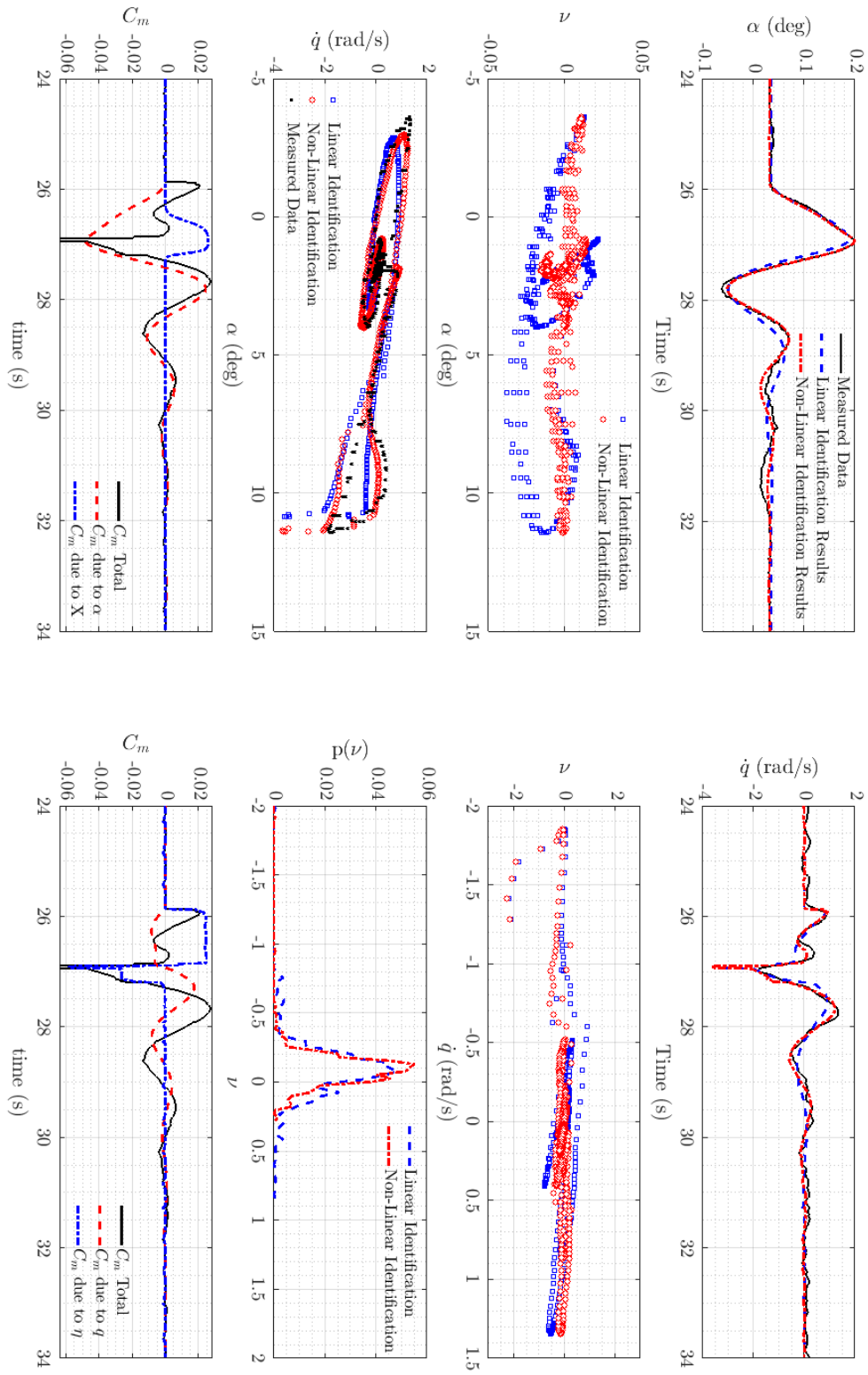

Figure 3.24: Identification results for data at 20 m/s.

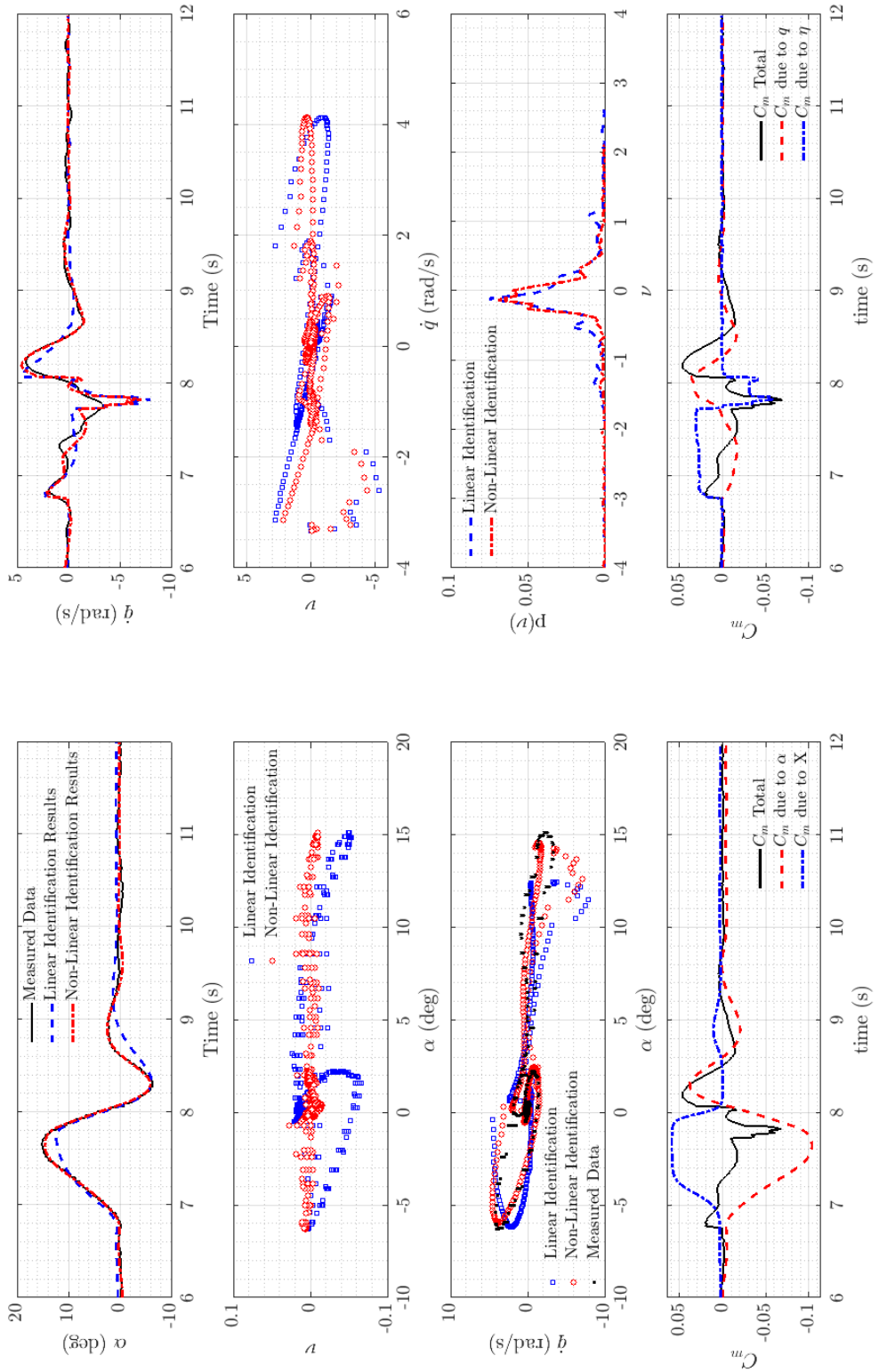

Figure 3.25: Identification results for data at 30 m/s.

moved to a point with a lower function value. In finding the step size Δx, the function $f(x)$ is approximated with a simpler function that reflects the behaviour of f around x within a neighbourhood N. Δx is computed by minimizing $f(x)$ over the neighbourhood N. If $f(x+\Delta x) < f(x)$, the new point is updated to $x+\Delta x$, otherwise the current point remains unchanged, but N (the region of trust) is reduced and the trial step computation is repeated.

Based on Equation 3.2.31, a function $c(\Theta)$ is defined as an inequality constraint subject to $\Theta_{\min} \leq \Theta \leq \Theta_{\max}$. This constraint can then be [54] :

$$\begin{aligned} c(\Theta) - \Theta_{\max} &\leq 0 \\ \Theta_{\min} - c(\Theta) &\leq 0 \end{aligned} \tag{3.2.32}$$

which can be simplified into the general form of:

$$c_i(\Theta) \leq 0, i = 1, \ldots, p \tag{3.2.33}$$

with p being the total number of constraints.

Combining Equation 3.2.31 and 3.2.33, this can be related to the following general problem:

$$\min_x f(x), \text{ subject to } h(x) \leq 0 \tag{3.2.34}$$

In applying the interior-point approach, this general problem is reformulated through the use of slack variables s_i for each constraint h, so that

$$\min_x f(x), \text{ subject to } h(x) + s = 0, \text{ and } s \geq 0 \tag{3.2.35}$$

The inequality constraint can be eliminated by introducing a barrier parameter $\mu(> 0)$ to prevent the solution from leaving the feasible region. This results in:

$$\min_{x,s} f_\mu(x, s) = \min_{x,s} f(x) - \mu \sum_{i=1}^{p} \ln(s_i), \text{ subject to } h(x) + s = 0 \tag{3.2.36}$$

By letting μ converge to zero, the minimum of Equation 3.2.36 will converge to the minimum of Equation 3.2.35 [160]. The solution of the barrier problem is conducted by introducing the Lagrangian and re-writing Equation 3.2.36 as:

$$\mathcal{L}(x, s, \kappa_h) = f(x) - \mu \sum_{i=1}^{p} \ln s_i + \kappa_h^T (h(x) + s) \tag{3.2.37}$$

where κ_h is the Lagrangian multiplier associated to the equality constrained. The optimal solution (x, s) for Equation 3.2.36 is then given by [161]:

$$\nabla_x \mathcal{L}(x, s, \kappa_h) = \nabla f(x) + A_I(x)\kappa_I = 0 \tag{3.2.38}$$

$$\nabla_s \mathcal{L}(x, s, \kappa_h) = -\mu S^{-1} e + \kappa_I = 0 \tag{3.2.39}$$

where $A_I(x)$ is matrix of constant gradient of $\left(\nabla h_I^{(1)}, \ldots, \nabla h_I^{(p)}\right)$, e denotes the vector of

ones with the same size as g, and S is a diagonal matrix of s.

By default, the `fmincon` algorithm solves the problem by using direct step (Newton) method. In the case where direct step does not converge (that is the projected Hessian is not positive definite), a conjugate gradient step using trust region is used.

The direct step method is defined by considering the Hessian of the Lagrangian f_μ:

$$H = \nabla^2 f(x) + \sum_i \kappa_i \nabla^2 h_i(x) \tag{3.2.40}$$

Based on this equation, the direct step (Δx, Δs) can then be defined as [159]:

$$\begin{bmatrix} H & 0 & J_h^T \\ 0 & S\Lambda & -S \\ J_h & -S & I \end{bmatrix} \begin{bmatrix} \Delta x \\ \Delta s \\ -\Delta\kappa \end{bmatrix} = - \begin{bmatrix} \nabla f - J_h^T \kappa \\ S\kappa - \mu e \\ h + s \end{bmatrix} \tag{3.2.41}$$

where J_h denotes the Jacobian of the constraint function h and Λ is a diagonal matrix of κ.

It is worth mentioning that when utilising the `fmincon` function, the users are obliged to build a cost function in a separate file as opposed to the model equation as expected from the previous modified Newton-Raphson method. In the case of aircraft system identification, the cost function is usually defined as[6]

$$J(\mathbf{\Theta}, \mathbf{R}) = \frac{1}{2} \sum_{i=1}^{N} [\mathbf{z}(i) - \mathbf{y}(i)]^T \widehat{\mathbf{R}}^{-1} [\mathbf{z}(i) - \mathbf{y}(i)] + \frac{N}{2} \ln |\mathbf{R}| \tag{3.2.42}$$

In this case the covariance matrix $\mathbf{R}$ is also calculated via relaxation methods. In addition to the model parameter x, the function also evaluates the value, gradient and Hessian of the objective function at the solution point x. Note that `fmincon` is a gradient-based method, where the function only works on problems where the objective and constraint functions are both continuous and have continuous first derivatives.

Example 3.2.1 ***Comparison of `oe` and `fmincon` routine***
This example is presented to compare the effectiveness of `oe` *and* `fmincon` *functions. Given the aforementioned dynamic wind tunnel model (see Section 3.2.2), a comparison of identification results from two different optimisation methods will be presented. The first method is the Modified Newton-Raphson implemented through* `oe` *function from SIDPAC [94]. The second method is the interior point algorithm implemented via the MATLAB function* `fmincon`*.*

In this case, the final equation of Equation 3.2.29 will be used to compare the optimisation methods with a similar set of initial parameter estimates as discussed in the earlier Section 3.2.2. Table 3.5 allows the comparison of estimation results obtained through the `oe` *and* `fmincon` *functions*[a]*. The results show that given similar initial guess values, both estimation algorithms give almost similar results with comparable standard deviations.*

[6]The cost function in Equation 3.2.42 is always scalar regardless of the dimension of R.

Parameter	oe		fmincon	
	$\hat{\Theta}$	$s(\hat{\Theta})$	$\hat{\Theta}$	$s(\hat{\Theta})$
V = 20 m/s (t: 24-34 s)				
$C_{M\alpha}$	-0.291	0.002	-0.291	0.003
C_{Mq}	-9.485	0.097	-9.488	0.251
$C_{M\delta_e}$	-2.205	0.019	-2.206	0.054
b_α (rad)	0.032	0.0002	0.032	0.0003
$\frac{dC_M}{dX}$	0.0226	0.001	0.026	0.002
λ	50.21	7.162	50.31	6.89
α^*(rad)	0.115	0.002	0.115	0.002
convergence time	189.46 s		61.39 s	
V = 30 m/s (t: 6-12 s)				
$C_{M\alpha}$	-0.395	0.007	-0.395	0.007
C_{Mq}	-13.98	0.149	-13.99	0.154
$C_{M\delta_e}$	-2.520	0.024	-2.522	0.026
b_α (rad)	-0.008	0.0011	-0.008	0.001
$\frac{dC_M}{dX}$	0.059	0.002	0.059	0.002
λ	17.08	0.780	17.07	0.765
α^*(rad)	0.095	0.002	0.095	0.002
convergence time	123.87 s		27.47 s	

Table 3.5: Comparison of non-linear model parameter obtained using `oe` and `fmincon`.

*Overall, **`fmincon`** has a faster convergence rate compared to the **`oe`** algorithm. Nevertheless both algorithms take time to converge and so are not applicable for real-time estimation. Presented in Figure 3.26 and 3.27 are the changes in parameters per iteration. The convergence rate is inversely proportional to the number of iterations. It is evident that **`fmincon`** converges with fewer iterations compared to the **`oe`** function. However, the **`oe`** function allows the user to look into the change of the Hessian matrix for each iteration. On the other hand, the **`fmincon`** function only allows the user to look into the Hessian for the final estimation. Observing changes in the Hessian matrix is essential because it is effectively an indicator for the accuracy of the identified parameter. Both in Figure 3.26 and 3.27, for the convergence of **`oe`** algorithm, the standard deviation of each parameter on each iteration is presented. It shows that as the convergence is approached the uncertainty bound is getting smaller, except for parameter a_1. The fact that uncertainty bounds is getting smaller indicates a better estimation parameter (as discussed in the following subchapter).*

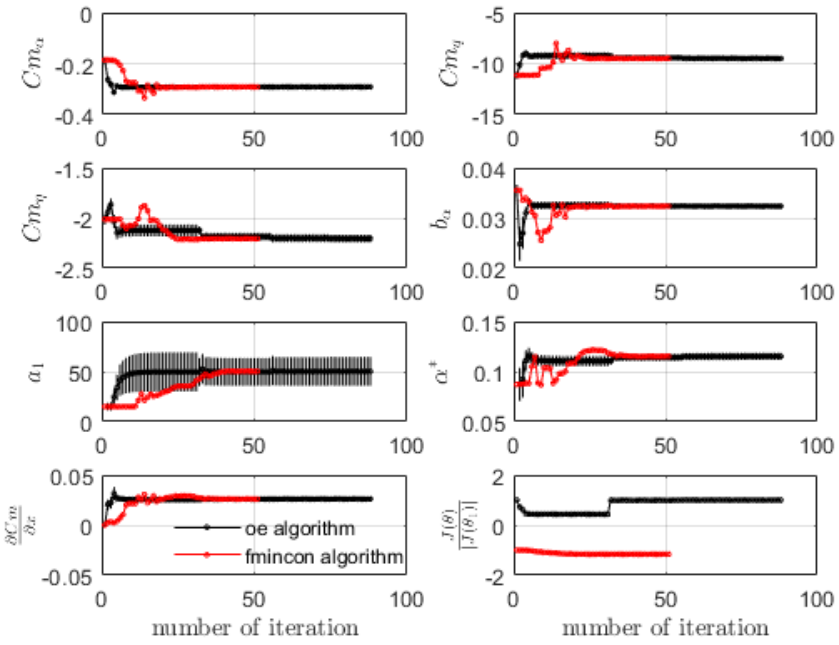

Figure 3.26: Parameter convergence comparison of `oe` and `fmincon` for 20 m/s cases.

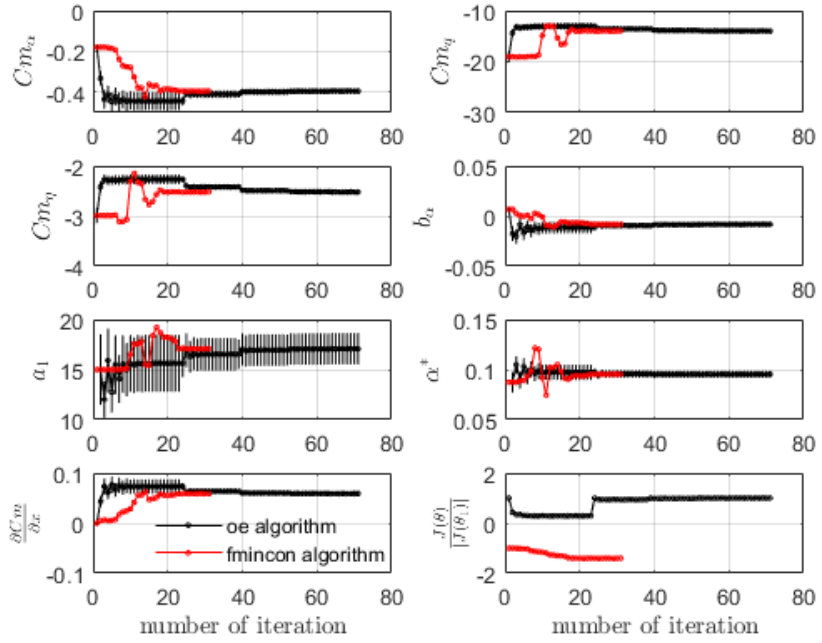

Figure 3.27: Parameter convergence comparison of `oe` and `fmincon` for 30 m/s cases.

[a]The identification procedure was carried out on : Intel(R) Core i5-4590 CPU @3.30 GHz - RAM 8.00 GB.

3.2.4 Confidence Intervals

One of the most important results from parameter estimation is the statistical accuracy of estimation results. A common criteria is the standard deviation, which is also known as the Cramér-Rao bound. The error covariance matrix is approximated by the Fisher information matrix for maximum likelihood estimation:

$$\mathbf{M} \equiv -E\left[\frac{\partial^2 \ln \mathbb{L}(\mathbf{Z}_n;\mathbf{\Theta})}{\partial\Theta\partial\Theta^T}\right] = \sum_{i=1}^{N} \frac{\partial \mathbf{y}^T(i)}{\partial\Theta_j}\hat{\mathbf{R}}^{-1}\frac{\partial \mathbf{y}^T(i)}{\partial\Theta_k} \tag{3.2.43}$$

where the Cramér-Rao inequality indicates the lower bound for the parameter covariance matrix and satisfies [94]:

$$\sigma_\Theta^2 = \mathrm{Cov}(\hat{\Theta}) \geq \mathbf{M}^{-1}_{\Theta=\hat{\Theta}} \tag{3.2.44}$$

Note that the Cramér-Rao bound tends to decrease with more data points. Furthermore, since the Cramér-Rao bound reflects the confidence in the estimated parameter, this criteria can also be used to refine the model structure. Tischler mentioned that large relative bounds indicate poor identifiability and so parameters with large bounds should be eliminated (or fixed) in the model structure [95]. Similarly, Jategaonkar emphasises that estimated parameters can be considered acceptable if the Cramér-Rao bounds satisfy $\mathrm{CR}_i \leq 20\%$ [54].

The confidence interval of the estimated parameters are derived from the Gaussian probability distribution. A common value selected for confidence level is 95% based on the t-distribution related to 2σ [94]: this means that there is a 95% probability that the true value of the estimated parameter Θ_i is inside the confidence interval of $[\hat{\Theta}_i - 2\sigma_i, \hat{\Theta}_i + 2\sigma_i]$. However, Jategaonkar suggests using a factor of 5 to 10 for realistic accounting for noise [54]. This factor is an ad-hoc approach to consider the fact that output error methods merge process and measurement noises along with deterministic modelling errors, that in turn corrupt the noise statistics. Another way of dealing with noise is by introducing coloured residuals [54, 94].

In addition to the confidence interval, the correlation coefficient is also useful to measure the statistical dependency between parameters. Similar to the idea of confidence interval, the correlation coefficient is also expected to be small for accurate estimation. The correlation coefficient is obtained from the off-diagonal terms of the Hessian matrix and defined as:

$$\rho_{\Theta_i\Theta_j} = \frac{p_{ij}}{\sqrt{p_{ii}p_{jj}}} \tag{3.2.45}$$

Example 3.2.2 ***The importance of weighting factor*** **R** ***in output error method***

This example is presented to underline the importance of the covariance matrix **R** *on the cost function. A comparison of the different cost functions is done using the* `fmincon` *function, because it allows the user to define the objective function separately. To start with, a simple cost function with different weighting function W is used to compare the identification results. Both experimental data sets (20 m/s and 30 m/s), as given in Section 3.2.2, will be used with the following cost functions:*

$$J_{W1}(\Theta) = \sum_{i=1}^{N} \begin{bmatrix} \nu_1(i) & \nu_2(i) \end{bmatrix}^T \begin{bmatrix} 1 & 0 \\ 0 & 1 \end{bmatrix} \begin{bmatrix} \nu_1(i) & \nu_2(i) \end{bmatrix} \tag{3.2.46}$$

$$J_{W2}(\Theta) = \sum_{i=1}^{N} \begin{bmatrix} \nu_1(i) & \nu_2(i) \end{bmatrix}^T \begin{bmatrix} 1 & 0 \\ 0 & 0.01 \end{bmatrix} \begin{bmatrix} \nu_1(i) & \nu_2(i) \end{bmatrix} \tag{3.2.47}$$

$$J_R(\Theta) = \sum_{i=1}^{N} \begin{bmatrix} \nu_1(i) & \nu_2(i) \end{bmatrix}^T \mathbf{R} \begin{bmatrix} \nu_1(i) & \nu_2(i) \end{bmatrix} \tag{3.2.48}$$

in which $\nu = z_i - y_i$, z_1 is the measurement of α, z_2 is the measurement of $\dot{q}$, and y is the model output with respect to the measurements.

Comparison results from the different weighting functions is presented in Figure 3.28 and 3.29 for 20 m/s and 30 m/s respectively. The estimated parameters are given in Table 3.6. More weight on the residual of α is seen to give a closer response with the estimation results using cost function from Equation 3.2.42. This highlights the importance of weighting on the maximum likelihood/output-error estimator. Furthermore, including the weighting function leads to improvements in the model response for α with minimum impact on the $\dot{q}$ variable.

Similarly, as presented in Table 3.6, the identified parameter for W_2 is closer to the original cost function used for the output-error estimator. However, the estimate standard deviations corresponding to the weighting function W_2 are very high at 30 m/s. Therefore, the identification results cannot be trusted even though the results are similar to the output-error cost function. This further underlines the importance of including the covariance matrix in the cost function, as the term $\log|\mathbf{R}|$ suggests that the cost function will converge as $\mathbf{R}$ goes to zero.

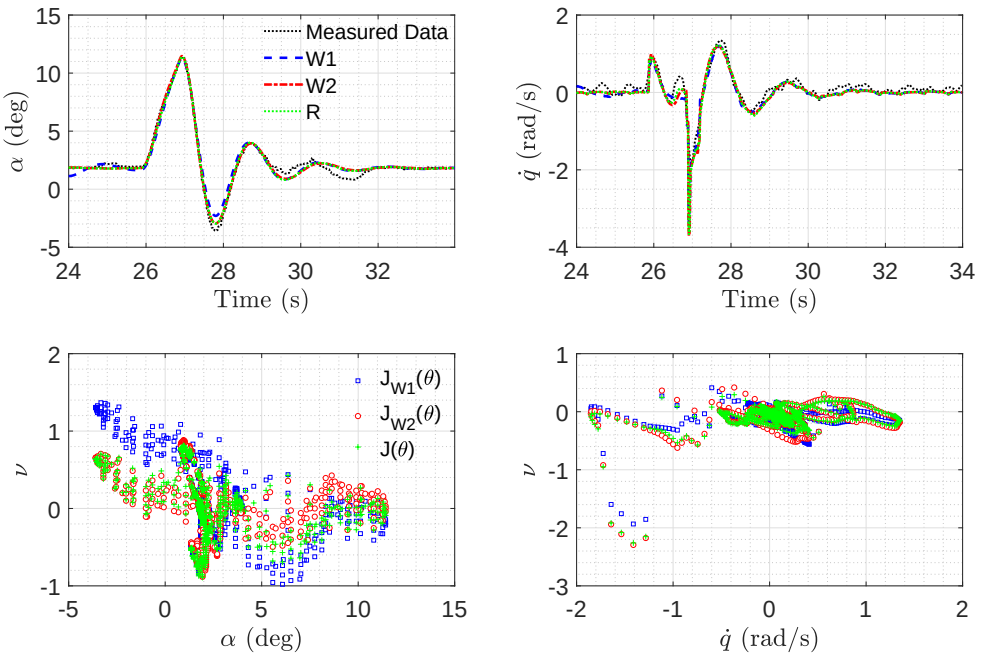

Figure 3.28: Identification results for various cost functions at 20 m/s.

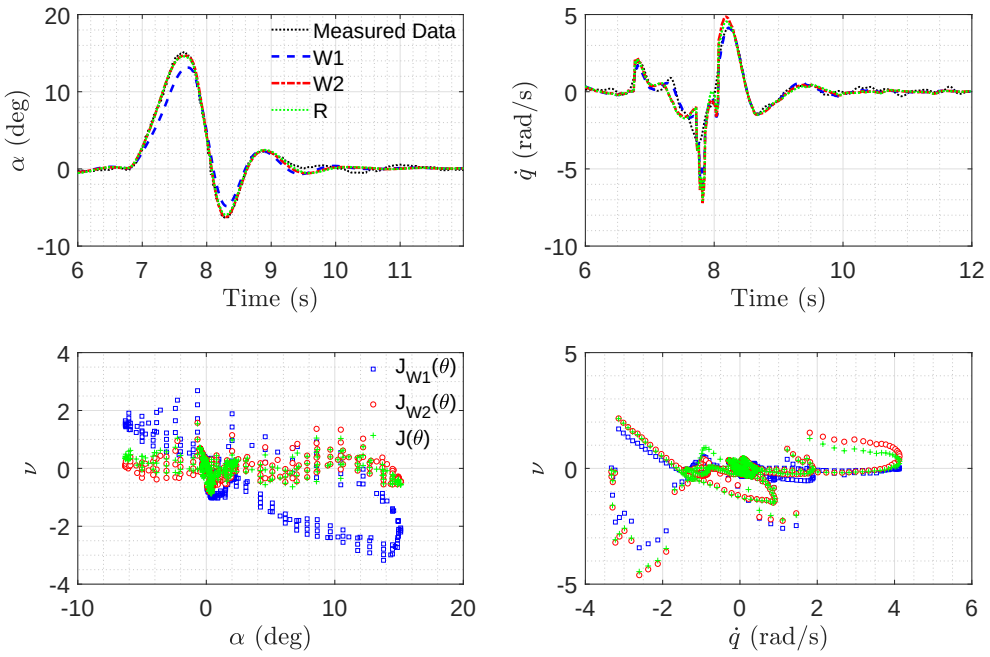

Figure 3.29: Identification results for various cost functions at 30 m/s.

Parameter	R^{-1}		$W1$		$W2$	
	$\hat{\Theta}$	$s(\hat{\Theta})$	$\hat{\Theta}$	$s(\hat{\Theta})$	$\hat{\Theta}$	$s(\hat{\Theta})$
V = 20 m/s (t: 24-34 s)						
$C_{M\alpha}$	-0.291	0.003	-0.395	0.019	-0.283	0.004
C_{Mq}	-9.488	0.251	-9.258	0.171	-9.929	0.296
$C_{M\delta_e}$	-2.206	0.054	-1.945	0.056	-2.292	0.018
b_α (rad)	0.032	0.0003	0.020	0.002	0.033	0.001
$\frac{dC_M}{dX}$	0.026	0.002	0.066	0.001	0.028	0.004
λ	50.31	6.89	10.67	0.555	39.56	2.744
α^*(rad)	0.115	0.002	0.130	0.006	0.128	0.005
V = 30 m/s (t: 6-12 s)						
$C_{M\alpha}$	-0.395	0.007	-0.464	0.210	-0.381	2.600
C_{Mq}	-13.99	0.154	-12.87	-4.15	-14.35	249
$C_{M\delta_e}$	-2.522	0.026	-2.020	0.731	-2.631	105
b_α (rad)	-0.008	0.001	-0.007	0.226	-0.007	46.23
$\frac{dC_M}{dX}$	0.059	0.002	-0.071	0.514	-0.055	53.9
λ	17.07	0.765	17.34	31.8	17.43	166
α^*(rad)	0.095	0.002	0.095	0.087	0.099	12.022

Table 3.6: Identification of non-linear model comparison using `fmincon` function with various weighting functions.

3.3 Subspace Identification

The previous section on regression and output-error methods are part of the white-box model, where the parameters have a physical meaning and a-priori information is needed. Aircraft system identification mostly deals with white-box models [54]. However, due to the numerous numbers of measurement and the lack of a-priori information these methods are not practical for structural model identification.

The most common time domain identification method in the area of modal parameter identification is called the realisation algorithm [162] which is defined as the "*process of constructing a state space representation from experimental data*" [116, 117]. The subspace method was developed based on the concept of system realisation and is part of the family of prediction error methods [125].

In this section, the utilisation of subspace identification method is discussed but restricted to discrete, linear, time-invariant system [126]. The mathematical model representing such systems is as follows:

$$\begin{aligned} \mathbf{x_{k+1}} &= A\mathbf{x_k} + B\mathbf{u_k} + w_k, \\ \mathbf{y_k} &= C\mathbf{x_k} + D\mathbf{u_k} + v_k \end{aligned} \tag{3.3.1}$$

where $\mathbf{x_k} \in \mathbb{R}^n$ is the state matrix with order n, $\mathbf{y_k} \in \mathbb{R}^l$ is the state output and $\mathbf{u_k} \in \mathbb{R}^m$ is the state input. The state and output measurement noise, w_k and v_k, are assumed to be zero mean white noise, with covariances defined as:

$$\mathbb{E}\left[\begin{pmatrix} w_p \\ v_p \end{pmatrix}\begin{pmatrix} w_p^T & v_p^T \end{pmatrix}\right] = \begin{pmatrix} Q & S \\ S^T & R \end{pmatrix}\delta_{pq} \tag{3.3.2}$$

where $Q \in \mathbb{R}^{n\times n}$, $S \in \mathbb{R}^{n\times l}$, and $R \in \mathbb{R}^{l\times l}$. The matrix $A \in \mathbb{R}^{n\times n}$ is the system matrix which describes the dynamics of the system through its eigenvalue characteristics, while the matrix $B \in \mathbb{R}^{n\times m}$ is the input matrix. The matrix $C \in \mathbb{R}^{l\times n}$ is the output matrix which relates the internal states to the measurement, and matrix $D \in \mathbb{R}^{l\times l}$ is the feedthrough matrix.

3.3.1 Notation

Subspace identification aims to find an appropriate order n and determine the system matrices in Equations 3.3.1 and 3.3.2 based on input and output measurements [126]. This method is applicable for both deterministic and stochastic systems. A system is known as a deterministic system if both process and measurement noises (see Equation 3.3.1), are identically zero. On the other hand the system is known as a stochastic system where there is no presence of external output u_k. In this case, it is not relevant to identify matrix B and D.

Subspace identification algorithm utilises the observability and controllability matrices for identification. A system is observable if the initial state value can be determined using the measurement of output y_k over a finite interval of time [163]. Mathematically, this

problem is captured by the observability matrix Γ_i:

$$\Gamma_i \triangleq \begin{pmatrix} C \\ CA \\ CA^2 \\ \dots \\ CA^{i-1} \end{pmatrix} \tag{3.3.3}$$

The matrix pair $\{A, C\}$ are considered to be observable if the rank of Γ_i is equal to n. On the other hand, a state is said to be controllable if the input can affect the state [163]. For a deterministic system, the reversed extended controllability matrix is defined as:

$$\Delta_i \triangleq \begin{pmatrix} A^{i-1}B & A^{i-2}B & \dots & AB & B \end{pmatrix}$$

The matrix pair $\{A, B\}$ are considered to be controllable if the vector Δ_i is linearly independent [163] and so a system is controllable if every state in the system is controllable. However, it is worth noting that controllable modes can either be stable or unstable [126].

Now that the observability matrix has been defined, steps that involve the Toeplitz and Hankel matrix can be discussed. These matrices play an important role in the subspace identification methods, in which the Toeplitz matrix consist of the B and D matrices of the system. The lower block triangular Toeplitz matrix H_i is defined as:

$$H_i \triangleq \begin{pmatrix} D & 0 & 0 & \dots & 0 \\ CB & D & 0 & \dots & 0 \\ CAB & CB & D & \dots & 0 \\ \dots & \dots & \dots & \ddots & \dots \\ CA^{i-2}B & CA^{i-3}B & CA^{i-4}B & \dots & D \end{pmatrix} \in \mathbb{R}^{li \times mi} \tag{3.3.4}$$

Furthermore, the Hankel matrix plays a vital role in the application of subspace identification methods. The example of the Hankel matrix for the measured input is as follows:

$$U_{0|2i-1} \triangleq \begin{array}{c} \\ \text{i} \\ \\ \text{i} \\ \\ \end{array} \overset{\overset{\text{j}}{\longleftrightarrow}}{\begin{pmatrix} u_0 & u_1 & u_2 & \dots & u_{j-1} \\ u_1 & u_2 & u_3 & \dots & u_j \\ \dots & \dots & \dots & \ddots & \dots \\ u_{i-1} & u_i & u_{i+1} & \dots & u_{i+j-2} \\ \hline u_i & u_{i+1} & u_{i+2} & \dots & u_{i+j-1} \\ u_{i+1} & u_{i+2} & u_{i+3} & \dots & u_{i+j} \\ \dots & \dots & \dots & \ddots & \dots \\ u_{2i-1} & u_{2i} & u_{2i+1} & \dots & u_{2i+j-2} \end{pmatrix}} \begin{array}{l} \\ \\ \\ \\ \text{“past”} \\ \\ \\ \\ \text{“future”} \end{array} \triangleq \begin{pmatrix} U_{0|i-1} \\ U_{0|2i-1} \end{pmatrix} \triangleq \begin{pmatrix} U_p \\ U_f \end{pmatrix}$$

$$
\begin{array}{c}
\overset{\text{j}}{\longleftrightarrow} \\
\triangleq \left\{ \begin{array}{c} \text{i+1} \\ \updownarrow \\ \\ \text{i-1} \\ \updownarrow \end{array} \right.
\left(\begin{array}{ccccc}
u_0 & u_1 & u_2 & \dots & u_{j-1} \\
u_1 & u_2 & u_3 & \dots & u_j \\
\dots & \dots & \dots & \ddots & \dots \\
u_{i-1} & u_i & u_{i+1} & \dots & u_{i+j-2} \\
\underline{u_i} & \underline{u_{i+1}} & \underline{u_{i+2}} & \dots & \underline{u_{i+j-1}} \\
u_{i+1} & u_{i+2} & u_{i+3} & \dots & u_{i+j} \\
\dots & \dots & \dots & \ddots & \dots \\
u_{2i-1} & u_{2i} & u_{2i+1} & \dots & u_{2i+j-2}
\end{array} \right)
\left\{ \begin{array}{c} \\ \updownarrow \\ \text{“past”} \\ \\ \\ \updownarrow \\ \text{“future”} \end{array} \right.
\end{array}
\triangleq \begin{pmatrix} U_{0|i} \\ U_{i+1|2i-1} \end{pmatrix} \triangleq \begin{pmatrix} U_p^+ \\ U_f^- \end{pmatrix}
$$

where $U_{0|2i-1}$, $U_{0|i-1}$, $U_{0|i}$ denotes the subscript of the first and last element of the first column in the Hankel matrix. The subscript p stands for “past”, while the subscript f stands for “future”, and the symbols $+$ and - stand for the addition and subtraction of one block row respectively.

Based on the definition of the Hankel matrix for the input design, the output block Hankel matrix $Y_{0|2i-1}$, Y_p, Y_f, Y_p^+, and Y_f^- are defined similarly. Then, the block Hankel matrix consisting of input and output can be described as:

$$W_{0|i-1} \triangleq \begin{pmatrix} U_{0|i-1} \\ Y_{0|i-1} \end{pmatrix} \triangleq \begin{pmatrix} U_p \\ Y_p \end{pmatrix} = W_p$$

Note that the example given here only consider a single input. Thus, for m number of inputs, the total number of rows for $U_{0|2i-1}$ matrix will be $2mi$. Given all data samples, the number of columns (j) is typically equal to $N - 2i + 1$, where N is the total number of data points.

The subspace identification algorithm is based on the assumption that the matrix pair $\{A, C\}$ is observable and the matrix pair $\left\{A, \left[B, Q^{1/2}\right]\right\}$ is controllable. All modes in the system are excited by either external input or process noise [126]. In the application of subspace identification and the establishment of the Hankel matrix, Overschee [126] suggested that the number of block rows i of the Hankel matrix should be larger than the maximum order of the system ($i > n$). However, for the application to flexible aircraft, Bucharles and Vacher [120] suggested the use of a square Hankel matrix to reduce the effect of noise.

3.3.2 Oblique Projection Algortihm

There are several algorithms behind the subspace identification methods. Amongst the classical ones are:

1. The Canonical Variate Analysis (CVA), based on weighted Singular Value Decomposition (SVD) and principal angle analysis [164],
2. Multivariate Output Error State Space (MOESP) which is based on orthogonalisation [165], and
3. Numerical algorithms for Subspace State Space System Identification (N4SID) which is based on oblique projection [166].

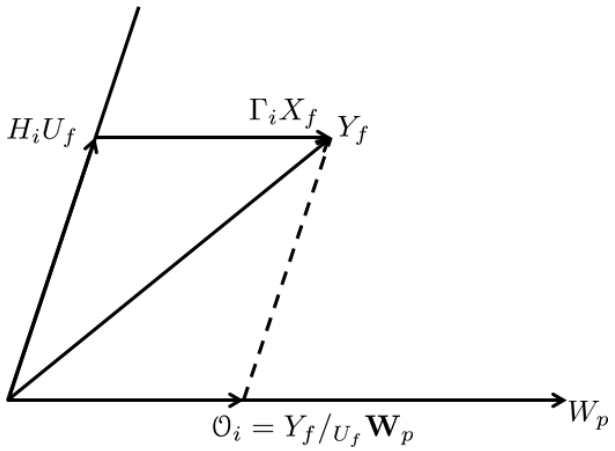

Figure 3.30: Oblique projection illustration for subspace identification method.

A thorough comparison between these algorithms can be found in References [167, 168]. The adopted subspace identification algorithm for this research work is based on the previous work and functions developed by Van Overschee and De Moor [126], which were extended in N4SID.

Consider the discrete system as presented in Equation 3.3.1. By utilising the observability, controllability and the Toeplitz matrix, the matrix input-output equations can be presented as:

$$Y_p = \Gamma_i X_p + H_i U_p \tag{3.3.5}$$

$$Y_f = \Gamma_i X_f + H_i U_f \tag{3.3.6}$$

$$X_f = A^i X_p + \Delta_i U_p \tag{3.3.7}$$

Now, $\mathcal{O}_i$ is defined as the oblique projection where:

$$\mathcal{O}_i = Y_f/_{U_f}\mathbf{W}_p \tag{3.3.8}$$

The problem can be illustrated graphically as shown in Figure 3.30. In the vector space, consider a vector of H_iU_f and Γ_iX_f. From the definition in Equation 3.3.6, the summation of both vectors yields a vector denoted as Y_f. On the other hand, consider that the avaliable data were Y_f, U_f which in line with vector H_iU_f, and vector $\mathbf{W}_p$. By decomposing the vector Y_f along U_f and vector $\mathbf{W}_p$, it resulted in $\mathcal{O}_i$. The graphic proof that $\mathcal{O}_i$ is equal with vector Γ_iX_f is presented in Figure 3.30.

Using the SVD technique, the oblique projection can be defined as follows:

$$W_1\mathcal{O}_iW_2 = \begin{pmatrix} U_1 & U_2 \end{pmatrix} \begin{pmatrix} S_1 & 0 \\ 0 & 0 \end{pmatrix} \begin{pmatrix} V_1^T \\ V_2^T \end{pmatrix} = U_1S_1V_1^T \tag{3.3.9}$$

The order of the system is dependent on the singular values of S, and now the extended observability matrix can be determined as:

$$\Gamma_i = U_1S_1^{1/2} \tag{3.3.10}$$

As presented in Equation 3.3.3, the first l rows of the observability matrix is the C matrix,

and so it can be easily extracted from the previous relation. Furthermore, by manipulating Γ, the matrix A can be calculated by utilising least-squares from the following relationship:

$$\begin{pmatrix} CA \\ CA^2 \\ \dots \\ CA^i \end{pmatrix} = A \begin{pmatrix} C \\ CA \\ \dots \\ CA^{i-1} \end{pmatrix} \tag{3.3.11}$$

For a stochastic system, matrices A and C represent the whole system. However, deterministic systems are not complete before the B and D matrices are identified. The identification is conducted by taking Equation 3.3.6 and multiplying it by $\Gamma_i^{\perp}$ and $U_f^{\dagger}$, which leads to:

$$\begin{aligned} \Gamma_i^{\perp} Y_f U_f^{\dagger} &= \Gamma_i^{\perp} \Gamma_i X_f U_f^{\dagger} + \Gamma_i^{\perp} H_i U_f U_f^{\dagger} \\ \Gamma_i^{\perp} Y_f U_f^{\dagger} &= \Gamma_i^{\perp} H_i \end{aligned} \tag{3.3.12}$$

Defining $L = \Gamma_i^{\perp}$ and $M = \Gamma_i^{\perp} Y_f U_f^{\dagger}$, Equation 3.3.12 can be rewritten as:

$$\mathbf{M} = \mathbf{L} H_i \tag{3.3.13}$$

and given the definition of matrix H_i in Equation 3.3.4, and defining the observability matrix without the last l row, $\underline{\Gamma_i}$. Equation 3.3.12 can be rewritten as:

$$\begin{pmatrix} M_1 \\ M_2 \\ \vdots \\ M_i \end{pmatrix} = \begin{pmatrix} L_1 & L_2 & \dots & L_{i-1} & L_i \\ L_2 & L_3 & \dots & L_i & 0 \\ \dots & \dots & \ddots & \dots & \dots \\ L_i & 0 & \dots & 0 & 0 \end{pmatrix} \begin{pmatrix} I_i & 0 \\ 0 & \underline{\Gamma_i} \end{pmatrix} \begin{pmatrix} D \\ B \end{pmatrix} \tag{3.3.14}$$

Thus, matrix B and D can also be extracted using linear regression.

This algorithm is implemented within the MATLAB function `subid` which is part of the function provided by Reference [126]. This function works for both the deterministic and stochastic system. For a more comprehensive mathematical derivation for the `subid` algorithm, readers are referred to References [126, 166].

It is also worth noting that Kalman filters play a vital role for this algorithm. In `subid` algorithm, the terminology of X_f in the previous equations changes into $\tilde{X}_i$ which is effectively the Kalman filter state sequence. The underlying assumptions for this algorithm are as follows:

1. The deterministic input u is uncorrelated with process and measurement noise.
2. Process and measurement noise are not identically zero.
3. Input u_k is persistently excited of order $2i$; meaning that the input covariance matrix R^{uu} has a rank of $2mi$, given m is the number of input, and i is number of block rows. The input covariance matrix is define as:

$$R^{uu} = \left[U_{0|2i-1} U_{0|2i-1}^{*} \right]$$

3.3.3 Stabilisation Diagrams

The algorithm presented in the previous section shows the importance of the OLS method in solving the subspace identification problems. However, in this case, the model order is typically overestimated to remove bias and to capture all relevant dynamics [118, 119, 169]. In practice, stabilisation diagrams have been used intensively as a standard tool for modal identification [162, 170]. The basic idea behind stabilisation diagrams is to identify a modal based on a set of experimental data with increasing model order number n (n being degrees-of-freedom and described as the pole location of the system matrix in the root-locus diagram). Van de Auweraer [169] stated that "*on an extensive range of problems, pole values of the physical eigenmodes always appear at a nearly identical frequency, while mathematical poles tend to scatter around the frequency range*".

The stabilisation diagram consists of frequency (pole position) on the X-axis and the system order on the Y-axis. By visualising the pole location on each model order, one can fix the model order number n and at the same time distinguish between the physical poles and mathematical poles. Due to the existence of the mathematical poles, stabilisation diagrams are more comprehensive than defining the optimal order only from singular values (in a deterministic case, or principal angle analysis in a stochastic case) like in other algorithms.

Typical stability criteria for visualising the stabilisation diagram for n^{th} order number are defined as follows [169, 170] :

1. the difference in the frequency is less than 1%:

$$\Delta\omega = \frac{\mid \omega_i - \omega_{i-1} \mid}{\omega_{i-1}} < 0.01 \tag{3.3.15}$$

2. the difference in the eigenvector is less than 2%:

$$\Delta\text{MAC} = 1 - \frac{\mid \Phi_i^T \Phi_{i-1} \mid^2}{\left(\Phi_i^T \Phi_i\right)\left(\Phi_{i-1}^T \Phi_{i-1}\right)} < 0.02 \tag{3.3.16}$$

3. the difference in damping is 5%:

$$\Delta\zeta = \frac{\mid \zeta_i - \zeta_{i-1} \mid}{\zeta_{i-1}} < 0.05 \tag{3.3.17}$$

where the frequency, damping and mode shapes of the structure are calculated from:

$$A = \Psi\Lambda\Psi, \quad \Lambda = \text{diag}(\lambda_i) \in C^{l\times n}, \quad i = 1, \ldots, n \tag{3.3.18}$$

$$\omega_i = \frac{\mid \ln(\lambda_\mathbf{i}) \mid}{\Delta t}, \quad i = 1, \ldots, n \tag{3.3.19}$$

$$\zeta_i = \frac{\text{real}\,(\lambda_i)}{\mid \ln(\lambda_\mathbf{i}) \mid}, \quad i = 1, \ldots, n \tag{3.3.20}$$

$$\mathbf{\Phi} = C\Psi \tag{3.3.21}$$

and MAC is known as Modal Assurance Criteria, which compares the similarity between

two eigenvector (Φ_i and Φ_j) as follow:

$$\text{MAC} = \frac{|\ \Phi_i^T \Phi_j\ |^2}{\left(\Phi_i^T \Phi_i\right)\left(\Phi_j^T \Phi_j\right)} \tag{3.3.22}$$

Where a value of MAC close to 1 indicates a correct pairing of the modes. Furthermore, according to Ewins [170] a MAC value between 0.9 - 1 is obtained for well-correlated modes and a value of 0.1 is an indication of uncorrelated modes.

Example 3.3.1 ***Structural Properties Identification from a Ground Vibration Test***

In this example, the subspace algorithm is used to identify the structural properties of an aluminium plate from GVT. This work aims to highlight the advantages and disadvantages of using the subspace approach with in an experimental setup.

The structure under test is a 90 cm long, 20 cm wide and 3 mm thick aluminium plate, clamped on one end and free on the other end. A stinger connecting the plate and a shaker is used to give external excitation. Figure 3.31 presents the test setup of the plate.

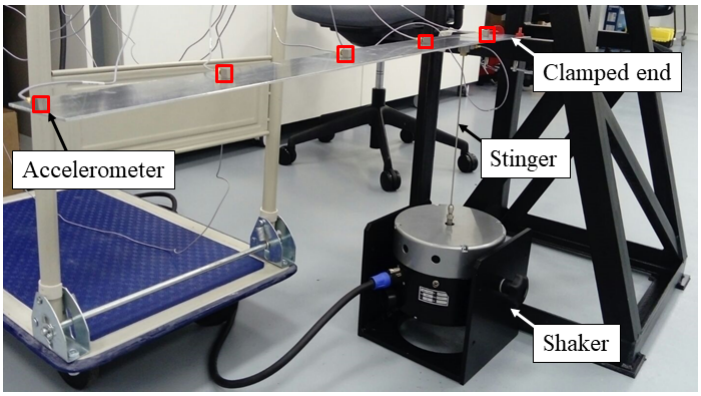

Figure 3.31: GVT setup for aluminium plate.

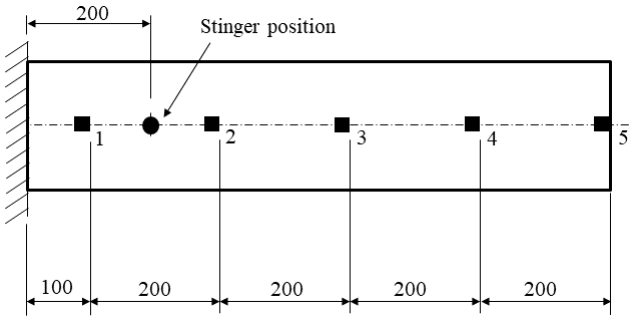

Figure 3.32: Position of the stinger and accelerometer.

A stochastic input with frequency ranging from 1 Hz to 100 Hz was chosen as the excitation input to the aluminium plate. The test was conducted numerous times, with combinations of sensor locations and external excitations. However, this example

only presents the experimental results in which the accelerometers were placed evenly along the length of the plate (as shown in Figure 3.32). The frequency response of the accelerometer signals given the stochastic input is presented in Figure 3.33.

By utilising the subspace algorithm on the experimental data, the model order and the identified pole locations can be displayed through a stabilisation diagram. There is no exact method for selecting the number of rows in the Hankel matrix. However, the number of the row should be less than $\frac{N+1}{4m}$*, where* N *is the number of data points and* m *is the number of inputs. Furthermore, Bucharles [120] suggested the use of a square Hankel matrix to minimise the effects of noise. To assess this, two stabilisation diagrams with two different number of row Hankel matrix (*$i = 10$ *and* $i = 30$*) are compared and presented in Figures 3.34 and 3.35. The figures show an overlay of pole location with the frequency response of the tip accelerometer. The stable poles that align with the peaks of the frequency response represent the physical poles.*

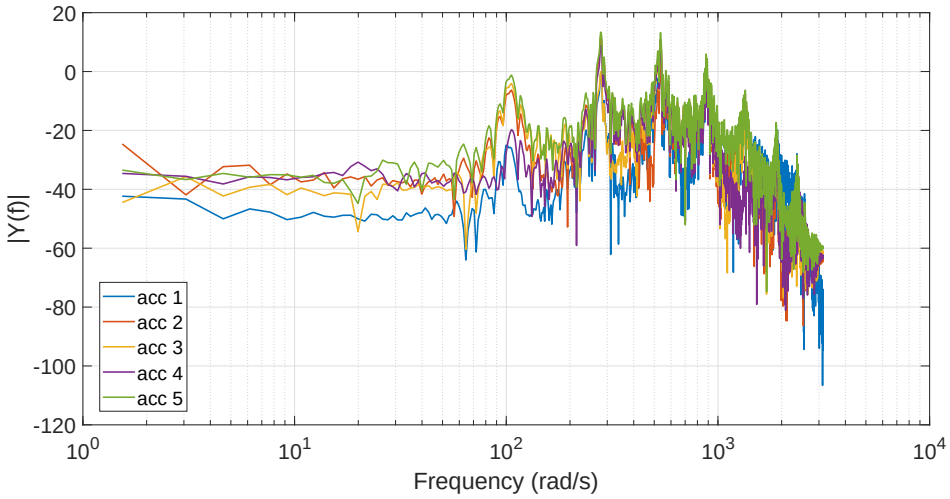

Figure 3.33: Frequency response of the accelerometer based on the experimental results.

In Figure 3.34 the blue circles represents stable poles, the $\times$ *represent unstable poles, and the dot represents the non-pair poles. For the sake of simplicity, Figure 3.35 only presents the stable poles. The maximum identified number of order is proportional to the number of row in the Hankel matrix (i) and the number of input (m), and so for ten rows of Hankel matrix the maximum order number is 50. In comparison, Figure 3.35 shows more stable poles especially at lower frequencies. On the contrary, as the number of rows in the Hankel matrix increases, the number of mathematical poles tend to grow as well. With an increasing number of poles, a routine that carefully picks the exact pole location that represents the physical poles is crucial. The physical pole location is essential for future analysis, not only to identify the modal frequencies and system damping but also for the identification of eigenvectors.*

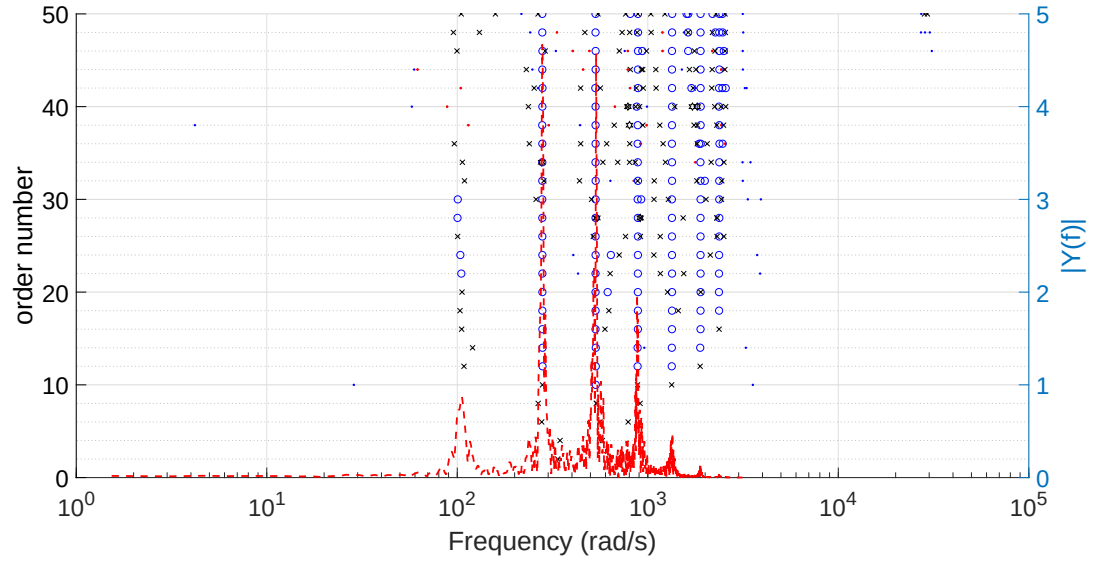

Figure 3.34: Stabilisation diagram for aluminium plate for i = 10.

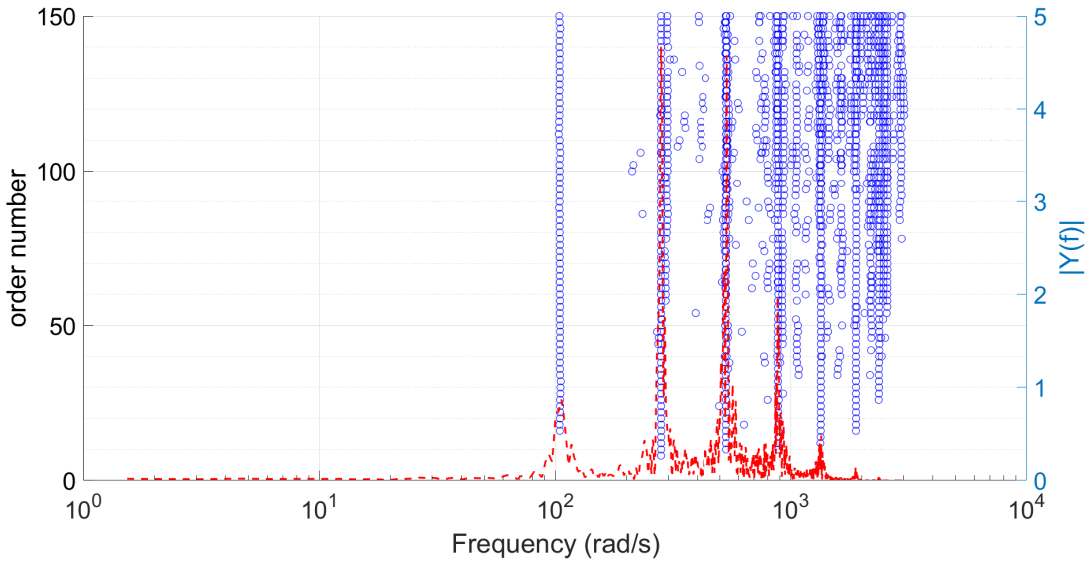

Figure 3.35: Stabilisation diagram for aluminium plate for i = 30.

Figure 3.36 presents the comparison of the theoretical and identified mode shapes based on the stabilisation diagram given in Figure 3.35, and the number order of 26. The figure shows that the identification results cannot detect the first mode shape, due to the location of the stinger which is not so close to the clamp and so not sufficiently excited for the first mode to be detected. Furthermore, the legend represents the identified frequencies. The numbers show less than 3 % difference between the theoretical and measured frequencies.

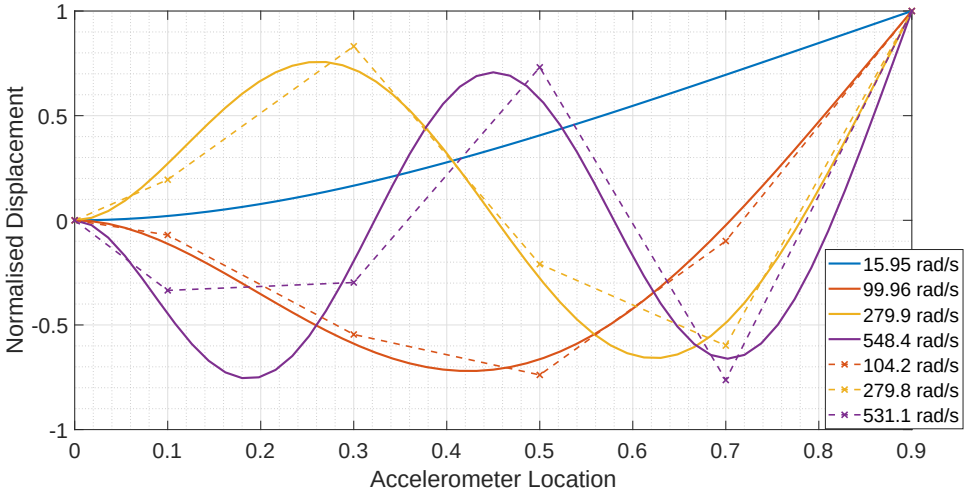

Figure 3.36: Comparison of theoretical and identified mode shapes (— : theoretical mode shapes, −−: identified mode shapes).

3.4 Summary

This chapter has explored system identification methodologies applied to rigid aircraft flight dynamics through regression and output error methods. It has also considered structural problems through the subspace identification method using data from a simple experiment. It was further confirmed that for full-scale aircraft small inputs lead to small perturbations in flight dynamics variables, making linear methods such as OLS appropriate for identifying aeroderivatives. On the other hand, for subscale aircraft with inappropriate inertia and mass scaling, small inputs were found to excite non-linear phenomena such as dynamic stall. Due to such non-linear dynamics, the OLS method is no longer suitable and instead the output-error method is more suited to identify a relevant non-linear model. This chapter also emphasised the importance of sensor placement and ensuring synchronised collection and filtering of sensor data. The following chapter applies the aforementioned identification method for aeroelastic system.

CHAPTER 4

Identification of Aeroelastic Systems

The work discussed in this chapter presents some use-cases where system identification methods are applied to characterise flexible aircraft. These demonstrates that there are several ways to identify an aeroelastic system. The focus has been put on two different identification methods applied to simulation results, to highlight respective limitations and possible applications. The chapter starts with the definition of the simulation framework and the aircraft of interest, and then continues with identification using a quasi-steady modelling approach, before demonstration with a generalised approach.

4.1 CA^{2}LM Framework

The modelling and simulation framework used for identification purposes is known as the Cranfield Accelerated Aircraft Loads Model (CA^{2}LM) [142, 143]. Developed in MATLAB/Simulink, the framework provides an environment for a loosely coupled aerodynamic and structural dynamics simulation of a generic large transport aircraft. This framework was originally developed to assess the handling qualities of a flexible aircraft with active loads control [143] and has been utilised to evaluate pilot-in-the-loop simulations [171, 172]. Later, this simulation framework was updated to accommodate a high aspect ratio wing aircraft and used to assess the handling qualities of flexible aircraft [142]. The framework is also equipped with a spoiler model used to study gust load alleviation [173]. A folding wingtip model has also been added to the framework and a detailed description of the mechanism is available in References [27, 174, 175]. In this section, the CA^{2}LM framework is used to simulate the Cranfield University AX-1 aircraft. The aircraft configuration is given in Figure 4.1; The red dots on the figure represent the beam element structural model of the aircraft.

In brief, Figure 4.2 presents the workflow of the CA^{2}LM framework. Control inputs available in the framework consist of elevator, rudder and aileron. The output of the framework is the aircraft rigid body dynamics calculated at the centre of gravity as well as the displacements, velocities and accelerations for each structural node. The core of the simulation is the aeroelastic forces and moments calculation that is connected with the

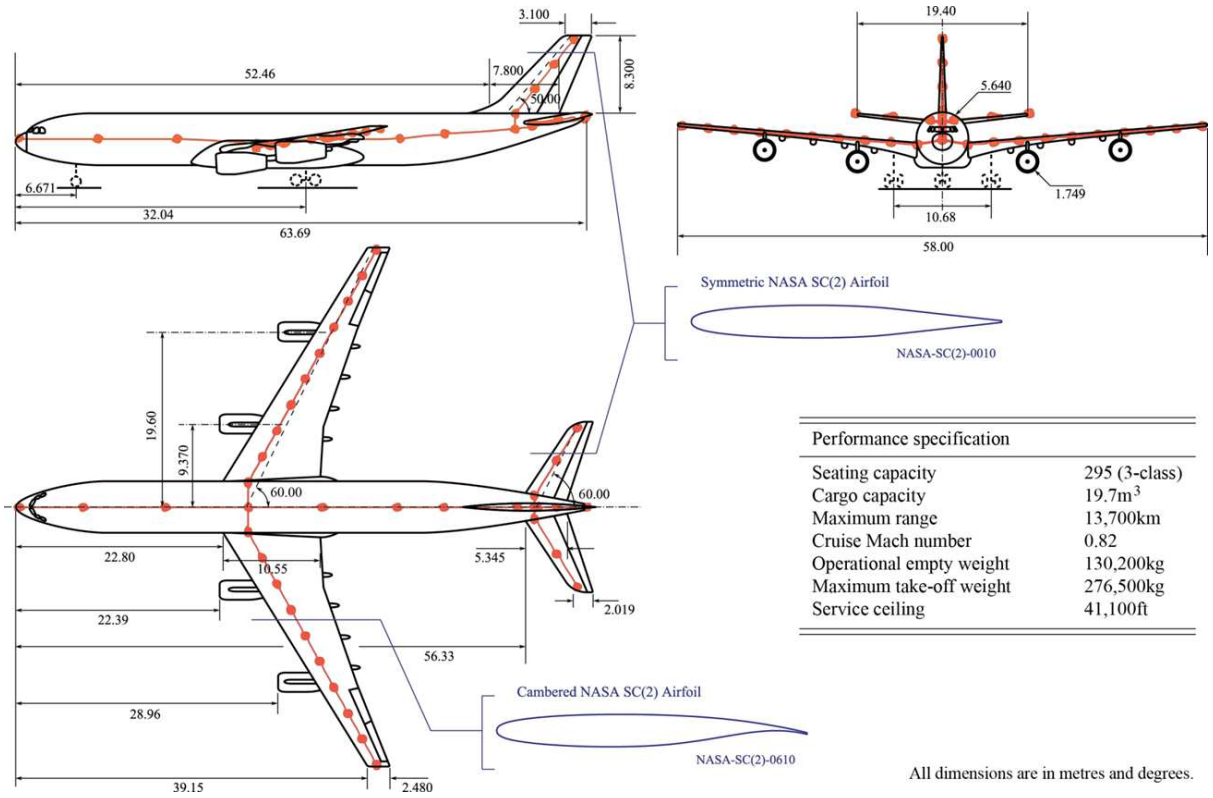

Figure 4.1: AX-1 aircraft configuration (Reproduced from Reference [27]).

6 DoF equations of motion. These are calculated through the loosely coupled structural dynamics and aerodynamic modules.

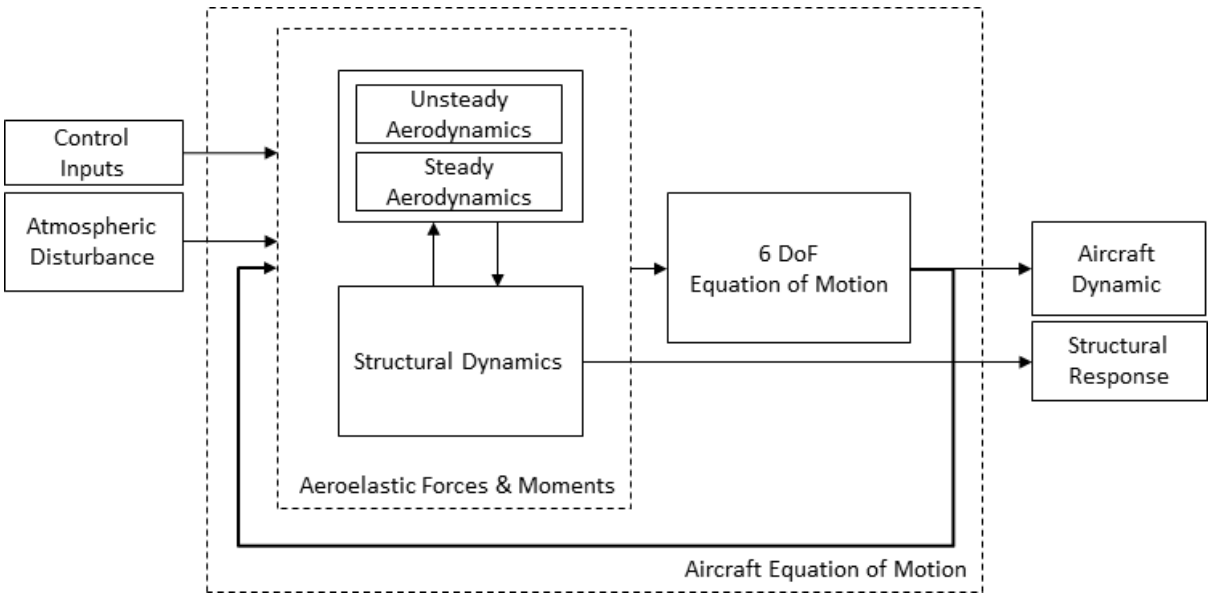

Figure 4.2: CA^{2}LM framework architecture.

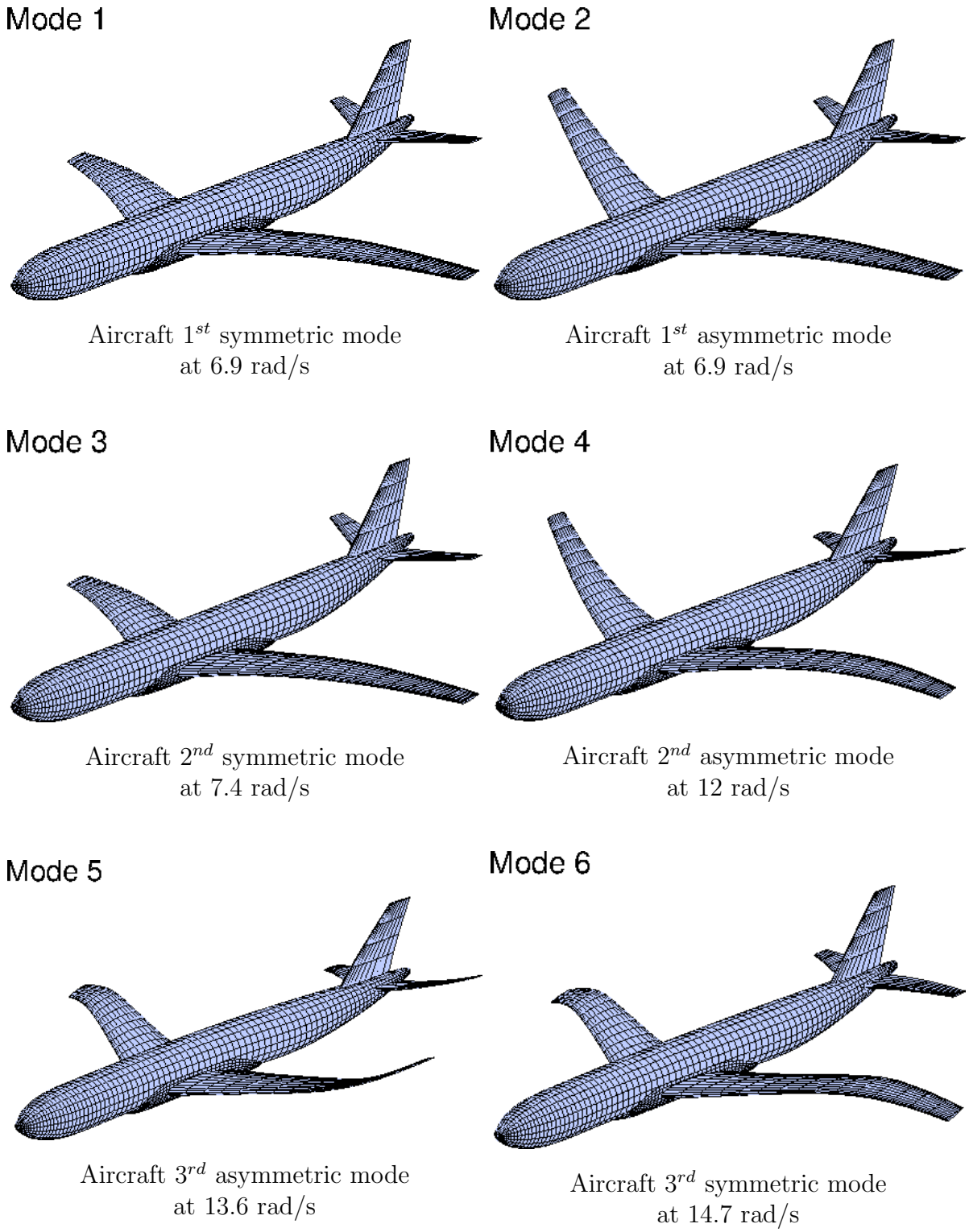

Aircraft 1^{st} symmetric mode at 6.9 rad/s

Aircraft 1^{st} asymmetric mode at 6.9 rad/s

Aircraft 2^{nd} symmetric mode at 7.4 rad/s

Aircraft 2^{nd} asymmetric mode at 12 rad/s

Aircraft 3^{rd} asymmetric mode at 13.6 rad/s

Aircraft 3^{rd} symmetric mode at 14.7 rad/s

Figure 4.3: Illustration of the structural mode shapes of the AX-1 aircraft.

4.1.1 Structural Dynamics Model

In general, the structural model can be written in the well-known form using the general displacement $\mathbf{d}$ as the state basis, and can be expressed in terms of a mass matrix $[M]$, a damping matrix $[C]$ and a stiffness matrix $[K]$:

$$[M]\ddot{\mathbf{d}} + [C]\dot{\mathbf{d}} + [K]\mathbf{d} = F \tag{4.1.1}$$

where F is the external applied forces that can be in the form of aerodynamic loads, gravitational force, and thrust. Solving the structural equation directly in a simulation framework is computationally expensive. Therefore, in the CA^{2}LM framework the modal approach is adopted by introducing mode shape Φ defined as:

$$\mathbf{d} = \Phi\eta \tag{4.1.2}$$

where η are the generalised coordinates. Using this relation, Equation 4.1.1 can be transformed into:

$$\ddot{\eta} = \frac{1}{\langle m \rangle}\left(\Phi^T F - \langle 2m\zeta\omega \rangle \dot{\eta} + \left\langle m\omega^2 \right\rangle \eta\right) \tag{4.1.3}$$

where $\langle m \rangle$ is the generalised mass, ω is the natural frequency, and ζ is the damping ratio. In CA^{2}LM , the damping ratio is assumed to be 3% for all modes; a typical assumption made in industry [143, 176]

The generalised velocity can be obtained by integrating the generalised acceleration $\ddot{\eta}$ with respect to time, and integrating the generalised velocity provides the generalised displacement. Furthermore, using the relation in Equation 6.2.6, and assuming that the mode shapes do not change with respect to time, the generalised displacement, velocity, and acceleration can be transformed into nodal displacement, velocity and acceleration as follows:

$$\mathbf{d} = \Phi\eta \tag{4.1.4}$$

$$\dot{\mathbf{d}} = \Phi\dot{\eta} \tag{4.1.5}$$

$$\ddot{\mathbf{d}} = \Phi\ddot{\eta} \tag{4.1.6}$$

This gives linear and angular displacements as well as linear and angular velocities of each structural node as an output of the structural dynamics block.

For AX-1 aircraft the structural dynamics are simplified by only considering 12 modes. Andrews [143] argued that this provided a realistic compromise between computational cost and model fidelity [143]. The first six structural modes of the aircraft and their respective frequencies are presented in Figure 4.3.

4.1.2 Aerodynamics Model

The aerodynamic forces and moments are calculated based on the position of each aerodynamic strip from the output of the structural block. The aerodynamic forces and moments are represented by the lift, drag and pitching moment coefficients, which are functions of Mach and Reynolds numbers. Here, the aerodynamic coefficients consist of

steady and unsteady components. A typical approach for modelling unsteady aerodynamics (typically used for flutter calculations) is via the Theodorsen function [177], which was developed considering a two-dimensional flat plate in inviscid and incompressible flow undergoing pitching and plunging. Theodorsen separated the non-circulatory part of the velocity potential from the circulatory part [17, 177, 178], as follows:

$$C_L = \underbrace{\frac{\pi}{2}\left[\ddot{h} + \dot{\alpha} - \frac{a}{2}\ddot{\alpha}\right]}_{\text{Non-Circulatory}} + \underbrace{2\pi C(k)\left[\alpha + \dot{h} + \frac{1}{2}\dot{\alpha}\left(\frac{1}{2} - a\right)\right]}_{\text{Circulatory}} \tag{4.1.7}$$

where a is the pitch axis location of the aerofoil with respect to half chord (pitch about the leading edge corresponds to a = -1 and $a = 1$ for trailing edge [179]), and $C(k)$ is the Theodorsen function which is dependent on the reduced frequency k.

The circulatory and non-circulatory contributions are part of the unsteady aerodynamics, and can explained as follows [17, 177, 180]:

- **Non-circulatory** also known as an apparent mass, is the term that represents the instantaneous change in the boundary conditions due to the acceleration of the aerofoil. The acceleration creates the pressure difference, causing the aerofoil to carry the surrounding air [143]. This term is essential for the calculation of control surface flutter at higher reduced frequencies [48]. The non-circulatory term decays rapidly with time [181], and is dependent on the instantaneous rate of change [182]. It can be approximated mathematically through a time constant [183]. However, for incompressible flow cases this term dies away instantaneously and therefore, does not need to be considered [143].
- **Circulatory** describes the lift and moment term due to flow vorticity [48] which is essential for calculating the lifting force. This term expresses the loading that builds up quickly and asymptotes to the steady-state values [183]. The change of lift for the circulatory function is proportional to the total lift obtained from the penetration of a sharp edge gust [180].

However, instead of using the Theodorsen model directly, an indicial model is utilised in CA^{2}LM [184, 185][1]. The indicial function consists of the circulatory and non-circulatory term and is given in a state space formulation[2], and normalised to Mach number [186]. The total aerodynamic forces and moments are calculated using modified strip theory [143, 187].

4.2 Quasi-Steady Approach

A way of understanding an aircraft's flight dynamics characteristics is through the force and moment coefficients, also known as aerodynamic derivatives. Etkin stated that there are two kinds of aerodynamic derivatives: ones which represent the rigid-body motion, and others that appear in the added equations of elastic degrees of freedom [188]. In

[1] Alternative solution rather than the indicial model can be utilisation of aerodynamic lag [19], or extending the Theodorsen's lift calculation for unsteady aerodynamics by formulating aeroelastic angle-of-attack for the combined chordwise, flapwise bending and torsion [133].

[2] Reader is referred to Reference [143] for the state space representation of the indicial model

the first case, the aircraft is considered as a point mass, and only in the second case the structural deformations are introduced. As mentioned in Section 2.2.4, there are six different ways to observe aeroelasticity [110, 131]. In this section only two of these will be further elaborated upon: 1) the quasi-steady approach through the rigid body equations and 2) modal truncation through the added elastic degrees of freedom. The choices between the approach based on the separation between the frequency of the rigid body mode and the structural mode. However, for particular applications, such as in the use of a flight simulator where the aeroelastic effects are typically not included, the quasi-steady approach can be a viable means of capturing airframe flexibility effect. It is also the cheapest formulation in terms of computational cost [131].

The assumption within the quasi-steady approach is that the structure reaches its equilibrium deformation instantaneously, neglected the unsteady aerodynamic effects [90]. In this case, the effect of structural flexibility is embedded within the rigid body coefficients. In 1970, Roskam developed a formulation for defining the longitudinal stability derivatives of elastic aircraft based on rigid body coefficients for application in the early design phase [189]. Here, the added term for elastic stability derivatives consists of zero mass and inertia effects. Both terms are functions of structural influence coefficient and dynamic pressure. A similar approach was also used by Jategaonkar who modelled aeroelasticity through the 'flex factor' which was a function of dynamic pressure and Mach number [54, 90].

In this section, the CA^{2}LM framework is used to identify the effect of structural deformation and quantify the structural influence coefficient of the generic flexible aircraft, known as AX-1. The aerodynamic coefficients of interest are those where the wing flexibility effects are significant. Related to the lateral and longitudinal dynamics of the aircraft, the coefficients of interest are: rolling moment due to roll rate (roll damping) C_{l_p}, aileron effectiveness $C_{l_{\delta_a}}$, and the lift slope C_{L_α}, as well as the pitch stiffness C_{M_α} and pitching moment due to the pitch rate (pitch damping) C_{M_q} is also of interest. The aerodynamic coefficient for the rigid configuration is then compared to a comparable large aircraft (Boeing 747) which is taken from Reference [190].

4.2.1 Simulation Set-Up

A set of simulations covering 44 flight conditions was conducted to capture the effect of flexibility on various stability and control derivatives (see Figure 4.4). These flight points capture quite a range of dynamic pressure and Mach number (see Table 4.1). In this study, the simulations were only conducted for one mass case, which was 80% Maximum Take-Off Weight (MTOW) with the centre of gravity at around 25% of the mean aerodynamic chord.

For lateral identification, an aileron pulse input is used to excite the dynamics of the aircraft. The aileron is then modified to give a symmetric doublet input which is used to excite the longitudinal dynamics of the aircraft. The reason behind the symmetric aileron input is that the aileron is expected to excite the wing symmetric modes more effectively than the elevator [101]. Furthermore, as both dynamics respond in a different frequency, a low frequency characterised by the time constant for lateral dynamics, and a slightly higher frequency for the short period mode, the input was designed differently so that it can captures the dynamics of interest.

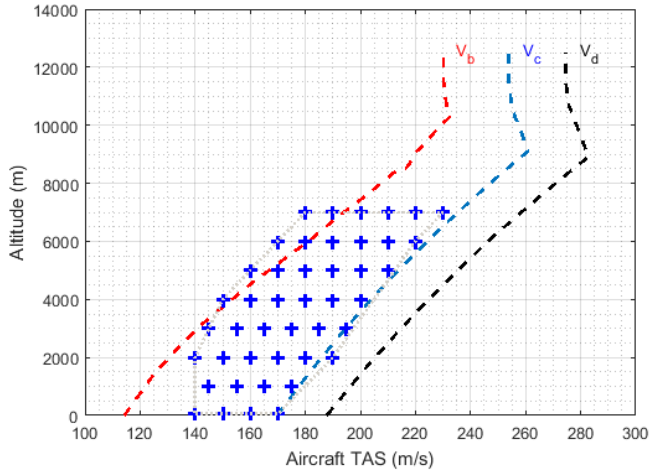

Figure 4.4: Flight condition of interest.

	Minimum	Maximum
Altitude (m)	50	7000
TAS (m/s)	140	230
Mach	0.41	0.74
$\bar{q}$ (Pa)	9.3×10^3	1.8×10^4
α_b $(^\circ)$	-1	3
Re	2×10^6	4×10^6

Table 4.1: Flight condition variables.

4.2.2 Identification Results

Before the application of quasi-steady identification, let us go back and look at the equations of motion that represent a flexible aircraft as developed by Waszak and Schmidt [132]. As an example, consider the small perturbation lateral dynamics of the flexible aircraft that can be presented as follows:

$$I_{xx}\dot{p} - I_{xz}\dot{r} = \bar{L}_0 + \underbrace{\bar{L}_p\frac{pb}{2U} + \bar{L}_r\frac{rb}{2U} + \bar{L}_\beta\beta + \bar{L}_{\delta_a}\delta_a}_{\text{rigid}} + \underbrace{\sum_{i=1}^{\infty}\bar{L}_{\eta_i}\eta_i + \sum_{i=1}^{\infty}\bar{L}_{\dot{\eta}_i}\frac{\dot{\eta}_i b}{2U}}_{\text{flexible}} \tag{4.2.1}$$

Here, the left hand side of the equation represents the rotational motion around the x-axis, which is identical to the conventional rigid-body equations of motion. Meanwhile, the right hand side represents the aerodynamic forcing functions that consist of the rigid-body and elastic degrees of freedom. The elastic degree of freedom is represented by the generalised structural stiffness and damping. The assumption here is that the variation of inertia due to the flexibility is negligible. By assuming a quasi-steady approach, the premise is that the change in the shape due to the flexibility is captured within the rigid body terms (in this case is $\bar{L}_p$ and $\bar{L}_{\delta_a}$). Therefore, Equation 4.2.1 is simplified as follow:

$$I_{xx}\dot{p} - I_{xz}\dot{r} = \bar{L}_0 + \bar{L}^*_p\frac{pb}{2U} + \bar{L}^*_r\frac{rb}{2U} + \bar{L}^*_\beta\beta + \bar{L}^*_{\delta_a}\delta_a \tag{4.2.2}$$

in which $\bar{L}^*_i$ represents the rigid body coefficient with flexibility effect. A similar approach is also used for the longitudinal dynamics. A comprehensive explanation on how rigid body dynamics can capture the flexibility effect is elaborated in the following sections.

Lateral Coefficients

As mentioned earlier, the lateral dynamic is excited through the aileron pulse input. In total 88 simulations were conducted for simulating both rigid and flexible structure. In this case, a longer aileron input was intentionally used to capture roll dynamics. Figure

4.5 presents the time history for both rigid and flexible structure at velocity of 180 m/s and altitude of 15,000 ft. The figure shows that both rigid and flexible aircraft is excited using a similar aileron pulse input of 5-degree amplitude. However, when the aircraft has a flexible structure, the response of the aircraft in terms of the amplitude of the roll rate and roll angle is reduced. Moreover, an inverse response of the tip deflection of the wing is seen indicating that the input is exciting the asymmetric aeroelastic mode.

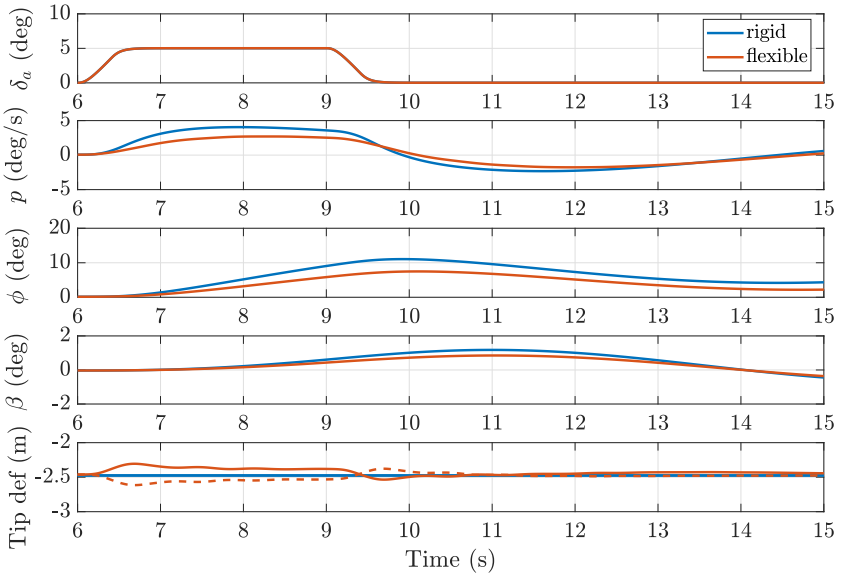

Figure 4.5: Time history of lateral motion from aileron input.

Giving the quasi-steady assumption as mentioned before, the identification of lateral coefficient is based on Equation 4.2.2. Due to the simplicity of the model equation, OLS method is chosen to identify the aerodynamics derivatives of interest. Here, the measurement equation is defined as:

$$z = \dot{p} - \frac{I_{xz}}{I_{xx}}\dot{r} \tag{4.2.3}$$

while the regressor matrix and parameter vector are given as:

$$X = \begin{bmatrix} \frac{b}{2U}p(1) & \frac{b}{2U}r(1) & \Delta\beta(1) & \Delta\delta_a(1) \\ \vdots & \vdots & \vdots & \vdots \\ \frac{b}{2U}p(N) & \frac{b}{2U}r(N) & \Delta\beta(N) & \Delta\delta_a(N) \end{bmatrix} \tag{4.2.4}$$

$$\hat{\Theta} = \begin{bmatrix} \bar{L}_p & \bar{L}_r & \bar{L}_\beta & \bar{L}_{\delta_a} \end{bmatrix}^T \tag{4.2.5}$$

Figure 4.6 presents the comparison between the simulation results and the model output of the roll dynamics for both rigid and flexible structure aircraft. The comparison between the simulation and identification results for the rigid structure shows a relatively good match, with a residual in an order of magnitude lower which is caused by the numerical error. On the contrary, for the aircraft with a more flexible structure, the residual is in the same order of magnitude as the identification results cannot capture the oscillation

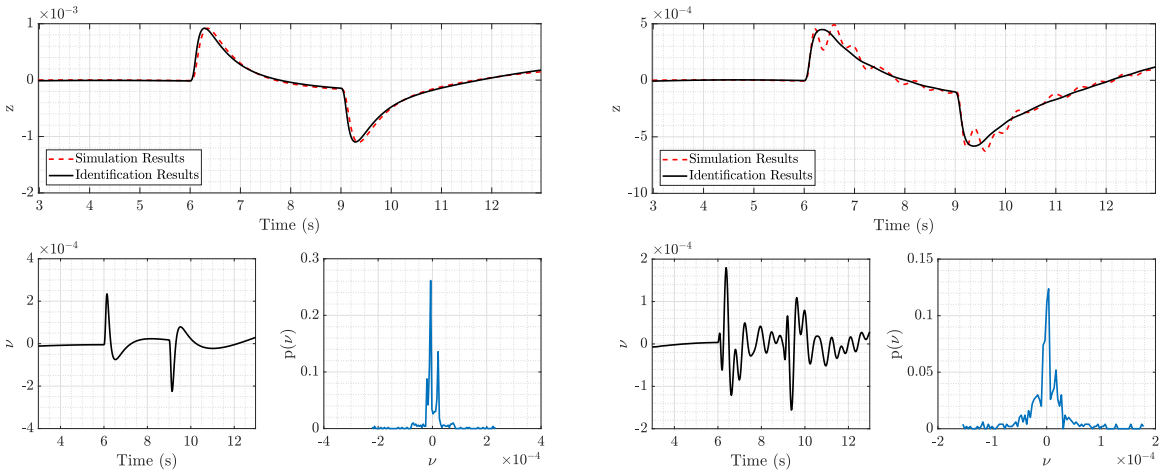

Rigid structure Flexible structure

Figure 4.6: Roll identification for rigid and flexible structure.

of the measured variables for the flexible structure configuration.

As mentioned previously, the assumption used here is that the most significant aeroelastic effects on roll dynamics are to be captured within the change in the roll damping value C_{l_p} and the change in the aileron effectiveness value $C_{l_{\delta_a}}$, which is a function of local aerodynamics and given as follows [145]:

$$\bar{L}_p = -\rho U \int_0^{b/2} \left[\frac{\partial C_l(\mathrm{y})}{\partial \alpha} + C_d(\mathrm{y}) \right] c(\mathrm{y}) \mathrm{y}^2 d\mathrm{y} \tag{4.2.6}$$

$$\bar{L}_{\delta_a} = -\rho U^2 \frac{\partial C_{l_{\delta_a}}(\mathrm{y})}{\partial \alpha} \int_{\mathrm{y}_1}^{\mathrm{y}_2} c(\mathrm{y}) \mathrm{y} d\mathrm{y} \tag{4.2.7}$$

where y is the lateral coordinate, y_1 and y_2 define the spanwise positions of the aileron and $\bar{c}(\mathrm{y})$ is the local chord at y [3]. Furthermore, the identified parameters are converted to non-dimensional terms using the following relation:

$$C_{l_i} = \frac{I_{xx}}{\bar{q} S b} \bar{L}_i; \qquad i = p, r, \beta, \delta_a \tag{4.2.8}$$

Figure 4.7 presents the comparison of the identified C_{l_p} value for the rigid and flexible structure as a function of dynamic pressure and the angle of attack. Here it is worth mentioning that the variance of the identified variables are less than 2%, highlighting the exceptional quality of the estimation process. The explanation for the C_{l_p} coefficient as elaborated in References [145] is as follows: when the aircraft experiences perturbations in the rolling moment with a positive angular acceleration of p, the wing perceives an induce component of velocity normal to the spanwise coordinate. Meaning that the down-going wing (in positive roll rate is the starboard wing), has a small increase of incidence, and vice versa the starboard has a small decrease of incidence. These decreases in the lift create

[3] Note that the assumption in the $\bar{L}_{\delta_a}$ equation is that the aileron effect is only effective on the specific spanwise position of the aileron. Meaning that there is no aerodynamic effect due to aileron on the nearby spanwise position. In reality, there is an interference effect which is ignored by the equation.

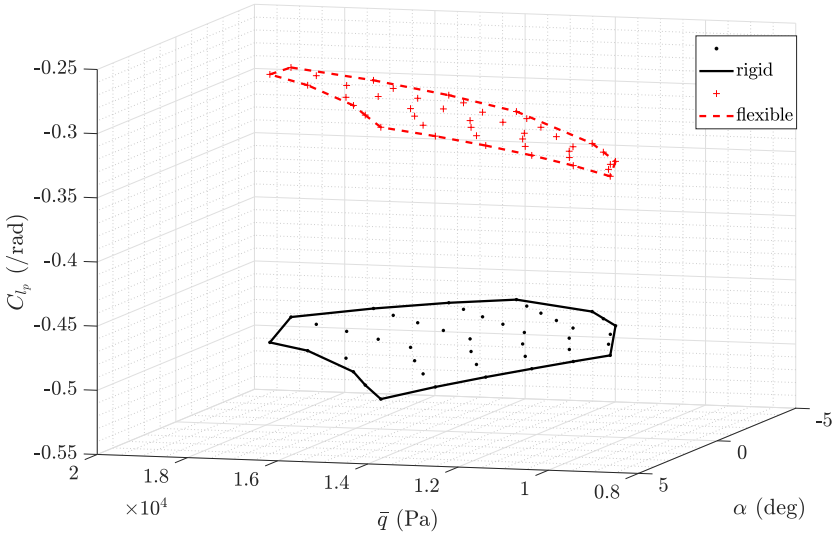

Figure 4.7: Identification of C_{l_p} results for rigid and flexible aircraft.

a rolling moment in the opposite direction (restoring moment). The aircraft undergoes the disturbing and restoring rolling moment until a steady roll rate is establishes. This restoring rolling moment is referred to as "*damping in roll*".

The identification results for the rigid structure are comparable to those of a similar aircraft configuration obtained from experiments as presented in Reference [190]. However, the absolute value of the coefficient is smaller when flexibility is introduced, meaning that the restoring rolling moment from the flexible wing structure is less than the restoring moment created by the rigid body structure. The fact that the restoring moment is decreasing means that the increase/decrease of the wing incidence due to the manoeuvre is lower as the flexibility of the wing adapts to the perturbation. Looking back into Equation 4.2.6, the source of the decreasing value might also come from the C_d(y) terms which varies due to wing flexibility.

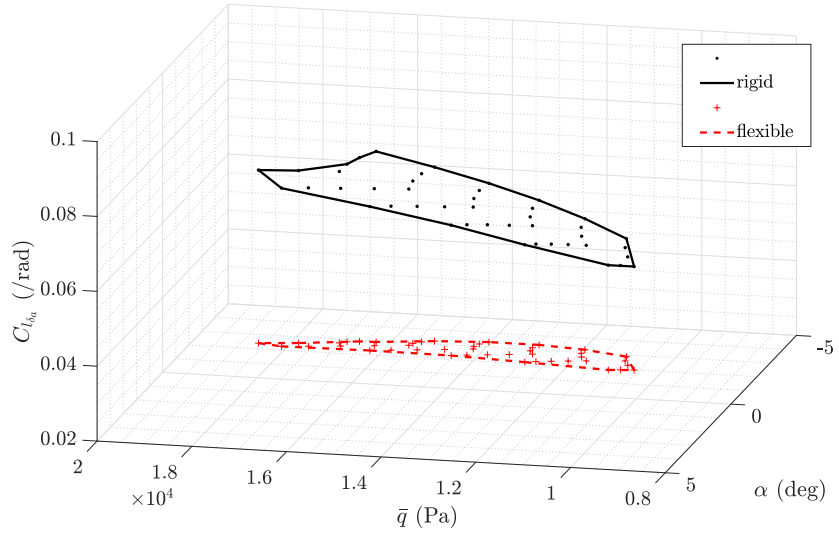

Figure 4.8: Identification of $C_{l_{\delta_a}}$ results for rigid and flexible aircraft.

The comparison of the $C_{l_{\delta_a}}$ value for both rigid and flexible structure is presented in Figure 4.8, again as the function of dynamic pressure $\bar{q}$ and angle of attack α. This coefficient presents a straightforward relation between the deflection of the aileron and the rolling moment it creates. Again, the $C_{l_{\delta_a}}$ value for rigid structure shows comparable results in relation to data for similar aircraft configurations in Reference [190]. Here, structural flexibility provides smaller aileron effectiveness, meaning that the change of lift distribution is lower when the wing is flexible. This fact leads to a similar conclusion with the change in the roll damping, which is that wing flexibility allows the structure to respond to the perturbation and creates lower change in the lift distribution.

Longitudinal Coefficients

The symmetric aeroelastic modes are of importance for the longitudinal case. Hence, the simulation framework was modified to allow symmetric aileron deflection. In this case, a doublet symmetric aileron input with the frequency around 1 Hz was used to excite the longitudinal dynamics of the aircraft. Due to the limitation of the actuator dynamics, it was not possible to excite the aileron at a higher frequency. Figure 4.9 presents the time history of the longitudinal dynamics at a velocity of 180 m/s and altitude of 15,000 ft.

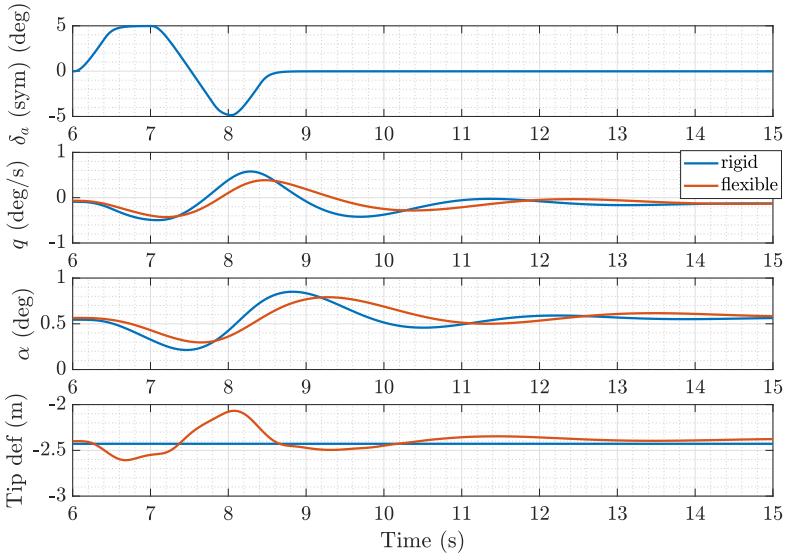

Figure 4.9: Time history of longitudinal motion from symmetric aileron input.

The time histories of the longitudinal dynamics show that by introducing flexibility the overall response, in terms of the aircraft angle of attack and pitch-rate (α and q), have a lower amplitude relative to the rigid body aircraft. A phase change is also observed in Figure 4.9, between the response from the flexible and rigid structure. It is also of interest to see the tip deflection of the aircraft's wing, in which the left and right wing tips are deflected in the same sense, indicating the input excites the symmetric structural wing mode.

An assumption of capturing the aeroelastic effect within the rigid body dynamics is applied in this section as well. As the input design is excited the SPPO mode, a similar approach as previously presented in Section 3.1.2 is used. Therefore, the model equation

for the application of the OLS method is defined as follows:

$$\dot{q} = M_\alpha \alpha + M_q \frac{q\bar{c}}{2U} + M_{\delta_{as}} \delta_{as} \tag{4.2.9}$$

$$\dot{w} - qU = L_\alpha \alpha + L_{\delta_{as}} \delta_{as} \tag{4.2.10}$$

where δ_{as} is symmetric aileron input.

Similar with the lateral coefficient identification, for the application of OLS method, the measurement equations are define as:

$$\begin{aligned} z_1 &= \dot{q} \\ z_2 &= \dot{w} - qU \end{aligned} \tag{4.2.11}$$

while the regressor matrix and parameter vector are given as:

$$X_1 = \begin{bmatrix} \alpha(1) & \frac{\bar{c}}{2U} q(1) & \Delta\delta_{as}(1) \\ \vdots & \vdots & \vdots \\ \alpha(N) & \frac{\bar{c}}{2U} q(N) & \Delta\delta_{as}(N) \end{bmatrix} \quad ; \quad \hat{\Theta}_1 = \begin{bmatrix} M_\alpha & M_q & M_{\delta_{as}} \end{bmatrix}^T$$

$$X_2 = \begin{bmatrix} \alpha(1) & \Delta\delta_{as}(1) \\ \vdots & \vdots \\ \alpha(N) & \Delta\delta_{as}(N) \end{bmatrix} \quad ; \quad \hat{\Theta}_2 = \begin{bmatrix} L_\alpha & L_{\delta_{as}} \end{bmatrix}^T$$

Here, there are only three coefficients of interest for the longitudinal dynamics (typical for the SPPO mode) namely the aircraft lift slope L_α, pitch stiffness M_α and pitch damping M_q.

In this case, the most significant contribution of the L_α coefficient comes from the wing planform and can be estimated as follows:

$$L_\alpha = \frac{1}{2}\rho U^2 \int_{-b/2}^{b/2} \frac{\partial C_L(\mathrm{y})}{\partial \alpha} \alpha(\mathrm{y}) \bar{c}(\mathrm{y}) d\mathrm{y} \tag{4.2.12}$$

For an aircraft with a flexible structure the local angle of attack at a particular section can be defined as a combination of the α at steady state, the local camber twist angle and the local elastic distortion angle [189].

Meanwhile, the pitch stiffness coefficient can be calculated as function of the lift slope with the following relationship:

$$M_\alpha = \frac{1}{2}\rho U^2 S \bar{c} C_{M_\alpha} \tag{4.2.13}$$

and assuming linear aerodynamic condition, the derivatives C_{M_α}, can be rewritten as:

$$C_{M_\alpha} = \frac{dC_M}{dC_L} \frac{dC_L}{d\alpha} \tag{4.2.14}$$

where the term $\dfrac{dC_L}{d\alpha}$ is the non-dimensional coefficient of L_α is as explained in Equation

4.2.12.

The last term of interest is the pitch damping coefficient M_q. The most significant contribution for this coefficient comes from the tailplane rather than the wing component. Reference [145] explains this coefficient as follows: " *when the aircraft experiences a small perturbation in pitching DoF, the tailplane experiences a normal velocity component due to the rotation about CG, which changes the local incidence of the tail. The change in the local incidence of the tail, changes the lift force of the tail. Hence, this force translated to the CG and creates pitching disturbance in the opposite direction*".

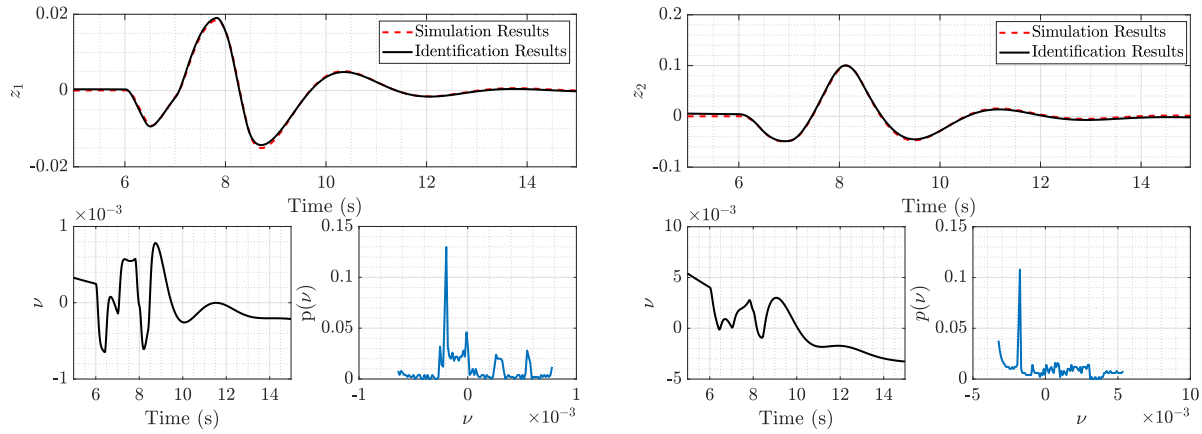

Figure 4.10: Identification of longitudinal coefficient for the aircraft with rigid structure.

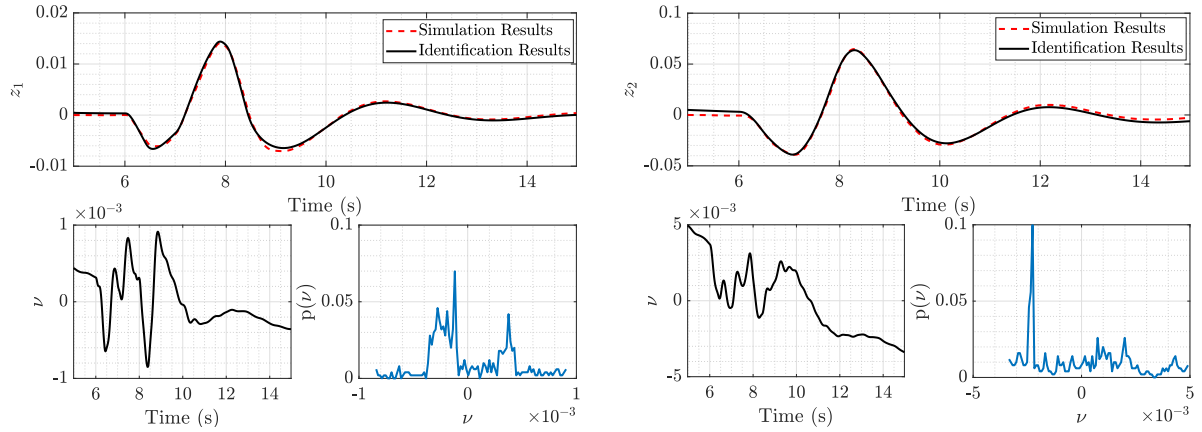

Figure 4.11: Identification of longitudinal coefficient for the aircraft with flexible structure.

Figure 4.10 and 4.11 presents the comparison of the simulation and identification results for both aircraft configuration with the rigid and flexible structure respectively. The measurement output on the figures are referred to Equation 4.2.11. All the comparison between the simulation output and the model output from identification process show matches with residuals of an order of magnitude lower. Also, the identified coefficient value is also comparable with a similar aircraft, except for C_{M_α} which is almost twice higher [190]. The identification results for all the coefficient are presented in Figure 4.12, 4.13 and 4.14 for both the rigid and flexible aircraft.

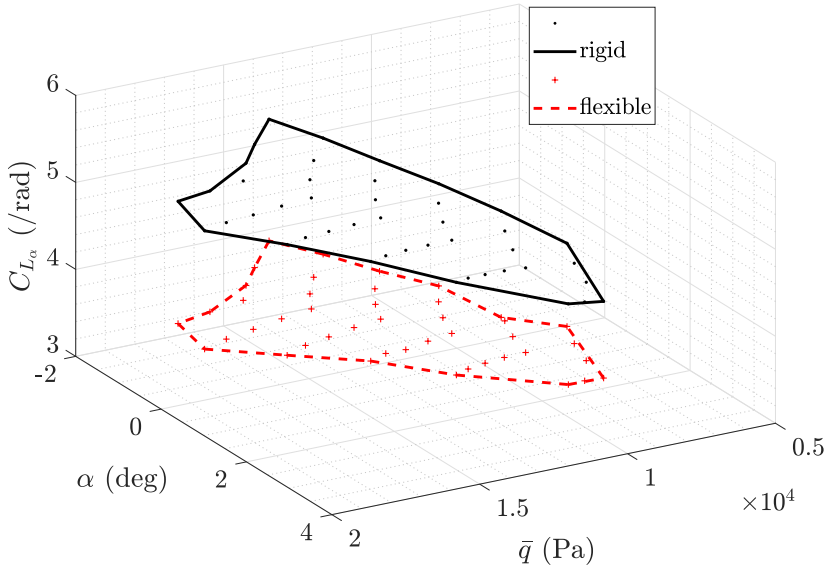

Figure 4.12: Identification of C_{L_α} for aircraft with rigid and flexible structure.

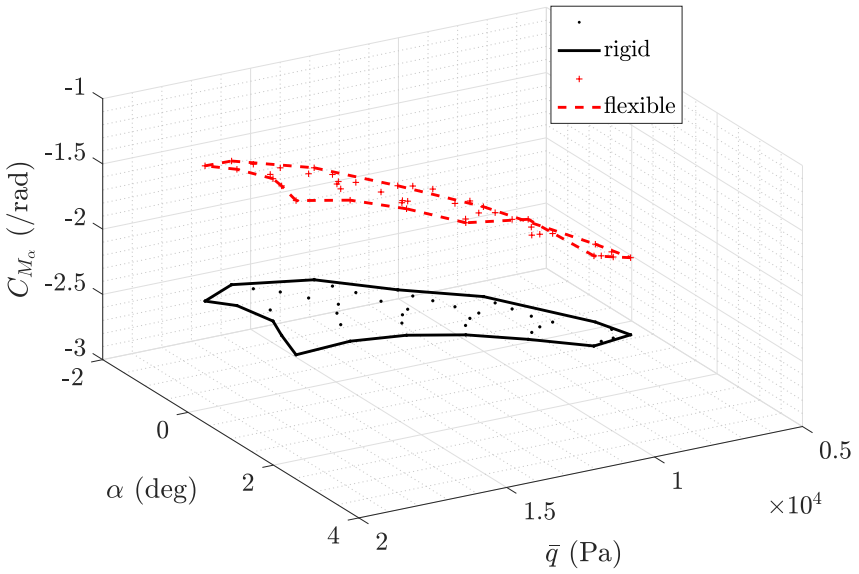

Figure 4.13: Identification of C_{M_α} for aircraft with rigid and flexible structure.

All results show that by using a rigid body approach, the flexible aircraft has a lower identified coefficient value when compared to the rigid aircraft. The changes in the C_{L_α} value is almost comparable with the changes in the C_{M_α}, in which for the flexible case the coefficient is around 0.8 times smaller than the rigid case.

On the other hand, it is argued that the C_{M_q} value is mostly affected by the tailplane. However, Reference [189] explains that on elastic aircraft there are two acting loads: the aerodynamic and inertial loading. Therefore, the stability derivatives for aeroelastic aircraft are formulated in two categories. The first is due to the aeroelastic effect in the absence of the inertial force (mass derivatives), while the second consist of stability

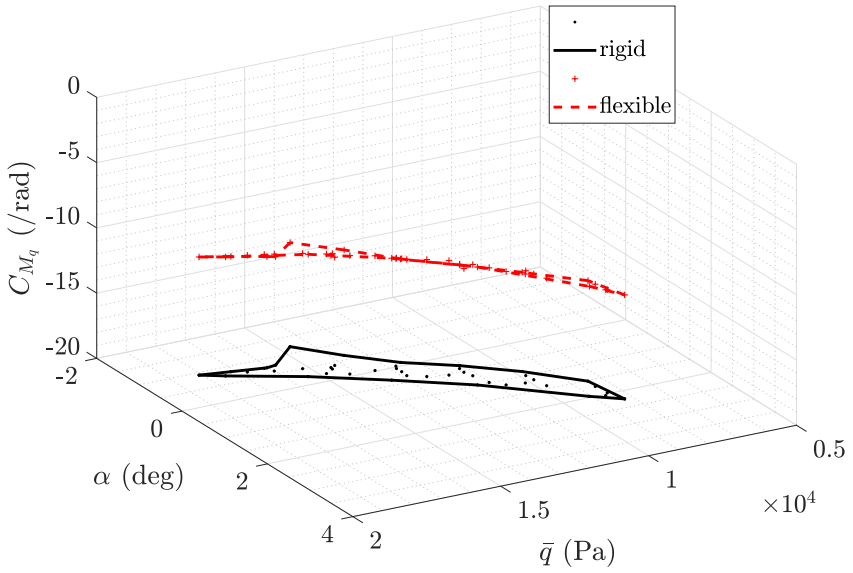

Figure 4.14: Identification of C_{M_q} for aircraft with rigid and flexible structure.

derivatives solely due to inertial forces (inertial derivatives). Interestingly, for the coefficient of pitching moment that depend on the pitch rate, Roskam showed the following formulation:

$$C_{M_{q\,flex}} = C_{M_{q_{\bar{E}}}} + C_{M_{q_I}} \tag{4.2.15}$$

in which the subscript $\bar{E}$ represents the mass derivatives, while the subscripts I represents the inertial derivatives. These inertial derivatives do not appear in the definition of lift slope and pitch stiffness coefficients, and this is most probably the source of the shift in the identified C_{M_q} value for the flexible structure configuration.

4.2.3 Application of the Correction Model

In this section, the method presented earlier is used to asses the handling quality of a flexible aircraft, particularly those which equipped with wingtip devices, using a flight simulator [27]. Having the right database and the effective methodology [29] can lead to an insight of the handling quality of the vehicle. To do so, a fast reduced order model is needed. For flight simulator application, it is common to model the flaps and undercarriages using a correction factor approach to add to to the clean wing aerodynamic properties [191]. The same concept is adopted here, which is to build a database based on a correction factor to quantify the effect of morphing wingtip for a flight simulator application.

For identification purposes, a set of simulations were conducted using the CA^{2}LM framework for 44 flight conditions, which consist of two wingtip sizes (hinge line at 10% and 20% wing semispan) with seven wingtip deflection Υ (0^o to 30^o, with 5^o increment in a symmetric manner). The simulation was also conducted for both rigid and flexible configuration. The illustration of the wingtip folding is presented in Figure 4.15.

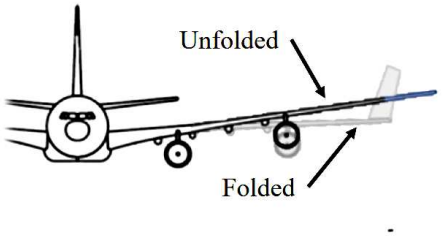

Figure 4.15: Illustration of morphing wingtip device.

		a_1	a_2	a_3	a_4	a_5	a_6	a_7
C_{l_p}	rigid	-	-	-1.137	-1.677	0.079	0.250	-0.184
	flexible	-0.134	-1.65×10^{-5}	-0.174	-	-	0.095	-
		b_1	b_2	b_3	b_4	b_5	b_6	b_7
$C_{l_{\delta_a}}$	rigid	-	-	-1.133	0.296	0.087	0.065	-
	flexible	-0.179	-2.67×10^{-5}	-	-	-	-	-

Table 4.2: Prediction model derivation.

A global model which can capture the flexibility effect as a function of dynamic pressure $\bar{q}$ [90], wingtip size ς, as well as wingtip deflection Υ is generated using MOF method which allows the inclusion of model structure determination process to help identify the most suitable model structure. The idea of developing a global model is adapted from work by Grauer and Morelli [151]. The following relationships are defined for identification purposes:

$$C_{l_p}^{\Upsilon} = C_{l_p}^{\Upsilon=0}{}_{\text{rigid}} \left(1 + \Delta C_{l_p}(\Upsilon, \varsigma, \bar{q})\right) \tag{4.2.16}$$

$$C_{l_{\delta_a}}^{\Upsilon} = C_{l_{\delta_a}}^{\Upsilon=0}{}_{\text{rigid}} \left(1 + \Delta C_{l_{\delta_a}}(\Upsilon, \varsigma, \bar{q})\right) \tag{4.2.17}$$

where the correction factors are defined as:

$$\Delta C_{l_p}(\Upsilon, \varsigma, q) = a_1 + a_2 q + \left(a_3\Upsilon + a_4\Upsilon^2\right)\varsigma + a_5\Upsilon + a_6\Upsilon^2 + a_7\Upsilon^3 \tag{4.2.18}$$

$$\Delta C_{l_{\delta_a}}(\Upsilon, \varsigma, q) = b_1 + b_2 q + \left(b_3\Upsilon + b_4\Upsilon^2\right)\varsigma + b_5\Upsilon + b_6\Upsilon^2 + b_7\Upsilon^3 \tag{4.2.19}$$

The baseline used here is the set of identified coefficients for the rigid configuration with zero wingtip deflection. Thus, for identification purposes the measurement output is defined as:

$$z = \frac{C_{l_p}^{\Upsilon} - C_{l_p}^{\Upsilon=0}{}_{\text{rigid}}}{C_{l_p}^{\Upsilon=0}{}_{\text{rigid}}} \tag{4.2.20}$$

The MOF method requires clear definitions of the order and polynomial dependencies of the variables. Here, the maximum order of the variables is 3, where only Υ is allowed to have a cubic term dependency. The identified coefficient as defined in Equations 4.2.18 and 4.2.19 are presented in Table 4.2. The identified coefficients and the predicted coefficients can be compared in Figures 4.16 and 4.17.

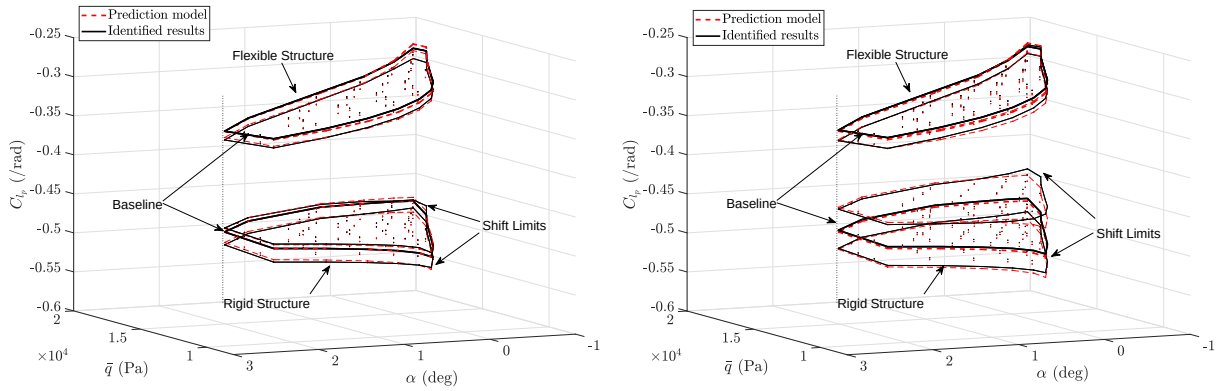

10% wingtip deflection 20% wingtip deflection

Figure 4.16: Matching plot for roll damping model.

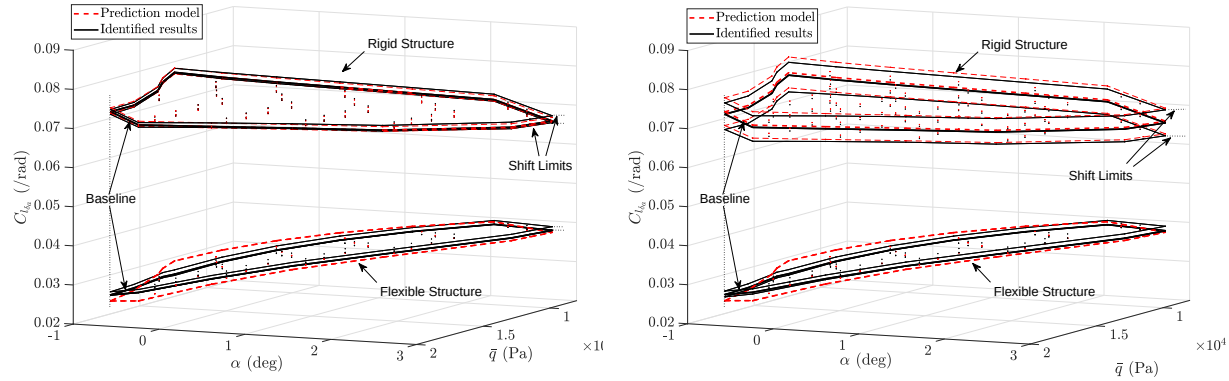

10% wingtip deflection 20% wingtip deflection

Figure 4.17: Matching plot for aileron effectiveness model.

Given the global prediction model, a validation of the prediction model is conducted using Equation 4.2.2 based on the values obtained from the prediction model. A comparison of the simulation results from the CA^{2}LM framework and the prediction model is presented in Figure 4.18. These results correspond to a flight condition with a velocity of 180 m/s (TAS) and an altitude of 10,000 ft. The input is an aileron pulse input for 5 seconds. It is worth mentioning that this flight condition is not part of the data set being used to develop the prediction model.

For the same input, the responses of both the prediction model and the CA^{2}LM framework are in agreement. However, a slight deviation after the initial input is observed for the rigid structure, due to the differences in the degree of freedom involved in the two simulations: CA^{2}LM framework is based on 6-DoF while the prediction model is a simple 1-DOF rolling moment equation neglecting lateral-directional coupling. However, the changes in aerodynamic derivatives are small for aircraft with flexible structures, as this configuration is more adaptable to perturbation. Furthermore, the difference comes from the sideslip angle, which in this case is treated as an input for both models and plays a significant role in the rigid body dynamics [28].

Overall, these results highlight the effectiveness of parameter estimation methods in

building a polynomial correction model to capture morphing wingtip and flexibility. As this polynomial formulation is easier to implement in a flight simulator environment for pilot-in-the-loop simulations without requiring physics-based models, as implemented in the more complex CA^{2}LM framework.

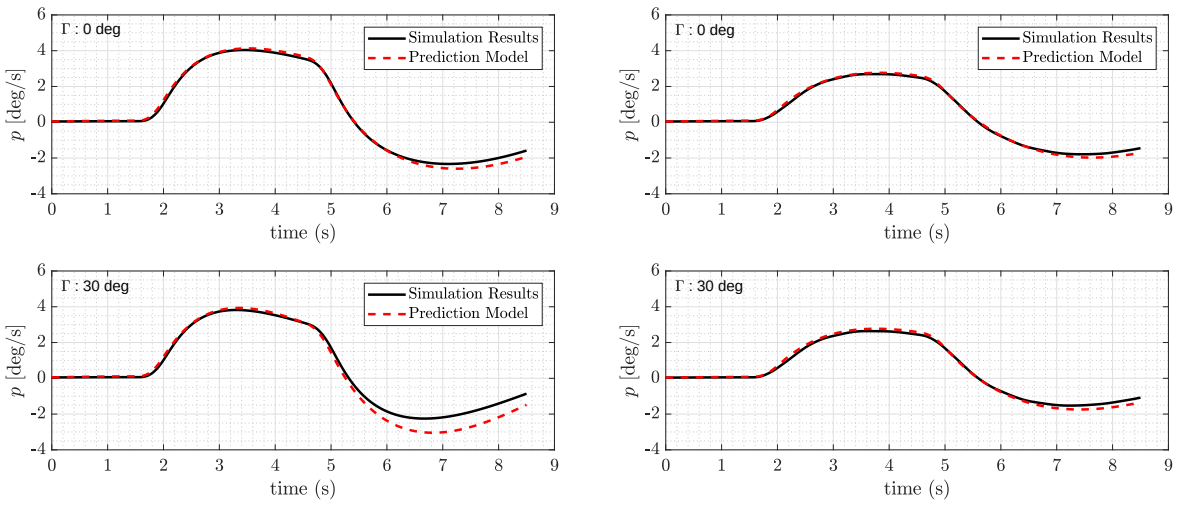

Validation for rigid model $\varsigma = 20\%$. Validation for flexible model $\varsigma = 20\%$.

Figure 4.18: Validation of global wingtip model.

4.3 Generalised Approach

In the previous section, the CA^{2}LM simulation framework was used to identify and compare flexible and rigid body aircraft using a quasi-steady approach, meaning that the flexibility effects were captured within the traditional rigid body coefficients. However, for explicit representation of aeroelastic effects a more generalised approach is needed. Here, a generalised model as developed by Waszak and Schmidt can be used [132]. The assumption underlying this modelling approach is that the structural deformation is small and the variance in the aircraft mass properties (such as centre of gravity and moments of inertia) due to flexibility are negligible. Furthermore, to solve the equations of motion, the structural deformations are represented via a finite set of orthogonal eigenmodes or modeshapes.

By adopting a generalised model, it is possible to observe both the rigid body and flexible body (generalised) derivatives of interests. These derivatives can give insight into the stability of the system through its eigenvalue for a particular flight condition. Therefore, it is also of interest to assess the change of the derivatives as a function of speed.

The objective of this section is to present a method for identifying aircraft aeroelastic modes through the use of multisine inputs and multivariate orthogonal functions [153]. The argument here is that by observing the change of aeroelastic derivatives in the time domain, the shift in damping and frequency of each eigenmode can be identified and used to assess system stability. By utilising the MOF approach, one can observe the change in the frequency and damping of the system as a function of airspeed [153]. It

should be noted that, since this approach solves the identification problem through the optimal model structure, in some cases the parameter of interest may be discarded from the model. For instance, if the parameter that is discarded is a variable related directly to the natural frequency of the system, the resulting model will not provide any meaningful insight.

4.3.1 Input Design

Here, the traditional flight test approach is used to excite aircraft dynamics. The process involves starting at trim condition, exciting the modes through the control surfaces and repeating at increasingly higher airspeeds. The input design is carefully chosen to excite the airframe over a range of frequencies that cover the dynamic modes of interests, particularly for parameter estimation.

In this section, the aeroelastic modes of interest are limited to the longitudinal dynamics. These modes are expected to be in the range of 0.2 to 2 Hz. Following the realisability consideration (as discussed in Chapter 2), the elevator is chosen to excite the modes rather than symmetric aileron deflection as in the previous section. This is due to the higher bandwith available on the elevator actuators.

Although a typical input type adopted for flutter envelope expansion programs is frequency sweep [192], here the potential of using orthogonal multi-sine inputs is explored [94] with a frequency range of 0.2 to 2 Hz (due to actuator bandwidth limitations). However, this input is within the range of the short period mode as well as the first two structural modes, which means that this input can effectively excite the modes and the corresponding model parameters. Figure 4.19 shows the input design both in time and frequency domains for the elevator. The time duration of the input is 15 seconds.

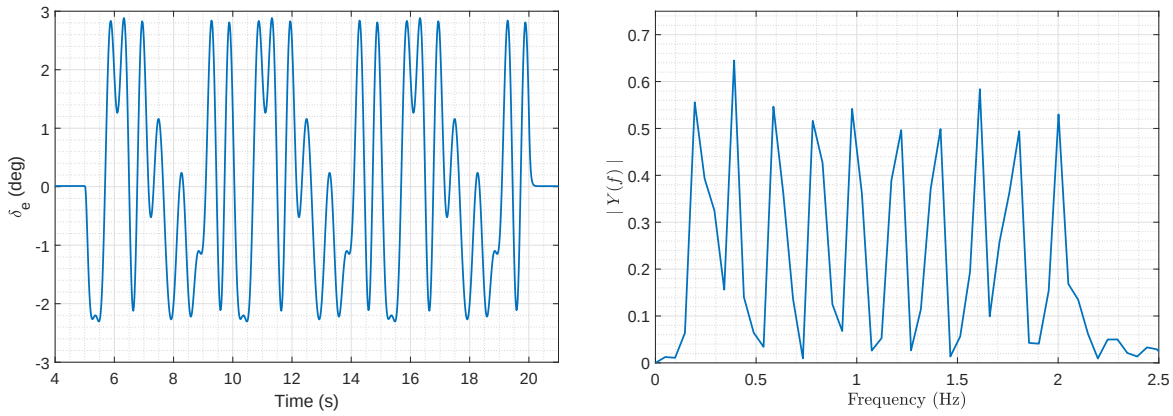

Figure 4.19: Elevator input in the time and frequency domain.

The simulation was conducted for speeds ranging from 160 m/s to 240 m/s at an altitude of 20,000 ft. The simulation results provide 6 DoF rigid body data at the centre of gravity. On the other hand, the structural model allows the user to observe the displacement, velocity and acceleration of the structural nodes. In an experimental flight test, the rigid body mode data can be obtained from the inertial measurement unit (IMU), while the acceleration of the nodes can be obtained by having distributed accelerometers on the aircraft structure [101].

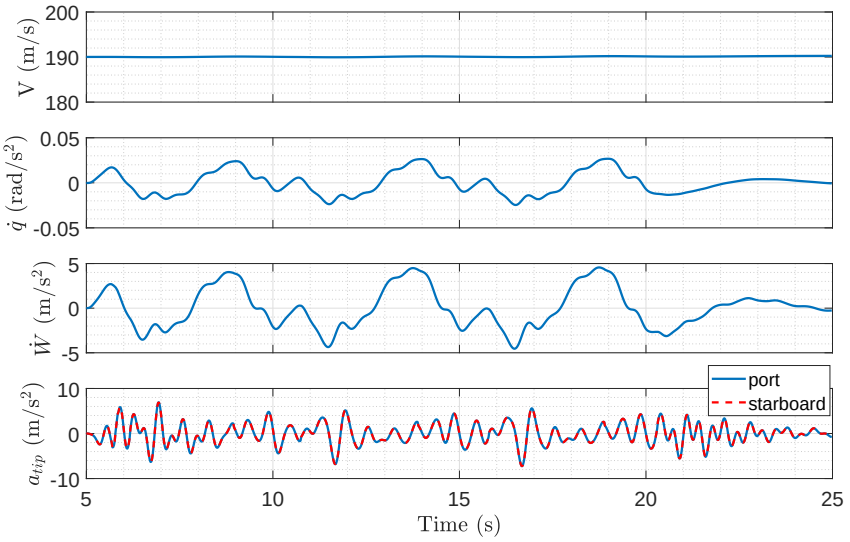

Figure 4.20: Simulation results for 190 m/s airspeed.

An example of aircraft response due to the input is presented in Figure 4.20. The figure shows the time history of the change in the aircraft velocity, the normal acceleration and the pitch rate for the given elevator input. Furthermore, the figure also shows the normal acceleration of the wingtip station highlighting the effects on the flexible structure. Here, the symmetric elevator deflections are seen to excite the symmetric wing bending modes around 2 Hz.

4.3.2 Identification Procedure

As evident in Figure 4.20, the input can be seen to excite the longitudinal modes, in particular the short period mode as shown by the change in the normal acceleration and pitch rate. The negligible change in airspeed shows that the phugoid mode has not been excited. On the other hand, the input only excites the symmetric structural mode (see Figure 4.3 for the illustration of the first six flexible modes), as shown by the comparison between the left and right wingtip acceleration.

The variables of interest here are not only the aerodynamics and generalised coefficients, but also their contribution in identifying the damping and frequency of the aeroelastic modes. Aeroelastic mode damping is of especial interest as its reduction in damping of an aeroelastic mode can be an indication of flutter. Past study has been conducted to identify the change in aeroelastic mode damping and frequency using the MOF method. However, using this method certain cases were found where the algorithm ignored a significant coefficient which was related to the frequency and damping of the system especially at higher velocities [153]. For this reason it is preferable to use the output error method in the identification of aeroelastic modes.

By assuming a small perturbation model and ignoring the lateral-directional terms, the equations of motion representing the short period and the first three flexible modes as

adopted from References [132] can be expressed as follows:

$$m(\dot{W} - qU - g\cos\theta) = Z_0 + Z_w + Z_q q + Z_{\delta_e} + \sum_{j=1}^{3} F^j_{Z\eta_j}\eta_j + \sum_{j=1}^{3} F^j_{Z_{\dot{\eta}_j}}\dot{\eta}_j + Z_T \quad (4.3.1)$$

$$I_y\dot{q} = M_0 + M_w w + M_q q + M_{\delta_e} + \sum_{j=1}^{3} M^j_{\eta_j}\eta_j + \sum_{j=1}^{3} M^j_{\dot{\eta}_j}\dot{\eta}_j + M_T \quad (4.3.2)$$

$$\dot{\theta} = q \quad (4.3.3)$$

$$m_1[\ddot{\eta}_1 + 2\zeta_1\omega_1\dot{\eta}_1 + {\omega_1}^2\eta_1] = Q^1_0 + Q^1_w w + Q^1_q q + Q^1_{\delta_e} + \sum_{j=1}^{3} Q^1_{\eta_j}\eta_j + \sum_{j=1}^{3} M^1_{\dot{\eta}_j}\dot{\eta}_j \quad (4.3.4)$$

$$m_2[\ddot{\eta}_2 + 2\zeta_2\omega_2\dot{\eta}_2 + {\omega_2}^2\eta_2] = Q^2_0 + Q^2_w w + Q^2_q q + Q^2_{\delta_e} + \sum_{j=1}^{3} Q^2_{\eta_j}\eta_j + \sum_{j=1}^{3} M^2_{\dot{\eta}_j}\dot{\eta}_j \quad (4.3.5)$$

$$m_3[\ddot{\eta}_3 + 2\zeta_3\omega_3\dot{\eta}_3 + {\omega_3}^2\eta_3] = Q^3_0 + Q^3_w w + Q^3_q q + Q^3_{\delta_e} + \sum_{j=1}^{3} Q^3_{\eta_j}\eta_j + \sum_{j=1}^{3} M^3_{\dot{\eta}_j}\dot{\eta}_j \quad (4.3.6)$$

The first two equations represent the rigid body mode, while the last three represents the flexible body mode. Here m is the total mass of the aircraft, m_j is the generalised mass for the j-th aeroelastic mode, and η_j represents the generalised coordinate. On the right hand side of the equation, Q^j represents the generalized force for the j-th mode, while F_Z and M represent the force in Z direction and moment around y-axis respectively. T represents the force and moment due to thrust.

A critical part in identifying the aeroelastic components of such a system is to specify the generalised coordinates, η. A common approach is to use mode shapes, which can be validated using GVT [48]. Here, the elastic deformation at position (x, y, z) on the structure is denoted by $\mathbf{d}$ can be written as :

$$\mathbf{d}(x, y, z, t) = \Phi(x, y, z)\eta(t) \quad (4.3.7)$$

where Φ is the mode shape or eigenfunction associated with the generalised coordinate. In this case, assuming that the mode shape is known, the generalised coordinate is calculated using the following relationship:

$$\eta(t) = \Phi(x, y, z)^{-1}\mathbf{d}(x, y, z, t) \quad (4.3.8)$$

Furthermore, assuming linear time invariant structure in which Φ is not a function of time, the velocity and acceleration of the generalised mode can also be defined as:

$$\dot{\eta}(t) = \Phi(x, y, z)^{-1}\dot{\mathbf{d}}(x, y, z, t) \quad (4.3.9)$$

$$\ddot{\eta}(t) = \Phi(x, y, z)^{-1}\ddot{\mathbf{d}}(x, y, z, t) \quad (4.3.10)$$

Figure 4.21 shows the measured acceleration of the structure, in which a_f is the acceleration at the center of fuselage, a_{wt} is the acceleration at the node located on the tip of

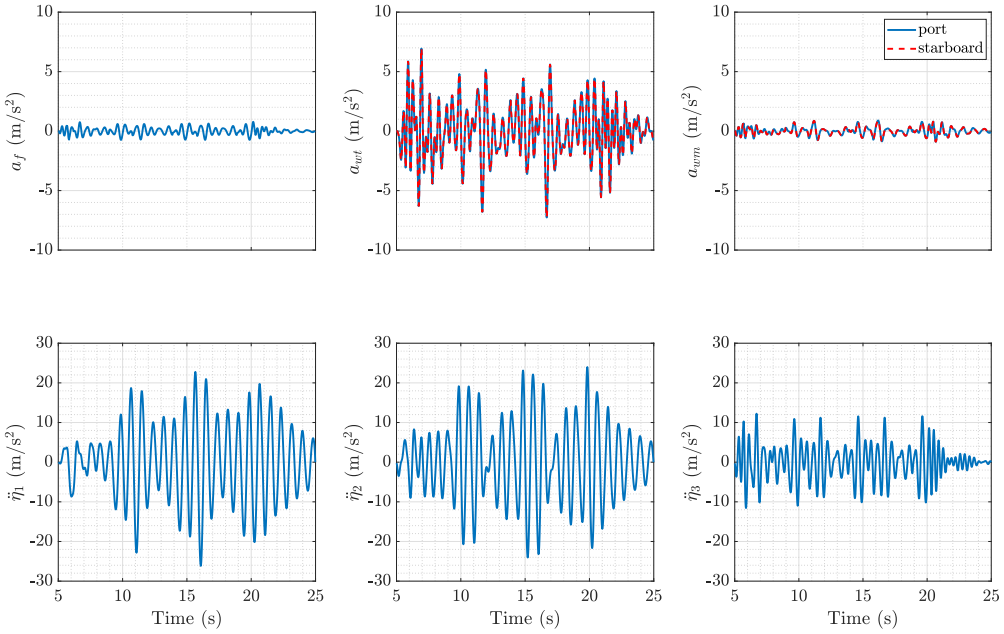

Figure 4.21: Transformation from structure to modal acceleration.

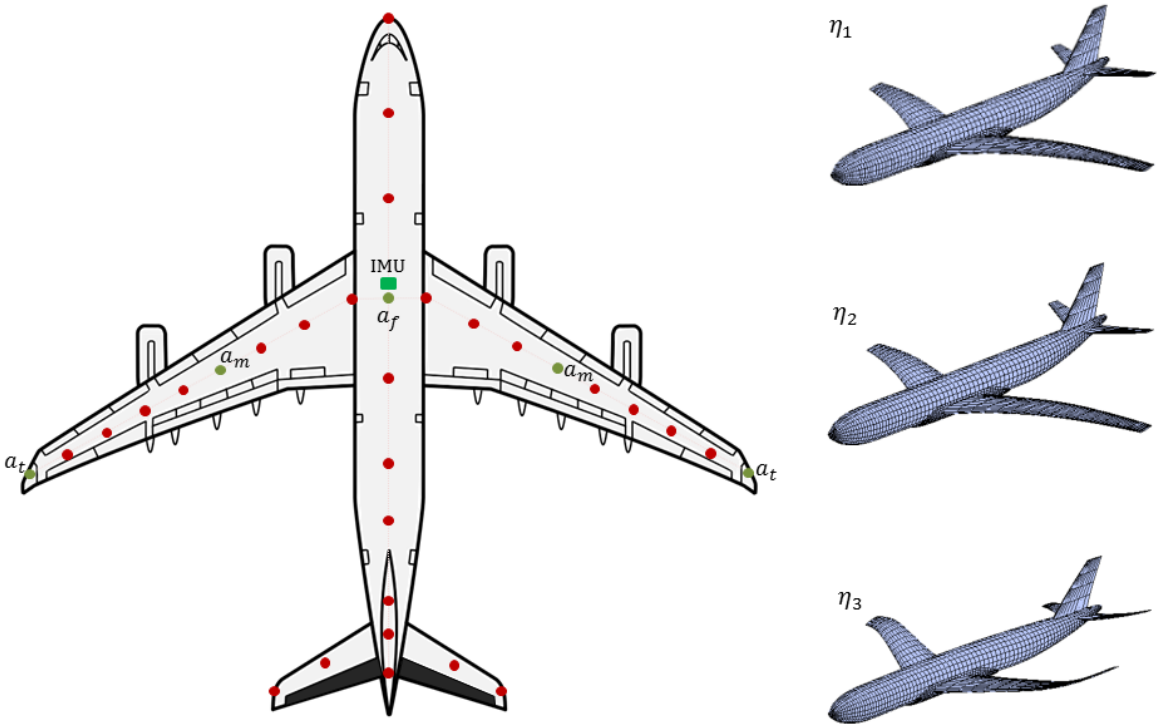

Figure 4.22: Sensor position for aeroelastic identification (red: 3 DoF accelerometer and 3 DoF gyroscope, black: control surface).

the wing (port and starboard), and a_{wm} represents the acceleration at the node on the middle of the wing (port and starboard), as presented in Figure 4.22[4]. Using the relation as expressed in Equation 4.3.10, the modal accelerations are calculated and presented as $\ddot{\eta}_1$, $\ddot{\eta}_2$ and $\ddot{\eta}_3$. In utilising the output error method, it is relatively straightforward to translate the equation of motion into the state-space form. The state space matrix that represented the aircraft dynamics for identification purposes is defined as :

$$\begin{bmatrix} \dot{x_R} \\ \dot{x_\eta} \end{bmatrix} = \begin{bmatrix} A_R & C_{\eta R} \\ C_{R\eta} & A_\eta \end{bmatrix} \begin{bmatrix} x_R \\ x_\eta \end{bmatrix} + \begin{bmatrix} B_R \\ B_\eta \end{bmatrix} u \tag{4.3.11}$$

A_R and A_η are the matrices related to rigid body motion and the aeroelastic modes respectively. $C_{\eta R}$ is the coupling characteristics that shows the contribution of the aeroelastic mode to the rigid body, and similarly $C_{R\eta}$ shows the contribution of the rigid body to the aeroelastic mode. Similarly, B_R and B_η show the contribution of control inputs to the rigid body and aeroelastic modes respectively. Here, as the model is only limited to the short period mode, the rigid body modes are represented by:

$$[x_R] = \begin{bmatrix} w & q & \theta \end{bmatrix} \tag{4.3.12}$$

and the flexible modes are given by:

$$[x_\eta] = \begin{bmatrix} \eta_1 & \dot{\eta_1} & \eta_2 & \dot{\eta_2} & \eta_3 & \dot{\eta_3} \end{bmatrix} \tag{4.3.13}$$

Hence, Equation 4.3.11 can be expanded as:

$$\begin{bmatrix} \Delta\dot{w} \\ \Delta\dot{q} \\ \Delta\dot{\theta} \\ \Delta\ddot{\eta}_1 \\ \Delta\dot{\eta}_1 \\ \Delta\ddot{\eta}_2 \\ \Delta\dot{\eta}_2 \\ \Delta\ddot{\eta}_3 \\ \Delta\dot{\eta}_3 \end{bmatrix} = \begin{bmatrix} \tilde{Z}_w & \tilde{Z}_q & -g\sin\theta_0 & \tilde{Z}_{\dot{\eta_1}} & \tilde{Z}_{\eta_1} & \tilde{Z}_{\dot{\eta_2}} & \tilde{Z}_{\eta_2} & \tilde{Z}_{\dot{\eta_3}} & \tilde{Z}_{\eta_3} \\ \tilde{M}_w & \tilde{M}_q & 0 & \tilde{M}_{\dot{\eta_1}} & \tilde{M}_{\eta_1} & \tilde{M}_{\dot{\eta_2}} & \tilde{M}_{\eta_2} & \tilde{M}_{\dot{\eta_3}} & \tilde{M}_{\eta_3} \\ 0 & 1 & 0 & 0 & 0 & 0 & 0 & 0 & 0 \\ \tilde{Q}^1_w & \tilde{Q}^1_q & 0 & \hat{Q}^1_{\dot{\eta_1}} & \hat{Q}^1_{\eta_1} & \tilde{Q}^1_{\dot{\eta_2}} & \hat{Q}^1_{\eta_2} & \tilde{Q}^1_{\dot{\eta_3}} & \hat{Q}^1_{\eta_3} \\ 0 & 0 & 0 & 1 & 0 & 0 & 0 & 0 & 0 \\ \tilde{Q}^2_w & \tilde{Q}^2_q & 0 & \tilde{Q}^2_{\dot{\eta_1}} & \tilde{Q}^2_{\eta_1} & \hat{Q}^2_{\dot{\eta_2}} & \hat{Q}^2_{\eta_2} & \tilde{Q}^2_{\dot{\eta_3}} & \tilde{Q}^2_{\eta_3} \\ 0 & 0 & 0 & 0 & 0 & 1 & 0 & 0 & 0 \\ \tilde{Q}^3_w & \tilde{Q}^3_q & 0 & \tilde{Q}^3_{\dot{\eta_1}} & \tilde{Q}^3_{\eta_1} & \tilde{Q}^3_{\dot{\eta_2}} & \tilde{Q}^3_{\eta_2} & \hat{Q}^3_{\dot{\eta_3}} & \hat{Q}^3_{\eta_3} \\ 0 & 0 & 0 & 0 & 0 & 0 & 0 & 1 & 0 \end{bmatrix} \begin{bmatrix} \Delta w \\ \Delta q \\ \Delta\theta \\ \Delta\dot{\eta}_1 \\ \Delta\eta_1 \\ \Delta\dot{\eta}_2 \\ \Delta\eta_2 \\ \Delta\dot{\eta}_3 \\ \Delta\eta_3 \end{bmatrix} + \begin{bmatrix} Z_{\delta_e} \\ M_{\delta_e} \\ 0 \\ Q^1_{\delta_e} \\ 0 \\ Q^2_{\delta_e} \\ 0 \\ Q^3_{\delta_e} \\ 0 \end{bmatrix} [\delta_e] \tag{4.3.14}$$

where:

$$\tilde{Z}_i = \frac{Z_i}{m} \tag{4.3.15}$$

$$\tilde{M}_i = \frac{M_i}{I_y} \tag{4.3.16}$$

$$\tilde{Q}^j_i = \frac{Q^j_i}{m_j}, \qquad i = w, q, \eta_1, \eta_2, \eta_3, \dot{\eta}_1, \dot{\eta}_2, \dot{\eta}_3 \tag{4.3.17}$$

$$\hat{Q}^j_{\dot{\eta}_j} = \tilde{Q}^j_{\dot{\eta}_j} - 2\zeta_j\omega_j \tag{4.3.18}$$

$$\hat{Q}^j_{\eta_j} = \tilde{Q}^j_{\eta_j} - {\omega_j}^2, \quad j = 1, 2, 3 \tag{4.3.19}$$

[4]In industry flutter testing is done with multi accelerometers. Some of these are located on the control surfaces to investigate control surface flutter, while some others are placed in the engine area.

and the model output is defined as:

$$\begin{bmatrix} \Delta\dot{w} \\ \Delta q \\ \Delta\ddot{\eta}_1 \\ \Delta\ddot{\eta}_2 \\ \Delta\ddot{\eta}_3 \end{bmatrix} = \begin{bmatrix} \tilde{Z}_w & \tilde{Z}_q & -g\sin\theta_0 & \tilde{Z}_{\dot{\eta}_1} & \tilde{Z}_{\eta_1} & \tilde{Z}_{\dot{\eta}_2} & \tilde{Z}_{\eta_2} & \tilde{Z}_{\dot{\eta}_3} & \tilde{Z}_{\eta_3} \\ 0 & 1 & 0 & 0 & 0 & 0 & 0 & 0 & \\ \tilde{Q}^1_w & \tilde{Q}^1_q & 0 & \hat{Q}^1_{\dot{\eta}_1} & \hat{Q}^1_{\eta_1} & \tilde{Q}^1_{\dot{\eta}_2} & \hat{Q}^1_{\eta_2} & \tilde{Q}^1_{\dot{\eta}_3} & \hat{Q}^1_{\eta_3} \\ \tilde{Q}^2_w & \tilde{Q}^2_q & 0 & \tilde{Q}^2_{\dot{\eta}_1} & \hat{Q}^2_{\eta_1} & \hat{Q}^2_{\dot{\eta}_2} & \hat{Q}^2_{\eta_2} & \tilde{Q}^2_{\dot{\eta}_3} & \hat{Q}^2_{\eta_3} \\ \tilde{Q}^3_w & \tilde{Q}^3_q & 0 & \tilde{Q}^3_{\dot{\eta}_1} & \tilde{Q}^3_{\eta_1} & \tilde{Q}^3_{\dot{\eta}_2} & \tilde{Q}^3_{\eta_2} & \hat{Q}^3_{\dot{\eta}_3} & \hat{Q}^3_{\eta_3} \end{bmatrix} \begin{bmatrix} \Delta w \\ \Delta q \\ \Delta\theta \\ \Delta\dot{\eta}_1 \\ \Delta\eta_1 \\ \Delta\dot{\eta}_2 \\ \Delta\eta_2 \\ \Delta\dot{\eta}_3 \\ \Delta\eta_3 \end{bmatrix} + \begin{bmatrix} Z_{\delta_e} \\ 0 \\ Q^1_{\delta_e} \\ Q^2_{\delta_e} \\ Q^3_{\delta_e} \end{bmatrix} [\delta_e] \tag{4.3.20}$$

4.3.3 Identification Results

The output-error methods being used to identify the rigid body as well as the aeroelastic coefficients in this section rely on the modified Newton-Raphson method[5]. Equations 4.3.14 and 4.3.20 are used as the model for the optimisation routine for output error method. And in total there are 45 coefficients that need to be identified.

As mentioned earlier, the application of output error methods needs a set of initial conditions. Here, the initial conditions are calculated using the OLS method. Table 4.3 presents the comparison of identified parameters from the OLS and output error method for an airspeed of 190 m/s. Furthermore, Equations 4.3.14 and 4.3.20 are utilised to compare the response of the output matrix based on the identified parameter. Using the equations as mentioned earlier the output from the identified parameter based on both OLS and OE method are compared with the simulation results, which are presented in Figures 4.23 to 4.27. Overall, the figures show that the output error method gives superior results when compared to the OLS method. This becomes evident when inspecting the magnitude of the residual ν. For the rigid body dynamics (Figures 4.23 and 4.24), the residuals from both methods are almost similar and of the same order of magnitude.

However, for the identification of the generalised mode (Figures 4.25 to 4.27), it is shown that the OLS methods has a tendency of a phase shift at a longer time step. The phase shift resulted in a higher residual for the OLS method. On the other hands, the output error methods have the residual in an order of magnitude lower. On the other hand, for both cases, the matching of simulation and identification results for the third flexible mode is quite poor with residuals almost at the same order of magnitude (see Figure 4.27). The poor identification of mode 3 is most likely because the input did not insert enough energy at the particular frequency, as the input excitation is limited from 0.2 to 2 Hz while the third structural mode was expected to be at around 2.3 Hz.

Following the procedure in Equation 4.3.7, the identified generalised acceleration can be used to calculate the acceleration of a specific node of the aircraft. Figure 4.28 shows the comparison between the node acceleration based on the simulation results and the identification results. The figure shows the acceleration at the node in the middle of the fuselage, middle of the wing, and the tip of the wing as noted in Figure 4.22.

[5]Newton-Raphson is a gradient based optimisation technique, as elaborated in Chapter 3.2

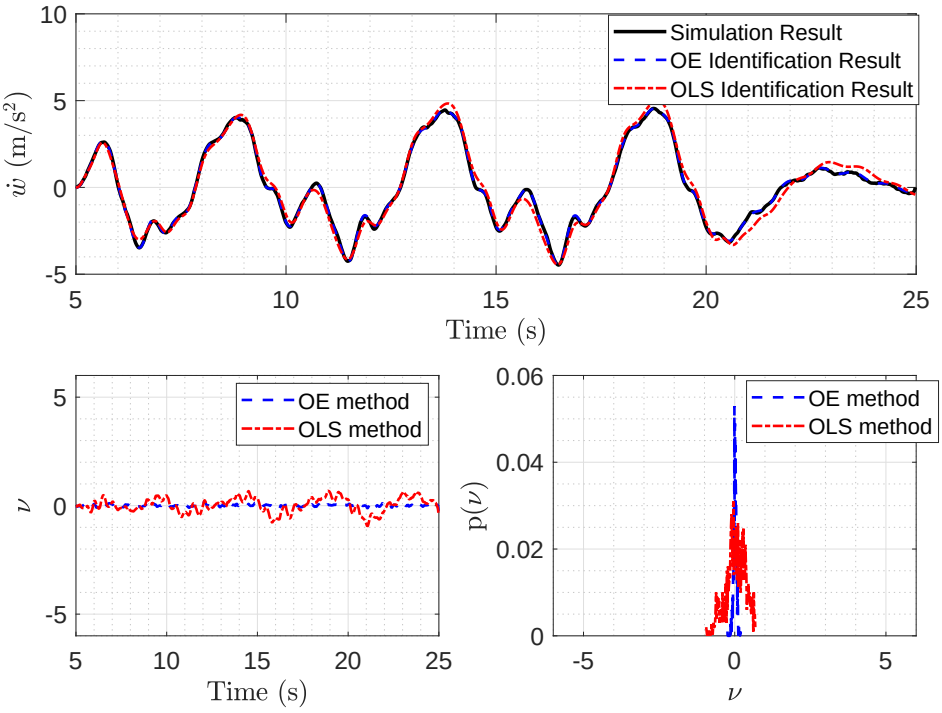

Figure 4.23: Identification of vertical speed at 190 m/s.

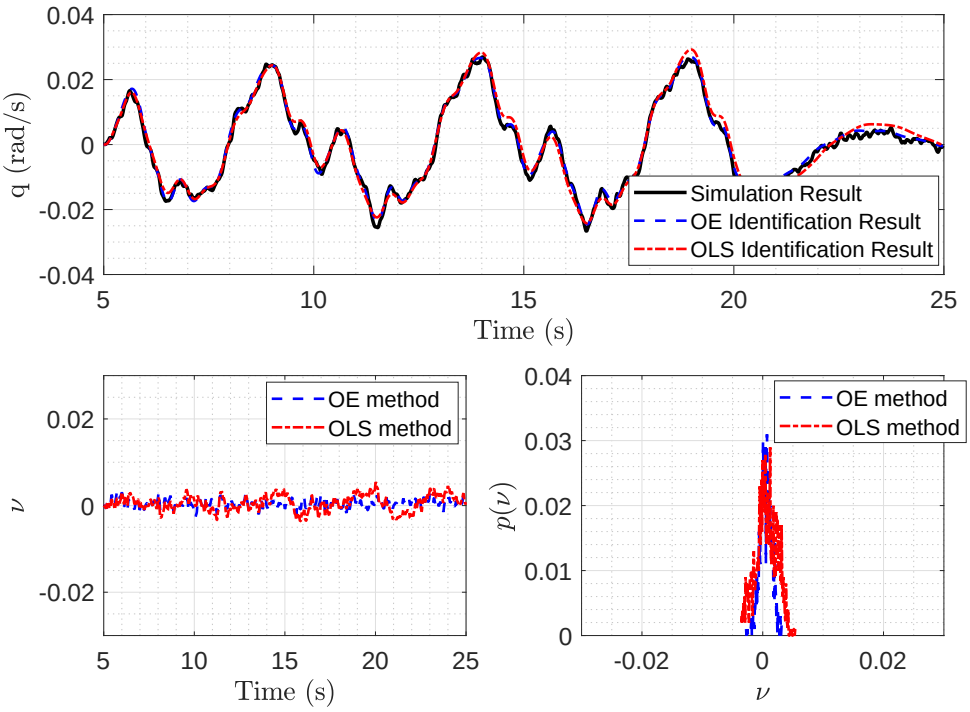

Figure 4.24: Identification of pitch rate at 190 m/s.

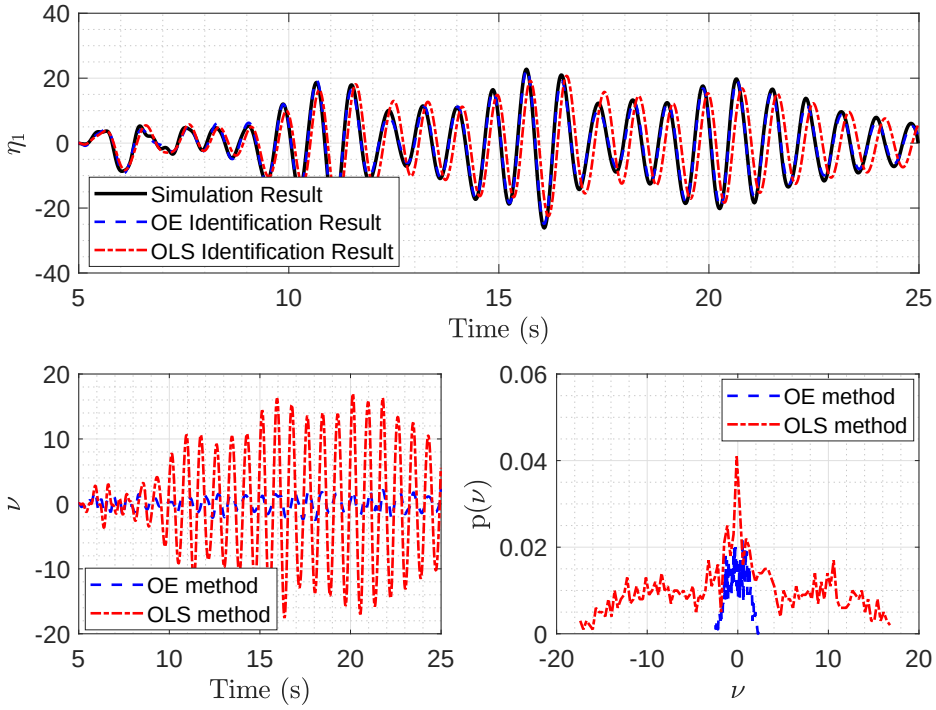

Figure 4.25: Identification of the 1^{st} generalised mode at 190 m/s.

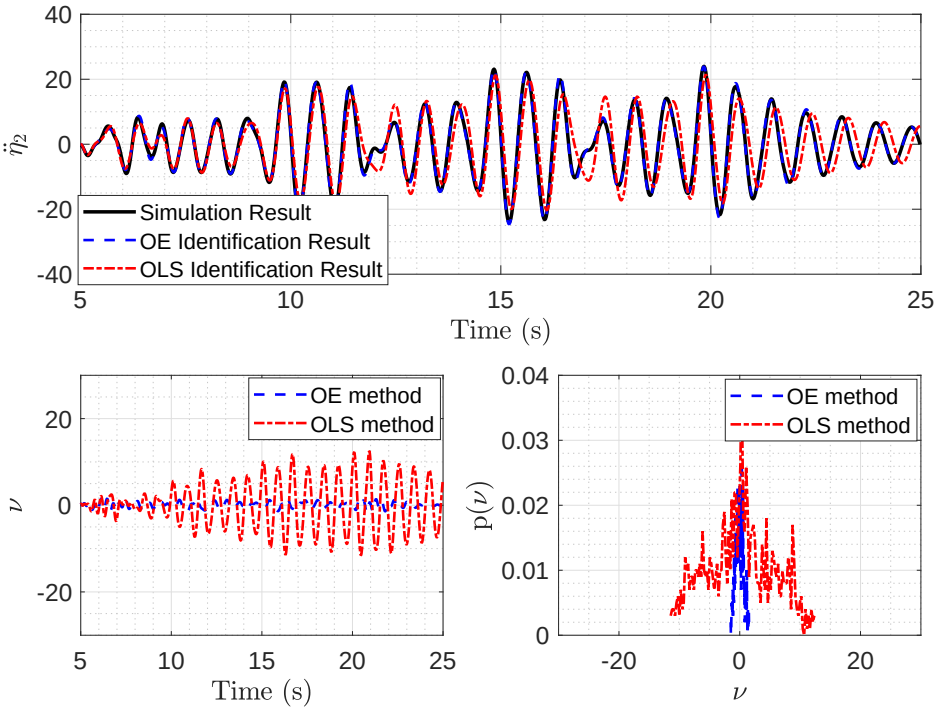

Figure 4.26: Identification of the 2^{nd} generalised mode at 190 m/s.

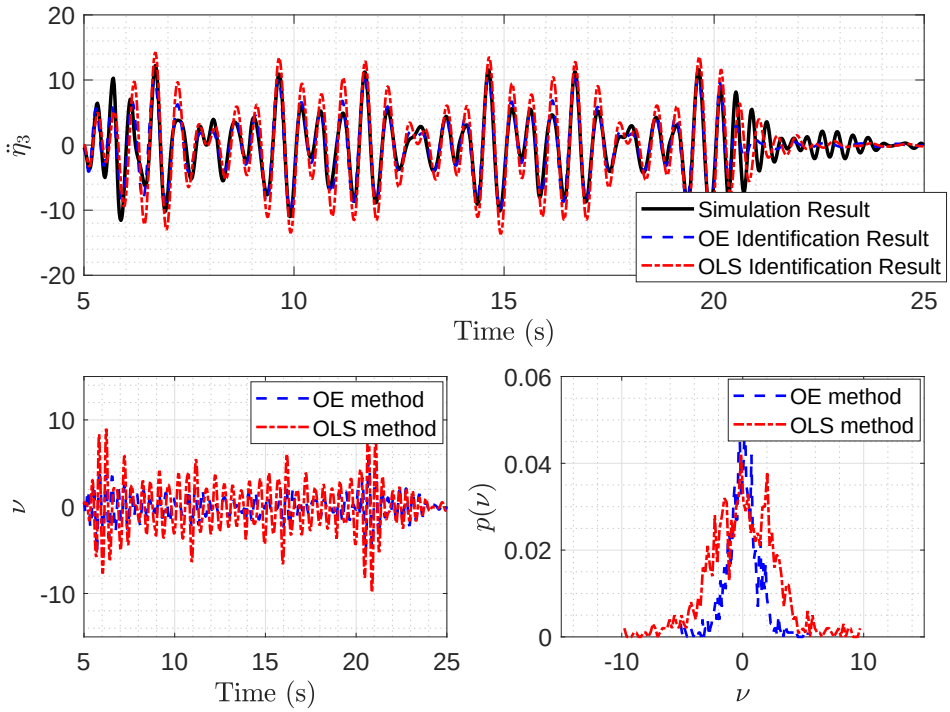

Figure 4.27: Identification of the 3^{rd} generalised mode at 190 m/s.

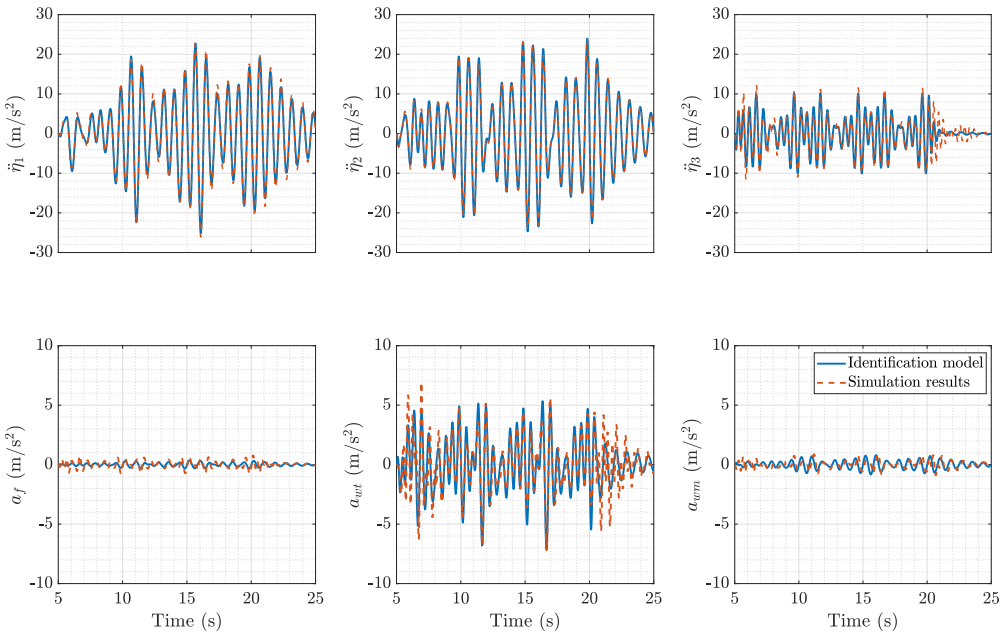

Figure 4.28: Transformation from modal to structural acceleration.

Least Squares Estimation								
Parameter	Values and relatives standard deviation							
	w	q	$\dot{\eta}_1$	η_1	$\dot{\eta}_2$	η_2	$\dot{\eta}_3$	η_3
$\tilde{Z}_i$	-0.411	190	-0.007	0.090	0.016	-0.803	-0.016	1.582
	(0.351)	(0.85)	(0.011)	(0.083)	(0.012)	(0.089)	(0.012)	(0.169)
$\tilde{M}_i$	-0.034	-0.209	0.002	0.053	0.001	-0.065	0.012	0.068
	(0.006)	(0.151)	(0.002)	(0.015)	(0.002)	(0.016)	(0.002)	(0.030)
$\tilde{Q}_i^1$	17.712	54.833	-1.764	-60.628	1.182	11.516	-0.275	-8.553
	(0.277)	(6.692)	(0.085)	(0.659)	(0.093)	(0.701)	(0.093)	(1.340)
$\tilde{Q}_i^2$	-8.44	53.68	0.171	0.363	-0.788	-55.71	-2.084	-15.62
	(0.296)	(7.14)	(0.091)	(0.703)	(0.099)	(0.748)	(0.099)	(1.430)
$\tilde{Q}_i^3$	11.74	212.56	-2.668	-12.99	2.125	18.68	-2.702	-194.5
	(0.979)	(23.62)	(0.301)	(2.326)	(0.329)	(2.474)	(0.328)	(4.729)
Output Error Estimation								
Parameter	Values and relatives standard deviation							
	w	q	$\dot{\eta}_1$	η_1	$\dot{\eta}_2$	η_2	$\dot{\eta}_3$	η_3
$\tilde{Z}_i$	-1.058	186	0.084	1.655	0.018	-1.039	-0.048	0.372
	(0.276)	(6.66)	(0.089)	(0.709)	(0.091)	(0.711)	(0.059)	(0.698)
$\tilde{M}_i$	-0.030	0.076	-0.004	0.061	0.008	-0.035	0.021	0.044
	(0.012)	(0.294)	(0.004)	(0.031)	(0.004)	(0.035)	(0.004)	(0.079)
$\tilde{Q}_i^1$	17.451	58.518	-2.559	-63.891	2.134	12.749	0.554	-10.452
	(0.850)	(29.61)	(0.163)	(1.822)	(0.183)	(1.753)	(0.290)	(4.589)
$\tilde{Q}_i^2$	-10.99	57.44	0.255	7.093	-0.722	-65.79	-2.692	-18.41
	(0.383)	(12.65)	(0.092)	(0.843)	(0.085)	(0.906)	(0.113)	(1.656)
$\tilde{Q}_i^3$	19.45	176.08	-1.948	-36.30	1.084	36.40	-5.345	-271.2
	(3.292)	(0.903)	(0.380)	(6.233)	(0.369)	(6.069)	(0.278)	(3.501)

Table 4.3: Identified aeroelastic parameters at velocity 190 m/s.

Nevertheless, as presented in Table 4.3 the identified parameters from both the OLS and output error method are in the same order of magnitude. Moreover, the table presents the confidence intervals of each identified parameter (2σ). Here, some of the identified parameters have a confidence interval in the same order of magnitude of the identified parameter, which indicates that the parameter is not well identified and can be removed from the model equation. However, some of these parameters are important in estimating the characteristics of the system. Furthermore, to simplify the estimation process, as well as to make it consistent, these parameters are retained in the system matrix and considered in calculating the damping and frequency of the system. Figure 4.29 shows the change in the system pole locations as a function of airspeed, clearly showing how certain structural modes become less stable as velocity increases.

The figure shows that there are four pole pairs of the system, representing four dynamic response modes, namely the SPPO, aeroelastic mode 1, aeroelastic mode 2 and aeroelastic mode 3. The figure also shows a shift in the pole location as a function of airspeed. Here, two significant shifts are visible: where one of the pole locations moves towards the more negative real axis value while the other is moving towards the positive real axis value indicating reduction in damping.

The identified parameter as given in Table 4.3 are used to build the system matrix as

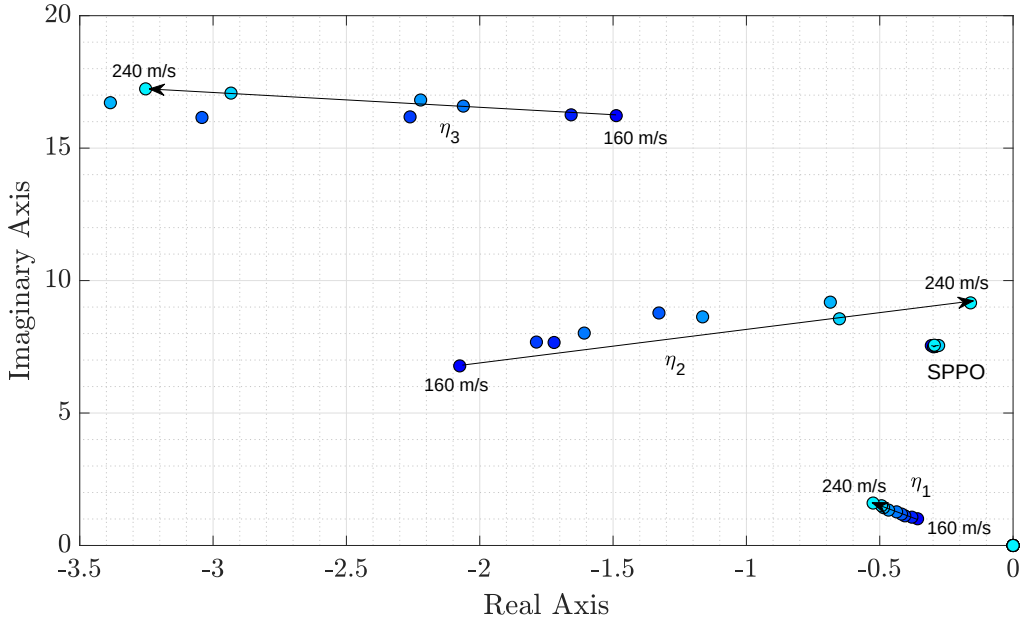

Figure 4.29: Location of system poles (The pole position at (0,0) is due to the relation of $q = \dot{\theta}$).

given in Equation 4.3.14. Here, the **A** matrix is of interest because it contains information of system stability characteristics through its eigenvalues and eigenvectors, defined as:

$$\begin{aligned} \det\left(\mathbf{A} - \lambda_i I\right) &= 0 \\ \left(\mathbf{A} - \lambda_i I\right)\Phi_i &= 0 \end{aligned} \tag{4.3.21}$$

where λ_i is the eigenvalue (pole location) and Φ_i is the eigenvector of the system. The eigenvalue usually consists of a real and imaginary number, thus the natural frequency ω_i and damping ratio ζ_i can be extracted as follows:

$$\lambda_i = \mathrm{a} + \mathrm{b}i$$

$$\omega_i = |\lambda_i| = \sqrt{\mathrm{a}^2 + \mathrm{b}^2} \tag{4.3.22}$$

$$\zeta_i = -\cos(< \lambda_i) = \frac{-\mathrm{a}}{|\lambda_i|} \tag{4.3.23}$$

However, the identified value inside the matrix **A** should also consider the parameter uncertainty bounds. These uncertainty bounds should be considered to calculate the uncertainty of the identified damping and frequency, which shows the quality of the resulting identified model parameter. A previous study of calculating the uncertainty bounds in frequency and damping for frequency domain identification is given in Reference [103]. In this work, the uncertainty bounds based on time domain identification will be calculated using delta method. This method is an adaptation of work by Döhler et al. [193] which derive uncertainty bounds for identified modal frequency and damping based on subspace identification methods applied to discrete systems. In this case, the delta method is used to characterise the uncertainty bounds of the eigenvalue of a continuous system based on the uncertain parameters need to build the matrix **A**.

Considering a vector of identified variables as $f(\hat{\theta})$, the delta methods suggest that the covariance of $f(\hat{\theta})$ can be approximated by [193]:

$$\text{cov}\left(f(\hat{\theta})\right) \approx J_f \text{cov}(\hat{\theta}) J_f^T \tag{4.3.24}$$

in which J_f is the sensitivity matrix given as the first derivatives of the $f(\hat{\theta})$.

Let us begin by considering the sensitivity of the system modal frequency and damping. Given these are a function of the real and imaginary components of the corresponding eigenvalue, the sensitivity with respect to the real and imaginary components can be expressed as follows:

$$\frac{\delta\omega}{\delta \text{a}} = \frac{\text{a}}{|\lambda_i|} \quad ; \quad \frac{\delta\omega}{\delta \text{b}} = \frac{\text{b}}{|\lambda_i|} \tag{4.3.25}$$

$$\frac{\delta\zeta}{\delta \text{a}} = \frac{-\text{b}^2}{(|\lambda_i|)^3} \quad ; \quad \frac{\delta\zeta}{\delta \text{b}} = \frac{\text{ab}}{(|\lambda_i|)^3} \tag{4.3.26}$$

or in matrix form, this can be expressed as:

$$\begin{bmatrix} J_{\omega_i,\lambda_i} \\ J_{\zeta_i,\lambda_i} \end{bmatrix} = \frac{1}{|\lambda_i|^3} \begin{bmatrix} |\lambda_i|^2 & 0 \\ 0 & 1 \end{bmatrix} \begin{bmatrix} \text{Re}(\lambda_i) & \text{Im}(\lambda_i) \\ -\text{Im}(\lambda_i)^2 & \text{Re}(\lambda_i)\text{Im}(\lambda_i) \end{bmatrix} \tag{4.3.27}$$

in which J_{ω_i,λ_i} is the sensitivity of ω_i to λ_i, while J_{ζ_i,λ_i} is the sensitivity of ζ_i to λ_i. Given, the eigenvalues are functions of the identified $\mathbf{A}$ matrix, let λ_i, Φ_i, and χ_i be i-th eigenvalue, left eigenvector and right eigenvector of $\mathbf{A}$, as follows:

$$\mathbf{A}\Phi_i = \lambda_i \Phi_i, \quad \chi_i^* \mathbf{A} = \lambda_i \chi_i^* \tag{4.3.28}$$

where * denotes the complex-conjugate transpose. Then, the sensitivity of the eigenvalues can be defined as:

$$\Delta\lambda_i = J_{\lambda_{i,\mathbf{A}}} \text{vec}(\Delta\mathbf{A}) \tag{4.3.29}$$

$$\Delta\Phi_i = J_{\Phi_{i,\mathbf{A}}} \text{vec}(\Delta\mathbf{A}) \tag{4.3.30}$$

in which 'vec' is the column-stacking vectorisation operator. Here, we are only interested in the sensitivity of the eigenvalues:

$$J_{\lambda_{i,\mathbf{A}}} = \frac{1}{\chi_i^* \Phi_i} \left(\Phi_i^T \otimes \chi_i^*\right) \tag{4.3.31}$$

where $\otimes$ denotes the Kronecker product. Furthermore, by defining λ_i as the i-th eigenvalue of $\mathbf{A}$, Döhler et al. [193] define the following relationship:

$$\Delta\omega_i = J_{\omega_i,\mathbf{A}} \text{vec}(\Delta\mathbf{A}) \tag{4.3.32}$$

$$\Delta\zeta_i = J_{\zeta_i,\mathbf{A}} \text{vec}(\Delta\mathbf{A}) \tag{4.3.33}$$

where:

$$\begin{bmatrix} J_{\omega_i,\mathbf{A}} \\ J_{\zeta_i,\mathbf{A}} \end{bmatrix} = \begin{bmatrix} J_{\omega_i,\lambda_i} \\ J_{\zeta_i,\lambda_i} \end{bmatrix} \begin{bmatrix} \text{Re}\left(J_{\lambda_i,\mathbf{A}}\right) \\ \text{Im}\left(J_{\lambda_i,\mathbf{A}}\right) \end{bmatrix} \tag{4.3.34}$$

Combining equation 4.3.34 and 4.3.27, the perturbation on frequency and damping as a function of **A** is defined as:

$$\mathrm{cov}\left(\begin{bmatrix}\omega_i\\ \zeta_i\end{bmatrix}\right) = \begin{bmatrix} J_{\omega_i,\mathbf{A}} \\ J_{\zeta_i,\mathbf{A}}\end{bmatrix} \mathrm{cov}(\mathrm{vec}(\mathbf{A})) \begin{bmatrix} J_{\omega_i,\mathbf{A}} \\ J_{\zeta_i,\mathbf{A}}\end{bmatrix}^T \tag{4.3.35}$$

in which the cov(vec(**A**)) is a diagonal matrix of covariances for related parameters. However, the **A** matrix does not only consist of the identified variables but also has known constants of ones and zeros. In this case, these values are included in the calculation in which the respective uncertainties are set to zero.

Based on Equation 4.3.35, the standard deviation of the identified damping and frequency can be calculated from the square root of the diagonal matrix. The damping and frequency based on the identified **A** matrix, as well as the variance of the identified damping and frequency, is given in Table 4.4. Moreover, Figure 4.30 and 4.31 show the changes in the modal frequencies and dampings as a function of the airspeed.

Frequency	Values and relatives standard deviation								
	160 m/s	170 m/s	180 m/s	190 m/s	200 m/s	210 m/s	220 m/s	230 m/s	240 m/s
mode 1	7.046	7.795	7.929	8.787	8.115	8.627	9.215	7.431	7.552
	(0.138)	(0.142)	(0.237)	(0.229)	(0.226)	(0.280)	(0.201)	(0.053)	(0.054)
mode 2	7.546	7.486	7.464	7.494	7.456	7.442	7.572	8.283	9.170
	(0.014)	(0.022)	(0.025)	(0.025)	(0.027)	(0.036)	(0.026)	(0.471)	(0.302)
mode 3	16.392	16.422	16.384	16.436	16.809	17.091	17.066	17.367	17.677
	(0.127)	(0.116)	(0.166)	(0.287)	(0.144)	(0.186)	(0.282)	(0.269)	(0.384)
Damping	Values and relatives standard deviation								
Ratio	160 m/s	170 m/s	180 m/s	190 m/s	200 m/s	210 m/s	220 m/s	230 m/s	240 m/s
mode 1	0.311	0.254	0.259	0.182	0.226	0.184	0.048	0.046	0.036
	(0.025)	(0.023)	(0.026)	(0.024)	(0.023)	(0.024)	(0.023)	(0.014)	(0.004)
mode 2	0.040	0.037	0.038	0.038	0.039	0.039	0.030	0.116	0.022
	(0.012)	(0.003)	(0.004)	(0.003)	(0.004)	(0.005)	(0.003)	(0.035)	(0.058)
mode 3	0.086	0.094	0.126	0.170	0.108	0.112	0.179	0.143	0.177
	(0.008)	(0.008)	(0.010)	(0.016)	(0.010)	(0.011)	(0.013)	(0.012)	(0.019)

Table 4.4: Identified modal parameters as a function of velocity.

As expected the aeroelastic frequency of interest is around the structural frequency (especially at the lower airspeed). As presented in Table 4.4, the identified aeroelastic frequency for mode 1 and mode 2 is quite close, which is in line with the structural mode at zero velocity at 7.31 and 7.8 rad/s respectively. However, behaviour of the aerodynamic forces are expected to change and so affect the aeroelastic modes. Overall, the figures show that the confidence interval of the identified frequency is less significant than the confidence interval of the identified damping. Furthermore, the damping of the modes exhibits significant variations to change in airspeed.

One of the many challenges in presenting the results is to define the identified frequency and damping of the modes and relate it to the particular modal characteristics. Here, the eigenvector has an important role. The MAC as elaborated previously in Chapter 3.3 has been utilised to track the change in the eigenvector for the respected eigenvalue. The eigenvector at a particular airspeed is compared to those at the lowest airspeed and compared with those with the highest MAC.

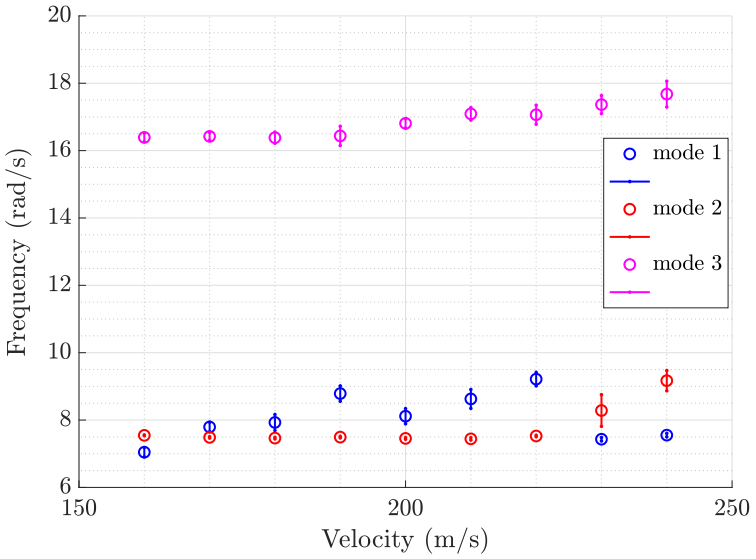

Figure 4.30: Frequency of the identified aeroelastic mode.

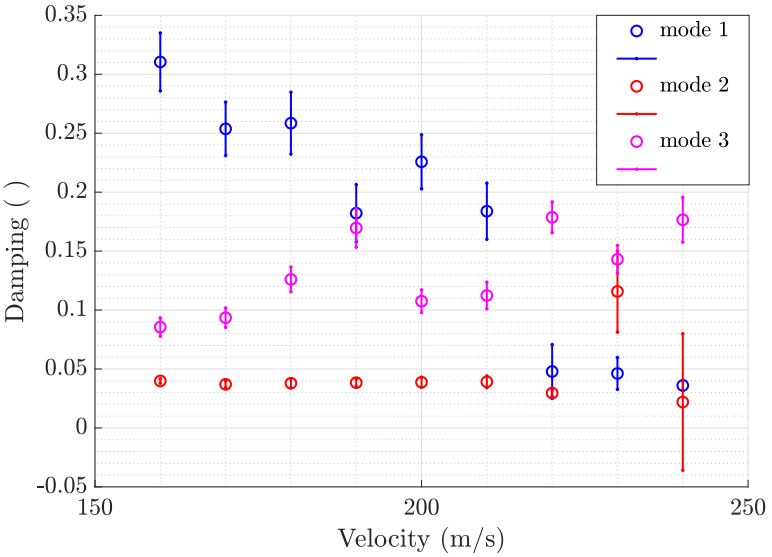

Figure 4.31: Damping of the identified aeroelastic mode.

Figure 4.31 clearly shows that the uncertainties in the identified modal parameters of mode 2 and 3, are increasing as airspeed increases. Furthermore, mode 1 has a higher uncertainty in the identified modal characteristics compared to the other modes. Despite the high uncertainty in the identified damping characteristics mode 1 has a higher damping ratio compared to mode 2. However, it is of interest to observe the change of damping as well as its confidence interval. From Figure 4.31 it can be seen that there is a possibility of negative damping for mode two at the speed of 240 m/s, which can be an indication of instability and flutter.

4.4 Summary

An aeroservoelastic simulation framework has been used with various parameter estimation methods to extract aerodynamic and aeroelastic derivatives. The first study illustrates a method for quantifying the effects of wing flexibility on flight dynamics using the simple OLS method. The resulting model can easily be implemented in flight simulators and used for assessing handling qualities. However, this method provides little insight into the structural dynamics of the airframe which is needed for identifying aeroelastic phenomena such as flutter. This limitation was addressed by adopting the output error approach for identifying flutter margins using the same flexible aeroservoelastic simulation model. Furthermore, the delta method was used for calculating the uncertainty bounds on the estimated model characteristics as a function of airspeed and therefore, providing conservative flutter speeds. The following chapter now moves away from system identification and focuses on dynamic scaling methods for developing subscale models suited to dynamic testing.

This page is intentionally left blank.

CHAPTER 5

Similitude and Dimensional Analysis

In developing a subscale model, it is essential to understand the concept of similitude. This concept is used to relate the measurements from one system to describe the behaviour of another similar system [46]; the application of similitude through the use of non-dimensional numbers is known as dimensional analysis. The concept of dimensional analysis comes from Greek concepts of geometric similarity, ratio and proportion [44]. Depending on the observations of interest, similitude requirements can be of geometric, kinematic and dynamic similarity. The concept of similitude is essential in designing the subscale model to ensure that the model can represent the full-scale dynamics.

5.1 Buckingham Π Theorem

The underlying principle of dimensional analysis is captured within the Buckingham Π theorem. It states that "*any complete physical relationship can be represented as one subsisting between a set of independent non-dimensional product combinations of the measures of the physical quantities concerned*" [43]. This theory shows that the full model of n dimensional parameters can be expressed as a combination of k measures of physical quantities (known as repeating variables) and therefore, there are $(n - k)$ non-dimensional quantities. This theorem is based on dimensional homogeneity, that is that the dimensions of the left-hand and right-hand sides of an equation should be the same. The proof of this theorem is beyond the scope of this thesis, however, the reader is referred to References [43, 44] for an in depth discussion and detailed mathematical derivations.

When applying this theorem, the standard basic dimensions are those of mass, length and time; denoted as $\mathcal{M}$, $\mathcal{L}$ and $\mathcal{T}$ respectively. Its application can be summarised as follows [46]:

- List all the dimensional parameters (n) that are involved in the problem and express them in basic dimensions.

- Select the repeating variables (k). The number of these variables needs to be equal to the number of the reference dimensions. The combination of the repeating variables should be able to represent the reference dimension ($\mathcal{M}$, $\mathcal{L}$ and $\mathcal{T}$).

- Form the Π terms of the non-repeating variables ($n - k$) by the product of the repeating variables.

In a scenario where not all of the similarity requirements are satisfied, the model is then called the distorted model. Distorted models are common in experimental testing due to the limitations of test facilities. A classic example is when Reynolds and Froude numbers are involved [46]. The distorted model is still useful although the interpretation of the model is more difficult. As mentioned by George E.P. Box, "*all models are wrong, but some are useful*".

5.2 Test Case : 2-DoF Aeroelastic Model

In this section, the principle of similitude is applied to a two DoF non-linear aeroelastic model to evaluate the implications of scaling factors on physical and dynamic properties.

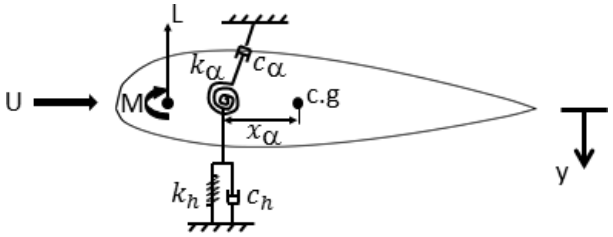

Figure 5.1: Two DoF aeroelastic system.

The 2-DoF aeroelastic model of interest is presented in Figure 5.1. This model is free to pitch and plunge through a spring-damper configuration with aerodynamic lift force and pitching moment acting as the external drivers. Here, positive plunge is moving downwards, in the opposite direction of the lift force, while positive pitch angle is in the same direction as the positive pitching moment. An adaptation of the non-linear 2-DoF aeroelastic equation of motions from References [58, 194] is used to assess the scaling methodology and evaluate the cause and effect of a distorted model. Wan and Cesnik stated that a linear scaling factor is applicable for a non-linear model[1] [66]. Thus, an attempt to scale down the 2-DoF non-linear model has been made, however, when it comes to assessing the distorted model effect, non-linearity adds extra complexity, especially when investigating the relationship between the system states.

Here, a 2-DoF linear model is developed based on the aforementioned non-linear aeroelastic equation of motion. Furthermore, to observe the importance of a constant term in the non-dimensionalisation process, a gravitational force has been added to the equation.

[1]The non-linear model of interest in Reference [66] contains geometric non-linearity, where the stiffness of the structure changes depending on its deformation. This case is similar to the 2-DoF aeroelastic model, in which the stiffness is dependent on the α value.

By having the added terms and the modification, the equations of motion representing the 2-DoF model can be expressed as follows:

$$\begin{bmatrix} m & mx_\alpha c_{1/2} \\ mx_\alpha c_{1/2} & I_\alpha \end{bmatrix} \begin{bmatrix} \ddot{h} \\ \ddot{\alpha} \end{bmatrix} + \begin{bmatrix} c_h & 0 \\ 0 & c_\alpha \end{bmatrix} \begin{bmatrix} \dot{h} \\ \dot{\alpha} \end{bmatrix} + \begin{bmatrix} k_h & 0 \\ 0 & k_\alpha \end{bmatrix} \begin{bmatrix} h \\ \alpha \end{bmatrix} = \begin{bmatrix} -L \\ M \end{bmatrix} + \begin{bmatrix} mg \\ 0 \end{bmatrix} \tag{5.2.1}$$

in which h represents the plunge motion and α represents the pitching motion, while L and M are the aerodynamic force and moment respectively. Note that this model was developed for a two dimensional aerofoil with unit span. Therefore, the wing area can be simplified to $S \simeq 2c_{1/2}$. Hence, the aerodynamic force and moment can be defined as:

$$L = \rho U^2 c_{1/2} C_{L_\alpha} \left[\alpha + \frac{\dot{h}}{U} + \left(\frac{1}{2} - a \right) c_{1/2} \frac{\dot{\alpha}}{U} \right] + \rho U^2 c_{1/2} C_{L_\beta} \beta \tag{5.2.2}$$

$$M = \rho U^2 c_{1/2}^2 C_{M_\alpha} \left[\alpha + \frac{\dot{h}}{U} + \left(\frac{1}{2} - a \right) c_{1/2} \frac{\dot{\alpha}}{U} \right] + \rho U^2 c_{1/2}^2 C_{M_\beta} \beta \tag{5.2.3}$$

where a is the length between elastic axis to midchord positive towards leading edge as percentage of the half chord length ($c_{1/2}$). Other system parameters are presented in Table 5.1.

Parameter	Value	Units	Description
$c_{1/2}$	0.135	m	Semi chord
m	12.3870	kg	Wing mass
I_α	0.065	kg.m^2	Mass moment of inertia about elastic axis
x_α	0.2467	-	Normalized to $c_{1/2}$
a	-0.6	-	Distance from mid chord to elastic axis, normalized to $c_{1/2}$
ρ	1.225	kg/m^3	Air density
b	1	m	Wing span
C_{L_α}	2π	/rad	Aerofoil lift coefficient due to α
k_h	1422.2	N/m	Stiffness coefficient for plunging motion
k_α	282	N/s^2	Torsional stiffness
C_{L_β}	3.358	/rad	Lift coefficient in respect to control surface deflection
c_h	82.29	N.s/m	Damping coefficient for plunging motion
c_α	3.6	N.s/rad	Damping coefficient for pitching motion
C_{M_α}	-0.6280	/rad	Aerofoil moment coefficient
C_{M_β}	-0.6350	/rad	Moment coefficient due to control surface deflection
U	20	m/s	Wind speed

Table 5.1: System parameters and definition.

5.2.1 Scaling Requirements

Scaling requirements must be defined and the parameters of interest need to be identified when defining the similitude relation. Based on Equation 5.2.1, the parameters of interest

and corresponding dimension are as follows:

$$\begin{array}{llll} m \doteq \mathcal{M} & I_\alpha \doteq \mathcal{ML}^2 & c_h \doteq \mathcal{MT}^{-1} & c_\alpha \doteq \mathcal{ML}^2\mathcal{T}^{-1} \\ k_h \doteq \mathcal{MT}^{-2} & k_\alpha \doteq \mathcal{ML}^2\mathcal{T}^{-2} & L \doteq \mathcal{MLT}^{-2} & M \doteq \mathcal{ML}^2\mathcal{T}^{-2} \\ \dot{\alpha} \doteq \mathcal{T}^{-1} & \ddot{\alpha} \doteq \mathcal{T}^{-2} & \mu \doteq \mathcal{MLT}^{-1} & g \doteq \mathcal{LT}^{-2} \\ c_{1/2} \doteq \mathcal{L} & \rho \doteq \mathcal{ML}^3 & U \doteq \mathcal{MT}^{-1} & \end{array} \tag{5.2.4}$$

There are 15 dimensional parameters ($n = 15$) and three repeating variables ($k = 3$) which results in 12 non-dimensional quantities. Furthermore, it is preferable to choose the repeating variables that are easy to control. In the case of wind tunnel experiments, the maximum allowable size, velocity and air density are dictated by the wind tunnel facility. Therefore, $c_{1/2}$, U and ρ are chosen as the repeating variables, that represent the geometric size, velocity and air density. This relation gives the non-dimensional unit as:

$$\Pi_1 = \Pi_1\left(m, \rho, U, c_{1/2}\right); \qquad \mathcal{M}^0\mathcal{L}^0\mathcal{T}^0 = \mathcal{M}\left(\frac{\mathcal{M}}{\mathcal{L}^3}\right)^a\left(\frac{\mathcal{L}}{\mathcal{T}}\right)^b(\mathcal{L})^c$$

$$\Pi_1 = \frac{m}{\rho c_{1/2}^3} \tag{5.2.5}$$

Applying the above terms to other variables leads to:

$$\Pi_2 = \Pi_2\left(I_\alpha, \rho, U, c_{1/2}\right) = \frac{I_\alpha}{\rho c_{1/2}^5} \tag{5.2.6}$$

$$\Pi_3 = \Pi_3\left(c_h, \rho, U, c_{1/2}\right) = \frac{c_h}{\rho U c_{1/2}^2} \tag{5.2.7}$$

$$\Pi_4 = \Pi_4\left(c_\alpha, \rho, U, c_{1/2}\right) = \frac{c_\alpha}{\rho U c_{1/2}^4} \tag{5.2.8}$$

$$\Pi_5 = \Pi_5\left(k_h, \rho, U, c_{1/2}\right) = \frac{k_h}{\rho U^2 c_{1/2}} \tag{5.2.9}$$

$$\Pi_6 = \Pi_6\left(k_\alpha, \rho, U, c_{1/2}\right) = \frac{k_\alpha}{\rho U^2 c_{1/2}^3} \tag{5.2.10}$$

$$\Pi_7 = \Pi_7\left(L, \rho, U, c_{1/2}\right) = \frac{L}{\rho U^2 c_{1/2}^2} \tag{5.2.11}$$

$$\Pi_8 = \Pi_8\left(M, \rho, U, c_{1/2}\right) = \frac{M}{\rho U^2 c_{1/2}^3} \tag{5.2.12}$$

$$\Pi_9 = \Pi_9\left(\dot{\alpha}, \rho, U, c_{1/2}\right) = \frac{\dot{\alpha} c_{1/2}}{U} \tag{5.2.13}$$

$$\Pi_{10} = \Pi_{10}\left(\ddot{\alpha}, \rho, U, c_{1/2}\right) = \frac{\ddot{\alpha} c_{1/2}^2}{U} \tag{5.2.14}$$

$$\Pi_{11} = \Pi_{11}\left(g, \rho, U, c_{1/2}\right) = \frac{g c_{1/2}}{U^2} \tag{5.2.15}$$

$$\Pi_{12} = \Pi_{12}\left(\mu, \rho, U, c_{1/2}\right) = \frac{\mu}{\rho U c_{1/2}} \tag{5.2.16}$$

The list of the scaling variables point towards the non-dimensional parameters that must be considered to ensure that an experiment on a subscale model can represent the full

scale behaviour. These variables are common in the subscale model development. Π_1 and Π_2 are known as the mass and inertia ratio, and Π_5 and Π_6 are the stiffness similarities that represent bending and torsional stiffness respectively. On the other hand, the aerodynamic force and moment coefficients are represented by Π_7 and Π_8, while Π_9 and Π_{10} represent the dependency on time. Π_9 is also known as the reduced frequency.

However, the non-dimensional damping terms as given by Π_3 and Π_4 are not typical for structural scaling. The reason behind this is because most scaling laws for an aeroelastic system do not consider structural damping in the equations of motion [65, 66, 71], or model it as functions of mass and stiffness matrices, for example the Rayleigh damping formulation [50]. Damping coefficient is a characteristic of the material being used. Therefore, the scaling laws of material damping relate to the material properties and the level of excitation [195]. Nevertheless, the test case presented in this subchapter is a theoretical model with a constant damping value that emphasises the need for considering the Π term for structural damping. Furthermore, Π_{11} is also known as the Froude number and it is important when gravity effects need to be accounted. Π_{12} represents the Reynolds number, which accounts for essential viscous effects. The fact that viscosity does not appear in the equations of motion (Equation 5.2.1) may be a reason for a distorted model [196].

5.2.2 Non-dimensional Equations of Motion

Even though the idea of developing scaling requirements is simple, the practical application becomes somewhat complicated. Say that the subscale model has been through experimental testing, the question is then how to relate the results with the full scale model. More importantly, how to be sure that the subscale model theoretically represents the full scale model. To overcome this issue, non-dimensional equations of motion are developed and used. Consider the equation of motion as presented in Equation 5.2.1 and then substitute Equation 5.2.3 into Equation 5.2.1. This yields:

$$\begin{bmatrix} m & mx_\alpha c_{1/2} \\ mx_\alpha c_{1/2} & I_\alpha \end{bmatrix} \begin{bmatrix} \ddot{h} \\ \ddot{\alpha} \end{bmatrix} + \begin{bmatrix} c_h & 0 \\ 0 & c_\alpha \end{bmatrix} \begin{bmatrix} \dot{h} \\ \dot{\alpha} \end{bmatrix} + \begin{bmatrix} k_h & 0 \\ 0 & k_\alpha \end{bmatrix} \begin{bmatrix} h \\ \alpha \end{bmatrix} = \begin{bmatrix} L_{\dot{h}} & L_{\dot{\alpha}} \\ M_{\dot{h}} & M_{\dot{\alpha}} \end{bmatrix} \begin{bmatrix} \dot{h} \\ \dot{\alpha} \end{bmatrix} + \begin{bmatrix} 0 & L_\alpha \\ 0 & M_\alpha \end{bmatrix} \begin{bmatrix} h \\ \alpha \end{bmatrix} + \begin{bmatrix} L_\beta \\ M_\beta \end{bmatrix} \begin{bmatrix} \beta \end{bmatrix} + \begin{bmatrix} mg \\ 0 \end{bmatrix} \tag{5.2.17}$$

where

$$L_{\dot{h}} = -\rho U c_{1/2} C_{L_\alpha} \tag{5.2.18}$$
$$L_{\dot{\alpha}} = -\rho U c_{1/2}^2 C_{L_{\dot{\alpha}}} \tag{5.2.19}$$
$$M_{\dot{h}} = \rho U c_{1/2}^2 C_{M_\alpha} \tag{5.2.20}$$
$$M_{\dot{\alpha}} = \rho U c_{1/2}^3 C_{M_{\dot{\alpha}}} \tag{5.2.21}$$
$$L_\alpha = -\rho U^2 c_{1/2} C_{L_\alpha} \tag{5.2.22}$$
$$M_\alpha = \rho U^2 c_{1/2}^2 C_{M_\alpha} \tag{5.2.23}$$
$$L_\beta = -\rho U^2 c_{1/2} C_{L_\beta} \tag{5.2.24}$$
$$M_\beta = \rho U^2 c_{1/2}^2 C_{M_\beta} \tag{5.2.25}$$

and

$$C_{L_{\dot{\alpha}}} = C_{L_\alpha}\left(\tfrac{1}{2} - a\right) \tag{5.2.26}$$

$$C_{M_{\dot{\alpha}}} = C_{M_\alpha}\left(\tfrac{1}{2} - a\right) \tag{5.2.27}$$

The adoption of the scaling methodology from Reference [69], shows that the state vector needs to be non-dimensionalised by half of the chord ($c_{1/2}$) using the following relationship:

$$\left\{ \begin{array}{c} \ddot{h} \\ \ddot{\alpha} \end{array} \right\} = \left[\begin{array}{cc} c_{1/2} & 0 \\ 0 & 1 \end{array} \right] \left\{ \begin{array}{c} \ddot{h}/c_{1/2} \\ \ddot{\alpha} \end{array} \right\} \tag{5.2.28}$$

Now defining:

$$T = \left[\begin{array}{cc} c_{1/2} & 0 \\ 0 & 1 \end{array} \right] \tag{5.2.29}$$

the coefficient matrix can be uniformly dimensionalised by pre-multiplying the Equation 5.2.25 by $\mathbf{T^T}$ such that:

$$\begin{gathered} \left[\begin{array}{cc} mc_{1/2}^2 & mx_\alpha c_{1/2}^2 \\ mx_\alpha c_{1/2}^2 & I_\alpha \end{array} \right] \left[\begin{array}{c} \ddot{h}/c_{1/2} \\ \ddot{\alpha} \end{array} \right] + \left[\begin{array}{cc} c_h c_{1/2}^2 & 0 \\ 0 & c_\alpha \end{array} \right] \left[\begin{array}{c} \dot{h}/c_{1/2} \\ \dot{\alpha} \end{array} \right] + \left[\begin{array}{cc} k_h c_{1/2}^2 & 0 \\ 0 & k_\alpha \end{array} \right] \left[\begin{array}{c} h/c_{1/2} \\ \alpha \end{array} \right] = \\ \left[\begin{array}{cc} L_{\dot{h}} c_{1/2}^2 & L_{\dot{\alpha}} c_{1/2} \\ M_{\dot{h}} c_{1/2} & M_{\dot{\alpha}} \end{array} \right] \left[\begin{array}{c} \dot{h}/c_{1/2} \\ \dot{\alpha} \end{array} \right] + \left[\begin{array}{cc} 0 & L_\alpha c_{1/2} \\ 0 & M_\alpha \end{array} \right] \left[\begin{array}{c} h/c_{1/2} \\ \alpha \end{array} \right] + \left[\begin{array}{c} L_\beta c_{1/2} \\ M_\beta \end{array} \right] \left[\begin{array}{c} \beta \end{array} \right] + \left[\begin{array}{c} mgc_{1/2} \\ 0 \end{array} \right] \end{gathered} \tag{5.2.30}$$

Notice that now the coefficient matrices have a single unit of kgm^2. Substitution of Equation 5.2.25 into 5.2.30, and dividing by $mc_{1/2}^2$ results in:

$$\begin{gathered} \left[\begin{array}{cc} 1 & x_\alpha \\ x_\alpha & \dfrac{I_\alpha}{mc_{1/2}^2} \end{array} \right] \left[\begin{array}{c} \ddot{h}/c_{1/2} \\ \ddot{\alpha} \end{array} \right] + \left[\begin{array}{cc} \dfrac{c_h}{m} & 0 \\ 0 & \dfrac{c_\alpha}{mc_{1/2}^2} \end{array} \right] \left[\begin{array}{c} \dot{h}/c_{1/2} \\ \dot{\alpha} \end{array} \right] + \left[\begin{array}{cc} \dfrac{k_h}{m} & 0 \\ 0 & \dfrac{k_\alpha}{mc_{1/2}^2} \end{array} \right] \left[\begin{array}{c} h/c_{1/2} \\ \alpha \end{array} \right] = \\ \frac{\rho U^2 c_{1/2}^2}{mc_{1/2}^2} \left(\left[\begin{array}{cc} \dfrac{c_{1/2}}{U} C_{L_\alpha} & \dfrac{c_{1/2}}{U} C_{L_{\dot{\alpha}}} \\ \dfrac{c_{1/2}}{U} C_{M_\alpha} & \dfrac{c_{1/2}}{U} C_{M_{\dot{\alpha}}} \end{array} \right] \left[\begin{array}{c} \dot{h}/c_{1/2} \\ \dot{\alpha} \end{array} \right] + \left[\begin{array}{cc} 0 & C_{L_\alpha} \\ 0 & C_{M_\alpha} \end{array} \right] \left[\begin{array}{c} h/c_{1/2} \\ \alpha \end{array} \right] + \left[\begin{array}{c} C_{L_\beta} \\ C_{M_\beta} \end{array} \right] \left[\begin{array}{c} \beta \end{array} \right] \right) + \left[\begin{array}{c} g/c_{1/2} \\ 0 \end{array} \right] \end{gathered} \tag{5.2.31}$$

Π_9 and Π_{10} represent the time dependency of the system dynamics. This emphasizes the need to look at the system in non-dimensional time. On the other hand, the natural frequency of the plunge motion ω_h can be defined from the relation between the stiffness and mass as follows:

$$\omega_h^2 = \frac{k_h}{m} \tag{5.2.32}$$

Furthermore, by defining the non-dimensional time as $\tau = \omega_h t$, the dynamics with respect to the non-dimensional time can be expressed as:

$$\mathring{x} = \frac{dx}{d\tau} = \frac{dx}{d(\omega_h t)} = \frac{1}{\omega_h}\frac{dx}{dt} = \frac{1}{\omega_h}\dot{x} \tag{5.2.33}$$

$$\mathring{\dot{x}} = \frac{d^2x}{d\tau^2} = \frac{dxdx}{d(\omega_h t)d(\omega_h t)} = \frac{1}{\omega_h^2}\frac{d^2x}{dt^2} = \frac{1}{\omega_h^2}\ddot{x} \tag{5.2.34}$$

Substituting the non-dimensional time into Equation 5.2.31 and division by ω_h^2 leads to:

$$\begin{bmatrix} 1 & x_\alpha \\ x_\alpha & \dfrac{I_\alpha}{mc_{1/2}^2} \end{bmatrix} \begin{bmatrix} \mathring{\dot{h}}/c_{1/2} \\ \mathring{\dot{\alpha}} \end{bmatrix} + \begin{bmatrix} \tilde{c}_h & 0 \\ 0 & \tilde{c}_\alpha \end{bmatrix} \begin{bmatrix} \mathring{h}/c_{1/2} \\ \mathring{\alpha} \end{bmatrix} + \begin{bmatrix} 1 & 0 \\ 0 & \tilde{k}_\alpha(\alpha) \end{bmatrix} \begin{bmatrix} h/c_{1/2} \\ \alpha \end{bmatrix} =$$

$$\frac{\rho U^2 c_{1/2}^2}{mc_{1/2}^2\omega_h^2} \left(\begin{bmatrix} \dfrac{c_{1/2}}{U}C_{L_\alpha}\omega_h & \dfrac{c_{1/2}}{U}C_{L_{\dot{\alpha}}}\omega_h \\ \dfrac{c_{1/2}}{U}C_{M_\alpha}\omega_h & \dfrac{c_{1/2}}{U}C_{M_{\dot{\alpha}}}\omega_h \end{bmatrix} \begin{bmatrix} \mathring{h}/c_{1/2} \\ \mathring{\alpha} \end{bmatrix} + \begin{bmatrix} 0 & C_{L_\alpha} \\ 0 & C_{M_\alpha} \end{bmatrix} \begin{bmatrix} h/c_{1/2} \\ \alpha \end{bmatrix} + \begin{bmatrix} C_{L_\beta} \\ C_{M_\beta} \end{bmatrix} \begin{bmatrix} \beta \end{bmatrix} \right) \tag{5.2.35}$$

$$+ \begin{bmatrix} g/c_{1/2}\omega_h^2 \\ 0 \end{bmatrix}$$

where

$$\tilde{c}_h = \frac{c_h}{k_h}\omega_h \tag{5.2.36}$$

$$\tilde{c}_\alpha = \frac{c_\alpha}{k_h c_{1/2}^2}\omega_h \tag{5.2.37}$$

$$\tilde{k}_\alpha(\alpha) = \frac{k_\alpha}{k_h c_{1/2}^2} \tag{5.2.38}$$

Introducing the Π relation as defined earlier, as

$$\Pi_1 = \frac{\rho c_{1/2}^3}{m} \tag{5.2.39}$$

$$\Pi_9 = \frac{\omega_h c_{1/2}}{U} \tag{5.2.40}$$

The constant on the right hand side of the equation, can be rearranged as:

$$\frac{\rho U^2 c_{1/2}^2}{mc_{1/2}^2\omega_h^2} = \frac{\rho c_{1/2}^2}{m}\frac{U^2}{c_{1/2}^2\omega_h^2} \tag{5.2.41}$$

$$\frac{g}{c_{1/2}\omega_h^2} = \frac{gc_{1/2}^2}{c_{1/2}U^2}\frac{U^2}{c_{1/2}^2\omega_h^2} \tag{5.2.42}$$

Note that in this case, a two dimensional aerofoil is being considered where the span is assumed to be 1 unit length. Thus, the wing surface area S, which used to build the non-dimensional aerodynamic coefficient is now consider as $2c_{1/2}$. Therefore, the term $\dfrac{\rho c_{1/2}^2}{m}$ is having a dimension of $\dfrac{\rho c_{1/2}^2 b}{m}$, in which b is the wingspan and considered as 1. Thus,

$\frac{\rho c_{1/2}^2}{m} \simeq \Pi_1$, and Equation 5.2.36 can be rearranged into[2]:

$$\begin{bmatrix} 1 & x_\alpha \\ x_\alpha & \frac{I_\alpha}{mc_{1/2}^2} \end{bmatrix} \begin{bmatrix} \mathring{\circ}h/c_{1/2} \\ \mathring{\circ}\alpha \end{bmatrix} + \begin{bmatrix} \tilde{c}_h & 0 \\ 0 & \tilde{c}_\alpha \end{bmatrix} \begin{bmatrix} \mathring{h}/c_{1/2} \\ \mathring{\alpha} \end{bmatrix} + \begin{bmatrix} 1 & 0 \\ 0 & \tilde{k}_\alpha(\alpha) \end{bmatrix} \begin{bmatrix} h/c_{1/2} \\ \alpha \end{bmatrix} =$$
$$\frac{\Pi_1}{\Pi_9^2} \left(\begin{bmatrix} C_{L_\alpha}\Pi_9 & C_{L_{\dot\alpha}}\Pi_9 \\ C_{M_\alpha}\Pi_9 & C_{M_{\dot\alpha}}\Pi_9 \end{bmatrix} \begin{bmatrix} \mathring{h}/c_{1/2} \\ \mathring{\alpha} \end{bmatrix} + \begin{bmatrix} 0 & C_{L_\alpha} \\ 0 & C_{M_\alpha} \end{bmatrix} \begin{bmatrix} h/c_{1/2} \\ \alpha \end{bmatrix} + \begin{bmatrix} C_{L_\beta} \\ C_{M_\beta} \end{bmatrix} \begin{bmatrix} \beta \end{bmatrix} \right) + \begin{bmatrix} \Pi_{11}/\Pi_9^2 \\ 0 \end{bmatrix} \tag{5.2.43}$$

Note that the non-dimensional time is not only affected by the dynamic rate but also should be considered for the control surface input. Therefore, the input design must be done considering of τ instead of t, using the relation $\Delta\tau = \omega_h \Delta t$. Furthermore, as Froude number is a requirement, the velocity scaling now is dependent on the geometry scaling ($S_g = S_v^2$).

5.2.3 Scaling Results for 2-DoF Model

Based on the previous discussion of non-dimensional equation of motion, the following subchapter illustrate the usefulness of non-dimensional equations of motion in developing a subscale model. Based on the Π requirements, the relation between the independent and dependent scaling factors is presented in Table 5.2. This table presents three different models:

1. Model A is the baseline model with no scaling of the independent variables parameters (as given in Table 5.1).
2. Model B is the model which has the scaling based on the air density, representing different altitude in the flight envelope.
3. Model C is the model which is four times smaller in geometry with the same Froude number, resulting in a 50% scaling in velocity compared to the baseline.

Figures 5.2 and 5.3 present the time and frequency response comparisons between the three different scaling parameters from similar initial conditions. Figure 5.2 presents the dimensional response while Figure 5.3 presents the non-dimensional response comparison. Figure 5.2 shows that the change in the independent variables regarding the air density (different flight altitude) did not affect the transient dynamics or the steady state response. This fact is in contrast with the intuitive expectation that the steady-state response will be shifted due to the different lift and pitching moment. However, the change in the aerodynamic force is compensated by the change in the structural properties. This shows that one subscale model with a particular structural property can only represent a particular flight condition. However, Model C, which is four times smaller than the actual

[2]The Π theory is based on a non-dimensional analysis, therefore $\frac{\rho c_{1/2}^2}{m} \simeq \frac{m}{\rho c_{1/2}^2} \simeq \Pi_1$.

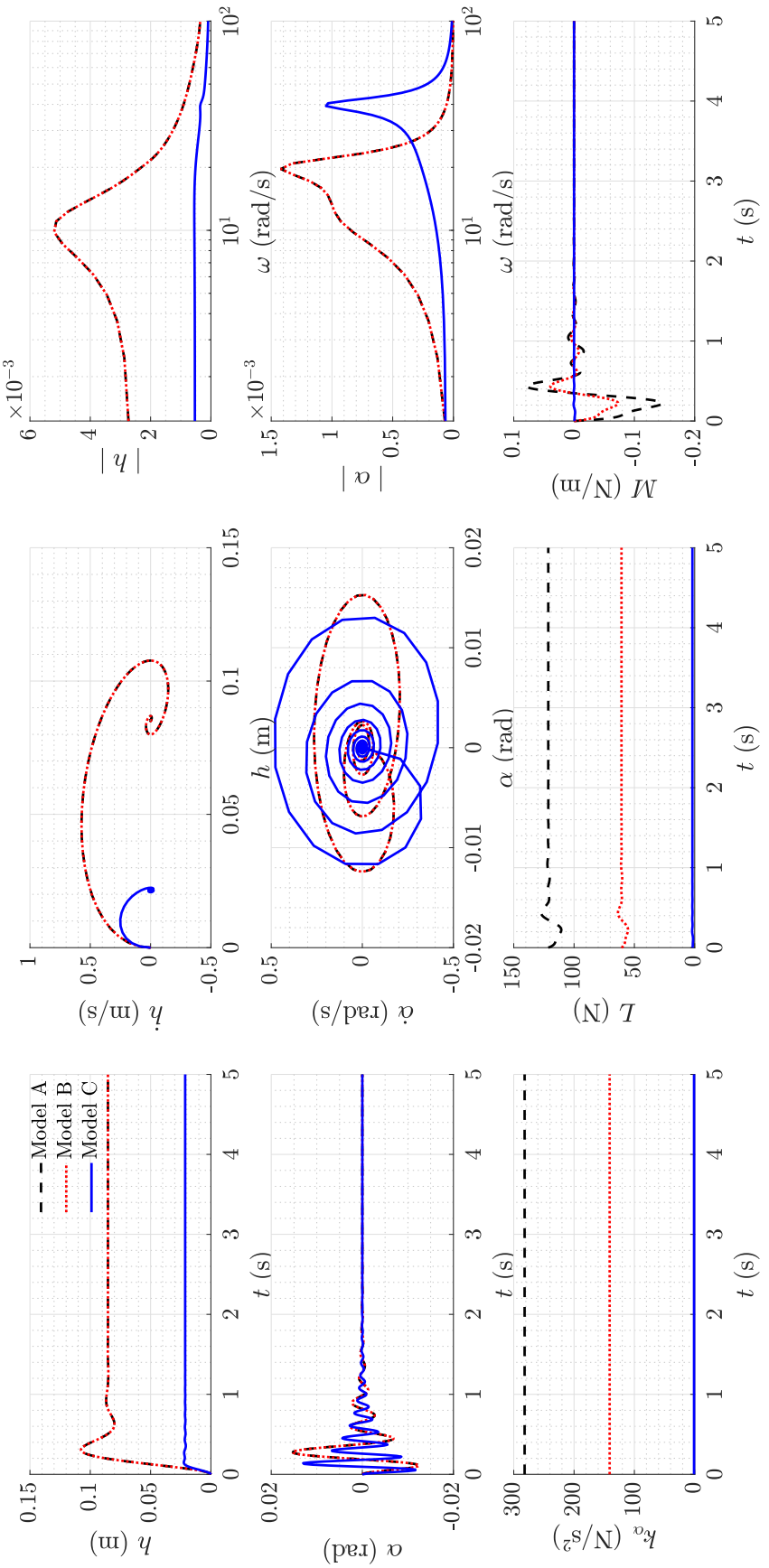

Figure 5.2: Dimensional response comparison for models A, B and C.

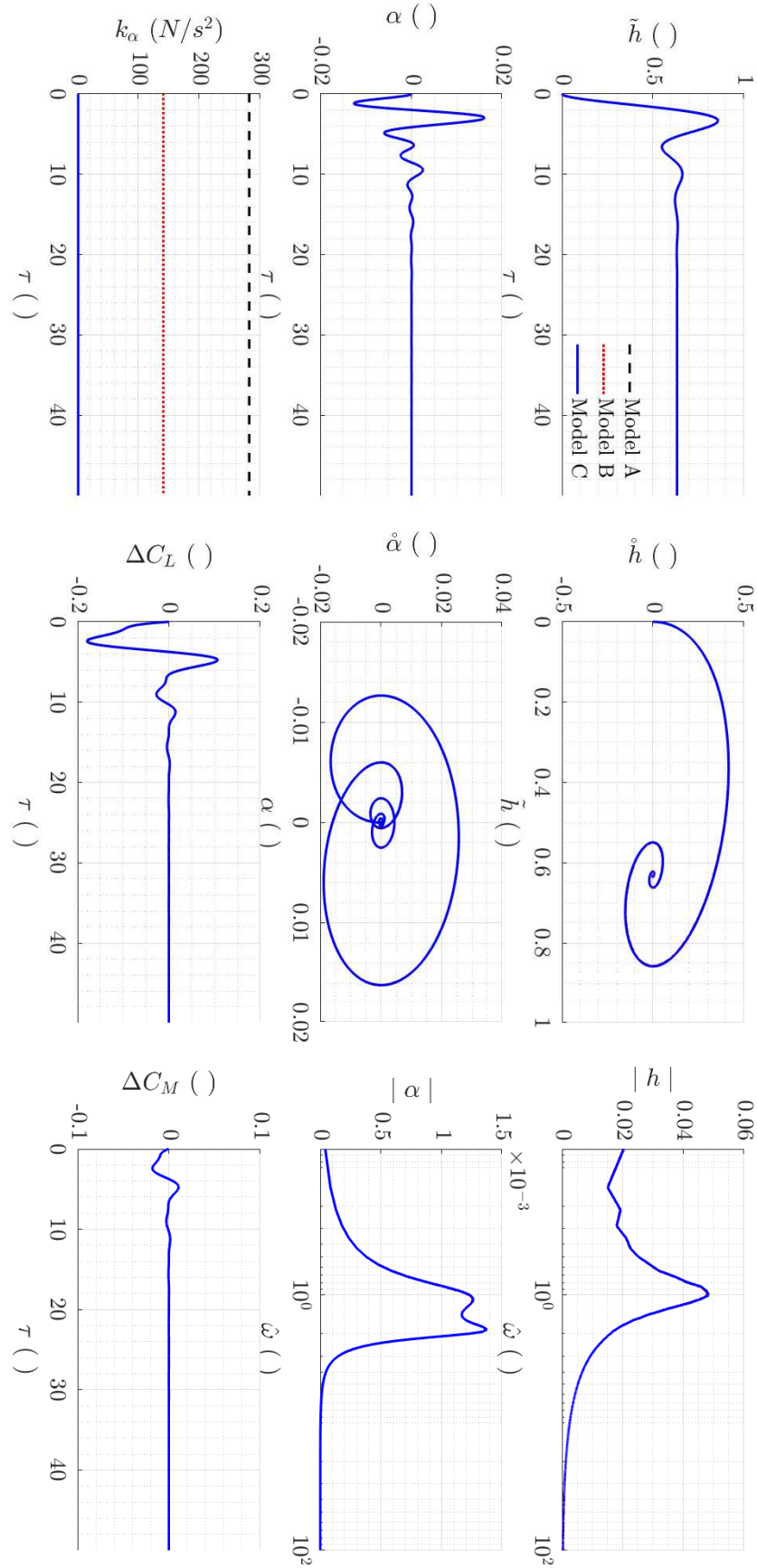

Figure 5.3: Identical non-dimensional responses for models A, B and C.

Scaling factor		Model A	Model B	Model C
Independent scaling factor :				
Geometrical scaling	S_g	1	1	1/4
Velocity scaling	S_U	1	1	1/2
Air Density scaling	S_ρ	1	1/2	1
Dependent scaling factor :				
Mass scaling	Π_1	1	1/2	1/64
Inertia scaling	Π_2	1	1/2	1/1024
Damping scaling	Π_3	1	1/2	1/32
Torsional damping scaling	Π_4	1	1/2	1/512
Bending stiffness scaling	Π_5	1	1/2	1/16
Torsional stiffness scaling	Π_6	1	1/2	1/256
Frequency scaling	Π_9	1	1	2

Table 5.2: Ideal relation between dependent and independent scaling factor.

model and flies at half of the speed, shows differences in both the transient dynamics as well as the steady state response. The difference in the transient dynamics is due to the difference in the frequency; the smaller the size, the higher the frequency response. On the other hand, the difference in the steady-state dynamics is proportional to the size difference which illustrates the different aerodynamic loading.

For the case where there are changes in the transient and steady-state dynamics, the non-dimensional equation of motion is useful. By comparing the response in a non-dimensional terms, it is easier to compare the response of two different models and ensure similitude. For example, in Figures 5.3 it is clear that all responses belong to a similar model even though the frequency response function shows slight differences in the amplitudes. The differences emphasise that the two models are similar but not the same, even considering k_α further emphasises this point.

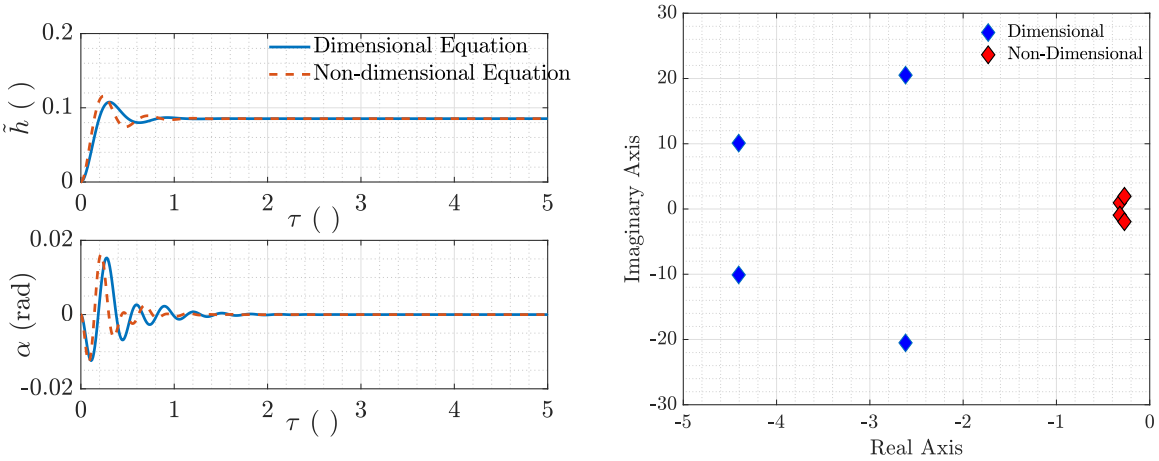

Figure 5.4: Comparison of time response and pole position of dimensional and non-dimensional systems.

It is also interesting to see the comparison of the response from the dimensional equation and the non-dimensional equation in Figure 5.4. Here, the response from the non-dimensional equation is converted using $c_{1/2}$ for the length scale and Π_9 for the time scale.

Both responses present similar steady-state values. However, the transient response is effected by a phase shift and slightly lower damping ratio. Mathematically the source of this comes from the fact that normalising the model with frequency, changes the pole and zero location of the system, which impacts system's damping. The difference in the response also emphasises the fact that some manipulation is needed to relate both dimensional and non-dimensional responses.

5.3 Parameter Variation Study

The main reason for using the non-dimensional equation of motion is to prove that the two models are similar. Here, the non-dimensional equations of motion are used to analyse the causal and effect of a distorted model through parameter variation study.

For this purpose, the Equation 5.2.43 is modified by removing the input matrix and added initial aerodynamic force and moment. Thus, Equation 5.2.43 becomes:

$$\begin{bmatrix} 1 & x_\alpha \\ x_\alpha & \dfrac{I_\alpha}{mc_{1/2}^2} \end{bmatrix} \begin{bmatrix} \Delta\mathring{\mathring{h}}/c_{1/2} \\ \Delta\mathring{\mathring{\alpha}} \end{bmatrix} = \begin{bmatrix} \dfrac{\Pi_1}{\Pi_9}C_{L_\alpha} - \tilde{c}_h & \dfrac{\Pi_1}{\Pi_9}C_{L_{\dot\alpha}} \\ \dfrac{\Pi_1}{\Pi_9}C_{M_\alpha} & \dfrac{\Pi_1}{\Pi_9}C_{M_{\dot\alpha}} - \tilde{c}_\alpha \end{bmatrix} \begin{bmatrix} \Delta\mathring{h}/c_{1/2} \\ \Delta\mathring{\alpha} \end{bmatrix} + \begin{bmatrix} -1 & \dfrac{\Pi_1}{\Pi_9^2}C_{L_\alpha} \\ 0 & \dfrac{\Pi_1}{\Pi_9^2}C_{M_\alpha} - \tilde{k}_\alpha(\alpha) \end{bmatrix} \begin{bmatrix} \Delta h/c_{1/2} \\ \Delta\alpha \end{bmatrix} + \begin{bmatrix} \Pi_{11}/\Pi_9^2 \\ 0 \end{bmatrix} + \begin{bmatrix} C_{L_0} \\ C_{M_0} \end{bmatrix} \tag{5.3.1}$$

the Δ here is used to show the perturbed value from its initial condition, while C_{L_0} and C_{M_0} are the lift force and pitching moment at the initial condition which define as:

$$C_{L_0} = C_{L_\alpha}\alpha_0 \tag{5.3.2}$$

$$C_{M_0} = C_{M_\alpha}\alpha_0 \tag{5.3.3}$$

where α_0 is the initial incidence angle setting.

There are four distorted models to be discussed in the following section, which includes the mismatched in the Froude number, aerodynamic characteristics, mass moment of inertia, and structural damping value.

Froude Number Distortion

In the case when the gravitational force is essential, the Froude number is a criteria needs to match. However, the consequences of matching the Froude number is that the velocity scaling is now dependent on the geometry scaling. It is worth noted that geometry, velocity and air density scaling are the independent variables which determine the dependent parameter such as the structural stiffness scaling. Figure 5.5 presents the comparison of a model that is scaled correctly and a model that scaled for a higher Froude number. Here, the higher Froude number obtained from a higher velocity scaling (1.5 times higher), which then translated to higher structural stiffness as presented in Table

5.3 as a distorted model. Thus, the system has a lower amplitude response, and this is apparent in the steady-state response in plunging motion. However, as the frequency is normalised, the response of both states are still at a similar frequency.

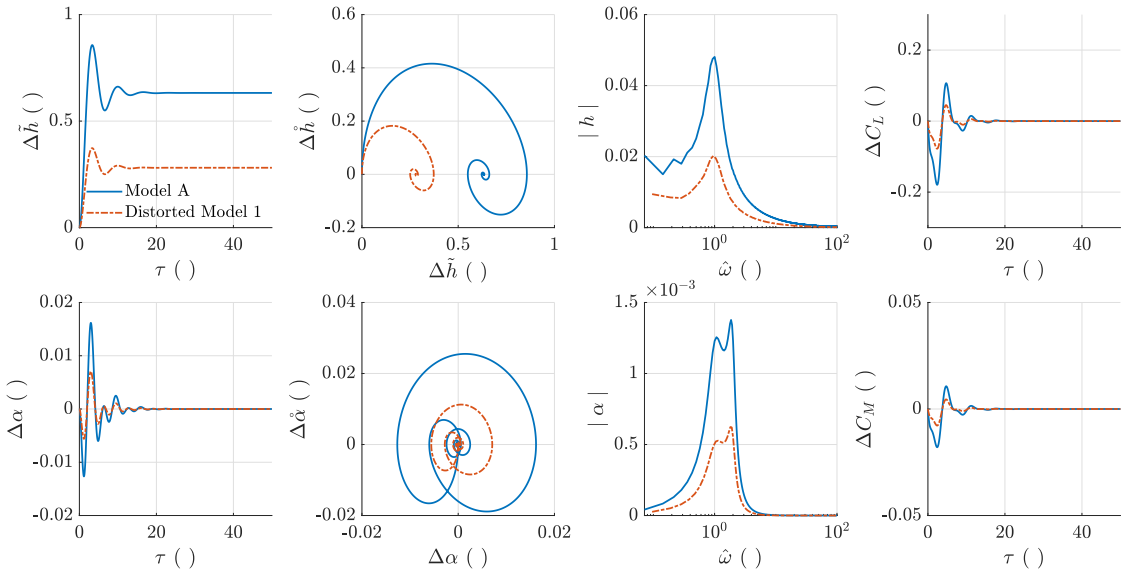

Figure 5.5: Distorted model in Froude number.

Parameter	Units	Model A	Scaled Model	Distorted Model 1
$c_{1/2}$	m	0.135	0.540	0.540
U	m/s	20	40	60
ρ	kg/m^3	1.225	1.225	1.225
m	kg	12.387	792.768	792.768
I_α	kg.m^2	0.065	665.6	665.6
k_h	N/m	1422.2	22755	51199
k_α	N/s^2	282	72192	162432
c_h	N.s/m	82.29	2633.3	3949.9
c_α	N.s/rad	3.6	1843.2	2764.8
C_{L_α}	/rad	2π	2π	2π
C_{M_α}	/rad	-0.628	-0.628	-0.628
C_{L_0}	-	0	0	0
C_{M_0}	-	0	0	0

The distorted model 1 are having the independent scaling factor of S_g=4, S_U=4, S_ρ=1. The dependent scaling factor are then calculated based on those independent scaling factor as presented on Table 5.2. Note that for ideal scaling, S_U=2.

Table 5.3: Parameter for distortion in Froude number study.

The fact that it has lower amplitude response means that in the linear area, the distorted model is still useful. This fact emphasises the statement by Ouellette [67] that the Froude number is less significant for short period mode and structural dynamics. On the contrary, when non-linearity at higher amplitude exist, the model can react differently, emphasising the statements by Wan and Cesnik [66], which highlights the importance of Froude number similarity. By looking at Figure 5.5, especially the time history of $\tilde{h}$, it can be seen that the difference in Froude number impacts the steady-state response.

Distortion in Aerodynamic Coefficient

One of the consequences of not matching Reynolds and Mach number is the difference in the aerodynamic coefficients [46]. Therefore, a study of the distorted model in aerodynamic coefficient given in Figure 5.6 as a comparison between Model A and distorted model that differ in the lift and moment coefficient (1.5 times higher). Here, the distorted model 1 is having ideal scaling relation with the actual model, except for the aerodynamic coefficient value as presented in Table 5.4. Noted that the change is on the aerodynamic slope and even the value is changing, it still assumed to be around the linear region and considered to be constant.

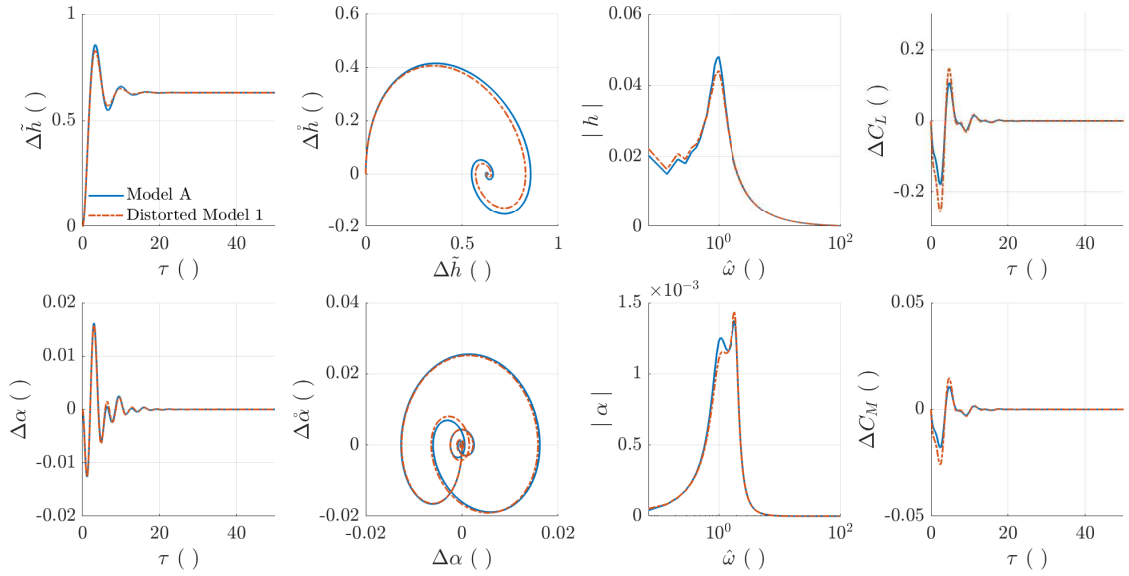

Figure 5.6: Distorted model in lift coefficient.

Parameter	Units	Model A	Scaled Model	Distorted Model 1
$c_{1/2}$	m	0.135	0.540	0.540
U	m/s	20	40	40
ρ	kg/m^3	1.225	1.225	1.225
m	kg	12.387	792.768	792.768
I_α	kg.m^2	0.065	665.6	665.6
k_h	N/m	1422.2	22755	22755
k_α	N/s^2	282	72192	72192
c_h	N.s/m	82.29	2633.3	2633.3
c_α	N.s/rad	3.6	1843.2	1843.2
C_{L_α}	/rad	2π	2π	3π
C_{M_α}	/rad	-0.628	-0.628	-0.942
C_{L_0}	-	0	0	0
C_{M_0}	-	0	0	0

The distorted model 1 are having the independent scaling factor of S_g=4, S_U=2, S_ρ=1. The dependent scaling factor are then calculated based on those independent scaling factor as presented on Table 5.2

Table 5.4: Parameter for distortion in aerodynamic coefficient study.

Figure 5.6 shows that the non-dimensional time response of Model A and the distorted model in aerodynamic coefficient is almost similar, except for the change in the aerody-

namic force and moment, which has higher amplitude. Counterintuitive with the relation in Equation 5.3.1, where the change in C_{L_α} and C_{M_α} are effecting the unsteady parameter. The comparison of the scaled model shows that in this case, the structural forces are dominant compares to the aerodynamic forces.

Distorted model in the Mass Moment of Inertia Value

It is possible that during the manufacturing process, the subscale model has errors in the mass distribution, which leads to a higher mass moment of inertia. Figure 5.7 presents the comparison of Model A and a distorted subscale model that has a different mass moment of inertia value (1.5 times higher), as given in Table 5.5.

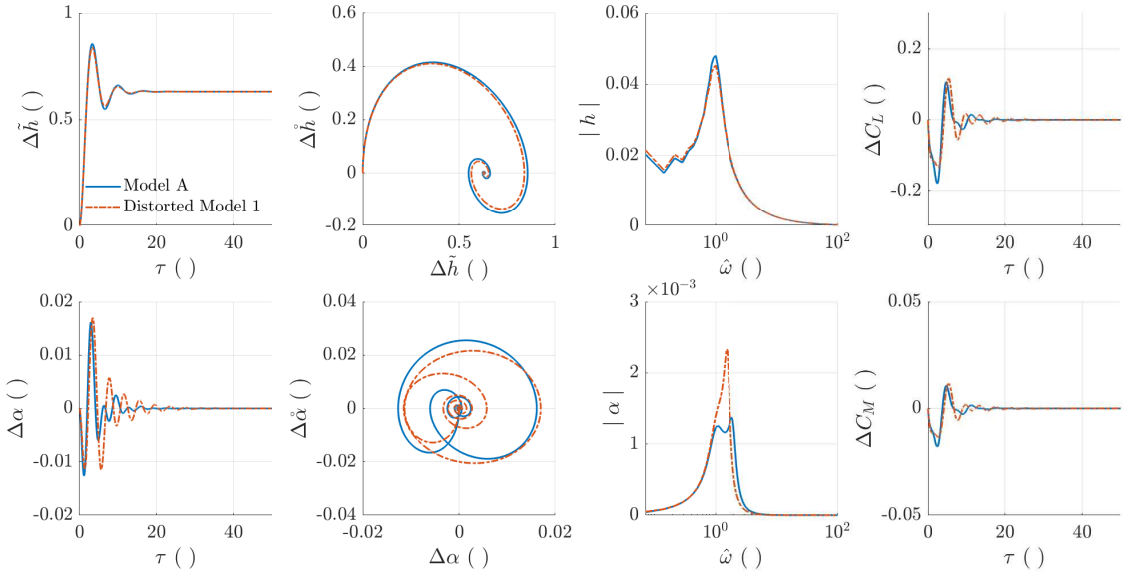

Figure 5.7: Distorted model in I_α value.

Parameter	Units	Model A	Scaled Model	Distorted Model 1
$c_{1/2}$	m	0.135	0.540	0.540
U	m/s	20	40	40
ρ	kg/m^3	1.225	1.225	1.225
m	kg	12.387	792.768	792.768
I_α	kg.m^2	0.065	665.6	998.4
k_h	N/m	1422.2	22755	22755
k_α	N/s^2	282	72192	72192
c_h	N.s/m	82.29	2633.3	2633.3
c_α	N.s/rad	3.6	1843.2	1843.2
C_{L_α}	/rad	2π	2π	2π
C_{M_α}	/rad	-0.628	-0.628	-0.628
C_{L_0}	-	0	0	0
C_{M_0}	-	0	0	0

The distorted model 1 are having the independent scaling factor of S_g=4, S_U=2, S_ρ=1. The dependent scaling factor are then calculated based on those independent scaling factor as presented on Table 5.2, except for Π_6 which is 384, ideally 256.

Table 5.5: Parameter for distortion in mass moment of inertia coefficient study.

The figure shows that the change in inertia value directly affects the angle of attack response, with a small effect on the plunge response. Time histories show that the α of model A is more damped than the distorted model. Also the frequency response of the distorted model is greater than model A.

Distorted model in the Structural Damping Value

Another possibility of uncertainties in the model property is the structural properties, such as the structural damping value. Figure 5.8 presents a case study of a distorted model, where the structural damping value is higher than expected (1.5 times more) as presented in Table 5.6.

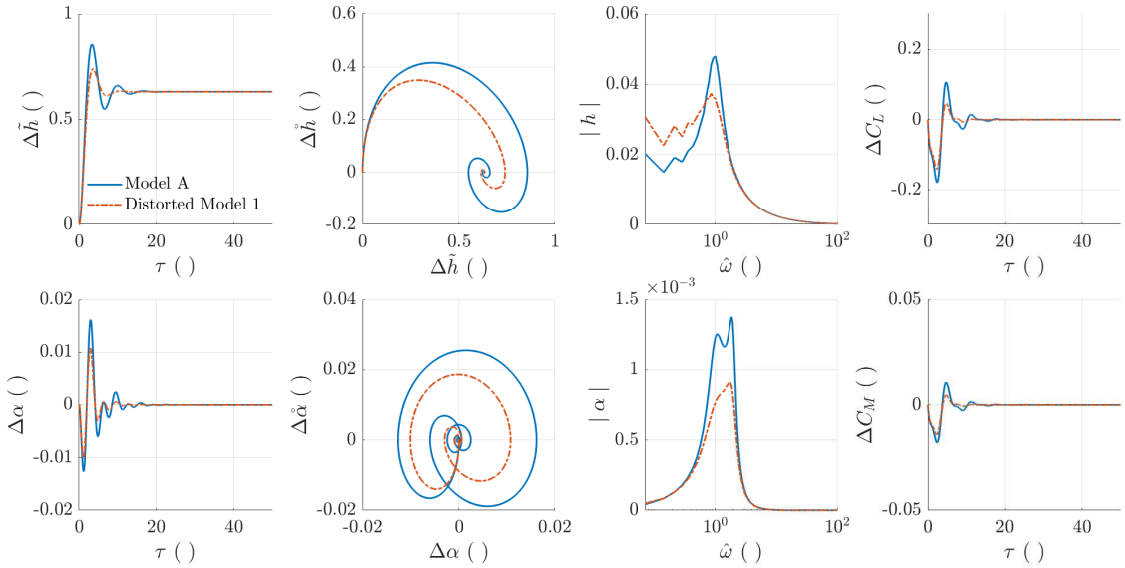

Figure 5.8: Distorted model in damping.

The figure shows that due to higher damping, the response of the system has a smaller amplitude response and settled faster. In the case where transient dynamics is essential to observe, in flutter case, for example, an attempt of having a model with comparable damping characteristics is important.

Parameter	Units	Model A	Scaled Model	Distorted Model 1
$c_{1/2}$	m	0.135	0.540	0.540
U	m/s	20	40	40
ρ	kg/m^3	1.225	1.225	1.225
m	kg	12.387	792.768	792.768
I_α	kg.m^2	0.065	665.6	665.6
k_h	N/m	1422.2	22755	22755
k_α	N/s^2	282	72192	72192
c_h	N.s/m	82.29	2633.3	3949.9
c_α	N.s/rad	3.6	1843.2	2764.8
C_{L_α}	/rad	2π	2π	2π
C_{M_α}	/rad	-0.628	-0.628	-0.628
C_{L_0}	-	0	0	0
C_{M_0}	-	0	0	0

The distorted model 1 are having the independent scaling factor of S_g=4, S_U=2, S_ρ=1. The dependent scaling factor are then calculated based on those independent scaling factor as presented on Table 5.2, except for Π_3 and Π_4 which is 1.5 times higher than the ideal factor.

Table 5.6: Parameter for distortion in damping coefficient study.

Discussion of the Results

The parameter variation study as presented earlier, shows the non-dimensional time response of a distorted model compared with the actual model. Since the model consist of many parameter, the study also try to show the dependency of some parameters to the dynamic characteristics of the model. To analyse the dependence of each parameter the Equation 5.3.1 is then translated into state-space form as follows:

$$\begin{bmatrix} 1 & x_\alpha & 0 & 0 \\ x_\alpha & \dfrac{I_\alpha}{mc_{1/2}^2} & 0 & 0 \\ 0 & 0 & 1 & 0 \\ 0 & 0 & 0 & 1 \end{bmatrix} \begin{bmatrix} \Delta\mathring{\mathring{h}}/c_{1/2} \\ \Delta\mathring{\mathring{\alpha}} \\ \Delta\mathring{h}/c_{1/2} \\ \Delta\mathring{\alpha} \end{bmatrix} =$$

$$\begin{bmatrix} \dfrac{\Pi_1}{\Pi_9}C_{L_\alpha} - \tilde{c}_h & \dfrac{\Pi_1}{\Pi_9}C_{L_{\dot\alpha}} & -1 & \dfrac{\Pi_1}{\Pi_9^2}C_{L_\alpha} \\ \dfrac{\Pi_1}{\Pi_9}C_{M_\alpha} & \dfrac{\Pi_1}{\Pi_9}C_{M_{\dot\alpha}} - \tilde{c}_\alpha & 0 & \dfrac{\Pi_1}{\Pi_9^2}C_{M_\alpha} - \tilde{k}_\alpha(\alpha) \\ 0 & 0 & 1 & 0 \\ 0 & 0 & 0 & 1 \end{bmatrix} \begin{bmatrix} \Delta\mathring{h}/c_{1/2} \\ \Delta\mathring{\alpha} \\ \Delta h/c_{1/2} \\ \Delta\alpha \end{bmatrix} + \begin{bmatrix} \Pi_{11}/\Pi_9^2 + L_0 \\ M_0 \\ 0 \\ 0 \end{bmatrix} \tag{5.3.4}$$

Which can be simply written as:

$$\begin{bmatrix} \Delta\mathring{\mathring{h}}/c_{1/2} \\ \Delta\mathring{\mathring{\alpha}} \\ \Delta\mathring{h}/c_{1/2} \\ \Delta\mathring{\alpha} \end{bmatrix} = \begin{bmatrix} \mathtt{L}_{\dot h} & \mathtt{L}_{\dot\alpha} & \mathtt{L}_h & \mathtt{L}_\alpha \\ \mathtt{M}_{\dot h} & \mathtt{M}_{\dot\alpha} & \mathtt{M}_h & \mathtt{M}_\alpha \\ 0 & 0 & 1 & 0 \\ 0 & 0 & 0 & 1 \end{bmatrix} \begin{bmatrix} \Delta\mathring{h}/c_{1/2} \\ \Delta\mathring{\alpha} \\ \Delta h/c_{1/2} \\ \Delta\alpha \end{bmatrix} + \begin{bmatrix} \mathtt{L}_C \\ \mathtt{L}_C \\ 0 \\ 0 \end{bmatrix} \tag{5.3.5}$$

where

$$\begin{bmatrix} \mathtt{L}_{\dot{h}} & \mathtt{L}_{\dot{\alpha}} & \mathtt{L}_{h} & \mathtt{L}_{\alpha} \\ \mathtt{M}_{\dot{h}} & \mathtt{M}_{\dot{\alpha}} & \mathtt{M}_{h} & \mathtt{M}_{\alpha} \\ 0 & 0 & 1 & 0 \\ 0 & 0 & 0 & 1 \end{bmatrix} = \begin{bmatrix} 1 & x_\alpha & 0 & 0 \\ x_\alpha & \dfrac{I_\alpha}{mc_{1/2}^2} & 0 & 0 \\ 0 & 0 & 1 & 0 \\ 0 & 0 & 0 & 1 \end{bmatrix}^{-1} \begin{bmatrix} \dfrac{\Pi_1}{\Pi_9} C_{L_\alpha} - \tilde{c}_h & \dfrac{\Pi_1}{\Pi_9} C_{L_{\dot{\alpha}}} & -1 & \dfrac{\Pi_1}{\Pi_9^2} C_{L_\alpha} \\ \dfrac{\Pi_1}{\Pi_9} C_{M_\alpha} & \dfrac{\Pi_1}{\Pi_9} C_{M_{\dot{\alpha}}} - \tilde{c}_\alpha & 0 & \dfrac{\Pi_1}{\Pi_9^2} C_{M_\alpha} - \tilde{k}_\alpha(\alpha) \\ 0 & 0 & 1 & 0 \\ 0 & 0 & 0 & 1 \end{bmatrix} \tag{5.3.6}$$

$$\begin{bmatrix} \mathtt{L}_C \\ \mathtt{L}_C \\ 0 \\ 0 \end{bmatrix} = \begin{bmatrix} 1 & x_\alpha & 0 & 0 \\ x_\alpha & \dfrac{I_\alpha}{mc_{1/2}^2} & 0 & 0 \\ 0 & 0 & 1 & 0 \\ 0 & 0 & 0 & 1 \end{bmatrix}^{-1} \begin{bmatrix} \Pi_{11}/\Pi_9^2 + L_0 \\ M_0 \\ 0 \\ 0 \end{bmatrix} \tag{5.3.7}$$

The value of these elements can be quantified using the least square approach on Equation 5.3.5 based on the following relations:

$$\mathring{\dot{\alpha}} = \mathtt{L}_{\mathring{\alpha}}\mathring{\alpha} + \mathtt{L}_{\alpha}\alpha + \mathtt{L}_{\mathring{h}}\mathring{h}/c_{1/2} + \mathtt{L}_{h}h/c_{1/2} + \mathtt{L}_{C} \tag{5.3.8}$$

$$\mathring{\dot{h}}/c_{1/2} = \mathtt{M}_{\mathring{\alpha}}\mathring{\alpha} + \mathtt{M}_{\alpha}\alpha + \mathtt{M}_{\mathring{h}}\dot{h} + \mathtt{M}_{h}h/c_{1/2} + \mathtt{M}_{C} \tag{5.3.9}$$

in which $\ddot{\alpha}$, $\ddot{h}$, $\dot{\alpha}$, $\dot{h}$, α and h can be obtained from the time response measurement of the simulated time response. And $\mathtt{L}_{\dot{\alpha}}$, $\mathtt{L}_{\alpha}$, $\mathtt{L}_{\dot{h}}$, $\mathtt{L}_{h}$, $\mathtt{L}_{C}$, $\mathtt{M}_{\dot{\alpha}}$, $\mathtt{M}_{\alpha}$, $\mathtt{M}_{\dot{h}}$, $\mathtt{M}_{h}$, and $\mathtt{M}_{C}$ are the identified parameter that builds the system matrix.

By estimating this parameter for both the ideal and distorted case, one can compare the results and used it to adjust the parameter in the distorted model to match as close as possible to the ideal case. The identified parameter of the ideal model, as well as the distorted model as discussed earlier are given in Table 5.7.

Parameter	Ideal Model	Distorted Model			
		Froude	Aero Coef.	Inertia	Damping
$\mathtt{L}_C$	0.65	0.29	0.65	0.64	0.65
$\mathtt{L}_{\mathring{\alpha}}$	-0.68	-0.68	-0.70	-0.67	-1.00
$\mathtt{L}_{\alpha}$	-1.02	-1.02	-1.02	-1.01	-1.02
$\mathtt{L}_{\mathring{h}}$	0.08	0.08	0.05	0.04	0.14
$\mathtt{L}_{h}$	0.31	0.31	-0.01	-0.01	0.31
$\mathtt{M}_C$	-0.06	-0.02	-0.06	-0.04	-0.06
$\mathtt{M}_{\mathring{\alpha}}$	0.06	0.06	0.06	0.04	0.08
$\mathtt{M}_{\alpha}$	0.09	0.09	0.09	0.06	0.09
$\mathtt{M}_{\mathring{h}}$	-0.53	-0.53	-0.52	-0.35	-0.79
$\mathtt{M}_{h}$	-3.83	-3.83	-3.81	-2.53	-3.83
$\tilde{\omega}_1$	1.01	1.01	1.01	1.01	1.01
$\tilde{\omega}_2$	1.96	1.96	1.96	1.59	1.95
ζ_1	0.334	0.334	0.347	0.335	0.489
ζ_2	0.136	0.136	0.134	0.109	0.204

Table 5.7: Identified parameter for ideal and distorted model.

Table 5.7 also presents the non-dimensional frequency and damping of the system based on the eigenvalue calculation of the identified A matrix. The calculated non-dimensional

frequency and damping are used as a basis in building a dimensionally scaled model. In this case, two models are considered to be dynamically scaled if the non-dimensional frequency and damping are within a considerable range. The range of similarity is unique depending on the needs of the experiment. Here, the frequency is expected within 5% range, where the damping is still considered similar within 25% range.

From the four cases of the distorted model, it shows that the distortion in Froude number has a similar dynamic response with the ideal case which is supported by the exact number of the identified parameter that builds the state matrix. However, it does differ in the value of $\mathtt{L}_C$, which suggest a different static response, as showed previously in Figure 5.5. Adjusting the value related to $\mathtt{L}_C$ can result in matching both static and dynamic response of both models. As showed in Equation 5.3.7, the adjustment of the static response is possible by adding L_0 value. Physically this is conducted by having a different angle of attack setting, as mentioned in Equation 5.3.3. Figure 5.9 and Table 5.8 presents the comparison of time response and the parameter value respectively for both the ideal and distorted model 2. Distorted model 2 is the distorted model in Froude number with adjusted initial value. Noted that the distorted model 2 is the adjusted model from the distorted model 1 (as presented in Figure 5.5).

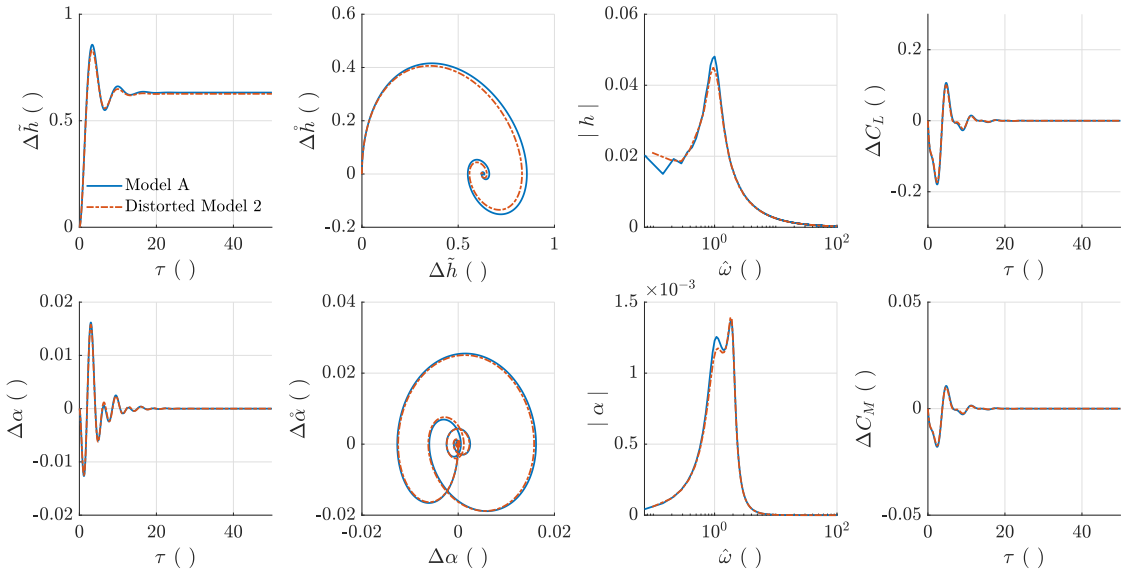

Figure 5.9: Distorted model in Froude number with changes in L_0 value.

On the other hand, for the distorted model in the aerodynamic coefficient, the results in Table 5.7 shows that the change in the frequency and damping value were less than 5%. Suggesting that, in this case, the distorted model in the aerodynamic coefficient has a negligible effect on the non-dimensional time response and no adjustment needed to the distorted model. However, the fact that no change needed in the aerodynamic coefficient distortion might be a unique case and needs to be checked for other flight conditions.

Furthermore, the results of the identified distorted model parameter show that distorted model in the mass moment of inertia and structural properties has a different dynamic response compare to the ideal scaled model. The distorted model in the mass moment of inertia changes the frequency response of 19%, while the distorted model in the structural damping changes the damping response of the model for more than 40%.

Parameter	Units	Model A	Scaled Model	Distorted Model	
				1	2
$c_{1/2}$	m	0.135	0.540	0.540	0.540
U	m/s	20	40	60	60
ρ	kg/m^3	1.225	1.225	1.225	1.225
m	kg	12.387	792.768	792.768	792.768
I_α	kg.m^2	0.065	665.6	665.6	665.6
k_h	N/m	1422.2	22755	51199	51199
k_α	N/s^2	282	72192	162432	162432
c_h	N.s/m	82.29	2633.3	3949.9	3949.9
c_α	N.s/rad	3.6	1843.2	2764.8	2764.8
C_{L_α}	/rad	2π	2π	2π	2π
C_{M_α}	/rad	-0.628	-0.628	-0.628	-0.628
C_{L_0}	-	0	0	0	0.345
C_{M_0}	-	0	0	0	0

Table 5.8: Parameter for distortion in Froude number study.

In the case of the distorted model in the mass moment of inertia, Table 5.7 shows that the non-dimensional frequency of the second mode was smaller than expected. The fact that the frequency response is different also presents in the non-dimensional time histories, Figure 5.7. The identified parameter at Table 5.7 shows that most of the different parameter were those that related to `M` parameter. In this case, it will be easier to adjust the parameter that closely related with this `M` parameter, which is stiffness and mass properties. As the distorted model has a more significant mass moment of inertia properties than expected, added more mass would only increase the mass moment of inertia properties and resulted in a much more different frequency. Thus, it is preferable to adjust the stiffness properties, in this case, the rotational stiffness (k_α). Trial and error can be conducted to adjust the distorted model so that it has a closer non-dimensional frequency response.

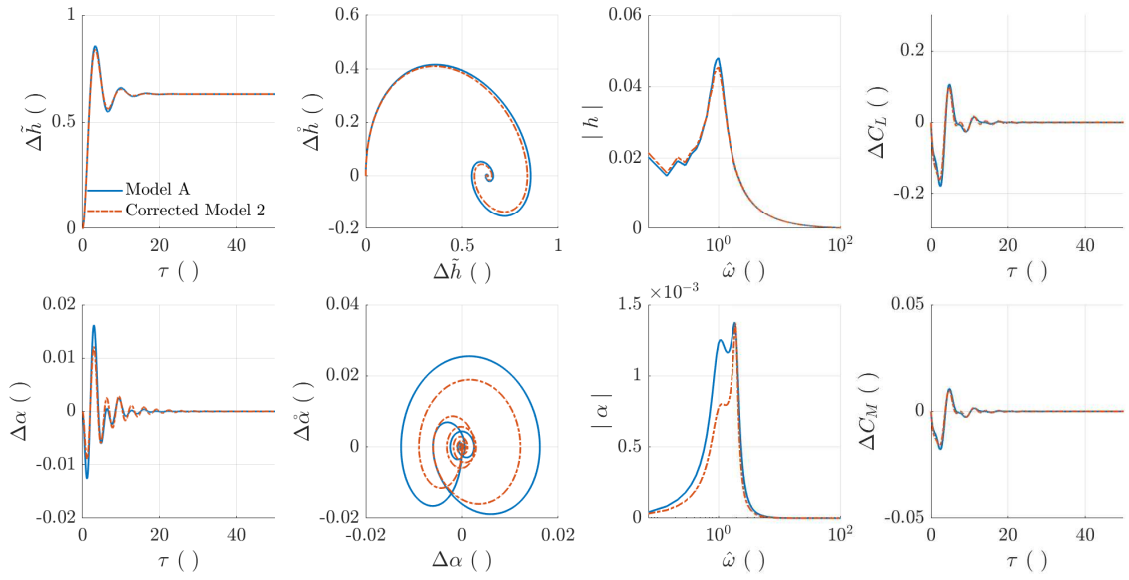

Figure 5.10: Distorted model in I_α value with changes in k_α value.

Parameter	Units	Model A	Scaled Model	Distorted Model	
				1	2
$c_{1/2}$	m	0.135	0.540	0.540	0.540
U	m/s	20	40	40	40
ρ	kg/m^3	1.225	1.225	1.225	1.225
m	kg	12.387	792.768	792.768	792.768
I_α	kg.m^2	0.065	665.6	998.4	998.4
k_h	N/m	1422.2	22755	22755	22755
k_α	N/s^2	282	72192	72192	108288
c_h	N.s/m	82.29	2633.3	2633.3	2633.3
c_α	N.s/rad	3.6	1843.2	1843.2	1843.2
C_{L_α}	/rad	2π	2π	2π	2π
C_{M_α}	/rad	-0.628	-0.628	-0.628	-0.628
C_{L_0}	-	0	0	0	0
C_{M_0}	-	0	0	0	0

Table 5.9: Parameter for distortion in mass moment of inertia coefficient study.

Figure 5.10 and Table 5.9 presents the comparison of time response and the parameter value respectively for both the ideal and adjusted model which has different mass moment of inertia value. Noted that the distorted model is labelled as distorted model 1 (as presented in Figure 5.7), while the adjusted distorted model labelled as distorted model 2 (as given in Figure 5.10). The distorted model 2 is having a more comparable frequency response, although it has a different damping response. The inability to match all the characteristics is a trade-off one should consider when developing a dynamic subscale model.

The last case of the distorted model is the distortion of the damping properties, in which the material properties of the subscale model can be the source of the distortion. Table 5.7 shows that the distorted model in the damping properties has a more comparable frequency response. However, it damped faster than the ideal model. Furthermore, from the identified parameter, it can be seen that almost all the identified parameter is similar except the parameter that is related to $\dot{\alpha}$ and $\dot{h}$. Here, the mass properties will be used to adjust the distorted model to have a closer response with the ideal scaled model.

Parameter	Units	Model A	Scaled Model	Distorted Model	
				1	2
$c_{1/2}$	m	0.135	0.540	0.540	0.540
U	m/s	20	40	40	40
ρ	kg/m^3	1.225	1.225	1.225	1.225
m	kg	12.387	792.768	792.768	1030.6
I_α	kg.m^2	0.065	665.6	665.6	865.3
k_h	N/m	1422.2	22755	22755	22755
k_α	N/s^2	282	72192	72192	108288
c_h	N.s/m	82.29	2633.3	3949.9	3949.9
c_α	N.s/rad	3.6	1843.2	2764.8	2764.8
C_{L_α}	/rad	2π	2π	2π	2π
C_{M_α}	/rad	-0.628	-0.628	-0.628	-0.628
C_{L_0}	-	0	0	0	0
C_{M_0}	-	0	0	0	0

Table 5.10: Parameter for distortion in damping coefficient study.

The mass properties are chosen as an adjusted variable because the non-dimensional

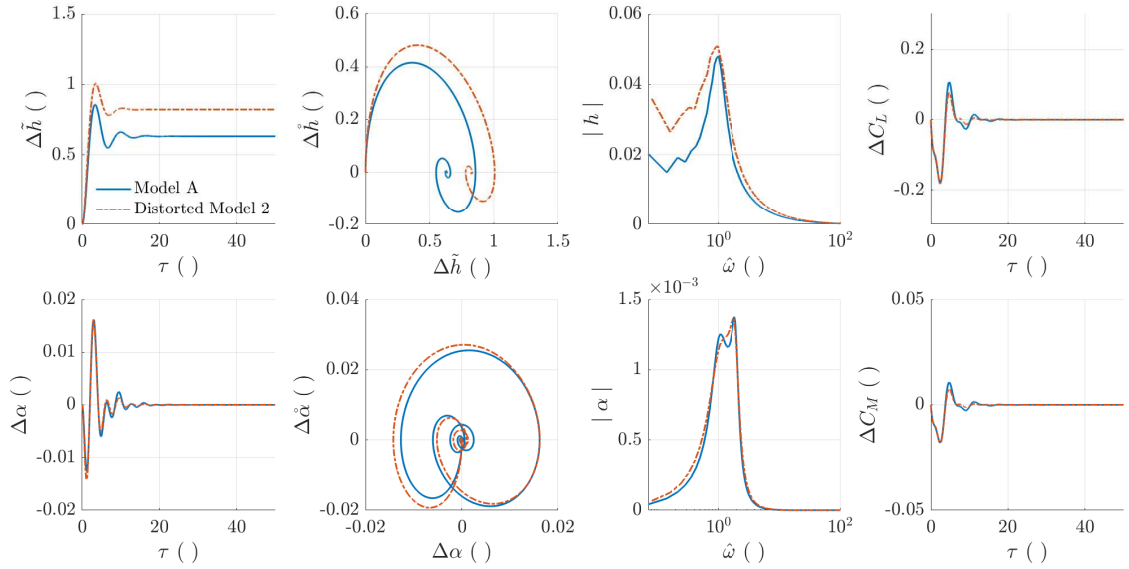

Figure 5.11: Distorted model in damping with changes in mass properties.

frequency is comparable with the ideal model, therefore no adjustment needed in stiffness properties. Furthermore, the static response of both models is also similar, meaning that no initial incidence setting needs to be adjusted. Table 5.10 presents the parameter comparison of the ideal model, the distorted model in damping coefficient (denote as distorted model 1), and the distorted model with update mass properties (denote as distorted model 2). The comparison of the non-dimensional time response for distorted model 1 and the ideal scale model is presented earlier in Figure 5.8, while the comparison between the distorted model 2 and the ideal scale model is given in Figure 5.11. Figure 5.11 shows that by updating the mass properties, the damping response of the distorted model 2 was closer to the ideal scaled model, altough the static response in height is differ.

The study of the distorted model is essential for developing a subscale model. In reality, the cause of the distorted model may come from the manufacturing error, uncertain in the material properties, or physical limitation. As some of these uncertainties can not easily be quantified, the adjustments needed for correcting the model is relying on experimental test and engineering intuition. However, it is preferable to adjust the model which is physically more accessible, such as changing the mass properties, adjusting the initial condition, or changing the stiffness properties. The study also shows that changing one of the parameters can impact the other parameter, therefore a trade-off needs to be considered.

5.4 Summary

The work discussed in this chapter demonstrates the importance of using non-dimensional terms for the analysis and assessment of scaling effects, and moreover it also emphasises the adjustments needed to compensate for distorted models where key similitude requirements are not met. The following problems that must be considered when developing

and interpreting test results from subscale models were highlighted:

- The non-dimensional formulation of the equation of motions is critical for developing and comparing the dynamics of subscale models.
- Comparison of the dynamic behaviour of different subscale models and full-scale aircraft must be based on non-dimensional time and non-dimensional frequency.
- Potential compromises in matching Froude number and/or aerodynamic coefficients for subscale models can be addressed through small modifications in key test parameters. For example via adjustments in angle-of-attack to ensure similar lift coefficients.

A simple theoretical model of a 2DoF pitch plunge aerofoil has been the use-case for this investigation and the study has provided insight into the fundamental trade-offs needed to satisfy the requirements for similitude. However, practical aspects of applying this theoretical scaling approach are discussed in the following chapter.

This page is intentionally left blank.

CHAPTER 6

HAR Wing Subscale Design

In this chapter, the concept of similitude is used to develop a subscale model of a High Aspect Ratio (HAR) wing. The work reported in this chapter is part of the BEAm Reduction and Dynamic Scaling (BEARDS) programme which aims to introduce the use of dynamically scaled models at the conceptual or early design stage. Here the focus is to develop a process for designing, manufacturing and testing dynamically scaled HAR wings [23] that are known to pose significant aeroelastic challenges.

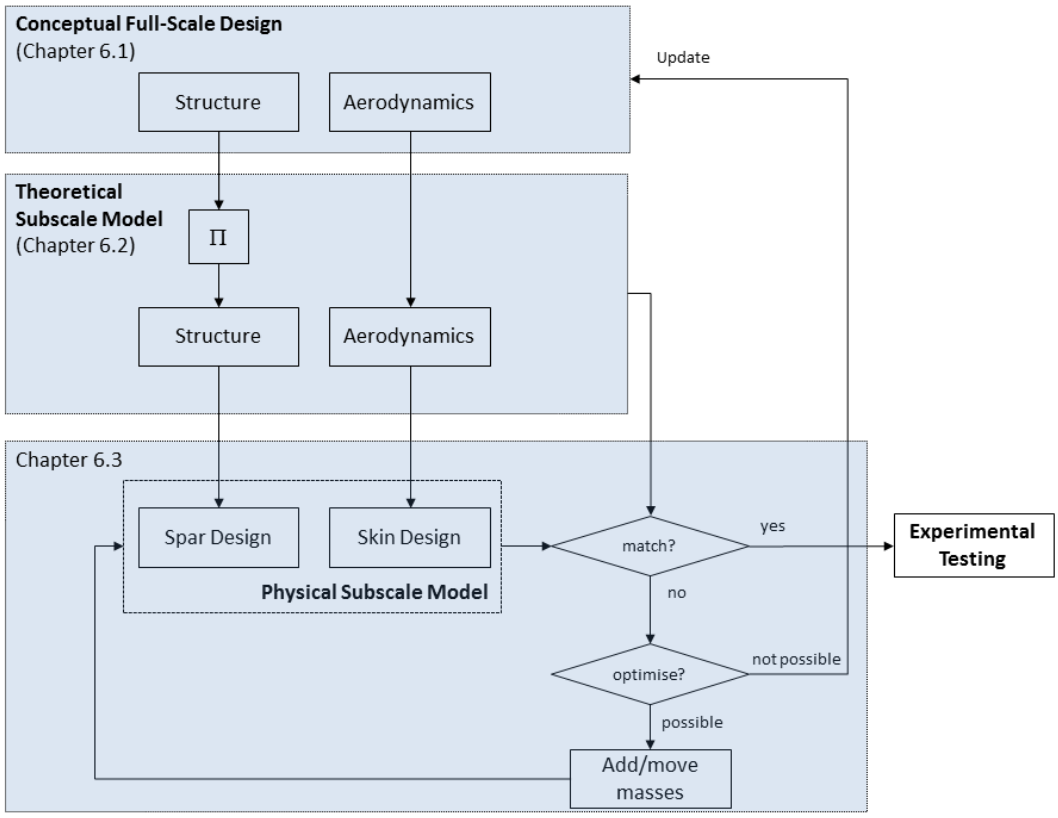

Figure 6.1: HAR wing scaling process.

The work looks more at the application of scaling laws and the development of theoretical models as prediction tools. The workflow reflects the methods used in developing subscale models and is shown in Figure 6.1. This chapter begins with a definition of the full-scale wing design, the assumptions behind the design development and the expected behaviour. These are followed by the derivation of the scaling laws required for the development of the subscale model. This chapter also provides a description of the fully coupled aeroelastic model used to compare the dynamic response of both the full scale aircraft and subscale models. The theoretical model is also used to evaluate the potential problem in developing a subscale model. The chapter continues with the development of the physical subscale model and associated challenges[1], along with the experimental validation through GVT and static wind tunnel testing. The chapter concludes by detailing the lessons learnt.

6.1 Conceptual Full-Scale Wing Design

The conceptual wing used for this study is known as XB-2 (eXperimental BeaRDS 2) and is presented in Figure 6.2. This figure also presents the axes system used when developing the model. The XB-2 wing is a simple and idealistic high aspect ratio wing with 0^o sweep angle at 25% of the chord, aspect ratio of 18.8, and a mean aerodynamic chord of 2.75 meters. The wing has a half-span of 24 meters and it utilises the NACA 23015 aerofoil profile. It has been optimised to cruise at 190 m/s and 35,000 ft [197]. The XB-2 is equipped with two spoilers and an aileron and designed such that the elastic axis is located around the aerodynamic centre in order to minimise the torsional aerodynamic loads.

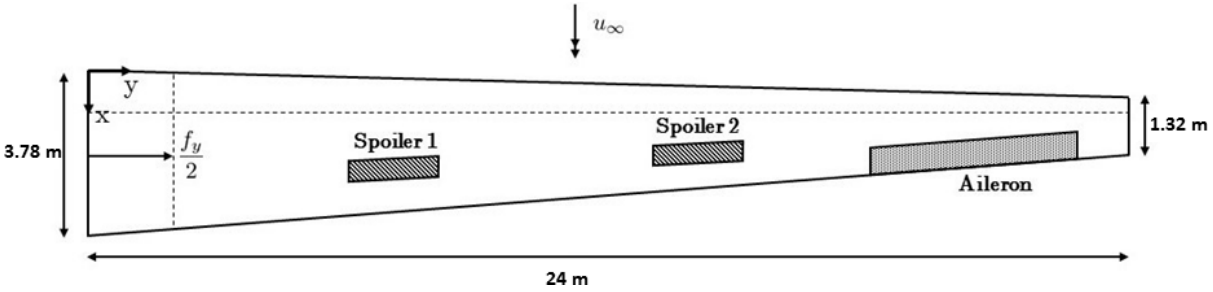

Figure 6.2: BeaRDS (XB-2) full-scale design.

This wing is designed for an aircraft similar to the Airbus A-320 which has a target MTOW of around 73,500 kg. Torenbeek estimated that the total wing weight is around 12% of MTOW [198]. Thus, the half-span wing mass was designed to be 4410 kg and was distributed linearly such that the first structural mode (in bending) occurred at around 0.7 Hz (see Figure 6.3). Theoretically, this first structural mode is close to the aircraft's short period pitch oscillation mode, indicating that there could be coupling between the rigid body modes and the aeroelastic modes. The wing is designed to be flexible, yet with deflections lower than 20% span so that wing deformation can be predicted using

[1]The physical subscale model is expected to represent the theoretical subscale model as part of validating the design process, especially those components related to nonlinear dynamic behaviour. However, due to the limitations of manufacturing processes the physical subscale model did not fully represent the theoretical subscale model. In this case, experiments using the physical subscale model can be used to validate the theoretical model being developed.

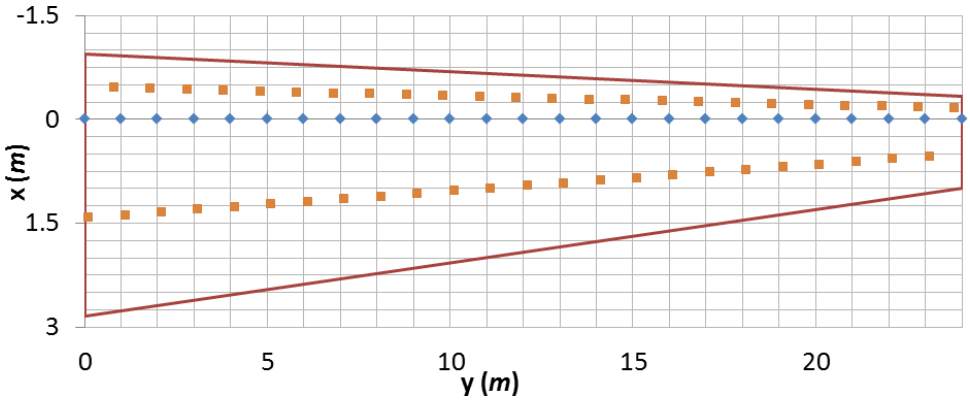

Figure 6.3: XB-2 Structural mass distribution (blue:node, red:lumped mass).

a linear approach. The reader is referred to References [197, 199] for a more thorough discussion on the XB-2's conceptual full-scale design methodology. A brief summary of XB-2 specifications is given in Table 6.1.

Parameter	**Symbol**	**Units**	**A320**	**XB-2**
Operating Weight Empty	OWE	kg	42,100	42,100
Maximum Take-Off Weight	$MTOW$	kg	73,500	73,500
Maximum Payload Weight	W_{pay}	kg	20,400	20,400
Cruise Altitude	h	m	11,280	11,280
Cruise Velocity	U_∞	Ma	0.78	0.6
Aerofoil			BAC 449	NACA
Thickness ratio	$\frac{t}{c}$	-	0.113	0.150
Lift at zero AoA	C_{l_0}	-	0.208	0.125
Zero lift AoA	α_0	rad	0.031	-0.022
Span	b	m	34.09	48.00
Aspect Ratio	AR	-	9.5	18.8
Reference area	S_{ref}	m^2	122.4	122.4
Sweep (LE)	Λ_{LE}	rad	0.471	0.026
Sweep ($\frac{c}{4}$)	$\Lambda_{\frac{c}{4}}$	rad	0.436	0.000
Root Chord	c_b	m	6.10	3.78
Streamwise c_b position	x_b	m	12.55	-
Tip Chord	c_t	m	1.62	1.32
Streamwise c_t position	l_t	m	20.35	
Taper Ratio	λ	-	0.240	0.350
Mean Aerodynamic Chord	$\bar{c}$	m	4.29	2.75

Table 6.1: Specification of XB-2 aircraft concept in comparison with the A320 aircraft.

A beam model was developed to represent the structural dynamics and it consisted of 25 nodes where each node has 6 DoF: three translational and three rotational. An in-house structural dynamic code based on Timoshenko beam element theory [200] was used to develop the structural model of the full-scale wing. The beam model also consisted of distributed lumped masses as shown in Figure 6.3. The mass distribution ensured that there was enough separation between the first bending and the first torsional mode.

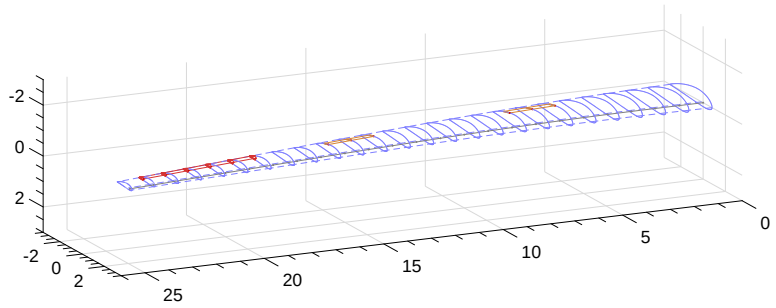

Mode 1 at 4.4 rad/s (bending)

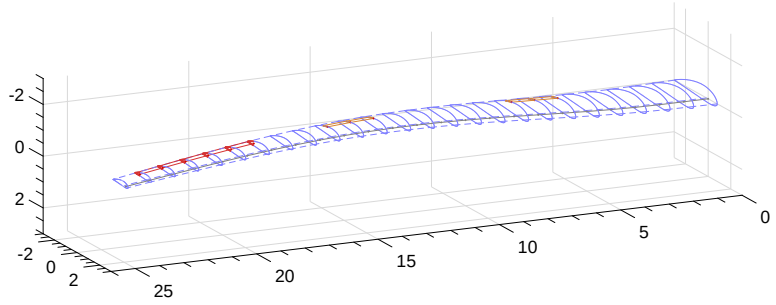

Mode 2 at 21.7 rad/s (bending)

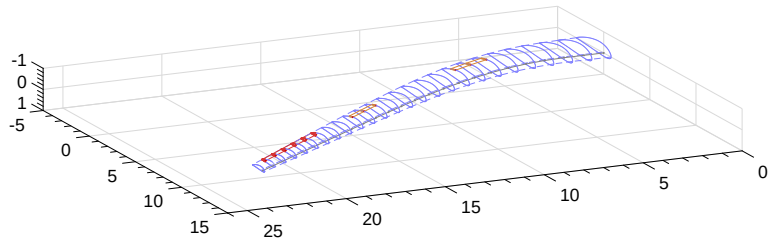

Mode 3 at 22 rad/s (lead-lag)

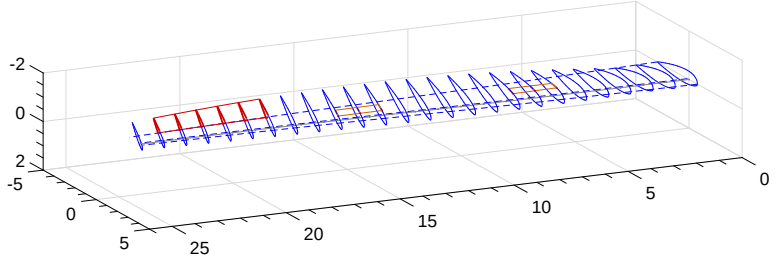

Mode 4 at 38.3 rad/s (torsional)

Figure 6.4: Mode shape of the theoretical full-scale wing.

Furthermore, NASTRAN [176] was used to validate the in-house tools as well as to observe the structural characteristics (such as modal frequencies and shapes) of the full-scale wing. Figure 6.4 illustrates the first four mode shapes of the full-scale wing. Furthermore, for experimental purposes, NASTRAN was also used to predict the flutter speed of the model. Also, the mass and stiffness matrices obtained from NASTRAN is then used as inputs for a theoretical framework model (BEaRDS^{TM}) to predict the behaviour of the conceptual full scale model. As BEaRDS^{TM} will be used to predict the full scale model, validation work of BEaRDS^{TM} is of importance. The validation work is presented in much later section via the subscale model, however it will be limited to the static case.

6.2 Theoretical Subscale Model Development

This section discusses the development of the subscale model based on the conceptual full-scale wing as presented earlier. The subscale model was developed through the application of the scaling process presented in Figure 6.5. Here, the scaling laws were applied to define the structural characteristics of the subscale model, while the aerodynamics were scaled down through the selection of a suitable flight condition. A theoretical framework was also developed to compare the theoretical aeroelastic response of the full-scale wing and the subscale model.

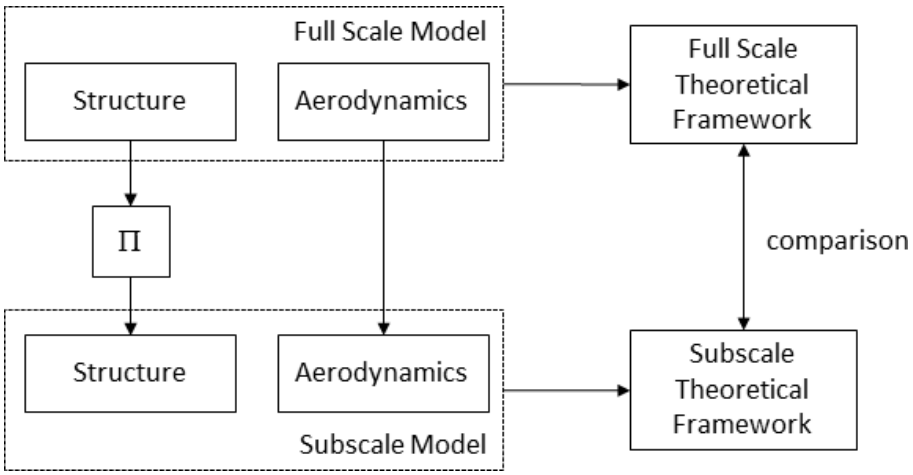

Figure 6.5: Flowchart of the scaling process.

Various names are going to be used in the following discussion for assigning the subscale model, and for clarity the reader is referred to the Table 6.2.

Name	Configuration / Note
Conceptual model ver.1	Initial model / scaled down from XB-2
Spar-Skin	Manufactured spar and skin
Conceptual model ver.2	20% more weight from ver.1
Conceptual model ver.3	Updated from ver.2 / adopting spar and skin
SSM	Manufactured spar, skin and lumped masses
Wind Tunnel	Manufactured spar, skin, lumped mass and rod

Table 6.2: Evolution of the subscale model.

The illustration of the subscale model development is presented in the flowchart given in Appendix C.

6.2.1 Theoretical Framework

A fluid-structure interaction framework known as BEARDS Theoretical Model (BEARDS^{TM}) was developed to observe the aeroelastic response of the wing design. The motivation behind the development of the theoretical framework was the need for:

1. checking the scaling procedures to ensure similitude between the theoretical subscale model and the full-scale wing and,
2. a tool to design the experiments for system identification purposes.

The framework architecture was based on the CA^{2}LM framework [142, 143] as mentioned in Chapter 4.1. However, while the CA^{2}LM framework accommodates the full aircraft configuration (see Figure 4.2), BEARDS^{TM} only considers the wing constrained at the root. Figure 6.6 presents the workflow of the BEARDS^{TM} and it illustrates the main difference between CA^{2}LM and BEARDS^{TM}. It is evident that the BEARDS^{TM} ignores the 6 DoF equations of motion.

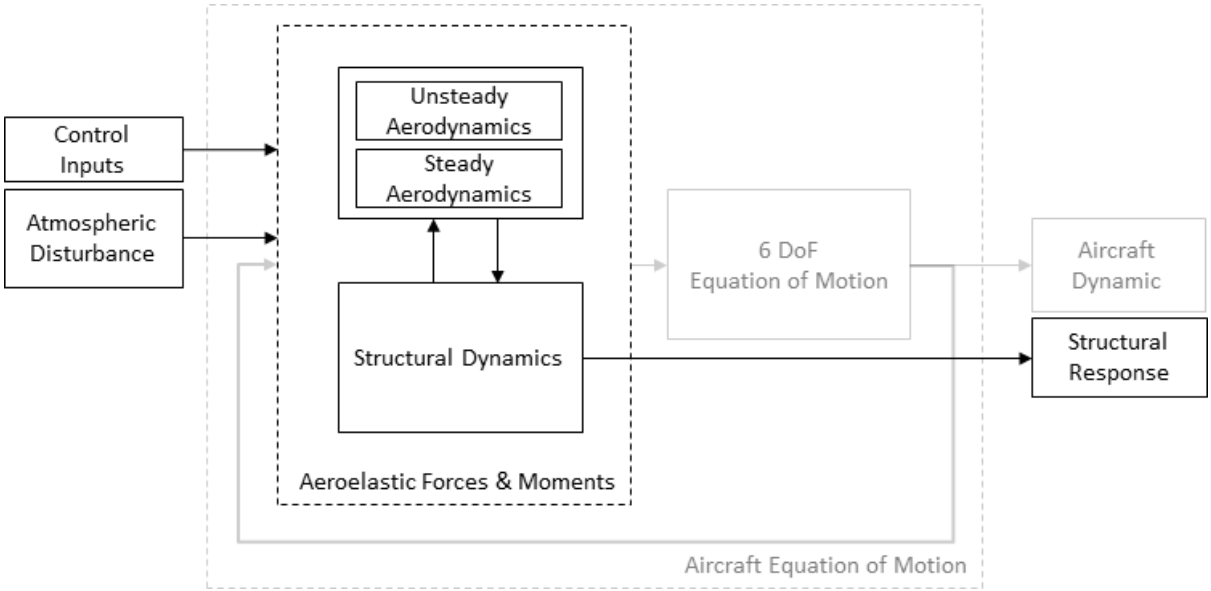

Figure 6.6: Workflow of BEARDS^{TM}, simplification from CA^{2}LM framework (gray).

The input to BEARDS^{TM} are the control surfaces (in this case aileron and spoiler) and atmospheric disturbance. The output of the BEARDS^{TM} is the structural response as well as the aerodynamic forces and moments along the wing. The simulation framework needs initialisation data which contains flight conditions, such as velocity, air density and the initial angle of attack relative to the root, as well as the structural properties such as the mass and stiffness of the structure.

The structural and aerodynamic blocks are the main module of BEARDS^{TM}. However, to accommodate differences in wing geometry and flight conditions, several adjustments were needed and these are detailed below:

Structural Dynamics Model

BEaRDS^{TM} solves the structural dynamic equation in modal form and requires the mass $[M]$ and stiffness $[K]$ matrices as inputs. The framework also allows automatic reading of the mass and stiffness matrices from NASTRAN '`.o4`' files. The only fundamental difference between BEaRDS^{TM} and the CA^{2}LM framework is the definition of the structural damping coefficient. In the CA^{2}LM framework the damping coefficient is fixed as 3%, while in BEaRDS^{TM} the damping matrix $[C]$ is a function of the stiffness matrix [50], as follows:

$$[C] = \lambda [K] \tag{6.2.1}$$

where λ is a constant of proportionality. In the case of the full-scale wing λ was chosen to be 0.013 [197], and this number was scaled accordingly for the subscale model.

Aerodynamics Model

Overall, only minor adjustments from CA^{2}LM framework were made to develop the aerodynamics block of BEaRDS^{TM} . The adjustment included the change in the number of aerodynamic strips, the aerodynamic look-up table data and the change in the indicial model. For simplification, the location of the aerodynamic strips in BEaRDS^{TM} were adjusted to be similar with the structural nodes. This leads to 25 equally distributed aerodynamic strips along the semi-span[2]. To calculate the aerodynamic forces, the aerodynamics block reads data from a set of look-up tables. As this wing has a different geometrical shape from the AX-1, an aerodynamic data set for the relevant aerofoil was generated by Carizzales et al. using AVL [202]. The aerodynamic coefficient data, as functions of Mach and Reynolds numbers, are presented in Appendix A. A significant adjustment was made to the aerodynamic indicial model for the subscale model. As the flight condition chosen from the subscale model allows for the incompressible flow assumption, the model assumes that the indicial angles change instantaneously. Therefore, the apparent mass (non-circulatory term) is not essential [143], and the time constant coefficient in the original CA^{2}LM model was ignored[3]. However, for the full-scale wing no changes in the aerodynamic indicial model were made.

6.2.2 Scaling Law

The simplified aeroelastic equations of motion can be written concisely as follows:

$$\underbrace{[M]\,\ddot{\mathbf{d}} + [C]\,\dot{\mathbf{d}} + [K]\,\mathbf{d}}_{\text{structure}} = \underbrace{[A_k]\,\mathbf{d} + [A_c]\,\dot{\mathbf{d}} + [A_m]\,\ddot{\mathbf{d}}}_{\text{aerodynamics}} \tag{6.2.2}$$

[2]CA^{2}LM framework has 25 aerodynamic strips along the wing semi-span in a cosine distribution, the difference in the distribution of the aerodynamic strips might affected the accuracy of the wing model [201]

[3]The reader is referred to Chapter 4.1 as well as Reference [143] for a comprehensive discussion on the aerodynamic model

where $\mathbf{d}$ is the state vector that represents 6 DoF:

$$\mathbf{d} = [\ x \quad y \quad z \quad \phi \quad \theta \quad \psi\ ]^T \tag{6.2.3}$$

while $[M]$ is the mass matrix that consists of mass S_m and inertia S_I for each node. $[K]$ is the structural stiffness that consists of bending and torsional stiffnesses. The right hand side of the equation represents the aerodynamic force, A_k, A_c, and A_m which are the aerodynamic stiffness, damping and mass respectively. Both aerodynamic stiffness and damping contribute to the overall aerodynamic forces and moments. In this equation the gravitational contribution is ignored. It should be noted that the half wing configuration is constrained at the root and consequently no rigid body dynamics can be observed.

Solving Equation 6.2.2 using a direct solver method in MATLAB is computationally expensive due to sparse system matrices that require extremely small time steps. To overcome this issue, the generalised method as presented in Equation 4.3.7 is preferable. Here, a similar approach of non-dimensional mode shapes as discussed in Chapter 5.2.2 is utilised, by defining:

$$\mathbf{d} = \begin{bmatrix} b & 0 & 0 & 0 & 0 & 0 \\ 0 & b & 0 & 0 & 0 & 0 \\ 0 & 0 & b & 0 & 0 & 0 \\ 0 & 0 & 0 & 1 & 0 & 0 \\ 0 & 0 & 0 & 0 & 1 & 0 \\ 0 & 0 & 0 & 0 & 0 & 1 \end{bmatrix} \bar{\mathbf{d}} = T\bar{\mathbf{d}} \tag{6.2.4}$$

where

$$\bar{\mathbf{d}} = \left\{\ \bar{x} \quad \bar{y} \quad \bar{z} \quad \phi \quad \theta \quad \psi\ \right\} \tag{6.2.5}$$

and

$$\bar{\mathbf{d}} = \bar{\Phi}\bar{\eta} \tag{6.2.6}$$

Therefore, Equation 6.2.2 can be transformed into modal coordinates such that:

$$\langle m \rangle \ddot{\bar{\eta}} + \langle 2m\zeta\omega \rangle \dot{\bar{\eta}} + \left\langle m\omega^2 \right\rangle \bar{\eta} = [a_k]\,\bar{\eta} + [a_c]\,\dot{\bar{\eta}} + [a_m]\,\ddot{\bar{\eta}} \tag{6.2.7}$$

where the left hand side of the equation are diagonal matrices of:

$$\langle m \rangle = \bar{\Phi}^T T^T [M] T \bar{\Phi} \tag{6.2.8}$$

$$\langle c \rangle = \bar{\Phi}^T T^T [C] T \bar{\Phi} = \langle 2m\zeta\omega \rangle \tag{6.2.9}$$

$$\langle k \rangle = \bar{\Phi}^T T^T [K] T \bar{\Phi} = \left\langle m\omega^2 \right\rangle \tag{6.2.10}$$

Furthermore, using the similitude relation as presented in Chapter 5, the non-dimensional equation of motion in the modal form is defined as:

$$\langle \bar{m} \rangle \mathring{\ddot{\bar{\eta}}} + \langle 2\bar{m}\zeta\bar{\omega} \rangle \mathring{\dot{\bar{\eta}}} + \left\langle \bar{m}\bar{\omega}^2 \right\rangle \bar{\eta} = \frac{\pi_2}{\pi_9^2} \left([\bar{a_k}]\,\bar{\eta} + \pi_9\,[\bar{a_c}]\,\mathring{\dot{\bar{\eta}}} + \pi_9^2\,[\bar{a_m}]\,\mathring{\ddot{\bar{\eta}}} \right) \tag{6.2.11}$$

where $\pi_2 = \dfrac{I}{\rho b^5}$ and $\pi_9 = \dfrac{\omega b}{U}$ is the inertia ratio and reduced frequency respectively. The

diagonal elements of $\langle \bar{m} \rangle$ and $\langle \bar{\omega} \rangle$ are the non-dimensional modal mass and frequency with respect to the first mode shape.

In developing the scaling laws, the similitude relations based on the repeating variables must be defined. The similitude relations consider geometry, velocity and air density, and these are dictated by the limitation of the wind tunnel. Based on the wind tunnel characteristics (Cranfield 8x6 Low-Speed Tunnel [203], see Table 6.3) and the full-scale wing (see Figure 6.2), the scaling laws have the following impact:

1. Given the subscale model is built for a wind tunnel experiment, it should be developed by considering the dimensions of the test section. Also, by taking into account the boundary layer of the tunnel wall, the scaled wing should only occupy a maximum of 90% of the test section. Since, this limitation dictates the geometrical scaling relation, the chosen geometrical scale is 1:16.

2. Air density based scaling takes into account the flight condition being considered for the full-scale aircraft, and its simulation in the wind tunnel. By considering the ISA atmosphere for the scaled model and cruise condition of the full-scale aircraft at 35,000 ft, this gives an air density ratio of 3.23:1.

3. Although the equations of motion do not consider the gravitational effect, implying that Froude number similarity is not important. However, matching Froude number is still considered in this case study because it dictates the relation between velocity and geometrical scaling. The velocity scale is given as square-root of the geometrical scale, resulting in a velocity scale of 1:4.

Test Section	:	2.4 m x 1.8 m
Mach number	:	0.15 (max)
Flow Speed	:	5 – 50 m/s
Reynolds number	:	3.6 $\times 10^6$ /m
Dynamic Pressure	:	up to 1.5 kN/m^2
Temperature	:	Ambient Temperature

Table 6.3: Specification of Cranfield 8x6 low speed tunnel (Obtained from Reference [203]).

Table 6.4 presents the independent scaling laws that consist of length, air density and velocity. These dictate the dependent scaling laws such as mass, inertia, structural stiffness (bending and torsional) and non-dimensional time.

The assumption in the development process has been that the non-dimensional aerodynamic properties (aerodynamic coefficients) are kept constant by maintaining a similar aerodynamic shape. This assumption is, in fact, neglecting the importance of Reynolds number effect to the aerodynamic coefficients as previously explained in Section 2.1.1. However, as it is challenging to satisfy the Reynolds number similarity, here the forces and moments acting on the subscale model are assumed to be proportional to those of the full-scale wing; thus, reducing the aeroelastic problem to a structural problem.

The mass and stiffness matrices, as given in Equation 6.2.2, represent the structural problem. Note that the damping matrix is assumed to be a function of mass and stiffness

Dimension	Unit	π	Scaling Factor Scaled Model	Scaling Factor Full Scale
Length	$\mathcal{L}$	S_g	1	16
Air Density	$\mathcal{ML}^{-3}$	S_ρ	3.23	1
Velocity	$\mathcal{LT}^{-1}$	S_U	1	4
Mass	$\mathcal{M}$	$\tilde{S}_M = S_\rho S_g^3$	1	16^3
Inertia	$\mathcal{ML}^2$	$\tilde{S}_I = S_\rho S_g^5$	1	16^5
Structural Stiffness	$\mathcal{MT}^{-2}$	$\tilde{S}_K = S_\rho S_U^2 S_g$	1	79.33
Torsional Stiffness	$\mathcal{ML}^2\mathcal{T}^{-2}$	$\tilde{S}_G = S_\rho S_U^2 S_g^2$	1	2.03×10^4
Non-dimensional time	$\mathcal{T}$	$\tilde{S}_T = \frac{S_g}{S_U}$	4	1
Proportional Structural Damping	$\mathcal{T}^{-1}$	$\tilde{S}_\lambda = \frac{S_U}{S_g}$	1	4

Table 6.4: Scaling factor used for BEARDS.

and it will be scaled accordingly. However, it is worth mentioning that due to the various units in the state matrix (see Equation 6.2.4), the contents of the mass and stiffness matrices correspond to these dimensions. For example, the mass matrix given by [50, 143]:

$$[M] = \begin{bmatrix} m & & & & & \\ 0 & m & & & & \\ 0 & 0 & m & Symmetric & & \\ 0 & m_z & m_y & I_x & & \\ m_z & 0 & -m_x & -I_{xy} & I_y & \\ -m_y & -m_x & 0 & -I_{xz} & -I_{yz} & I_z \end{bmatrix} \tag{6.2.12}$$

The diagonal terms of the mass matrix are in kg and kgm^2, while some of the off-diagonal terms (m_x, m_y, and m_z) are in kgm. Similarly, the variables that build the stiffness matrix have three different dimensions. Therefore, by utilising the T matrix as defined in Equation 6.2.4, the mass and stiffness matrices are transformed into:

$$\left[\tilde{M}\right] = T^T [M] T \tag{6.2.13}$$

$$\left[\tilde{K}\right] = T^T [K] T \tag{6.2.14}$$

By doing so, the mass matrix is now in the uniform dimension of kgm^2 and similarly the stiffness matrix is in the dimension of kgm^2/s^2. This simplifies the process needed to scale down the whole matrix using the following relation:

$$\left[\tilde{M}_{sc}\right] = \tilde{S}_I \left[\tilde{M}\right] \tag{6.2.15}$$

$$\left[\tilde{K}_{sc}\right] = \tilde{S}_K \tilde{S}_G^2 \left[\tilde{K}\right] \tag{6.2.16}$$

in which $\left[\tilde{M}_{sc}\right]$ and $\left[\tilde{K}_{sc}\right]$ are the mass and stiffness matrices for the subscale model with consistent units, while $\tilde{S}_I$, $\tilde{S}_K$, and $\tilde{S}_G$ are detailed in Table 6.4.

Furthermore, the application of the scaling factors in Table 6.4 yield the geometrical definition of the scaled model as presented in Table 6.5. It is worth noting that the

Parameter	Symbol	Units	XB-2	xb-2
Cruise Altitude	h	m	11,280	0
Air Density	ρ	kg/m^3	0.3796	1.225
Cruise Velocity	U	m/s	190	47.5
Aspect Ratio	AR	-	18.8	18.8
Semi span	b	m	24	1.5
Reference area	S_{ref}	m^2	122.4	0.478
Sweep (LE)	Λ_{LE}	rad	0.026	0.026
Sweep ($\frac{c}{4}$)	$\Lambda_{\frac{c}{4}}$	rad	0.000	0.000
Root Chord	c_b	m	3.78	0.236
Tip Chord	c_t	m	1.32	0.083
Taper Ratio	λ	-	0.350	0.350
Mean Aerodynamic Chord	$\bar{c}$	m	2.75	0.172
Aerofoil	-	-	NACA 23015	NACA 23015
Aerofoil	-	-	NACA 23015	NACA 23015
Reynold Number ($\bar{c}$)	Re	-	4.39 $\times 10^7$	6.87$\times 10^5$
Mach Number	Ma	-	0.5584	0.14
Estimated Mass	m	kg	4410	3.42
1^{st} Bending Freq.	ω_{η_1}	rad/s	4.4	17.4
2^{nd} Bending Freq.	ω_{η_2}	rad/s	21.7	86.9
1^{st} Lagging Freq.	ω_{η_3}	rad/s	22	87.9
1^{st} Torsion Freq.	ω_{η_4}	rad/s	38.3	154

Table 6.5: Dimension of the full-scale XB-2 model and subscale xb-2 model.

table also presents the Reynolds and Mach number for the subscale model, as well as the expected structural frequencies.

6.2.3 Theoretical Comparison

Theoretical models in MATLAB/Simulink were used to compare the aeroelastic response of the full-scale (XB-2) wing and the subscale (xb-2) model to assess the effects of scaling. If the subscale model was scaled correctly, a comparable aeroelastic response was expected. This section starts by first comparing the structural dynamics and continues with the comparison of aeroelastic response through the BEaRDS^{TM} .

Structural Comparison

The structural model was scaled down based on the relations given in Table 6.4 and by applying Equations 6.2.15 and 6.2.16. The comparison between the structural matrix of the full-scale wing and subscale model was achieved by analysing the structural characteristics in terms of mode shapes and the natural frequencies. In this case, the `eig` function from MATLAB library was used for extracting the eigenvector (mode shape) and eigenvalue (frequency) from mass and stiffness matrices.

Comparison of the first four modal frequencies is presented in Table 6.6. The consequences of length and velocity scaling is that the frequency of the subscale model is four

times higher than that of the full-scale model for all modes. Moreover, the table also shows the comparison of the mode shapes in terms of MAC values.

Mode Shape	Frequency [rad/s]		MAC	
	Full-scale	Subscale	Φ	$\bar{\Phi}$
1^{st} Bending	4.4	14.4	0.383	1.0
2^{nd} Bending	21.7	86.9	0.222	1.0
1^{st} Lagging	22	87.9	0.334	1.0
1^{st} Torsion	38.3	154	0.976	1.0

Table 6.6: Comparison of modal properties.

The MAC is a quantitative metric that allows us to compare the similarity between models. As mentioned in Chapter 3, the MAC value of 1 means that the two mode shapes are identical, while 0 implies that there is no similarity. In this case, dimensional mode shapes (Φ) and non-dimensional mode shapes ($\bar{\Phi}$) are compared, where:

$$\mathbf{d} = \Phi\eta, \qquad \mathbf{d} = \left\{ \begin{array}{cccccc} x & y & z & \phi & \theta & \psi \end{array} \right\} \tag{6.2.17}$$

$$\bar{\mathbf{d}} = \bar{\Phi}\bar{\eta}, \qquad \bar{\mathbf{d}} = \left\{ \begin{array}{cccccc} \bar{x} & \bar{y} & \bar{z} & \phi & \theta & \psi \end{array} \right\} \tag{6.2.18}$$

The main difference here is that Φ has dimensions of meter and rad/deg, while $\bar{\Phi}$ is non-dimensional. The translational components have been non-dimensionalised with respect to the characteristic length (b). Comparing the dimensional mode shape of the full-scale and subscale model it is evident that the MAC value is very low (less than 0.5) for the first three mode shapes and almost 1 for the torsional mode. Even though, after considering Figure 6.7, the first four mode shapes of the subscale model are comparable with the full-scale model as given in Figure 6.4. However, when comparing the non-dimensional mode shapes the MAC value is exactly one, meaning that the two non-dimensional mode shapes are in-fact identical. The fact that the mode shape is identical when it is normalised to the characteristic length emphasises the importance and the application of dimensional analysis in structural dynamics.

Aeroelastic Comparison

For an aeroelastic system, the aerodynamic characteristics are of importance. As mentioned earlier, the aerodynamic characteristics of the full-scale wing and the subscale model are different because both models operate at different Reynolds and Mach numbers. Figure 6.8 allows the comparison of results obtained from BEaRDS^{TM} for the subscale and the full-scale wing as a function of the Froude number. The design Froude number is found to be 12.4 based on the semi-span b used as the characteristics length. The use of semi-span is convenient for presenting the static tip deflection in percentage. Both models exhibit a similar behaviour in which both the total lift and pitching moment coefficient increase with angle-of-attack. However, it is also evident that the subscale model produces smaller aerodynamic forces and moments. The difference in aerodynamic coefficients is the consequence of not being able to match the required Reynolds and Mach numbers. However, the change in the aerodynamic forces and moments also affects the static deflection and the static twist angle. As shown in Figure 6.8, the tip deflection of the subscale model for a similar angle of attack is less than the expected full-scale model.

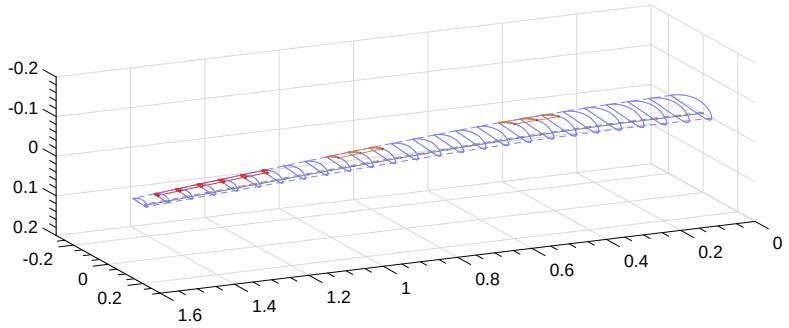

Mode 1 at 17.4 rad/s (bending)

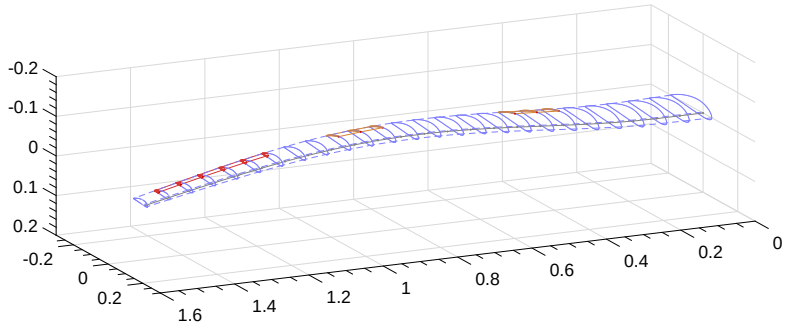

Mode 2 at 86.9 rad/s (bending)

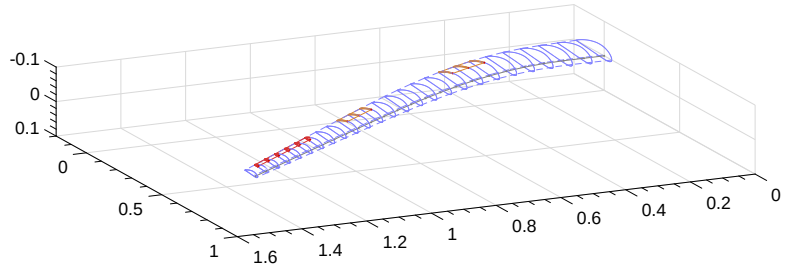

Mode 3 at 87.9 rad/s (lead-lag)

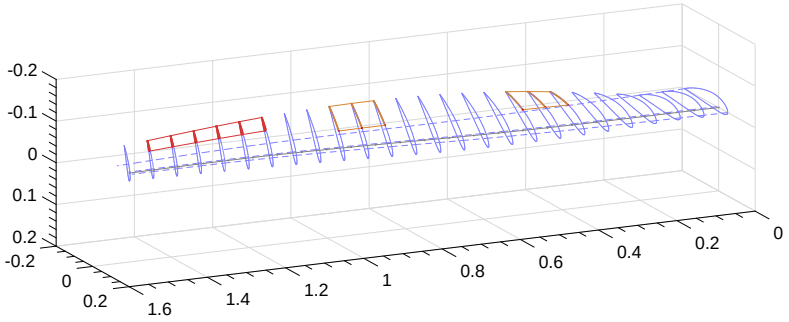

Mode 4 at 154 rad/s (torsion)

Figure 6.7: Structural mode shape of the theoretical subscale model.

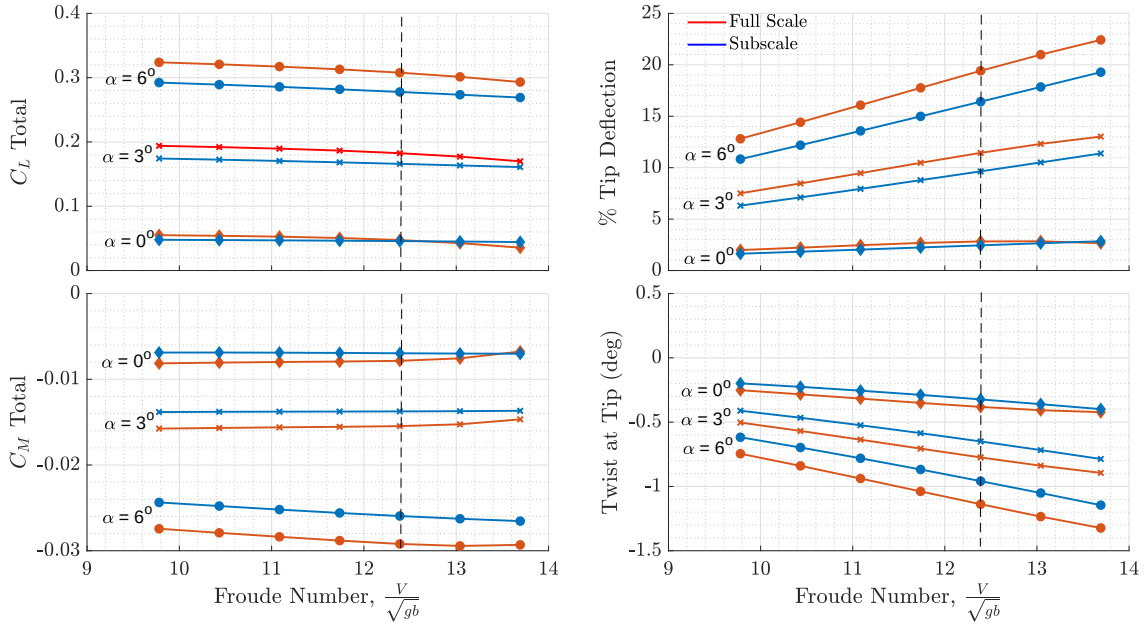

Figure 6.8: Static response comparison as a function of Froude number.

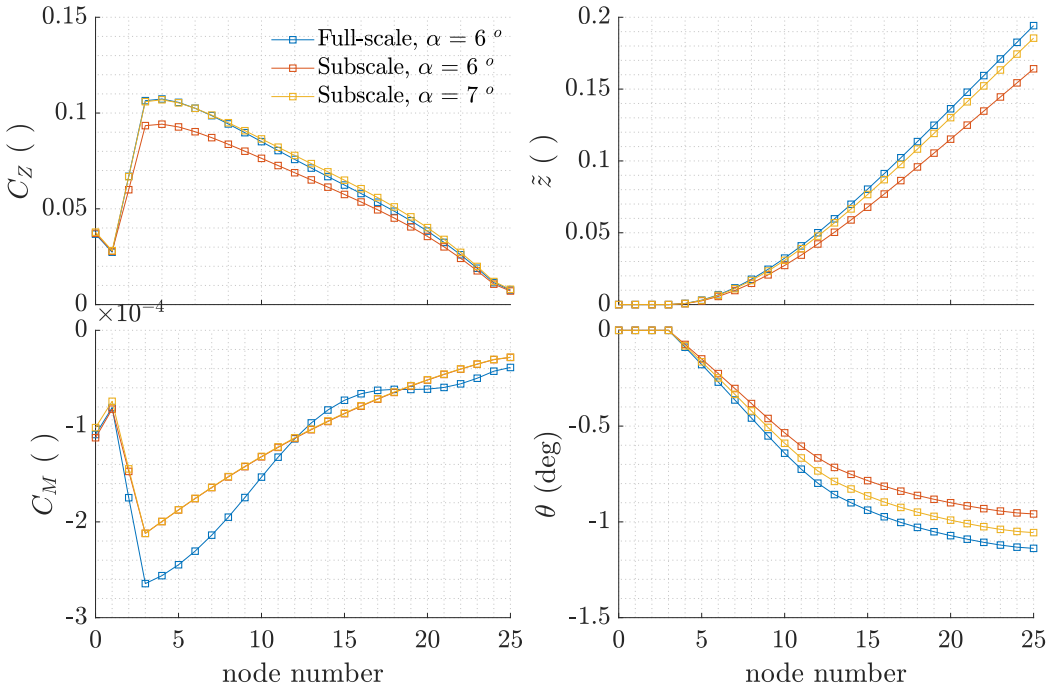

Figure 6.9: Comparison of the force and moment distribution along the semispan.

Moreover, it is also of interest to investigate the spanwise distribution of the aerodynamic loading and its effect on the static shape as presented in Figure 6.9. The flight condition represented in this figure is the target speed, which is at Froude number 12.4 (190 m/s at 35,000 ft for full-scale model and 47.5 m/s at 0 ft for the subscale model). However, as mentioned earlier, the subscale model tends to have a smaller tip deflection due to lower aerodynamic forces and moments. Considering this as a static problem, Chapter 5 mentioned that adding initial force L_0 can solve the difference in the static deflection, which can be obtained by adding α_0. Therefore, in Figure 6.9, the subscale model is simulated for 6 degrees (designed α) and 7-degree angle-of-attack. The figure shows that by setting the angle-of-attack one degree higher than expected, the lift distribution between the full-scale and subscale model are almost comparable. However, the necessary change in the pitching moment distribution cannot be achieved solely via this change. Although small, differences in the pitching moment have secondary order affects on the static wingtip deflection. Also, the difference in the twist angle is less than 1 degree and therefore it can be deemed negligible.

6.3 Physical Subscale Model Development

In the previous section, the full-scale wing and the development of its theoretical subscale model were discussed. For clarity reasons, the theoretical full-scale and subscale model later is noted as a full-scale conceptual and subscale conceptual model. The work in the following section discusses the physical development of the subscale conceptual model.

6.3.1 Spar and Skin Design

The idea behind the physical subscale design is that the xb-2 model can be built by combining independently designed spar and skin, where the spar is designed to match the structural stiffness and the skin is designed to provide the aerodynamic shape. The skin was made using PolyJet printing technology and a proof-of-concept study of this technology was conducted using the xb-1 wing design [24]. The use of PolyJet printing is essential in the development of an aeroelastic subscale model as this method can change the conventional manufacturing method in developing an aeroelastic subscale model. Conventionally, gaps between pods are needed to allow the aeroelastic subscale models to freely deform; the use of PolyJet printing helps to eliminate the need for such gaps by printing a flexible material between pods, without affecting the stiffness properties of the model. An assessment of the effects of the 3-D PolyJet printing technology to the overall stiffness of the model is given in Appendix B. The results show that by printing rigid and elastic pods alternately, a consistent aerodynamic shape is obtained and less than 5% influence is added to the overall stiffness of the model [24].

Spar Design

The structural definition of the subscale model was presented earlier along with the structural characteristics and its comparison to the full-scale design. Here, a spar was

optimised and developed to match the stiffness matrix of the theoretical subscale model. The optimisation method for the development of the spar model was performed by Pontillo et al. and the reader is referred to References [23, 173] for an in-depth discussion. However, some key considerations were:

1. The total length of the subscale model is expected to be 1.5 meters, however, to give some space for the skin attachment, the spar is layed out to have a length of 1.45 m.

2. The spar is designed to match bending stiffness (EI_{xx}) and in-plane stiffness (EI_{zz}), which is dictated by the stiffness matrix of the theoretical subscale model.

3. The wing shape constrains the width of the spar. Therefore, to match the stiffness, the cross-sectional area of the spar is varied over the outer half of the span.

4. The spar is built using aluminium to be as light as possible, and it should be noted that the matching of the mass distribution was ignored for the optimisation routine.

5. For experimental purposes (ground/wind tunnel testing), a clamp was manufactured at the root section.

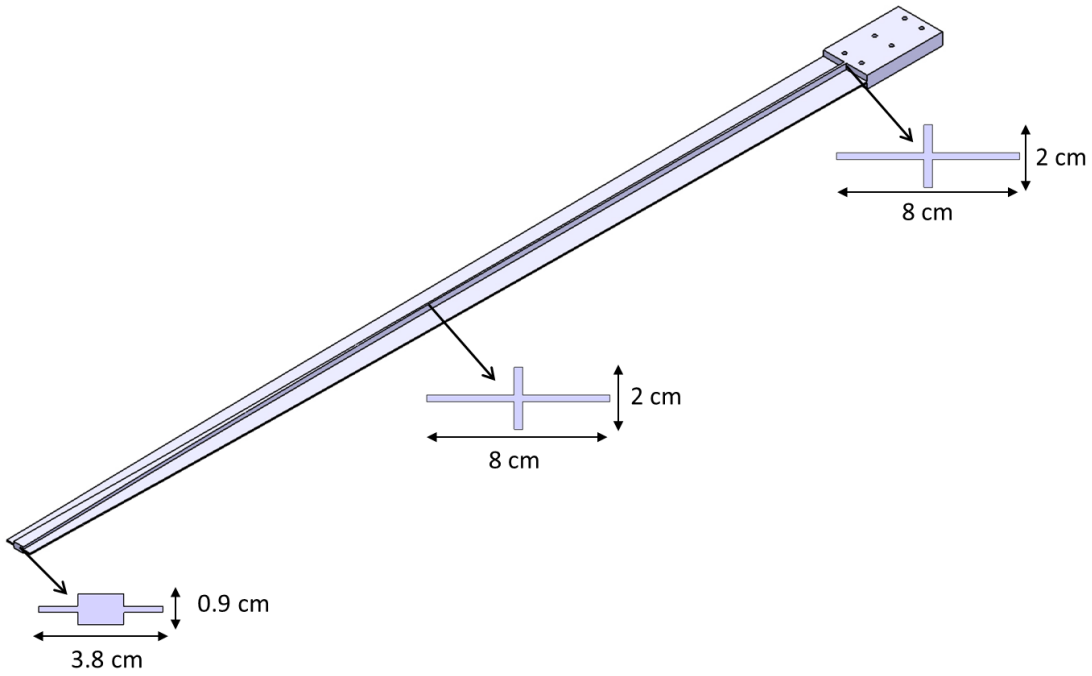

Figure 6.10: Final spar design with cross section.

The CAD model of the final spar design is presented in Figure 6.10, showing the optimised spar cross-section. The structural characteristics of the spar obtained from the CAD model are transformed into NASTRAN using beam elements. This model consists of 25 nodes with the first three nodes constrained in all DoF to replicate the clamp section. It is worth mentioning that the total mass of the spar was expected to be around 0.65 kg which is less than 25% of the total target weight.

	Target Model	Spar Model
Mode 1	1^{st} Bending - 17.4 rad/s	1^{st} Bending - 35.2 rad/s
Mode 2	2^{nd} Bending - 86.9 rad/s	1^{st} Lagging - 177 rad/s
Mode 3	1^{st} Lagging - 87.9 rad/s	2^{nd} Bending - 204 rad/s
Mode 4	1^{st} Torsion - 154 rad/s	1^{st} Torsion - 415 rad/s
Total Mass	3.42 kg	0.65 kg

Table 6.7: Frequency comparison of the target sub-scale and spar model.

The dynamic response of the spar model was analysed using NASTRAN solver SOL103. Table 6.7 shows the comparison of modal frequencies for the target subscale model and the spar design. Since the spar has less mass than the target model, the natural frequency of the spar is expected to be much higher than the target model. However, once the skin is attached, the spar and skin combine have a higher mass that leads to lower natural frequency.

Skin Design

As the spar was designed to match the stiffness, the skin provides the aerodynamic shape of the subscale model. The wing design was done by Pontillo [173] for which the following key features were considered:

1. The skin has to be printed with the shape of NACA 23015.
2. The thickness of the skin shell is 2 mm, except at the leading and trailing edge of the wing which is not hollow to reinforce the aerodynamic profile (see Figure 6.11).
3. The skin is designed to allow enough flexibility to bend without buckling. So, digital ABS was used for the rigid part and agilus was used for the elastic part as used in Reference [24]. A thin elastic-pod was printed in between two rigid pods to ensure the flexibility under load.
4. Distributed pillars were printed along with the skin for attachment to the spar (see Figure 6.11). These pillars also allow the transfer of aerodynamic load to the spar.
5. The skin is printed in a modular fashion as presented in Figure 6.12. The modular design provides the flexibility to modify the design (such as added wingtip devices) as well as to mitigate costs due to damage [24].
6. Some windows are located on the skin to allow access to the spar, pillars and instrumentation systems. These windows are located on the wide rigid pods that include space for control surfaces.
7. A pocket was designed at the wing tip to place additional mass, a passive flutter suppression mechanism.

The CATIA model of the skin is presented in Figure 6.12. The purple colour shows the control surface locations, while the pink colour highlights the location of the elastic pods. All elastic pods have a length of 1 cm and the length of the rigid pod is varied depending

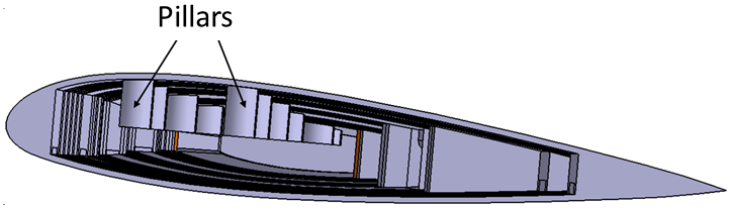

Figure 6.11: Cross-sectional cut of the skin.

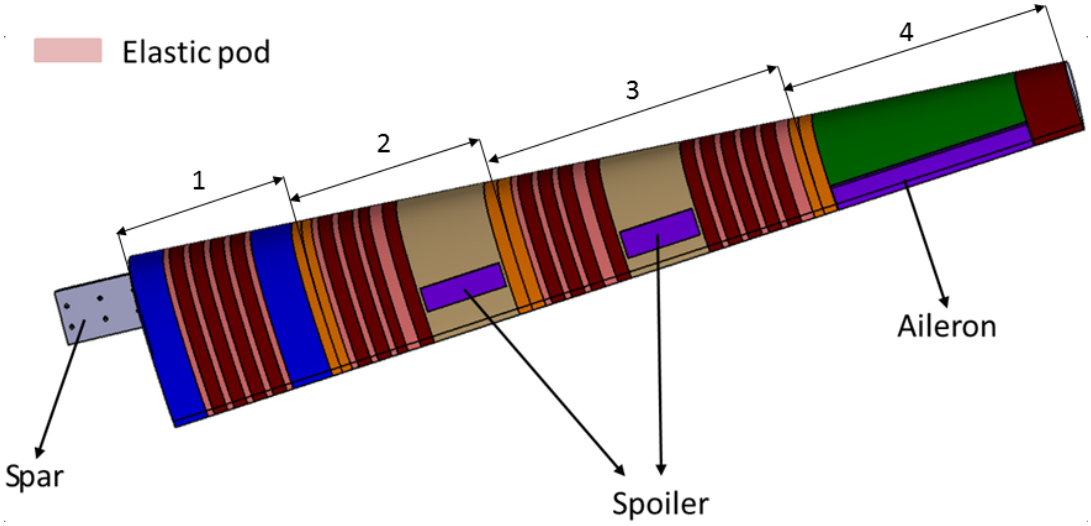

Figure 6.12: Wing design.

on the location of the control surfaces and windows. Cross-sectional material properties are extracted from CAD model, such as weight, CG location and the mass moments of inertia. These properties are added as lumped masses to the NASTRAN spar model. The position of the skin and its CG locations in the chordwise and spanwise directions are shown in Figure 6.13. For clear referencing, the NASTRAN model of the spar (and skin) will be addressed from now on as FE model. The target model was designed such that the location of the lumped masses were as close as possible to the quarter chord line. In practice, the CG of the skin was found to be more towards the trailing edge at around 40% chord.

The total weight of the skin was expected to be around 1.5 kg, making the total mass

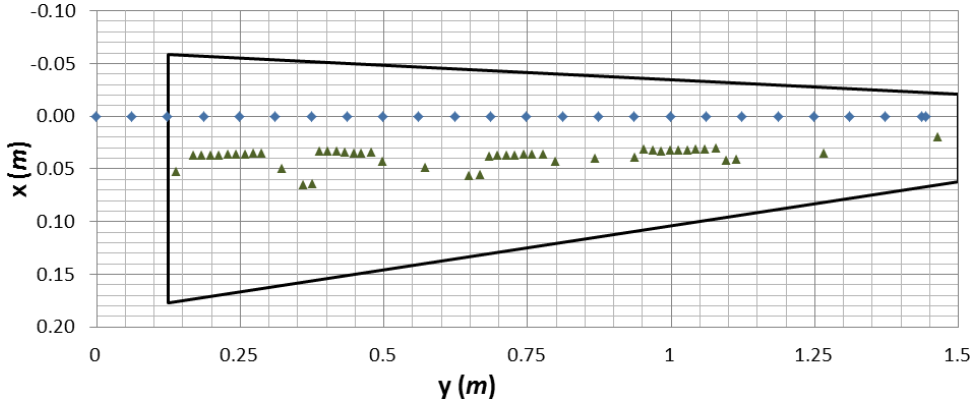

Figure 6.13: Center of gravity position of the skin and spar.

of the subscale wing 2.18 kg, lower than the total target mass of 3.42 kg. The weight of the spar and skin are deliberately lower than the target to allow space for added mass due to joints, instrumentation systems as well as servo actuators. Moreover, this allows some space to distribute lumped masses needed to match the targeted frequencies and mode shapes. The NASTRAN model is used to predict the structural behaviour of the spar and skin configuration, and the results are presented in Table 6.8.

	Conceptual Subscale Model	FE Spar Model	FE Spar-Skin Model
Mode 1	1^{st} Bending - 17.4 rad/s	1^{st} Bending - 35.2 rad/s	1^{st} Bending - 19.5 rad/s
Mode 2	2^{nd} Bending - 86.9 rad/s	2^{nd} Bending - 177 rad/s	1^{st} Torsion - 50.6 rad/s
Mode 3	1^{st} Lagging - 87.9 rad/s	1^{st} Lagging - 204 rad/s	1^{st} Lagging - 99.2 rad/s
Mode 4	1^{st} Torsion - 154 rad/s	1^{st} Torsion - 415 rad/s	2^{nd} Bending - 102 rad/s
Total Mass	3.42 kg	0.65 kg	2.18 kg

Table 6.8: Comparison of modal frequencies and shapes.

As expected, combining the spar and skin reduced the structural frequencies. However, the predicted frequencies were still slightly higher than the targeted frequencies. These differences were adjusted by placing lumped masses along the wing. This also allows to match the total target wing weight.

Furthermore, the addition of the skin shifted the overall CG towards the trailing edge and consequently changed the chordwise moment of inertia. This reduced frequency of the torsional mode for the spar-and-skin configuration when compared to the conceptual model. In fact, the torsional mode replaced the second bending mode (see Table 6.8). Having such a configuration inside the wind tunnel can lead to flutter at a lower velocity.

6.3.2 Conceptual Design Update

The initial Spar-Skin model resulted in less mass compared to the total target mass, but a higher mass moment of inertia value (I_{yy}) relative to the conceptual design, as shown in Figures 6.14[4]. The consequences of having a lighter model resulted in higher dynamic frequency in bending and lagging, while the higher I_{yy} value affected the dynamic frequency of the torsional mode. The shift of the torsional mode frequency towards the first bending mode frequency reduced flutter margin that is highly undesirable.

Now, as mentioned in Chapter 5, a distorted model in the mass moment of inertia resulted in a different angle-of-attack response. One of the solutions to this problem is by increasing the torsional stiffness. However, changing the torsional stiffness is not possible as this means changing the manufactured spar configuration.

The remainder of this research work aims to use the manufactured Spar-Skin model for wind tunnel experiments. Therefore, the conceptual model needs to be updated by

[4]It is of interest to look at the mass (and inertia) at y=1.26 m. The FE Spar-Skin model shows a higher mass value. This is because of the aileron which was physically printed as solid and consequently shifted the CG to the trailing edge. Furthermore, the I_{yy} distribution of the concept model is not realistic as in practice this expected to be a quadratic distribution from root to tip.

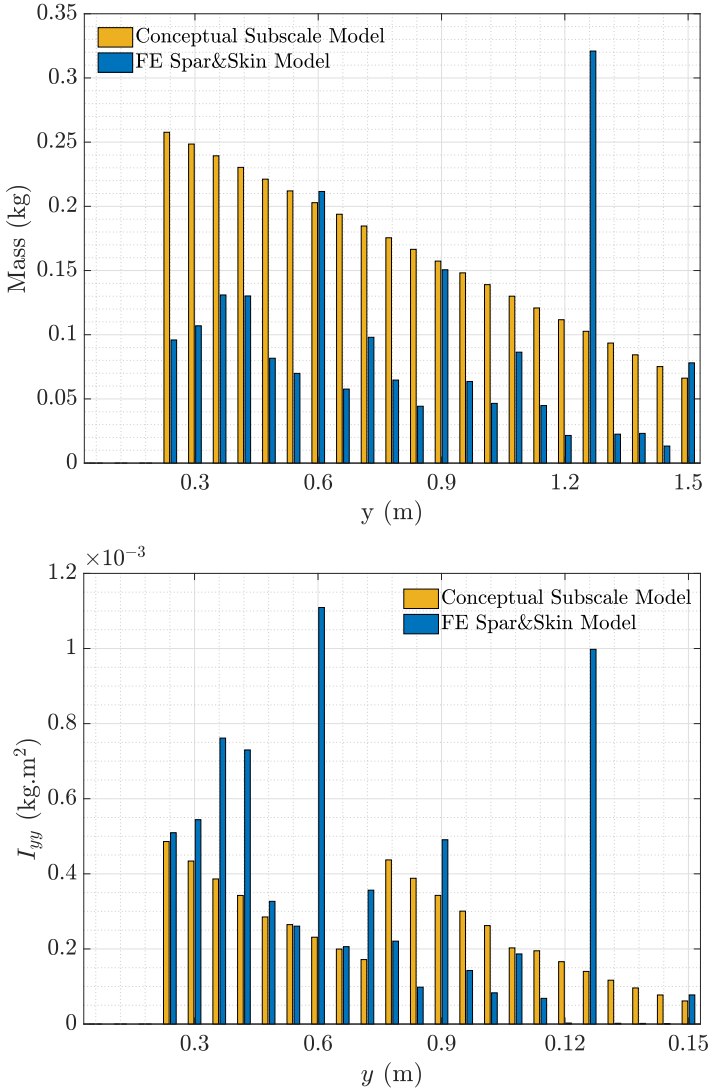

Figure 6.14: Comparison of mass and inertia distribution of the conceptual model and the FE Spar-Skin model.

increasing its mass by 20%[5]. This results in a total target mass of 4.27 kg instead of 3.42 kg and therefore, a lower structural frequency as presented in Table 6.10. This model will now be referred to as conceptual model ver.2. The mass and inertia distributions of both conceptual models are shown in Figure 6.15. The yellow bars represents the first conceptual model, while the red bars is the conceptual model ver.2 which is now the new target model. For comparison purposes, the mass and inertia distributions of the FE Spar-Skin model is also presented with the blue bars.

Ideally, to match the structural response as closely as possible with that of the conceptual design, lumped masses need to be optimally placed along key spanwise and chordwise position along the wing. Optimisation routines, such as those used in Finite Element

[5]The increment of 20% mass conducted by increasing the mass of each lumped mass by 20%, which will affect the static deflection of the conceptual design aircraft. The number is chosen to give enough flexibility in terms of modifying the already manufactured spar and skin, without much affecting the underlying assumption of the full-scale wing development.

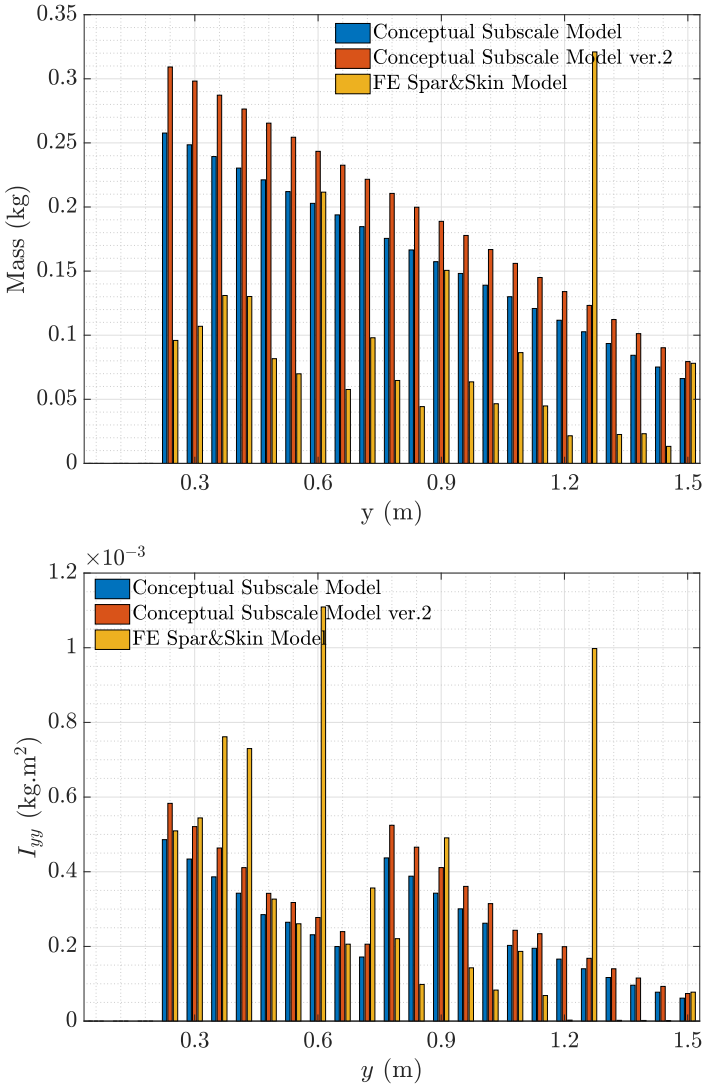

Figure 6.15: Comparison of the updated conceptual model and the FE Spar-Skin model.

	Conceptual Model	Conceptual Model v.2
Mode 1	1^{st} Bending - 17.4 rad/s	1^{st} Bending - 15.7 rad/s
Mode 2	2^{nd} Bending - 86.9 rad/s	2^{nd} Bending - 77.5 rad/s
Mode 3	1^{st} Lagging - 87.9 rad/s	1^{st} Lagging - 78.1 rad/s
Mode 4	1^{st} Torsion - 154 rad/s	1^{st} Torsion - 148 rad/s
Total Mass	3.42 kg	4.27 kg

Table 6.9: Structural frequency of the conceptual model ver.2.

Model Updating methods [204, 205] are thus needed prior to manufacturing. However, since the spar and skin were already manufactured, a compromise had to be made. As a result the lumped masses were used to match only the first bending mode and ensuring a flutter speed above 60 m/s.

The initial attempt to match the first bending frequency is by ensuring that the mass and I_{yy} distribution are as close as possible to the conceptual model ver.2. This was done by calculating the size and location of the lumped mass in the chordwise direction (x)

for each node[6] as follows :

$$\Delta m_i = m_i^t - m_i^s \tag{6.3.1}$$

$$\Delta I_{yy_i} = {I_{yy_i}}^t - {I_{yy_i}}^s \tag{6.3.2}$$

$$\text{if} \quad \Delta I_{yy_i} < 0, \quad x_i = 0$$

$$\Delta I_{yy_i} > 0, \quad x_i = \sqrt{\frac{\Delta I_{yy_i}}{\Delta m_i}} \tag{6.3.3}$$

for which m_i^t, m_i^s are the target mass and spar-and-skin mass at grid i respectively, while ${I_{yy_i}}^t$, ${I_{yy_i}}^s$ are the mass moment of inertia at grid i respectively. The value x is the position in chordwise direction defined from 25% chord, for which negative x represents leading edge direction and positive x is in the trailing edge direction. The position of the lumped mass is also calculated in the z-direction by considering the thickness of the skin without changing the aerodynamic shape. Note that this optimisation is an idealistic approach and the arising limitations will be addressed later.

However, as this configuration can also be considered as a conceptual model, for brevity it will be referred to as conceptual model ver.3. This model will be the basis of the target model being manufactured. This conceptual model is evaluated by modelling the lumped masses in NASTRAN and using SOL 103 to obtain the structural characteristics. Table 6.10 presents the respecting mode shape and frequencies of the conceptual model ver.3, while the mass and inertia distributions are presented in Figure 6.16. Note that in some nodes the I_{yy} value will still remain large.

	Conceptual Model	Conceptual Model ver.2	Conceptual Model ver.3
Mode 1	1^{st} Bending - 17.4 rad/s	1^{st} Bending - 15.7 rad/s	1^{st} Bending - 16.3 rad/s
Mode 2	2^{nd} Bending - 86.9 rad/s	2^{nd} Bending - 77.5 rad/s	1^{st} Torsion - 48 rad/s
Mode 3	1^{st} Lagging - 87.9 rad/s	1^{st} Lagging - 78.1 rad/s	2^{nd} Bending - 82.3 rad/s
Mode 4	1^{st} Torsion - 154 rad/s	1^{st} Torsion - 148 rad/s	1^{st} Lagging - 83.8 rad/s
Total Mass	3.42 kg	4.27 kg	4.21 kg

Table 6.10: Structural frequency of the target, updated target sub-scale model ver.2, and updated target sub-scale model ver.3.

The NASTRAN model has then been used to determine flutter modes using SOL 145. In this case, the aerodynamic shape is calculated assuming it to be a flat plate. Figure 6.17 presents the variation of damping and frequency for the conceptual design ver.3 with respect to velocity. The figure shows that the first six aeroelastic modes are stable until 70 m/s, which indicates that the flutter speed is more than 70 m/s[7]. Therefore, it can be concluded that this model can be tested safely inside a wind tunnel (the tunnel maximum velocity is 50 m/s). Note that, the target design of the wing has now moved to conceptual design ver.3.

[6]The 1.5 meter wingspan is divided into 25 equal nodes for FE model development.

[7]The damping values in the figure are obtained from NASTRAN. In NASTRAN, the flutter is calculated using PK method [176], where the equation of motion is written such that negative damping illustrate stability.

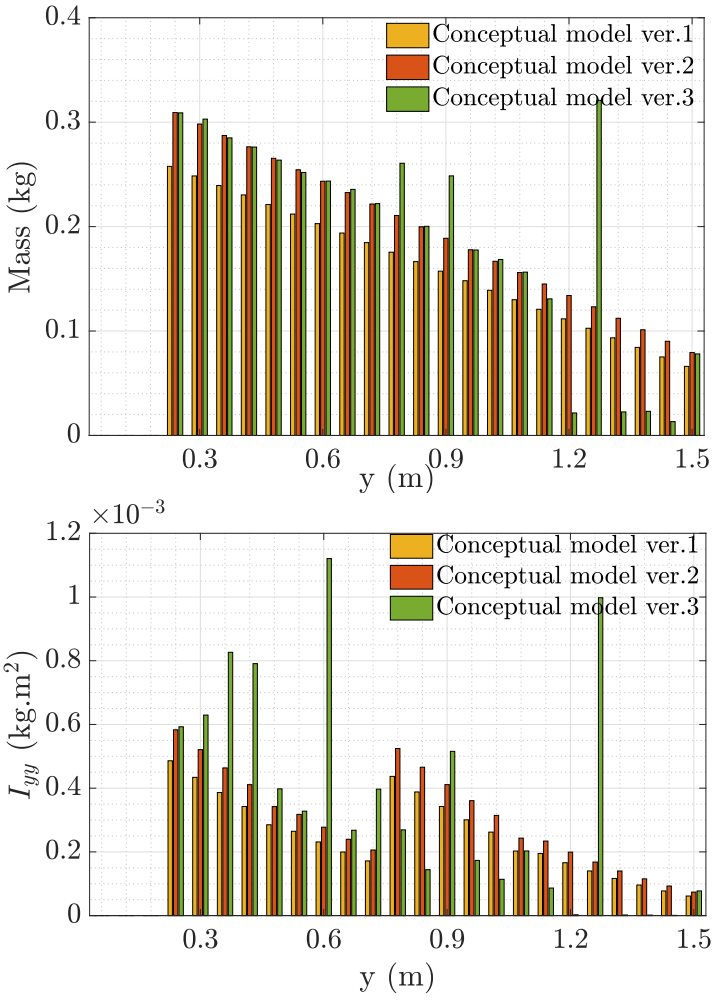

Figure 6.16: Evolution of the updated conceptual model.

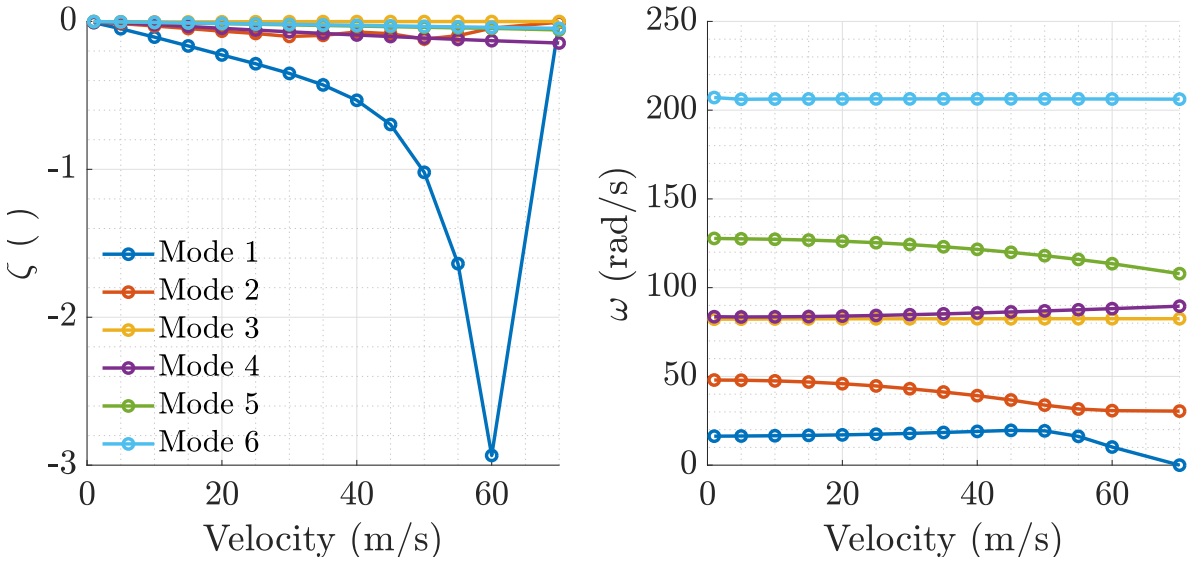

Figure 6.17: Flutter speed prediction of conceptual model ver.3.

6.3.3 Wind Tunnel Subscale Model

The manufactured spar and skin has limited physical space for further modifications due to the load transfer pillars and instrumentation system. Moreover, applying Equation 6.3.3 in optimising the lumped mass position results showed that some of these should be positioned on the grid point which is physically impossible. Therefore, high density brass was used for manufacturing the actual lumped mass and an attempt was made to position the masses such that the result was close to the conceptual design ver.3.

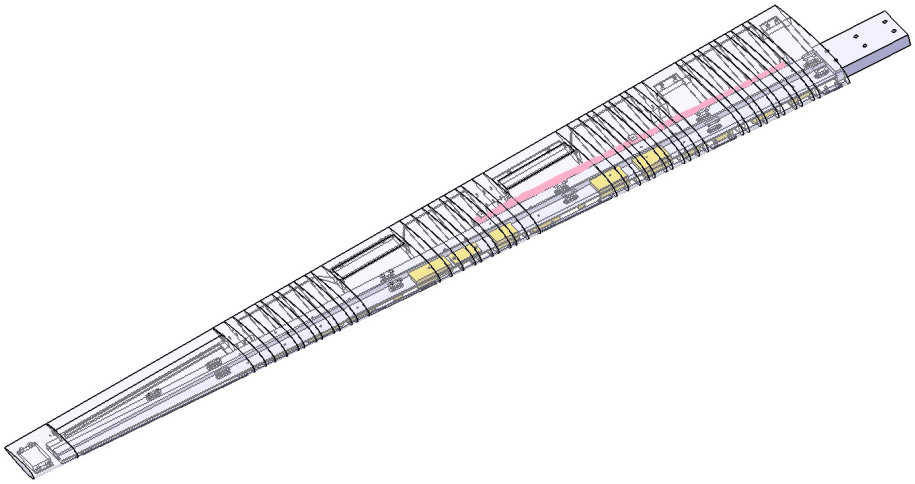

Figure 6.18: CATIA wind tunnel model (yellow represents the lumped masses, pink highlights the position of the rod).

The manufactured Spar-Skin model was hence updated with lumped brass-massed and is now referred to as Spar-Skin-Mass (SSM) configuration. However, transferring the SSM model to NASTRAN resulted in a lower flutter velocity than the conceptual model ver.3 (around 30 m/s, as evident in Figure 6.21). Therefore, on top of the SSM model, a 72 cm cylindrical rod was mounted to the spar to increase torsional stiffness. This rod has a diameter of 10 cm with 1 mm thickness and was located near the root, as shown in Figure 6.18. This rod also impacted the bending flexibility of the subscale model. The final model tested inside the wind tunnel is the spar-skin-mass-rod configuration. In the following text, the configuration of spar-skin-mass-rod will be called the wind tunnel model, and the CATIA model of the configuration has been presented in Figure 6.18.

The NASTRAN model was updated based on the lumped mass and rod configuration to represent the FE SSM model and the FE wind tunnel model. Modal frequencies and shapes are compared in Table 6.18. It is clear that by placing the lumped masses the change in the bending frequency is negligible, but the torsional mode has moved to a higher frequency. Although there is enough separation between the first bending and torsion modes for the FE SSM model, the flutter speed is still quite low at around 30 m/s. On the other hand, adding the rod to the spar increases the torsional rigidity, confirmed by the fact that now the torsional mode has replaced the second bending mode and it occurs at a much higher frequency (evident in Table 6.18). The mode shape of the wind tunnel model is given in Figure 6.19. Furthermore, flutter prediction on the

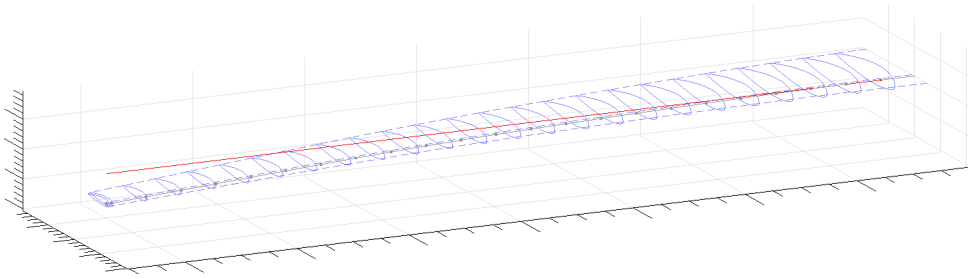

Mode 1 at 24 rad/s (bending)

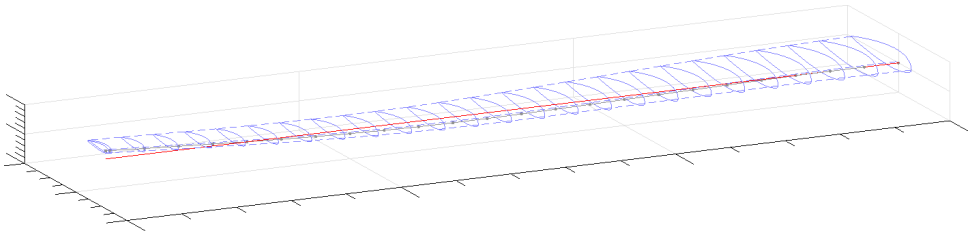

Mode 2 at 85.8 rad/s (bending)

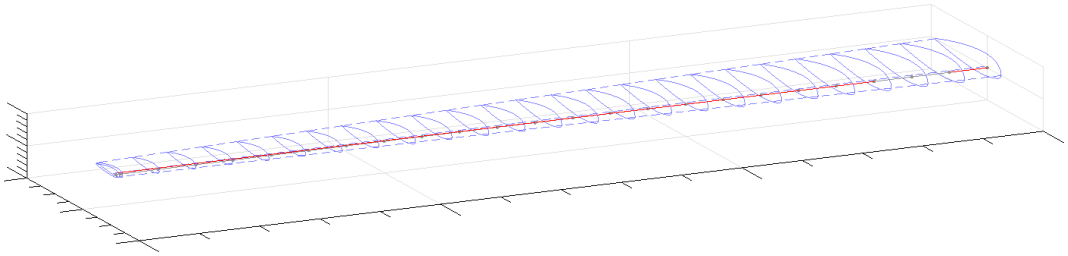

Mode 3 at 109.8 rad/s (torsion)

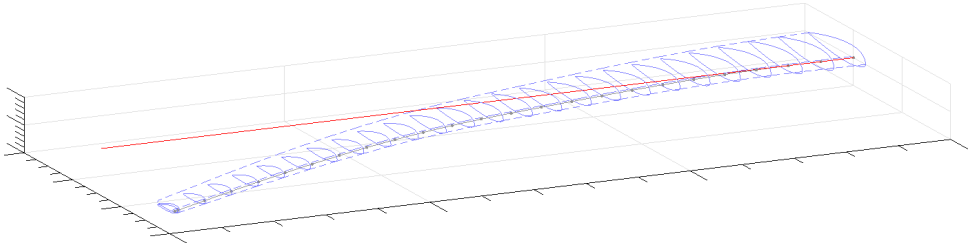

Mode 4 at 117.6 rad/s (lead-lag)

Figure 6.19: Structural mode shapes of the FE wind tunnel model.

FE wind tunnel model results in a flutter speed of around 47.5 m/s. Thus, the FE wind tunnel model was made safe for wind tunnel testing at speed below 45 m/s. However, the FE model is based on numerous assumptions and simplifications. Such as, ignoring the lumped masses due to instrumentation system, pre-defining structural damping and simplifying the aerodynamic model. In the next section, the FE model will be validated using GVT.

	Conceptual Model ver.3	FE SSM	FE wind tunnel
Mode 1	1^{st} Bending - 16.3 rad/s	1^{st} Bending - 16.1 rad/s	1^{st} Bending - 24.0 rad/s
Mode 2	1^{st} Torsion - 48 rad/s	1^{st} Torsion - 63.9 rad/s	2^{nd} Bending - 85.8 rad/s
Mode 3	2^{nd} Bending - 82.3 rad/s	2^{nd} Bending - 77.8 rad/s	1^{st} Torsion - 109.8 rad/s
Mode 4	1^{st} Lagging - 83.8 rad/s	1^{st} Lagging - 81.7 rad/s	1^{st} Lagging - 117.6 rad/s
Total Mass	4.21 kg	3.91 kg	4.09 kg

Table 6.11: Structural frequency comparison of updated and manufactured model.

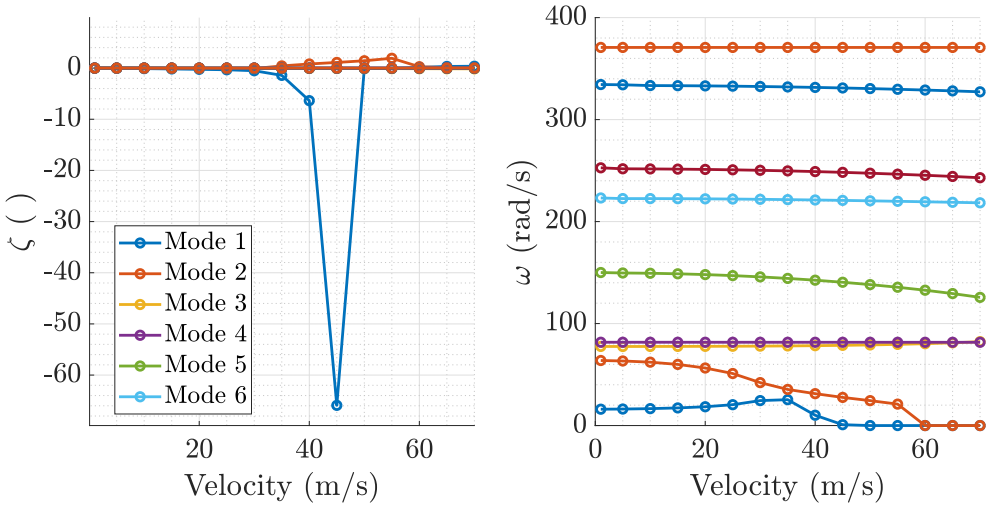

Figure 6.20: Flutter speed prediction for the SSM configuration.

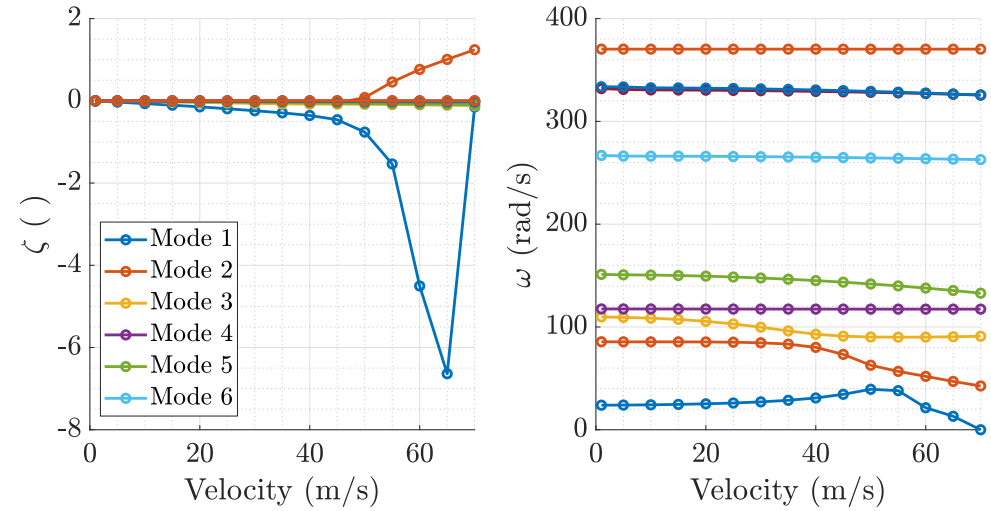

Figure 6.21: Flutter speed prediction for the FE wind tunnel configuration.

6.4 Experimental Validation

6.4.1 Structural Validation

A GVT was carried out to validate the FE model of the previous configurations of spar, Spar-Skin, as well as the final wind tunnel model. Overall, the GVT was carried out with the use of random-on-random (RoR) vibration over a frequency range of 1 to 50 Hz. The excitation was introduced to the spar structure via a stinger that was attached to the underside of the spar root. The spar was mounted to a rigid structure using the designed clamping fixture at the spar root. The structural dynamics were characterised by using five uni-axial accelerometers. The test set-up is presented in Figure 6.22.

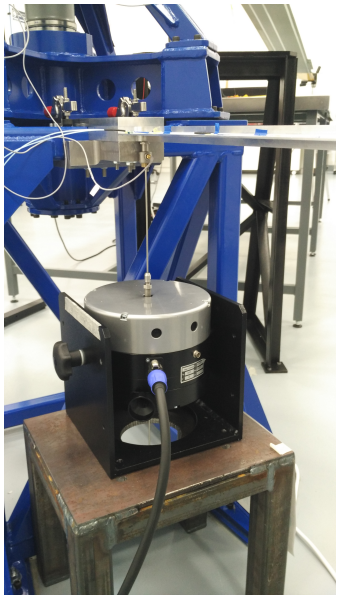

Instrumentation set-up

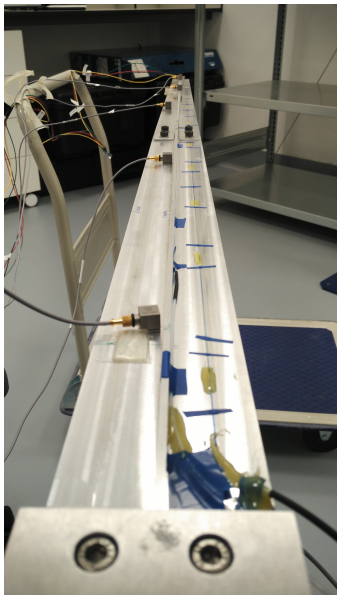

Test bench

Figure 6.22: Example of the GVT setup for spar configuration.

To ensure that the desired target modes were captured as accurately as possible, a sensor placement approach based on error minimisation (developed by Weber [107]) was used. This methodology aims to minimise the total error between theoretical and experimental mode shapes by minimising the following cost function:

$$J = \sqrt{\frac{1}{n}\sum_{i=1}^{m}\sum_{j=1}^{n}(\Phi_{ij} - \hat{\Phi_{ij}})^2} \tag{6.4.1}$$

where Φ is the numerical mode shape, $\hat{\Phi}$ is the sensor mode shape, m is the number of target mode shapes to be considered and n is the number of nodal points. Each mode shape was treated with equal importance essential for recovering experimental mode shapes of interest. As uni-axial accelerometer were used, only the bending modes could be identified from the GVT test results through subspace identification methods as presented earlier in Chapter 3.

Spar Only Configuration

A compromise had to be made during the manufacturing of the spar. The total length of the spar which is 1.45 m was difficult to machine in one piece. Therefore, the spar was manufactured in two equal halves and welded together afterwards. To ensure that the welding seam did not fatigue during the structural testing, a bridge was fixed around the welding joint (see Figure 6.23). This resulted in an update to the developed NASTRAN model by where the additional support was modelled as a lumped mass. Results showed that the change in frequency as well as mode shape were negligibly small.

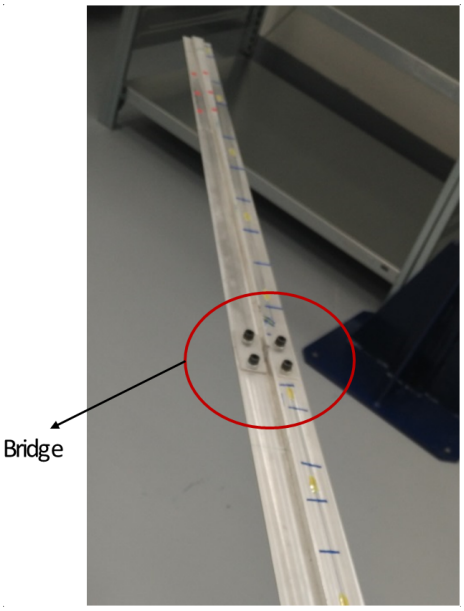

Figure 6.23: Bridged spar.

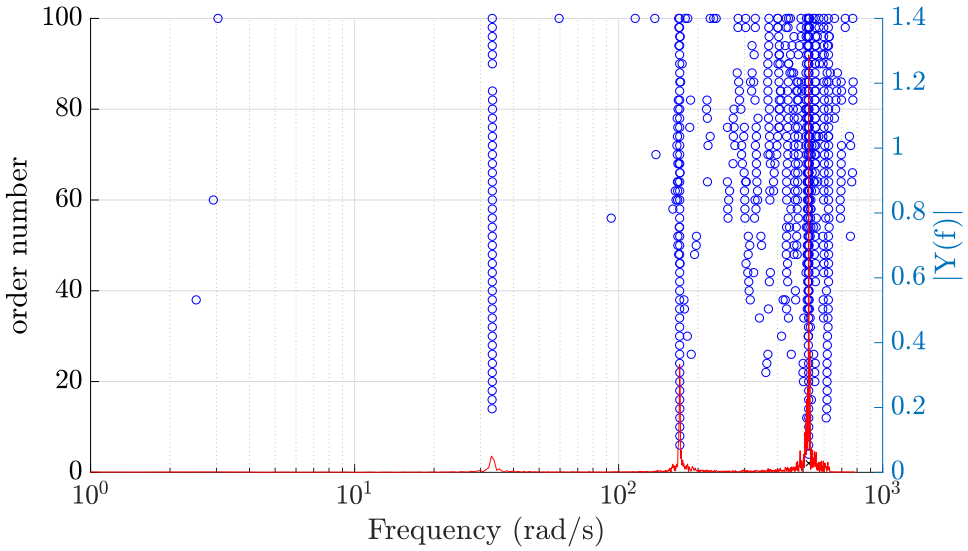

Figure 6.24: Stabilisation diagram of the Spar configuration.

The stabilisation diagram of the GVT results is presented in Figure 6.25. Which shows three clear peaks of frequency response obtained from the accelerometer at the tip of the

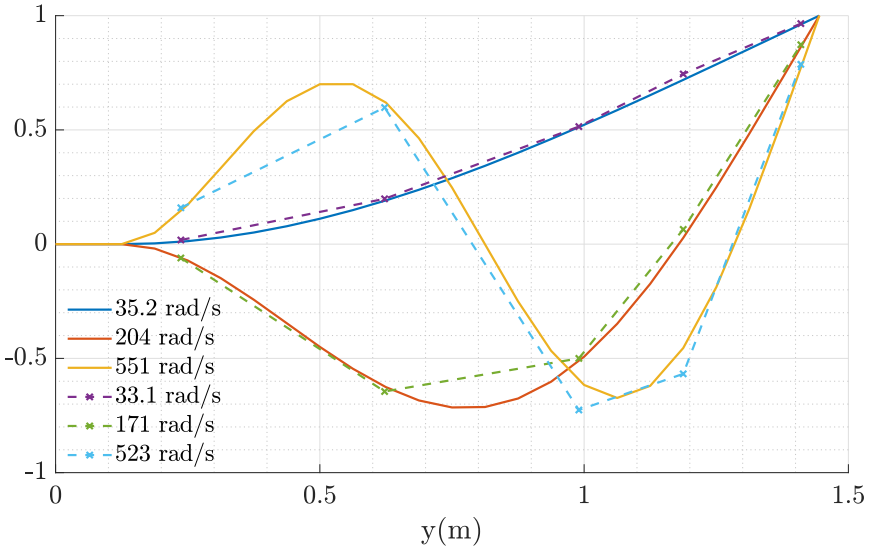

Figure 6.25: Identified mode shape from GVT on the spar (— : theoretical mode shape, −−: identified mode shape).

spar. Based on this diagram, a model order of 30 was chosen and the corresponding mode shapes and frequencies are shown in Figure 6.25. The comparison between the natural frequencies from the experimental results and the FE model is given in Table 6.12. The table also shows the comparison of mode shape in terms of MAC (as mentioned previously in Chapter 3 and 4.3). The difference between the FE model and the identified frequencies are less than 15%, while the MAC shows that the mode shapes are almost identical.

	Spar Model		Differences		Damping ratio
	Theoretical	Experimental	Freq.	MAC	GVT
1^{st} Bending	35.2 rad/s	33.1 rad/s	5%	0.999	0.34 %
2^{nd} Bending	177 rad/s	171 rad/s	12 %	0.993	0.09 %
1^{st} Lagging	204 rad/s	-	-	-	-
1^{st} Torsion	415 rad/s	-	-	-	-
3^{rd} Bending	551 rad/s	523 rad/s	5 %	0.967	0.16 %

Table 6.12: Comparison of numerical spar and manufactured spar frequency.

Spar and Skin Configuration

As mentioned earlier, the skin was designed to hold the aerodynamic shape while having minimum impact on the overall stiffness. However, since the aileron was printed as a solid, it introduced significant inertial effects. Furthermore, the ailerons were designed to be fixed once assembled. Thus, an initial GVT test for the Spar-Skin configuration was carried out with the aileron and spoiler removed as shown in Figure 6.26. For the GVT of the Spar-Skin configuration, the accelerometers were placed at similar locations as for the previous test.

Figure 6.27 presents the stabilisation diagram for the GVT results of the Spar-Skin configuration, in comparison to the frequency response function obtain from the accelerometer

Figure 6.26: Spar and skin GVT setup.

at the tip. Except for the first peak at relatively low frequency (around 21 rad/s), the higher frequencies exhibit a rather noisy response but a clear stable pole can be observed at around 90 rad/s. In this case 30 was also chosen as the order number for identification purposes and the identified frequencies and respective mode shapes are given in Figure 6.28 and summarised in Table 6.13. It is clear that the first mode, which is the first bending frequency, is well identified with only 10% error and MAC value almost 1. However, for the higher modes, there are some discrepency between the identify mode shape and the theoretical mode shape. This is emphasising the fact that the NASTRAN model is not well representing the physical model that being tested, especially since the aileron and spoiler is not being installed during GVT testing. Furthermore, the results from the GVT also suggest that due to the mass distribution, except for the first mode, it is clear if the other modes are not a pure bending mode.

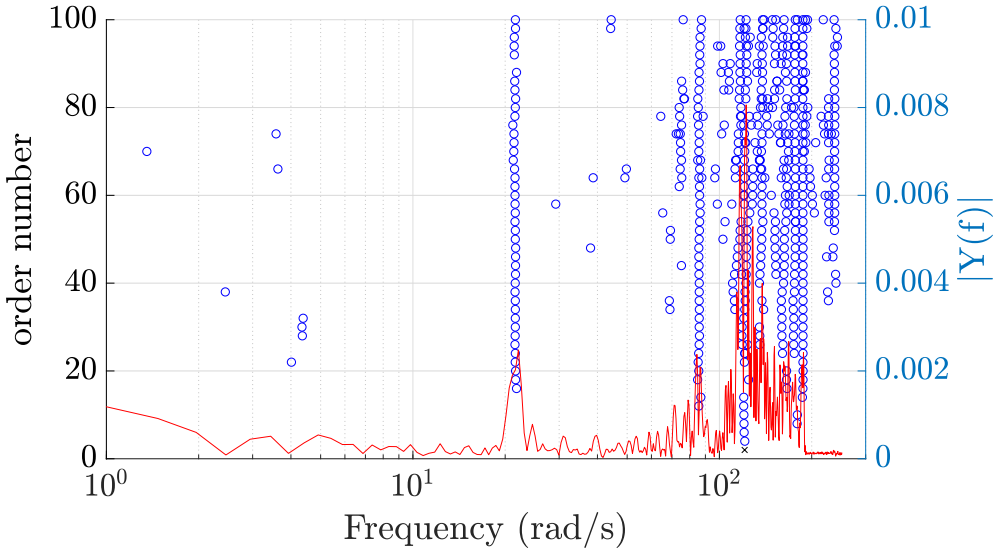

Figure 6.27: Stabilisation diagram from the GVT of the spar and skin.

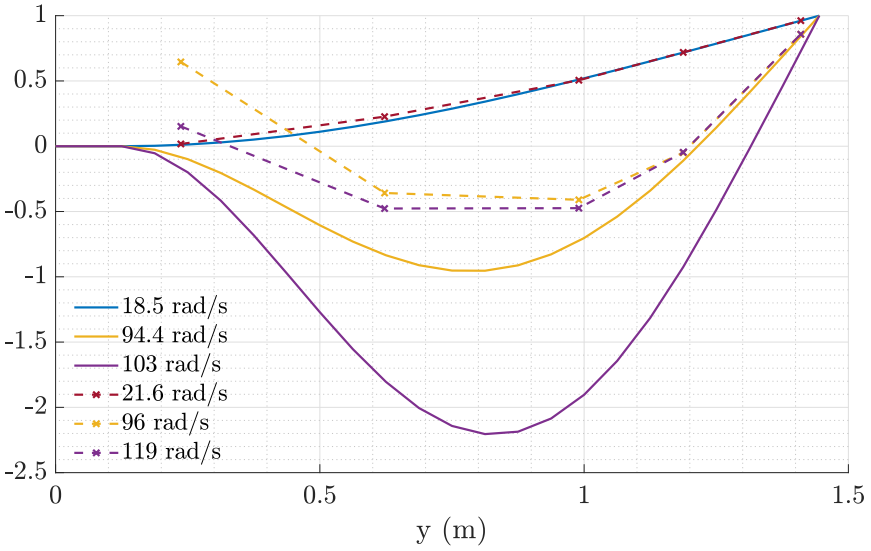

Figure 6.28: Identified mode shape from the spar and skin configuration (— : theoretical mode shape, −−: identified mode shape).

	Spar and Skin Model		Differences		Damping ratio
	Theoretical	Experimental	Freq.	MAC	GVT
1^{st} Bending	19.5 rad/s	21.6 rad/s	10%	0.999	1.7 %
Mode 2	50.6 rad/s	-	-	-	-
Mode 3	99.2 rad/s	96 rad/s	2%	0.838	21 %
Mode 4	102 rad/s	118.5 rad/s	16%	0.650	1.9 %

Table 6.13: Comparison of numerical and manufactured spar and skin configuration.

Wind Tunnel Model Configuration

One of the objectives of testing the wind tunnel configuration is to validate the FE model in order to validate the flutter prediction. On top of the Spar-Skin configuration, this configuration now includes the lumped masses and rod, as well as the control surfaces, such as aileron and spoiler. The accelerometer is attached to the skin using double-sided tape at the same location as the previous test, except for those at 1.2 m from the root. Only 4 accelerometers were used in total.

Figure 6.29 presents the wind tunnel model configuration, and it shows some of the locations of the brass lumped masses which were attached to the spar the rod, as well as the attachment point of the skin to the spar. Here the aileron is fixed at 0 °.

Figure 6.30[8] presents the stabilisation diagram of the wind tunnel model and the frequency content of the accelerometer located near the tip. Overall, there are three observable frequency peaks. These peaks are in-line with the identified stable poles. Figure 6.31 presents the corresponding identified frequencies and mode shapes. It is interesting to observe the effect of the added cylinder rod, which switches the order of the bending and torsional mode. This mode switch affects the predicted flutter frequency.

[8]Noted that the data presented in this figure has higher sampling rate compared to the previous configuration, resulting in more noisy data.

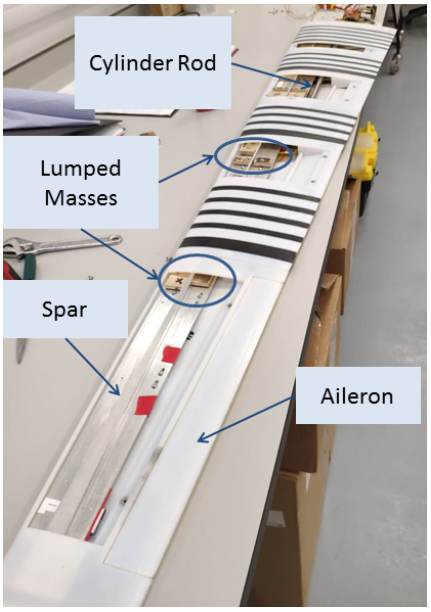

Figure 6.29: Wind tunnel model setup.

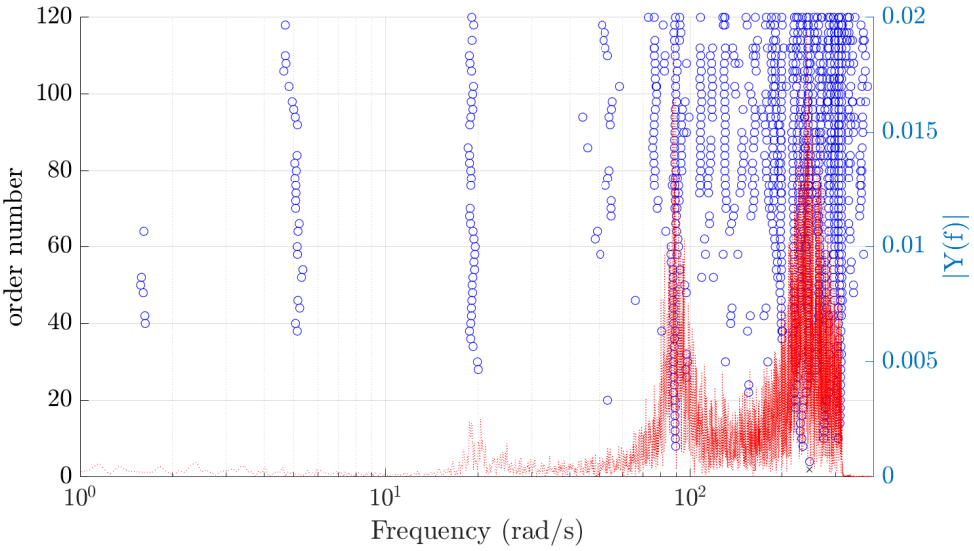

Figure 6.30: Stabilisation diagram from the GVT of the FE wind tunnel model.

In comparison to the previous spar and skin model, the identified mode in the wind tunnel configuration is much clearer. The first and second bending of the wind tunnel model were identified within less than 15% discrepancy and a MAC value of 0.99 as shown in Table 6.14. This level of agreement between the experimental and the FE mode allowed this model to be tested inside the wind tunnel.

6.4.2 Static Wind Tunnel Tests

Static wind tunnel testing for the subscale model was conducted to validate the simulation framework, known as BEaRDS^{TM}. The experiments were conducted in the Cranfield 8x6 wind tunnel facility. The wing was mounted vertically from the top of the tunnel (see

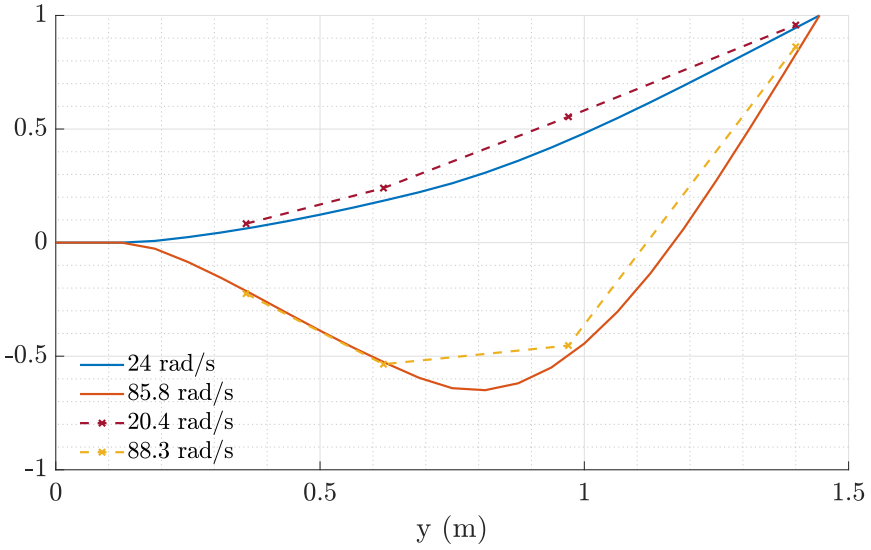

Figure 6.31: Identified mode shape from the FE wind tunnel model (— : theoretical mode shape, −−: identified mode shape).

	Wind Tunnel Model		Differences		Damping ratio
	Theoretical	Experimental	Freq.	MAC	GVT
1^{st} Bending	24 rad/s	20.4 rad/s	14%	0.992	5.8 %
2^{nd} Bending	85.8 rad/s	88.3 rad/s	3%	0.991	4.2 %
1^{st} Torsion	109.8 rad/s	-	-	-	-
1^{st} Lagging	117.6 rad/s	-	-	-	-

Table 6.14: Comparison of theoretical and experimental modes for the wind tunnel model.

Figure 6.33), and a balance allowed the measurement of the aerodynamic forces (lift and drag). The test matrix for the static wind tunnel model was designed to cover airspeeds from 20 m/s to 40 m/s, to avoid the predicted flutter speed of 47.5 m/s. This covers the chord based Reynolds number range of 2.3 $\times 10^5$ to 4.6 $\times 10^5$. Furthermore, the angle of attack varied from -2 to 6 degrees. The experiments provide a total of 25 measurement points and these data points are compared to BEARDS^{TM} predictions.

The theoretical predictions of aeroelastic static response from BEARDS^{TM} is presented in Figure 6.32. The figure shows the variation of C_L, C_M and the respective tip deflections and twist angles. All these responses are presented as a function of Froude number, to remain consistent with the comparisons in Section 6.2.3. It is worth mentioning that after the loop in the wing design, the wind tunnel model is stiffer than the conceptual model, especially with the added rod which not only contributes to the increased torsional stiffness but also to the bending stiffness of the wing. The increase of stiffness results in a much lower tip deflection. The maximum tip deflection was found to be around 5% of the wing semi-span, as opposed to the first conceptual design which was around 20% deflection.

A total of 122 data points (see Table 6.15) at different angles of attack and various airspeeds have been collected. The comparison of the total lift, as a function of the Froude number and α is presented in Figures 6.34. The figure shows that the measured

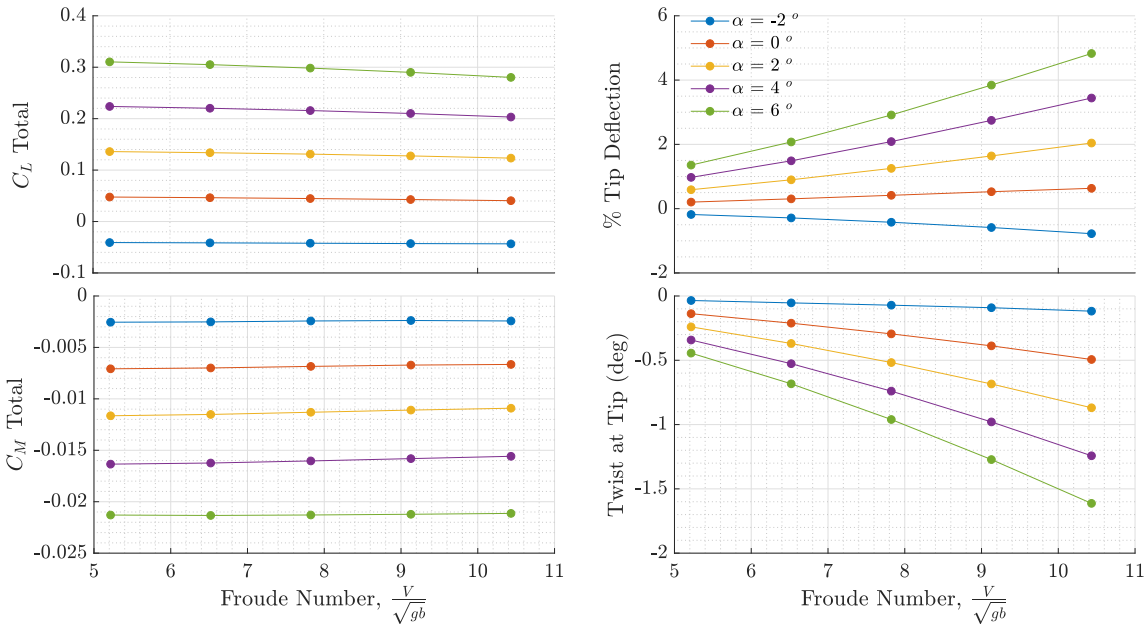

Figure 6.32: BEARDS^{TM} prediction for the static wind tunnel experiments.

Run	α	Wind Tunnel Velocity, U (m/s)								
Run 01	-2 °	20	25	30	35	40	35	30	25	20
Run 02	-2 °	20	25	29.9	35	39.9	35	30	25	20
Run 03	-2 °	20	25	30	35	40				
Run 05	6 °	20	25	30	35	40	34.9	30	25	20
Run 06	4 °	20	25	30.1	35	39.9	35	30	25	20
Run 07	2 °	20	25	30	35	40	35	30.1	25	20
Run 08	0 °	20	25	30	35	40	34.9	30	25	20
Run 09	-2 °	20	25	30	34.9	40	34.9	30	25	20
Run 10	6 °	20	25	29.9	35	39.9	35	30.1	25	20
Run 11	4 °	20	25	30	35	40	35	30	25	20
Run 12	2 °	19.9	25	30	34.9	40	35	30.1	25	19.9
Run 13	0 °	19.9	25	30	34.9	40	35	30	25.1	20.1
Run 14	-2 °	20.1	24.9	30	34.9	40	35	30.1	25.1	19.9

Table 6.15: Wind tunnel test matrix.

lift forces and the simulated lift forces are within the same order of magnitude, and overall, BEARDS^{TM} predictions show a similar trend with the experiment measurement. The comparison between the BEARDS^{TM} prediction and the data points from the wind tunnel experiments is presented in Figure 6.34.

A non-dimensional comparison between the prediction and experimental results was also made (as shown in Figure 6.35). In particular, C_{L_0} and C_{L_α} was obtained using a simple OLS method through the following standard expression:

$$C_L = C_{L_0} + C_{L_\alpha}\alpha \tag{6.4.2}$$

where C_L is the lift coefficient, C_{L_0} is the lift coefficient at $\alpha = 0$, C_{L_α} is the lift slope

Figure 6.33: The xb-2 wing inside the wind tunnel facility (left: wind speed 0 m/s, right: wind speed 40 m/s).

and α is the angle-of-attack. By utilising OLS the measurement equation was defined as:

$$z = C_L + \nu \tag{6.4.3}$$

where ν represents the measurement noise and the regressor matrix and parameter vector are given as:

$$X = \begin{bmatrix} 1 & \alpha(1) \\ \vdots & \vdots \\ 1 & \alpha(N) \end{bmatrix} \tag{6.4.4}$$

$$\hat{\Theta} = \begin{bmatrix} C_{L_0} & C_{L_\alpha} \end{bmatrix} \tag{6.4.5}$$

The variation of C_{L_α} for various Reynolds numbers was calculated based on the experimental results and then compared with the predictions from BEaRDS^{TM} (see Table 6.16). Errors remaining lower than 10% provide a degree of validation of BEaRDS^{TM} code.

6.5 Summary

The work carried out in this chapter presented the challenges in developing a conceptual aeroelastic subscale model, especially highlighting the difficulties in weight and inertia scaling, while using novel 3-D PolyJet printing technology. It has been shown that using a subscale model as proof-of-concept can be a significant challenge since a more detailed

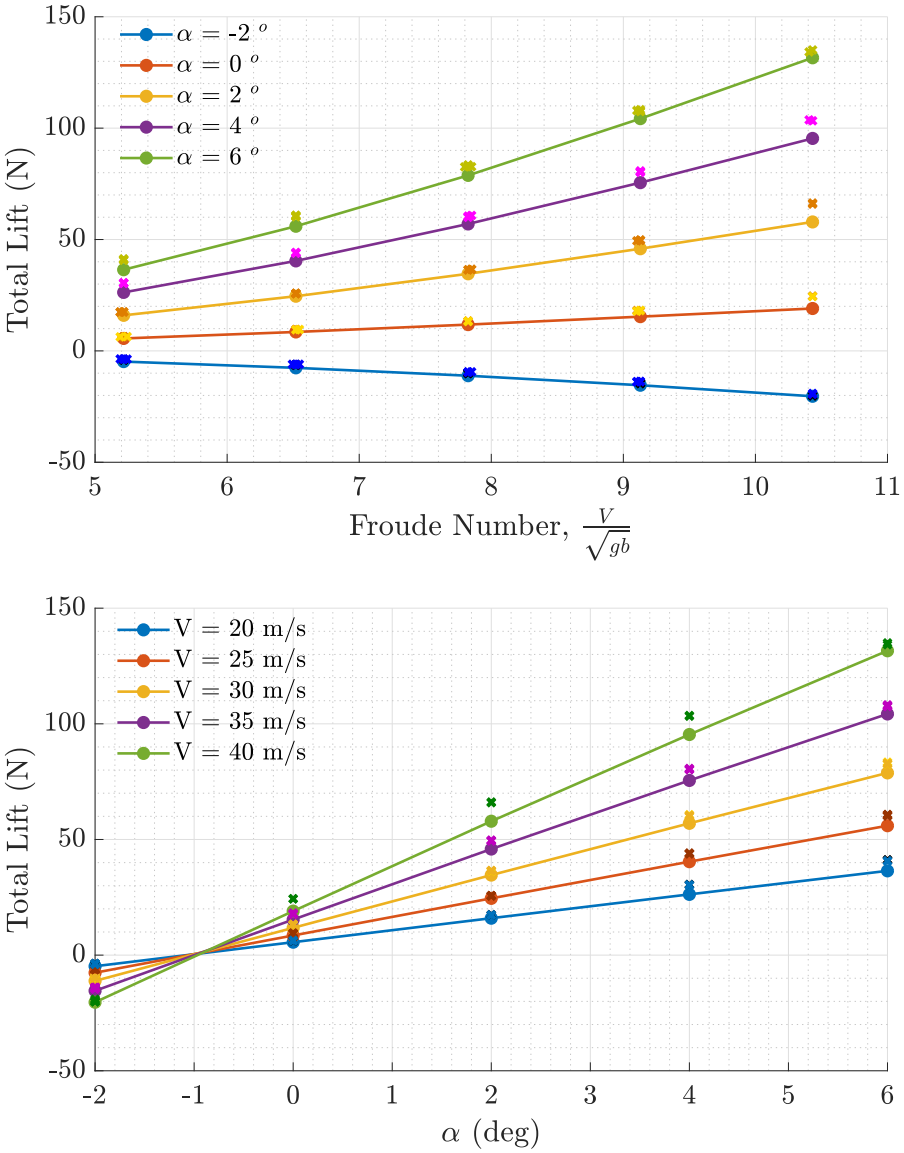

Figure 6.34: Comparison of the total lift forces between wind tunnel and BEARDS^{TM} results (×: BEARDS^{TM} , • wind tunnel).

Velocity	Re	Lift Coefficient C_{L_α} (/°)		%
		BEARDS^{TM}	Wind tunnel results	error
20 m/s	2.32 ×10^5	0.044	0.048 ± 0.0007	8 %
25 m/s	2.89 ×10^5	0.043	0.046 ± 0.0004	6.5 %
30 m/s	3.47 ×10^5	0.043	0.044 ± 0.0002	2.3 %
35 m/s	4.05 ×10^5	0.042	0.043 ± 0.0005	2.3 %
40 m/s	4.63 ×10^5	0.041	0.042 ± 0.0015	2.4 %

Table 6.16: Comparison of C_{L_α} value between BEARDS^{TM} and wind tunnel results.

configuration is needed when manufacturing. This work emphasises the following as the key lessons learned in developing a HAR wing subscale model:

- The spar location at 25% chord can be considered to be very optimistic. It is

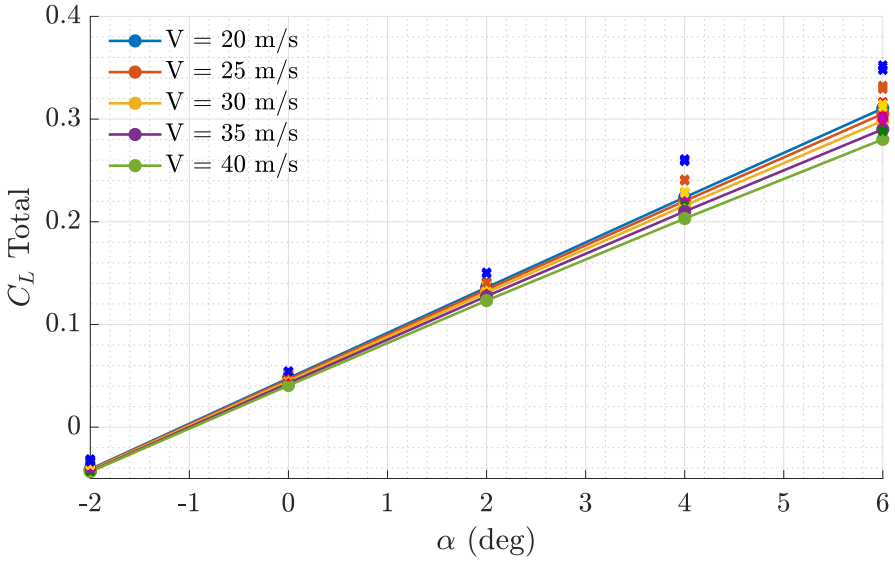

Figure 6.35: Comparison of C_L with as a function of α.

preferable to locate the spar at the elastic axis (around 40% chord) rather than the aerodynamic center.

- 3D PolyJet printing results in a skin mass distribution, that must be considered during spar optimisation. For example, the spar may need to be designed with higher torsional rigidity.
- For an idealistic conceptual design, iteration loops are needed to update the conceptual model. In this case clearer design requirements are needed.
- In practice, increasing the torsional rigidity (for example by having an additional rod), resulted in the switching of the first torsional mode with the second bending mode. This also affected the overall stiffness of the wing that led to lower structural flexibility.
- The weight contribution of a small section should not be underestimated for subscale model development. For example, the solid printed aileron section was found to have a significant impact on the structural behaviour of the wing.

This page is intentionally left blank.

CHAPTER 7

Conclusions & Further Work

The development of technology demonstrators has always been a significant component of aircraft development. However, very few of these have been a close dynamically scaled version of the final design. The lack of dynamically scaled demonstrators is a symptom of the challenging nature of applying the concepts of similitude to manufacture a representative scaled vehicle. Dynamic scaling itself is a hard design problem and the interpretation of the consequent results has its own challenges [138] and requires engineers to have a strong understanding of dimensional analysis.

The use of subscale models through dynamic scaling as part of the aircraft design process is common practice in the aerospace industry. However, today this process employs a range of subscale models where each is designed and used for a very specific purpose. For example, geometrically scaled models are used for wind tunnel testing and aeroelastic scaled models for flutter tests. These models provide the designer with a means of risk mitigation and increased confidence in their designs and thus, help avoid problems much later in the development process. On the other side, the practice of SID has been essential for design validation through dynamic experiments, especially flight tests. So combining dynamic testing using subscale models and processing test results using SID can be a beneficial tool to test the proof-of-concept at the early design stage. It can reduce the overall cycle time for development, which is especially important for a novel design. The work presented in this thesis is set within this context and aimed to develop a methodology to investigate the behaviour of aeroelastic systems by combining subscale modelling techniques with the field of system identification.

The current practice of subscale modelling is presented in Chapter 1. This chapter also presented the context of this work and its aim and objectives in more detail. The detailed technical conclusions can be found at the end of the chapter. However, the top level learning points from this thesis can be listed as follows:

- Although developing appropriately scaled dynamic models require careful study and numerous trade-offs, novel manufacturing techniques such as PolyJet printing can be a solution in developing a flexible subscale model. This technique allows a single printed model, which eliminates the needs of gap between section and ensure the continuity of the surface.

- The experimental testing of a subscale model requires significant care, especially in terms of experimental design (input design), because inappropriate inputs can easily excite the non-linear dynamics of such models when compared to the full scale vehicle.

- In identification of flexible aircraft, the OLS method is not as effective as the OE method. OE method is needed especially for observing the structural behaviour of the aeroelastic vehicle. However, OLS method can be a useful algorithm to provide initial guess for the OE approach. It should also be noted that the accurate identification of structural dynamics may require another method such as the subspace identification.

- Although the last chapter did not completely link dynamic scaling and system identification, it did highlight the practical trade-offs and compromises needed in the development of dynamically scaled models and the challenges faced when approaching the testing phase.

7.1 Recommendation of Further Work

The work described and discussed in this thesis relies on a number of assumptions. The main conclusions can be strengthened further by addressing these assumptions via the following future work items:

- A dynamic test inside the wind tunnel model will give insight into the aeroelastic behaviour of the subscale model through system identification, such as those given in Chapter 4. Combination of subspace identification and output error method can be used for identification of model dynamics.

- The current theoretical framework being developed for the subscale model ignores the stall conditions and since a subscale model is prone to stall at a lower angles of attack (as shown in Chapter 3), a theoretical framework developed to capture this phenomena will be useful.

- In the current framework, the Lift forces are calculated as perpendicular to the freestream velocity. However, when the wing is bends due to structural flexibility, the Lift forces should be perpendicular with the aerofoil section, creating follower forces along the spanwise direction. This effect has not been considered in the current framework. An improvement of the framework to consider this force will allow more accurate aeroelastic modelling.

- The scaling laws are developed by simplifying the aeroelastic problem into a structural problem and ignores the difference in aerodynamic behaviour. Considering the differences in aerodynamic behaviour can lead to a more comprehensive optimisation process in developing the subscale model.

- The development of subscale model needs to consider the mass contribution of skin from the beginning, and by doing so, this will result in a more optimised spar design and has more torsional stiffness.

- The use of the PolyJet printing technology has been presented and the NASTRAN FE model has been shown to provide close results to the experimental results. However, to further understand the impact of structural damping due to the skin, a specific test is needed.

- The identification of structural modes through GVT was conducted using accelerometers placed at specific locations along with the spar. These sensor positions only allow the identification of the bending mode. A more suitable structural identification setup is needed to validate the manufactured model by identifying the remaining modes.

- The identification of structural modes through GVT was conducted using uni-axial accelerometers, more robust sensors that can capture more combined modes such as the use of 6 DoF sensors, or a Fibre-Bragg gratings will be of interest to gain more insight into the structural properties.

7.2 Dissemination of Results

7.2.1 Journal Articles

- **Regressor Time-Shifting to Identify Longitudinal Stability and Control Derivatives of the Jetstream 3102**
  Sezsy Yusuf, Mudassir Lone, Alastair Cooke, Nicholas Lawson, *Aerospace Science and Technology*, 69:218-225, 2017
  The Jetstream 31 G-NFLA aircraft is used as a national flying laboratory test vehicle for flight dynamics research and teaching purposes. It has been the subject of much theoretical and experimental modelling and therefore, the need for generating validation data through flight testing is critical. In this paper, the aircraft's short period pitch oscillation mode characteristics are identified using data from sixteen flight tests. An identification procedure based on the least squares method and reduced order state-space model is used and the need for pre-processing regressors due to the effects of sensor location and instrumentation delays is highlighted. It has been shown that time-shifting the regressors based on relative locations of the angle of attack vanes and the inertial measurement unit results in significant reductions in uncertainty bounds of the estimated aeroderivatives and also a model that provides a closer match to flight test data. The estimated models are validated using separate flight test data and the variations in aeroderivatives over a range of airspeeds and centre of gravity positions are also presented.

- **Parameters Estimation Methodology for the Nonlinear Rolling Motion of Finned Cylindrical Body**
  Momtaz Abadir, Sezsy Yusuf, Alessandro Pontillo, Mudassir Lone, *Aerospace Science and Technology*, 84:787-798, 2019
  Identification of nonlinear roll dynamics of finned cylindrical bodies is a critical step when assessing free motion stability and trajectories of aerially dispensed munitions or decoys. In this paper the authors present a parameter estimation process

that focuses on identifying nonlinear aerodynamic models that characterise the roll dynamics of a cylindrical body with wrap around fins using data from a series of dynamic wind tunnel tests. This is a three step approach that combines ordinary least squares, stepwise regression and the augmented output-error method, and it is initially tested using simulation data corrupted by white Gaussian noise and then applied to the wind tunnel data. Roll and roll rate dynamics were captured through a series of high angle of attack free-to-roll tests carried out at an airspeed of 35 m/s corresponding to a Reynolds number of 800,000. The results and discussion in this paper demonstrate how simulation can be used to develop and mature a system identification routine followed by its assessment through wind tunnel test data. It is shown that high order nonlinear models with up to 14 terms can be parameterized to provide high levels of agreement with roll and roll rate dynamics observed in the dynamic wind tunnel tests.

- **Identification of In-Flight Wingtip Folding Effects on the Roll Characteristics of a Flexible Aircraft**
  Gaétan Dussart, Sezsy Yusuf, Mudassir Lone, *Aerospace*,6,63:1-27, 2019
  Wingtip folding is a means by which an aircraft's wingspan can be extended, allowing designers to take advantage of the associated reduction in induced drag. This type of device can provide other benefits if used in flight, such as flight control and load alleviation. In this paper, the authors present a method to develop reduced order flight dynamic models for in-flight wingtip folding which are suitable for implementation in real-time pilot-in-the-loop simulations. Aspects such as the impact of wingtip size and folding angle on aircraft roll dynamics are investigated along with failure scenarios using a time domain aeroservoelastic framework and an established system identification method. The process discussed in this paper helps remove the need for direct connection of complex physics based models to engineering flight simulators and the need for tedious programming of large look-up-tables in simulators. Instead it has been shown that a generic polynomial model for roll aeroderivatives can be used in small roll perturbation conditions to simulate the roll characteristics of an aerodynamic derivative based large transport aircraft equipped with varying fold hinge lines and tip deflections. Moreover, the effects of wing flexibility are also considered.

7.2.2 Conference Papers

1. Application of Multivariate Orthogonal Functions to Identify Aircraft Flutter Modes
   Sezsy Yusuf, Octavio Chavez, Mudassir Lone, *AIAA Atmospheric Flight Mechanics Conference, AIAA SciTech Forum*, Grapevine, 2017

2. Modelling Framework for Handling Qualities Analysis of Flexible Aircraft
   Vilius Portapas, Sezsy Yusuf, Mudassir Lone, Ettiene Coetzee, *AIAA Modeling and Simulation Technologies Conference*, Grapevine, 2017.

3. Flexible High Aspect Ratio Wing: Low Cost Experimental Model and Computational Framework

Alessandro Pontillo, David Hayes, Gaétan Dussart, Guillermo Lopez, Martin Carrizales, Sezsy Yusuf, Mudassir Lone, *AIAA Atmospheric Flight Mechanics Conference*, Kissimmee, 2018.

4. Effect of Wingtip Morphing on the Roll Mode of a Flexible Aircraft
Gaétan Dussart, Sezsy Yusuf, Mudassir Lone, *AIAA/ASCE/AHS/ASC Structures, Structural Dynamics, and Materials Conference*, Kissimmee, 2018.

5. Method to Assess Lateral Handling Qualities of Aircraft with Wingtip Morphing
Gaétan Dussart, Sezsy Yusuf, Vilius Portapas, Guillermo Lopez, Mudassir Lone,*AIAA Atmospheric Flight Mechanics Conference*, Kissimmee, 2018.

6. Aeroelastic Scaling for Flexible High Aspect Ratio Wings
Sezsy Yusuf, Alessandro Pontillo, Simone Weber, David Hayes, Mudassir Lone, *AIAA Scitech 2019 Forum*, San Diego, 2019.

7. High Aspect Ratio Wing Design Using the Minimum Exergy Destruction Principle
David Hayes, Alessandro Pontillo, Sezsy Yusuf, Mudassir Lone, James Whidborne, *AIAA SciTech Forum*, San Diego, 2019.

This page is intentionally left blank.

References

[1] Daniel P. Raymer. *Aircraft Design: A Conceptual Approach.* American Institute of Aeronautics and Astronautics, Washington, DC, USA, 1992. ISBN-13:978-1563478307.

[2] Jan Roskam. *Aircraft Design, Parts I-VIII.* DAR Corporation, Lawrence, K.S., USA, 2000. ISBN: 9781884885242.

[3] Luis R. Miranda, Robert D. Elliot, and William M. Baker. A Generalized Vortex Lattice Method for Subsonic and Supersonic Flow Applications. Technical report, National Aeronautics and Space Administration, California, USA, 1977.

[4] Lawrence S. Schuster. NASTRAN/FLEXTAB Procedure for Static Aeroelastic Analysis. Technical report, National Aeronautics and Space Administration, California, USA, 1984.

[5] Juan J. Alonso, Patrick LeGresley, and Victor Pereyra. Aircraft Design Optimization. *Mathematics and Computers in Simulation*, 79:1948–1958, 2009. doi:10.1016/j.matcom.2007.07.001.

[6] Marco Nunez, Varun Chander Datta, Arturo Molina-Cristobal, Marin Guenov, and Atif Riaz. Enabling Exploration in the Conceptual Design and Optimisation of Complex Systems. *Journal of Engineering Design*, 23(10-11):852–875, 2012. doi:10.1080/09544828.2012.706800.

[7] Mehran A.A. Oroumieh, Malekm S. Mohammad B., Mahmud Ashrafizaadeh, and Taheri S. Mahmoud. Aircraft Design Cycle Time Reduction using Artificial Intelligence. *Aerospace Science and Technology*, 26(1):244–258, 2013. doi:10.1016/j.ast.2012.05.003.

[8] Thomas L. Jordan, William M. Langford, and Jeffrey S. Hill. Airborne Subscale Transport Aircraft Research Testbed - Aircraft Model Development. In *Proceedings of the AIAA Guidance, Navigation, and Control Conference and Exhibit*, San Fransisco, California, USA, 2005. doi:10.2514/6.2005-6432.

[9] Kevin Cunningham, John V. Foster, Eugene A. Morelli, and Austin M. Murch. Practical Application of a Subscale Transport Aircraft of Flight Research in Control Upset and Failure Conditions. In *AIAA Atmospheric Flight Mechanics Conference and Exhibit*, Honolulu, Hawaii, USA, 2008. doi:10.2514/6.2008-6200.

[10] Joseph Chambers. *Modeling Flight : The Role of Dynamically Scaled Free-Flight Models in Support of NASA's Aerospace Programs.* National Aeronautics and Space Administration, Washington, USA, 2010. ISBN : 978-0-16-084633-5.

[11] Edward M. Kraft. After 40 Years Why Hasn't the Computer Replaced the Wind Tunnel? *ITEA Journal 2010*, 31(3):329–346, 2010.

[12] Ravindra V. Jategaonkar, W. Mönnich, Dietrich Fischenberg, and B. Krag. Identification of C-160 Simulator Data Base from Flight Data. 27(8):1031–1038, 1994. doi:10.1016/D1474-6670(17)47844-X.

[13] Mark B. Tischler. System Identification Methods for Aircraft Flight Control Development and Validation. Technical Report 95-A-007, National Aeronautics and Space Administration, USA, 1995.

[14] Wind Tunnel Tests Further Validate Aerodynamic Design and Support Fuel Efficiency Projections of the CSeries Aircraft. https://www.bombardier.com/en/media/newsList/details.30266-wind-tunnel-tests-further-validate-aerodynamic-design-and-support-fuel-efficiency-projections-of-the-cseries-aircraft.bombardiercom.html. Accessed on 14/03/2019.

[15] Eugene A. Morelli. Global Nonlinear Aerodynamic Modeling Using Multivariate Orthogonal Functions. *Journal of Aircraft*, 32(2):270–277, 1995. doi:10.2514/3.46712.

[16] D. Bruce Owens, Jay M. Brandon, Mark A. Croom, C. Michael Fremaux, Eugene H. Heim, and Dan D. Vicroy. Overview of Dynamic Test Techniques for Flight Dynamics Research at NASA LaRC. In *25th AIAA Aerodynamic Measurement Technology and Ground Testing Conference, Fluid Dynamics and Co-located Conferences*, San Francisco, California, USA, 2006. doi:10.2514/6.2006-3146.

[17] Isadore E. Garrick and Wilmer H Reed III. Historical Development of Aircraft Flutter. *Journal of Aircraft*, 18(11):897–912, 1981. doi:10.2514/3.57579.

[18] Christophe Le Garrec and Francois Kubica. In-Flight Structural Modes Identification for Comfort Improvement by Flight Control Laws. *Journal of Aircraft*, 42(1):90–92, 2005. doi:10.2514/1.3733.

[19] Christian Reschke and Gertjan Looye. Comparison of Model Integration Approaches for Flexible Aircraft Flight Dynamics Modelling. In *Proc. of International Forum on Aeroelasticity and Structural Dynamics*, Munich, Germany, 2005. doi:10.1016/D1474-6670(17)47844-X.

[20] Louis V. Schmidt. *Introduction to Aircraft Flight Dynamics*. American Institute of Aeronautics and Astronautics, Reston, USA, 1998. ISBN:1563472260,9781563472268.

[21] Stephen D. Carnduff, Sascha D. Erbsloeh, Alastair K. Cooke, and Michael V. Cook. Characterizing Stability and Control of Subscale Aircraft from Wind-Tunnel Dynamic Motion. *Journal of Aircraft*, 46(1):137–147, 2009. doi:10.2514/1.36730.

[22] Patrick C. Murphy and Vladislav Klein. Estimation of Unsteady Aerodynamic Models from Dynamic Wind Tunnel Data. In *NATO RTO AVT-189 Specialist Meeting*, number RTO-MP-AVT-189, NF1676L-13082, Portsdown West, United Kingdom, 2011. Accessed from https://ntrs.nasa.gov/archive/nasa/casi.ntrs.nasa.gov/20110016506.pdf.

[23] Sezsy Yusuf, Alessandro Pontillo, Simone Weber, David Hayes, and Mudassir Lone. Aeroelastic Scaling for Flexible High Aspect Ratio Wings. In *AIAA Atmospheric Flight Mechanics Conference*, San Diego, California, USA, 2019. doi:10.2514/6.2019-1594.

[24] Alessandro Pontillo, David Hayes, Gaétan Dussart, Guillermo Lopez, Martin Carrizalez, Sezsy Yusuf, and Mudassir Lone. Flexible High Aspect Ratio Wing: Low Cost Experimental Model and Computational Framework. In *AIAA Atmospheric Flight Mechanics Conference, AIAA SciTech Forum*, Orlando, Florida, USA, 2018. doi:10.2514/6.2018-1014.

[25] Sezsy Yusuf, Mudassir Lone, Alastair K. Cooke, and Nicholas J. Lawson. Regressor Time-Shifting to Identify Longitudinal Stability and Control Derivatives of the Jetstream 3102. *Aerospace Science and Technology*, 69:218–225, 2017. doi:10.1016/j.ast.2017.06.003.

[26] Alessandro Pontillo, Sezsy Yusuf, Guillermo Lopez, Dominic Rennie, and Mudassir Lone. Investigating Pitching Moment Stall Through Dynamic Wind Tunnel Test. *Journal of Aerospace Engineering*. in press.

[27] Gaétan Dussart, Sezsy Yusuf, and Mudassir Lone. Effect of Wingtip Morphing on the Roll Mode of a Flexible Aircraft. In *2018 AIAA/ASCE/AHS/ASC Structures, Structural Dynamics, and Materials Conference*, Kissimmee, Florida, USA, 2018. doi:10.2514/6.2018-1683.

[28] Gaétan Dussart, Sezsy Yusuf, and Mudassir Lone. Identification of In-Flight Wingtip Folding Effects on the Roll Characteristics of a Flexible Aircraft. *Aerospace*, 6(63), 2019. doi:10.3390/aerospace6060063.

[29] Gaétan Dussart, Sezsy Yusuf, Vilius Portapas, Guillermo Lopez, and Mudassir Lone. Method to Assess Lateral Handling Qualities of Aircraft with Wingtip Morphing. In *AIAA Aeroelasticity and Flight Dynamics Conference, AIAA SciTech Forum*, Orlando, Florida, USA, 8-12 January 2018. doi:10.2514/6.2018-1015.

[30] Raymond L. Bisplinghof, Holt Ashley, and Robert L. Halfman. *Aeroelasticity*. Addison-Wesley, Reading, MA, USA, 1955. ISBN-13:978-0-486-69189-3.

[31] Anshal I. Neihouse and Philip W. Pepoon. Dynamic Similitude Between a Model and a Full-Scale Body for Model Investigation at Full-Scale Mach Number. Technical report, National Advisory Committee for Aeronautics, Washington, 1950.

[32] Chester H. Wolowicz and James S. Bowman. NASA Technical Paper 1435 Similitude Requirements and Scaling Relationships as Applied to Model Testing. Technical Report August, National Aerospace and Space Administration, 1979.

[33] Arthur R. Collar. The Expanding Domain of Aeroelasticity. *The Aeronautical Journal*, 50(428):613–636, 1946. doi:10.1017/S0368393100120358.

[34] John D. Anderson Jr. *A History of Aerodynamics and Its Impact on a Flying Machines*. Cambridge University Press, Cambridge, UK, 1997. ISBN: 9780521669559.

[35] Peretz P. Frieddmann. Aeroelastic Scaling for Fixed and Rotary-Wing Aircraft with Applications. In *41st AIAA/ASME/ASCE/AHS/ASC Structures, Structural Dynamics, and Materials Conference and Exhibit*, Atlanta, 2000. doi:10.2514/6.2000-1688.

[36] NASA 20-Foot Spin Tunnel. https://crgis.ndc.nasa.gov/historic/20-Foot_Spin_Tunnel. Accessed on 5/5/2019.

[37] Max M. Munk and Edward P. Warner. Comparing the Performance of Geometrically Similar Airplanes. Technical report, National Advisory Committee for Aeronautics, USA, 1924.

[38] Patrick C. Murphy, Vladislav Klein, and Neal T. Frink. Unsteady Aerodynamic Modeling in Roll for the NASA Generic Transport Model. In *AIAA Atmospheric Flight Mechanics Conference*, Minneapolis, Minnesota, USA, 2012. doi:10.2514/6.2012-4652.

[39] Mark French and Franklin E. Eastep. Aeroelastic Model Design Using Parameter Identification. *Journal of Aircraft*, 33(1):198–202, 1996. doi:10.2514/3.46922.

[40] Julien Ertveldt, John Lataire, Rik Pintelon, and Steve Vanlanduit. Frequency-Domain Identification of Time-Varying Systems for Analysis and Prediction of Aeroelastic Flutter. *Mechanical Systems and Signal Processing*, 47(1-2):225–242, 2014. doi:10.1016/j.ymssp.2013.08.020.

[41] Gloria Stenfelt and Ulf Ringertz. Design and Construction of Aeroelastic Wind Tunnel Models. *The Aeronautical Journal*, 119(1222):1585–1599, 2015. doi:10.1017/S0001924000011416.

[42] Deman Tang and Earl H. Dowell. Experimental Aeroelastic Models Design and Wind Tunnel Testing for Correlation with New Theory. *Aerospace*, 3(2):1–25, 2016. doi:10.3390/aerospace3020012.

[43] William J. Duncan. *Physical Similarity and Dimensional Analysis: An Elementary Treatise*. Arnold, London, 1953.

[44] Garrett Birkhoff. *Hydrodynamics. A study in Logic, Fact, and Similitude*. Princenton University Press, New Jersey, 1960. ISBN:9780691625911.

[45] Airfoil Tools. http://airfoiltools.com/, October 2014. Accessed on 27/04/2019.

[46] Donald F. Young, Bruce R. Munson, Theodore H. Okiishi, and Wade W. Huebsch. *A Brief Introduction to Fluid Mechanics*. John Wiley & Sons, Inc., Denver, USA, 2007. ISBN:978-0-470-03962-5.

[47] Stefan Bogos and Ion Stroe. Similarity Criteria for "Full" and "Scale" Aircraft on the Lateral Stabilty Analysis. *UPB Scientific Bulletin, Series D*, 74(4):13–26, 2012.

[48] Jan R. Wright and Jonathan E. Cooper. *Introduction to Aircraft Aeroelasticity and Loads*. John Wiley & Sons, Inc., Chichester, United Kingdom, 2nd edition, 2007. ISBN:978-1-118-48801-0.

[49] Max Scherberg and R.V. Rhode. Mass Distribution and Performance of Free Flight Models. Technical report, National Advisory Committee for Aeronautics, Washington, 1927.

[50] Janusz S. Przemieniecki. *Theory of Matrix Structural Analysis*. McGraw-Hill, USA, 1968. ISBN-13:9780070509047.

[51] Akshay Raju Kulkarni, Gianfranco La Rocca, and Leo L M Veldhuis. Degree of Similitude Estimation for Sub-Scale Flight Testing. In *AIAA Scitech Forum 2019*, San Diego, California, 2019. doi:10.2514/6.2019-1208.

[52] Jennifer Heeg, Charles V. Spain, and Jose A. Rivera. Wind Tunnel to Atmospheric Mapping for Static Aeroelastic Scaling. In *45th AIAA/ASME/ASCE/AHS/ASC Structures, Structural Dynamics & Material Conference*, Palm Springs, California,USA, 19-22 April 2004. doi:10.2514/6.2004-2044.

[53] Eli Livne. Aircraft Active Flutter Suppression: State of the Art and Technology Maturation Needs. *Journal of Aircraft*, 55(1):410–450, 2018. doi:10.2514/1.C034442.

[54] Ravindra V. Jategaonkar. *Flight Vehicle System Identification: A Time Domain Methodology*. American Institute of Aeronautics and Astronautics, Inc., Reston, USA, 2006. ISBN : 978-1-56347-836-9.

[55] David K. Schmidt and David L. Raney. Modelling and Simulation of Flexible Flight Vehicles. *Journal of Guidance, Control, and Dynamics*, 24(3):539–546, 2001. doi:10.2514/2.4744.

[56] Carlos E.S. Cesnik and Weihua Su. Nonlinear Aeroelastic Modeling and Analysis of Fully Flexible Aircraft. In *Proceedings of 46th AIAA/ASME/ASCE/AHS/ASC Structures,Structural Dynamics and Materials Conference*, Austin, Texas, USA, 2005. doi:10.2514/6.2005-2169.

[57] Mayuresh J. Patil and Dana J. Taylor. Gust Response of Highly Flexible Aircraft. In *47th AIAA/ASME/ASCE/AHS/ASC Structures, Structural Dynamics, and Materials Conference*, Newport, Rhode Island, USA, 2006. doi:10.2514/6.2006-1638.

[58] Jeonghwan Ko, Thomas W. Strganac, and Andrew J. Kurdila. Stability and Control of a Structurally Nonlinear Aeroelastic System. *Journal of Guidance, Control, and Dynamics*, 21(5):718—-725, 1998. doi:10.2514/2.4317.

[59] Thomas E. Noll, Stephen D. Ishmael, Bart Henwood, Marla E. Perez-Davis, Geary C. Tiffany, John Madura, Matthew Gaier, John M. Brown, and Ted Wierzbanowski. Technical Findings, Lessons Learned, and Recommendations Resulting from the Helios Prototype Vehicle Mishap. In *Meeting Proceedings RTO-MP-AVT-145*, pages 3.4–1 – 3.4–18, Neuilly-sur-Seine, France, 2007. Accessed from: https://apps.dtic.mil/docs/citations/ADA478771, 03/04/2019.

[60] Christopher M. Shearer and Carlos E.S. Cesnik. Nonlinear Flight Dynamics of Very Flexible Aircraft. *Journal of Aircraft*, 44(5):1528–1545, 2007. doi:10.2514/1.27606.

[61] P. Frank Pai. *Highly Flexible Structures: Modeling, Computation, and Experimentation*. American Institute of Aeronautics and Astronautics, Inc., 2007. ISBN:978-1-60086-192-5.

[62] Chong-Seok. Chang, Mayuresh J Patil, and Dewey H Hodges. Flight Dynamics of Highly Flexible Flying Wings. *Journal of Aircraft*, 45(2):538–545, 2008. doi:10.2514/1.17640.

[63] Anthony S. Pototzky. Scaling Laws Applied to a Modal Formulation of the Aeroelastic Equations. In *43rd AIAA/ASME/ASCE/AHS/ASC Structures, Structural Dynamics, and Materials Conference*, Denver, Colorado, USA, 2002. doi:10.2514/6.2002-1598.

[64] Johnhenri R. Richardson, Ella M. Atkins, Pierre T. Kabamba, and Anouck R. Girard. Scaling of Airplane Dynamic Response to Stochastic Gusts. *Journal of Aircraft*, 51(5):1554–1566, 2014. doi:10.2514/1.C032410.

[65] Tang Bo, Wu Zhigang, and Yang Chao. Aeroelastic Scaling Laws for Gust Load Alleviation Control System. *Chinese Journal of Aeronautics*, 29(1), 2015. doi:10.1016/j.cja.2015.12.001.

[66] Zhiqiang Wan and Carlos E.S. Cesnik. Geometrically Nonlinear Aeroelastic Scaling for Very Flexible Aircraft. *AIAA Journal*, 52(10):2251–2260, 2014. doi:10.2514/1.J052855.

[67] Jeffrey Ouellette. *Modeling and Scaling of a Flexible Subscale Aircraft for Flight Control Development and Testing in the Presence of Aeroservoelastic Interactions*. PhD thesis, Virginia Polytechnic Institute and State University, 2013.

[68] Eric Ting, Sonia Lebofksy, Nhan T. Nguyen, and Khanh V. Trinh. Static Aeroelastic Scaling and Analysis of a Sub-Scale Flexible Wing Wind Tunnel Model. In *55th AIAA/ASME/ASCE/AHS/ASC Structures, Structural Dynamics, and Materials Conference*, National Harbor, Maryland, USA, 2014. doi:10.2514/6.2014-0838.

[69] Anthony P. Ricciardi, Charles A.G. Eger, Robert A. Canfield, and Mayuresh J. Patil. Nonlinear Aeroelastic-Scaled-Model Optimization Using Equivalent Static Loads. *Journal of Aircraft*, 51(6):1842–1851, 2014. doi:10.2514/1.C032539.

[70] Vanessa L. Bond, Robert A. Canfield, Afzal Suleman, and Maxwell Blair. Aeroelastic Scaling of a Joined Wing for Nonlinear Geometric Stiffness. *AIAA Journal*, 50(3):513–522, 2012. doi:10.2514/1.41139.

[71] Anthony P. Ricciardi, Robert A. Canfield, Mayuresh J. Patil, and Ned Lindsley. Nonlinear Aeroelastic Scaled-Model Design. *Journal of Aircraft*, 53(1):20–32, 2016. doi:10.2514/1.C033171.

[72] Christian Spada, Frederico Afonso, Fernando Lau, and Afzal Suleman. Nonlinear Aeroelastic Scaling of High Aspect-Ratio Wings. *Journal of Aerospace Science and Technology*, 63:363–371, 2017. doi:10.1016/j.ast.2017.01.010.

[73] Deman Tang and Earl H. Dowell. Experimental and Theoretical Study on Aeroelastic Response of High-Aspect-Ratio Wings. *AIAA Journal*, 39(8):1430–1441, 2001. doi:10.2514/2.1484.

[74] Pedro Pereira, Luis Almeida, Afzal Suleman, Vanessa Bond, Robert Canfield, and Bliar Maxwell. Aeroelastic Scaling and Optimization of a Joined-Wing Aircraft Concept. In *3rd AIAA Multi Disciplinary Design Optimization Specialists Conference*, Honolulu, Hawaii, USA, 2007. doi:10.2514/6.2007-1889.

[75] Jonathan D. Bartley-Cho and Joseph A. Henderson. Design and Analysis of HiLDA/AEI Aeroelastic Wind Tunnel Model. In *28th AIAA Applied Aerodynamic Conference*, Honolulu, Hawaii, USA, 2008. doi:10.2514/6.2008-7191.

[76] Styles of Wing Construction. https://www.airfieldmodels.com/information_source/math_and_science_of_model_aircraft/rc_aircraft_design/styles_of_wing_construction.htm. Accessed on 29/03/2019.

[77] Flight Mechanic : Wings (Part One). http://www.flight-mechanic.com/wings-part-one. Accessed on 29/03/2019.

[78] Christopher D. Regan and Brian R. Taylor. mEAWing1: Design, Build, Test. In *AIAA Athmospheric Flight Mechanics Conference*, San Diego, USA, 2016. doi:10.2514/6.2016-1747.

[79] Krzysztof Olasek and Piotr Wiklak. Application of 3D Printing Technology in Aerodynamic Study. *Journal of Physics: Conference Series 530*, 530:1–7, 2014. doi:10.1088/1742-6596/530/1/012009.

[80] Cyrus Aghanahafi and Saeed Daneshmand. Integration of Three-Dimensional Printing Technology for Wind-Tunnel Model Fabrication. *Journal of Aircraft*, 47(6):2130–2135, 2010. doi:10.2514/1.C031032.

[81] Weijun Zhu, Dichen Li, Zhengyu Zhang, Ke Ren, Xinglei Zhao, Dangguo Yang, Wei Zhang, Yan Sun, and Yiping Tang. Design and Fabrication of Stereolithpgraphy-based Aeroelastic Wing Models. *Rapid Prototyping Journal*, 17(4):298–307, 2011. doi:10.1108/13552541111138423.

[82] Sebastiano Fichera, Shakir Jiffri, and Mottershead John E. Design and Wind Tunnel Test of a MODular aeroelastic FLEXible wing (MODFLEX). In *Proceedings of the International Conference on Noise and Vibration Engineering, ISMA*, Leuven, Belgium, 2016.

[83] Alexander M. Pankonien and Gregory W. Reich. Multi-Material Printed Wind-Tunnel Flutter Model. *AIAA Journal*, 56(2):793–807, 2018. doi:10.2514/1.J056097.

[84] 3D Print Bureau Website. https://www.3dprintbureau.co.uk/processes/polyjet, July 2019. Accessed on 17/07/2019.

[85] Tuan D. Ngo, Alireza Kashani, Gabriele Imbalzano, Kate T.Q. Nguyen, and David Hui. Additive Manufacturing (3D Printing): A Review of Materials, Methods, Applications and Challenges. *Composites Part B: Engineering*, 143:172–196, 2018. doi:10.1016/j.compositesb.2018.02.012.

[86] Richard E. Maine and Kenneth W. Iliff. Identification of Dynamic Systems. Theory and Formulation. Technical Report 1138, National Aeronautics and Space Administration, California, USA, 1985.

[87] Lofti A. Zadeh. From Circuit Theory to System Theory. *Proceedings of the IRE*, 50(5):856–865, 1962. doi:10.1109/JRPROC.1962.288302.

[88] Lennart Ljung. Perspectives on System Identification. *Annual Reviews in Control*, 34(1):1–12, 2010. doi:10.1016/j.arcontrol.2009.12.001.

[89] Peter G. Hamel and Ravindra Jategaonkar. Evolution of Flight Vehicle System Identification. *Journal of Aircraft*, 33(1):9–28, 1996. doi:10.2514/3.46898.

[90] Ravindra Jategaonkar, Dietrich Fischenberg, and Wolfgang van Gruenhagen. Aerodynamic Modeling and System Identification from Flight Data-—Recent Applications at DLR. *Journal of Aircraft*, 41(4):681–691, 2004. doi:10.2514/1.3165.

[91] K. Charles Wang and Kenneth W. Iliff. Retrospective and Recent Examples of Aircraft Parameter Identification at NASA Dryden Flight Research Center. *Journal of Aircraft*, 41(4):752–764, 2004. doi:10.2514/1.332.

[92] Alain Bucharles, Christelle Cumer, Georges Hardier, Béatrice Jacquier, Alexandre Janot, Thierry Le Moing, Cédric Seren, Clément Toussaint, and Pierre Vacher. An Overview of Relevant Issues for Aircraft Model Identification. *AerospaceLab Journal*, (4):1–21, 2012.

[93] Ermin Plaetschke and Gerhard Schulz. Practical Input Signal Design. Technical report, AGARD Lecture Series 104, 1979.

[94] Vladislav F. Klein and Eugene A. Morelli. *Aircraft System Identification. Theory and Practice*. American Institute of Aeronautics and Astronautics, United States, 2006. ISBN:1563478323,9781563478321.

[95] Mark B. Tischler and Robert K. Remple. *Aircraft and Rotorcraft System Identification. Engineering Methods with Flight Test Examples*. American Institute of Aeronautics and Astronautics, Inc., 2006. ISBN:978-1-56347-837-6.

[96] Ed Bachelder, Peter Thompson, David Klyde, and Daniel Alvarez. A New System Identification Method Using Short Duration Flight Test Inputs. In *AIAA Atmospheric Flight Mechanics Conference*, Portland, Oregon, USA, 2011. doi:10.2514/6.2011-6445.

[97] John W. Dykes and Dimitri N. Mavris. A Methodology for the Robust Design Optimization of Flight Dynamic System Identification Experiments. In *AIAA Atmospheric Flight Mechanics Conference*, San Diego, California, USA, 2016. doi:10.2514/6.2016-2008.

[98] Eugene A. Morelli. Multiple Input Design for Real-Time Parameter Estimation in the Frequency Domain. In *13th IFAC Conference on System Identification*, volume 23, pages 639–644, Rotterdam, The Netherlands, 2003. doi:10.1016/S1474-6670(17)34833-4.

[99] Eugene A. Morelli. Flight-Test Experiment Design for Characterizing Stability and Control of Hypersonic Vehicles. *Journal of Guidence, Control, and Dynamics*, 32(3):949–959, 2009. doi:10.2514/1.37092.

[100] Patrick Guillaume, Peter Verboven, Steve Vanlanduit, and Eli Parloo. Multisine excitations – new developments and applications in modal analysis. In *Proceedings of the International Modal Analysis Conference - IMAC*, pages 1543–1549, Kissimme, Florida, USA, 2001.

[101] Bruno Giordano, De Oliveira Silva, and Wulf Mönnich. System Identification of Flexible Aircraft in Time Domain. In *AIAA Atmospheric Flight Mechanics Conference*, Minneapolis, Minnesota, USA, 2012. doi:10.2514/6.2012-4412.

[102] Kioumars Najmabadi, Bruce Fritchman, and Chuong Tran. A Process for Model Identification and Validation of Dynamical Equations for a Flexible Transport Aircraft. In *AGARD Symposium on "System Identification for Integrated Aircraft Development and Flight Testing"*, pages 13.1 – 13.13, Madrid, Spain, 1998.

[103] Jared A. Grauer, Jennifer Heeg, and Eugene A. Morelli. Real-Time Frequency Response Estimation Using Joined-Wing SensorCraft Aeroelastic Wind-Tunnel Data. In *AIAA Atmospheric Flight Mechanics Conference, Guidance, Navigation, and Control and Co-located Conferences*, Minneapolis, Minnesota, USA, 2012. doi:10.2514/6.2012-4641.

[104] Eric W. Weisstein. Nyquist Frequency. From MathWorld–A Wolfram Web Resource. http://mathworld.wolfram.com/NyquistFrequency.html. Accessed on 01/04/2019.

[105] Jared A. Grauer and Matthew J. Boucher. Identification of Aeroelastic Models for the X-56A Longitudinal Dynamics Using Multisine Inputs and Output Error in the Frequency Domain. *Aerospace*, 6(2):24, 2019. doi:10.3390/aerospace6020024.

[106] Jacques V.G. van Nunen and Gérard Piazzoli. eroelastuc Flight Test Techniques and Instrumentation. Technical Report AGARD-AG-160, North Atlantic Treaty Organisation, 1979.

[107] Simone Weber. *Fibre Optic Sensing for Measuring Rotor Blade Structural Dynamics*. PhD thesis, Cranfield University, 2019.

[108] Majeed Mohamed. System Identification of Flexible Aircraft in Frequency Domain. *Aircraft Engineering and Aerospace Technology*, 89(6):826–834, 2017. doi:10.1108/AEAT-09-2015-0214.

[109] Johan Schoukens, Rik Pintelon, and Yves Rolain. Time Domain Identification, Frequency Domain Identification. Equivalencies! Differences? In *56th AIAA/ASCE/AHS/ASC Structures, Structural Dynamics, and Materials Conference*, Kissimmee, Florida, USA, 2004. doi:10.23919/ACC.2004.1383679.

[110] Robert C. Schwanz and William R. Wells. Estimation of Elastic Aircraft Parameters Using the Maximum Likelihood Method. Technical Report TN D-7647, NASA, Edwards, CA, USA, 1974.

[111] Majeed Mohamed, Jatinder Singh, and Indra Narayan Kar. Identification of Aerodynamic Derivatives of a Flexible Aircraft. *Journal of Aircraft*, 49(2):654–658, 2012. doi:10.2514/1.C031318.

[112] Harald Pfifer and Brian Danowsky. System Identification of a Small Flexible Aircraft. In *AIAA Atmospheric Flight Mechanics Conference*, San Diego, CA, USA, 2016. doi:10.2514/6.2016-1750.

[113] Jared A. Grauer and Matthew J. Boucher. Aeroelastic Modeling of X-56A Stiff-Wing Configuration Flight Test Data. In *AIAA Atmospheric Flight Mechanics Conference*, Grapevine, Texas, USA, 2017. doi:10.2514/6.2017-0699.

[114] Hassan Haddadpour and Rohollah D. Firouz-Abadi. True Damping and Frequency Prediction for Aeroelastic Systems: The PP Method. *Journal of Fluids and Structures*, 25(7):1177–1188, 2009. doi:10.1016/j.jfluidstructs.2009.06.006.

[115] Eli Nissim and Glenn B. Gilyard. Method for Experimental Determination of Flutter Speed by Parameter Identification. In *30th Structures, Structural Dynamics and Materials Conference*, Mobile, AL, USA, 1989. doi:10.2514/6.1989-1324.

[116] Hirotugu Akaike. Stochastic Theory of Minimal Realization. *IEEE Transaction on Automatic Control*, 19(6):667–674, 1974. doi:10.1109/TAC.1974.1100707.

[117] Jer-Nan Juang and Richard S. Pappa. An Eigensystem Realization Algorithm for Modal Parameter Identification and Model Reduction. *Journal of Guidance, Control, and Dynamics*, 8(5):620–627, 1985. doi:10.2514/3.20031.

[118] Edwin Reynders, Rik Pintelon, and Guido De Roeck. Uncertainty Bounds on Modal Parameters Obtained from Stochastic Subspace Identification. *Mechanical Systems and Signal Processing*, 22(4):948–969, 2008. doi:10.1016/j.ymssp.2007.10.009.

[119] Bart Peeters and Guido De Roeck. Stochastic System Identification for Operational Modal Analysis: A Review. *Journal of Dynamic System Measurement and Control*, 123(4):659–667, 2001. doi:10.1115/1.1410370.

[120] Alain Bucharles and Pierre Vacher. Flexible Aircraft Model Identification for Control Law Design. *Aerospace Science and Technolgy*, 6(8):591–597, 2002. doi:10.1016/S1270-9638(02)01197-5.

[121] Daniela C. Rebolho, Eduardo M. Belo, and Flávio D. Marques. Aeroelastic Parameter Identification in Wind Tunnel Testing via the Extended Eigensystem Realization Algorithm. *Journal of Vibration and Control*, 20(11):1607–1621, 2014. doi:10.1177/1077546312474015.

[122] Christophe Le Garrec, Marc Humbert, and Michel Lacabanne. Identification of the Aeroelastic Model of a Large Transport Civil Aircraft for Control Law Design and Validation. In *22nd Congress of the International Council of the Aeronautical Sciences*, Harrogate, UK, 2005.

[123] Thiago H.L. Pinto, Roberto G.A. da Silva, and Guilherme R. Begnini. Comparative Study of System Identification Methods Aplied to Aeroelastic Models Tested in Wind Tunnel. In *29th Congress of the International Council of the Aeronautical Sciences*, St. Petersburg, Russia, 2014.

[124] S Joe Qin. An Overview of Subspace Identification. *Computers and Chemical Engineering*, 30(10–12):1502–1513, 2006. doi:10.1016/j.compchemeng.2006.05.045.

[125] Tohru Katayama. *Subspace Methods for System Identification*. Springer, Liepzig, Germany, 2006. ISBN:978-1-85233-981-4.

[126] Peter Van Overschee and Bart De Moor. *Subspace Identification for Linear Systems*. Kluwer Academic Publishers, Dordrecht, The Netherlands, 1996. ISBN:978-1-4613-0465-4.

[127] Maher Abdelghani, Michel Verhaegen, Peter Van Overschee, and Bart De Moor. Comparison Study of Subspace Identification Methods Applied to Flexible Structure. *Mechanical Systems and Signal Processing*, 12(5):679–692, 1998. doi:10.1006/mssp.1998.0169.

[128] Ilhan Tuzcu. On the Stability of Flexible Aircraft. *Aerospace Science and Technology*, 12(5):376–384, 2008. doi:10.1016/j.ast.2007.09.003.

[129] Henrik Hesse and Rafael Palacios. Reduced Order Aeroelastic Models for Dynamics of Maneuvering Flexible Aircraft. *AIAA Journal*, 52(8):1717–1732, 2014. doi:10.2514/1.J052684.

[130] Ronald D. Milne. Dynamics of the Deformable Aeroplane. Technical Report 3345, Aeronautical Research Council Reports and Memoranda, London, UK, 1962.

[131] Robert C. Schwanz. Formulation of Equation of Motion of an Elastic Aircraft for Stability and Control and Flight Control Applications. Technical Report AD/A 006 391, National Technical Information Service, Edwards, CA, USA, 1972.

[132] Martin R. Waszak, Carey S. Buttril, and David K. Schmidt. Modeling and Model Simplification of Aeroelastic Vehicles: an Overview. Technical report, National Aeronautics and Space Administration, 1992.

[133] Nhan T. Nguyen and Ilhan Tuzcu. Flight Dynamics of Flexible Aircraft with Aeroelastic and Inertial Force Interactions. In *AIAA Atmospheric Flight Mechanics Conference*, Chicago, Illinois, USA, 2009. doi:10.2514/6.2009-6045.

[134] Henry McDonald, James Ross, David Driver, and Stephen Smith. Wind Tunnel and Flight. In *Conference: 10th International Symposium on Applications of Laser Techniques to Fluid Mechanics*, Libon, Portugal, 2000.

[135] Jewel B. Barlow, William H. Rae, and Alan Pope. *Low-Speed Wind Tunnel Testing*. John Wiley & Sons, Inc., New York, USA, 3rd edition, 1999. ISBN:978-0-471-55774-6.

[136] Walter C. Williams, Hubert M. Drake, and Fischel Jack. Some Correlations of Flight-Measured and Wind-Tunnel Measured Stability and Control Characteristics of High-Speed Airplanes. Technical Report 62, North Atlantic Treaty Organisation, Brussels, Belgium, 1956.

[137] Karl Pettersson and Arthur Rizzi. Aerodynamic Scaling to Free Flight Conditions: Past and Present. *Progress in Aerospace Science*, 44(4):295–313, 2008. doi:10.1016/j.paerosci.2008.03.002.

[138] Dennis M. Bushnell. Scaling: Wind Tunnel to Flight. *Annual Review Fluid Mechanichs*, 38(38):111–128, 2006. doi:10.1146/annurev.fluid.38.050304.092208.

[139] A. Barry Haines. Scale Effects on Aircraft and Weapon Aerodynamics. Technical Report AGARD-AG-323, North Atlantic Treaty Organisation, Essex, UK, 1994.

[140] Lance W. Traub. Drag Extrapolation to Higher Reynolds Number. *Journal of Aircraft*, 46(4):1458–1461, 2009. doi:10.2514/1.43952.

[141] Nhu Van Nguyen, Maxim Tyan, Jae-Woo Lee, and Sangho Kim. Investigations on Stability and Control Characteristics of a CS-VLA Certified Aircraft Using Wind Tunnel Test Data. *Proc IMechE Part G: J Aerospace Engineering*, 230(14):2728–2743, 2016. doi:10.1177/0954410016632016.

[142] Vilius Portapas. *Handling Qualities of High Aspect Ratio Wing Aircraft*. PhD thesis, Cranfield University, 2018.

[143] Stuart P. Andrews. *Modelling and Simulation of Flexibility Aircraft: Handling Qualities with Active Load Control*. PhD thesis, Cranfield University, 2011.

[144] Fred C. Schweppe. *Uncertain Dynamic Systems*. Prentice-Hall, Upper Saddle River, NJ, 1973. ISBN-13:978-0139355936.

[145] Michael V. Cook. *Flight Dynamics Principles: A Linear Systems Approach to Aircraft Stability and Control*. Elsevier Aerospace Engineering Series. Butterworth-Heinemann, Amsterdam, the Netherlands, 3rd edition, 2013.

[146] Pierre-Daniel Jameson. Development of an online parameter estimation capability for aircraft. In *27th International Congress of the Aeronautical Sciences, ICAS*, Nice, France, 2010.

[147] Alastair K. Cooke. Data Pack for the Jetstream 31. Technical report, Cranfield University, 2013.

[148] Robert F. Stengel. *Flight Dynamics*. Princeton University Press, Princeton, NJ, 2004. ISBN: 9780691114071.

[149] Alastair K. Cooke. A Simulation Model of the NFLC Jetstream 31. Technical Report 0402, Cranfield University, May 2006.

[150] Jared A. Grauer, Eugene A. Morelli, and Murri Daniel G. Flight-Test Techniques for Quantifying Pitch Rate and Angle-of-Attack Rate Dependencies. *Journal of Aircraft*, 54(6):2367–2377, 2017. doi:10.2514/1.C034407.

[151] Jared A. Grauer and Eugene A. Morelli. Generic Global Aerodynamic Model for Aircraft. *Journal of Aircraft*, 52(1):13–20, 2015. doi:10.2514/1.C032888.

[152] Eugene A. Morelli. Efficient Global Aerodynamic Modeling from Flight Data. In *AIAA Aerospace Science Meeting including the New Horizons Forum and Aerospace Exposition*, Nashville, Tennessee, USA, 2012. doi:10.2514/6.2012-1050.

[153] Sezsy Yusuf, Octavio Chavez, and Mudassir Lone. Application of Multivariate Orthogonal Functions to Identify Aircraft Flutter Modes. In *AIAA Atmospheric Flight Mechanics Conference*, Grapevine, Texas, 9-13 January 2017. doi:10.2514/6.2017-0695.

[154] Momtaz Abadir, Sezsy Yusuf, Alessandro Pontillo, and Mudassir Lone. Parameters Estimation Methodology for the Nonlinear Rolling Motion of Finned Cylindrical Body. *Aerospace Science and Technology*, 84:782–798, 2019. doi:10.1016/j.ast.2018.11.013.

[155] Lawrence W. Carr, Kenneth W. McAlister, and William J. McCorskey. Analysis of the Development of Dynamic Stall Based on Oscillating Airfoil Experiments. Technical Report D-8382, National Aeronautics and Space Administration, 1977.

[156] Dietrich Fischenberg. Identification of an Unsteady Aerodynamic Stall Model from Flight Test Data. In *20th Atmospheric Flight Mechanics Conference, Guidance, Navigation, and Control*, Baltimore, MD, USA, 1995. doi:10.2514/6.1995-3438.

[157] Stephen D. Carnduff and Alastair K. Cooke. Application of Aerodynamic Model Structure Determination to UAV Data. *The Aeronautical Journal*, 115(1169):481–492, 2011. doi:10.1017/S0001924000006126.

[158] Mikhail Goman and Alexander Khrabrov. State-Space Representation of Aerodynamic Characteristics of an Aircraft at High Angles of Attack. *Journal of Aircraft*, 31(5):1109–1115, 1994. doi:10.2514/3.46618.

[159] Constrained Nonlinear Optimization Algorithms. https://uk.mathworks.com/help/optim/ug/constrained-nonlinear-optimization-algorithms.html. Accessed on 16/01/2019.

[160] Richard H. Byrd, Mary E. Hribar, and Jorge Nocedal. An Interior Point Algorithm for Large-Scale Nonlinear Programming. *SIAM Journal on Optimization*, 9(4):877–900, 1999. doi:10.1137/S1052623497325107.

[161] Richard H. Byrd, Jean Charles Gilbert, and Jorge Nocedal. A Trust Region Method Based on Interior Point Techniques for Nonlinear Programming. *Journal of Mathematical Programming*, 89(1):149–185, 2000. doi:10.1007/PL00011391.

[162] System Identification Methods for (Operational) Modal Analysis: Review and Comparison. *Archives of Computational Methods in Engineering*, 19(1):51–124, 2012. doi:10.1007/s11831-012-9069-x.

[163] Rudolf E. Kalman. On the General Theory of Control Systems. *IFAC Proceedings*, 1(1):4491–502, 1960. doi:10.1016/S1474-6670(17)70094-8.

[164] Wallace E. Larimore. Statistical Optimality and Canonical Variate Analysis System Identification. *Signal Processing*, 52(2):131–144, 1996. doi:10.1016/0165-1684(96)00049-7.

[165] Michel Verhaegen. Identification of the Deterministic Part of MIMO State Space Model Given in Innovation Form from Input-Output Data. *Automatica*, 30(1):61–74, 1994. doi:10.1016/0005-1098(94)90229-1.

[166] Peter Van Overschee and Bart De Moor. N4SID: Subspace Algorithms for the Identification of Combined Deterministic-Stochastic Systems. *Automatica*, 30(1):75–93, 1994. doi:10.1016/0005-1098(94)90230-5.

[167] Wouter Favoreel, Sabina Van Huffel, Bart De Moor, Vasile Sima, and Michel Verhaegen. Comparative Study Between Three Subspace Identification Algorithms. In *European Control Conference*, pages 821–826, Karlsruhe, Germany, 1999. doi:10.23919/ECC.1999.7099407.

[168] Slim Hachicha, Kharrat Maher, and Abdessattar Chaari. N4SID and MOESP Algorithms to Highlight the Ill-conditioning into Subspace Identification. *International Journal of Automation and Computing*, 11(1):30–38, 2014. doi:10.1007/s11633-014-0763-z.

[169] Herman Van der Auweraer and Peeters Bart. Discriminating Physical Poles from Mathematical Poles in High Order Systems: Use and Automation of the Stabilization Diagram. In *Proceedings of the 2004 IEEE Instrumentation and Measurement Technology Conference*, Como, Italy, 2004. doi:10.1109/IMTC.2004.1351525.

[170] David J. Ewins. *Modal Testing: Theory, Practice and Application*. Research Studies Press LTD, Hertfordshire, England, 2000. ISBN: 978-0-863-80218-8.

[171] Mudassir Lone. *Pilot Modelling for airframe loads analysis*. PhD thesis, Cranfield University, 2013.

[172] Mudassir Lone, Chi Kin Lai, Alastair K. Cooke, and James Whidborne. Framework for Flight Loads Analysis of Trajectory-Based Manoeuvres with Pilot Models. *Journal of Aircraft*, 51(2):637–650, 2014. doi:10.2514/1.C032376.

[173] Alessandro Pontillo. *Working title*. PhD thesis, Cranfield University, 2019.

[174] Gaétan Dussart. *On the Use of Active In-Flight Wingtip Dihedral Folding Systems for Large Civil Aircraft*. PhD thesis, Cranfield University, 2019.

[175] Andrea Castrichini, Vijayakumari Hodigere Siddaramaiah, Dario E. Calderon, Jonathan E. Cooper, Thomas Wilson, and Yves Lemmens. Preliminary investigation of use of flexible folding wing tips for static and dynamic loads alleviation. *Aeronautical Journal*, 121(1235):73–94, 2016. doi:10.1017/aer.2016.108.

[176] MSC.Nastran 2001. Quick Reference Guide, 2001.

[177] Theodore Theodorsen. General theory of aerodynamic instability and the mechanism of flutter. Technical report, NACA-TR-496, National Advisory Committee for Aeronautics, 1949.

[178] Boyd Perry. Comparison of Theodorsen's Unsteady Aerodynamic Forces with Doublet Lattice Generalized Aerodynamic Forces. Technical Report TM-2017-219667, National Aeronautica and Space Administration, Virginia, USA, 2017.

[179] Steven L. Brunton and Clarence W. Rowley. Modeling the Unsteady Aerodynamic Forces on Small-Scale Wings. In *47th AIAA Aerospace Sciences Meeting Including The New Horizons Forum and Aerospace Exposition*, Orlando, Florida, USA, 2009. doi:10.5214/6.2009-1127.

[180] J. Gordon Leishman. Indicial Lift Approximations for Two-Dimensional Subsonic Flow as Obtained from Oscillatory Measurements. *Journal of Aircraft*, 30(3):340–351, 1993. doi:10.2514/3.46340.

[181] Bernard Mazelsky. Determination of Indicial Lift and Moment of a Two-Dimensional Pitching Airfoil at Subsonic Mach Numbers from Oscillatory Coefficients with Numerical Calculations for a Mach Number of 0.7. Technical Report NACA TN 2613, National Advisory Committee for Aeronautics, 1952.

[182] Arun I. Jose, J. Gordon Leishman, and James D. Baeder. Unsteady Aerodynamic Modeling with Time-Varying Free-Stream Mach Numbers. *Journal of The American Helicopter Society*, 51(4):299–318, 2006. doi:10.4050/JAHS.51.299.

[183] J. Gordon Leishman. Validation of Approximate Indicial Aerodynamic Functions for Two-Dimensional Subsonic Flow. *Journal of Aircraft*, 25(10):914–922, 1988. doi:10.2514/3.45680.

[184] John W. Edwards, Holt Ashley, and John V. Breakwell. Unsteady Aerodynamic Modeling for Arbitrary Motions. *AIAA Journal*, 17(4):365–374, 1979. doi:10.2514/3.7348.

[185] Comandur Venkatesan and Peretz P. Friedmann. New Approach to Finite-State Modeling of Unsteady Aerodynamics. *AIAA Journal*, 24(12):1889–1879, 1986. doi:10.2514/3.9545.

[186] J. Gordon Leishman and K.Q. Nguyen. State-Space Representation of Unsteady Airfoil Behaviour. *AIAA Journal*, 28(5):836–844, 1990. doi:10.2514/3.25127.

[187] Johannes Weissinger. The Lift Distribution of Swept-Back Wings. Technical Report NACA-TM-1120, NACA Langley Aeronautical Laboratory, Langley Field, VA, USA, 1947.

[188] Bernard Etkin. *Dynamics of Atmospheric Flight*. Dover Publications, Inc, New York, USA, 1st edition, 2000. ISBN: 9780486445229.

[189] Jan Roskam. Comments, Interpretation and Application of a Method for Predicting Aerodynamic Characteristics of Large Flexible Airplanes. In *AGARD - Aeroelastic Effect from a Flight Mechanics Standpoint*, Marseille, France, 1970.

[190] Robert K. Heffley and Wayne F. Jewell. Aircraft Handling Qualities Data. Technical Report NASA-CR-2144, Systems Technology, Inc., Hawthorne, CA, USA, 1972.

[191] David Allerton. *Principles of Flight Simulation*. John Wiley & Sons, Inc., 2009. ISBN:0470682191.

[192] Dario H. Baldelli, Jie Zeng, Rick Lind, and Chuck Harris. Flutter-Prediction Tool for Flight-Test-Based Aeroelastic Parameter-Varying Models. *Journal of Guidance, Control, and Dynamics*, 32(1):158–171, 2009. doi:10.2514/1.36584.

[193] Michael Döhler, Falk Hille, Laurent Mevel, and Werner Rücker. Estimation of Modal Parameters and Their Uncertainty Bounds from Subspace-Based System Identification. In *IRIS Industrial Safety and Life Cycle Engineering - Technologies / Standards / Applications*, pages 91–106, 2013.

[194] Peter Baranyi. Tensor Product Model-Based Control of Two-Dimensional Aeroelastic System. *Journal of Guidance Control and Dynamics*, 29(2):391–400, 2006. doi:10.2514/1.9462.

[195] Stephen H. Crandall. On Scaling Laws for Material Damping. Technical Report D-1467, National Aeronautics and Space Administration, Washington, 1962.

[196] The Lift Coefficient, Glenn Research Center. https://www.grc.nasa.gov/www/k-12/airplane/liftco.html. Accessed on 13/02/2019.

[197] David Hayes. *Exergy Methods for Commercial Aircraft: Integrating the Laws of Thermodynamics into all Disciplines of Aircraft Design*. PhD thesis, Cranfield University, 2019.

[198] Egbert Torenbeek. Development and Application of a Comprehensive, Design-sensitive Weight Prediction Method for Wing Structures of Transport Category Aircraft. Technical report, Delft University of Technology, The Netherlands, 1992.

[199] David Hayes, Alessandro Pontillo, Sezsy Yusuf, Mudassir Lone, and James F. Whidborne. High Aspect Ratio Wing Design Using the Minimum Exergy Destruction Principle. In *AIAA Atmospheric Flight Mechanics Conference*, San Diego, California, USA, 2019. doi:10.2514/6.2019-1592.

[200] Stephen Timoshenko and James N. Goodier. *Theory of Elasticity*. McGraw-Hill, 3rd ed., 1970.

[201] Mark Drela. *Flight Vehicle Aerodynamics*. MIT Press, 2014.

[202] Martin A. Carrizales, Mudassir Lone, and Estela Bragado Aldana. Non-Elliptic Wing Lift Distribution Wings to Decrease Vertical Tailplane Size in Commercial Aircraft. In *AIAA Scitech 2019 Forum*, San Diego, California, USA, 2019. doi:10.2514/6.2019-0265.

[203] Cranfield University 8x6 Wind Tunnel. https://www.cranfield.ac.uk/facilities/8x6-wind-tunnel. Accessed on 10/12/2018.

[204] John E. Mottershead, Michael Link, and Michael I. Friswell. The Sensitivity Method in Finite Element Model Updating: A Tutorial. *Mechanical Systems and Signal Processing*, 25(7):2275–2296, 2011. doi:10.1016/j.ymssp.2010.10.012.

[205] Michael I. Friswell and John E. Mottershead. *Finite Element Model Updating in Structural Dynamics*. Kluwer Academic Publishers, The Netherlands, 1995. ISBN:978-94-015-8508-8.

APPENDIX A

BeaRDS™ Aerodynamic Look-Up Table

The following aerodynamic data were the look-up tables used within the aerodynamic blocks of BeaRDS^{TM} theoretical framework. The data represents s NACA-23015 aerofoil, and consists of C_{L_α}, C_M at $C_L = 0$, α at $C_L = 0$, and C_D at $C_L = 0$.

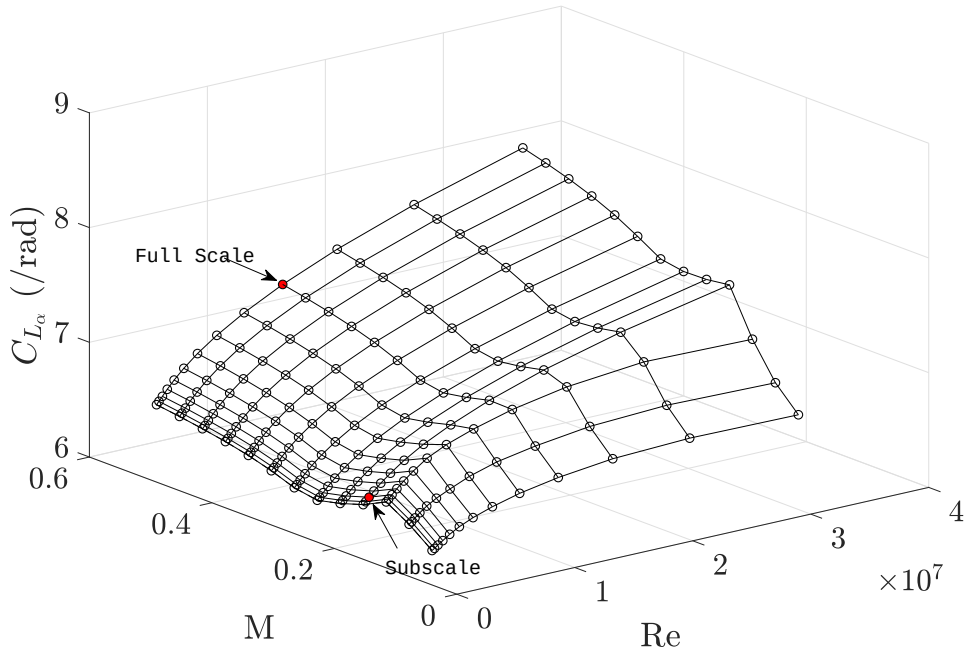

Figure A.1: C_{L_α} data.

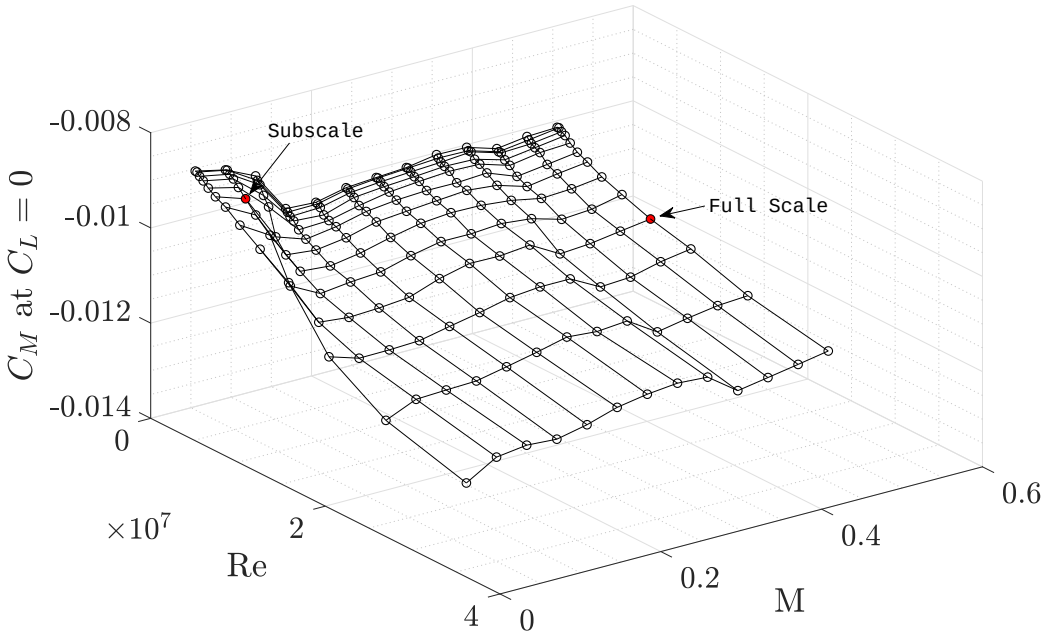

Figure A.2: C_M at $C_L = 0$ data.

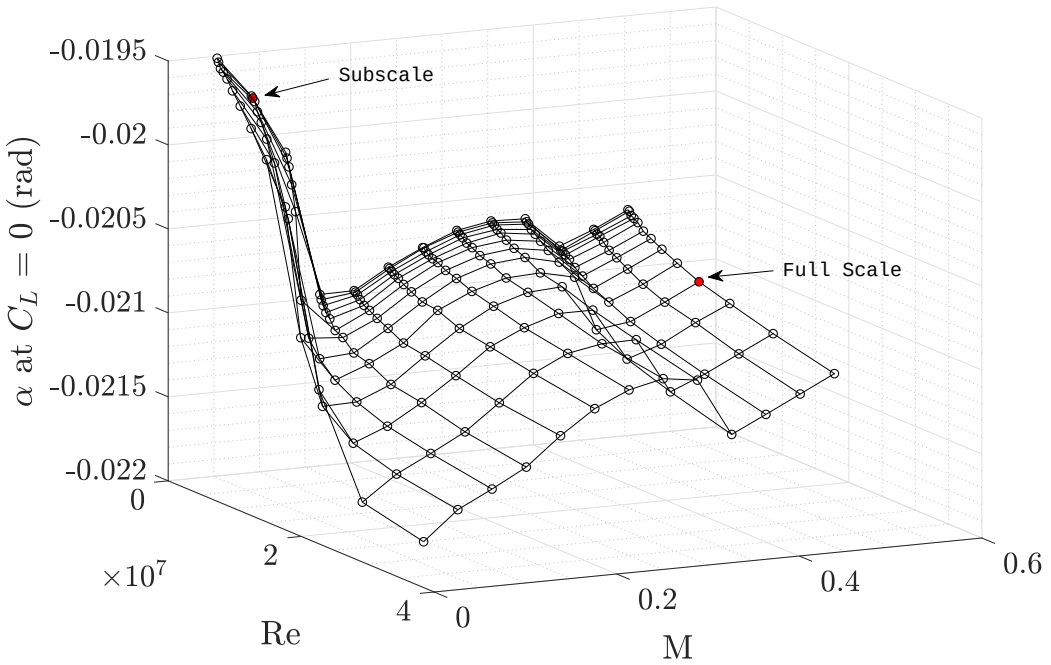

Figure A.3: α at $C_L = 0$ data.

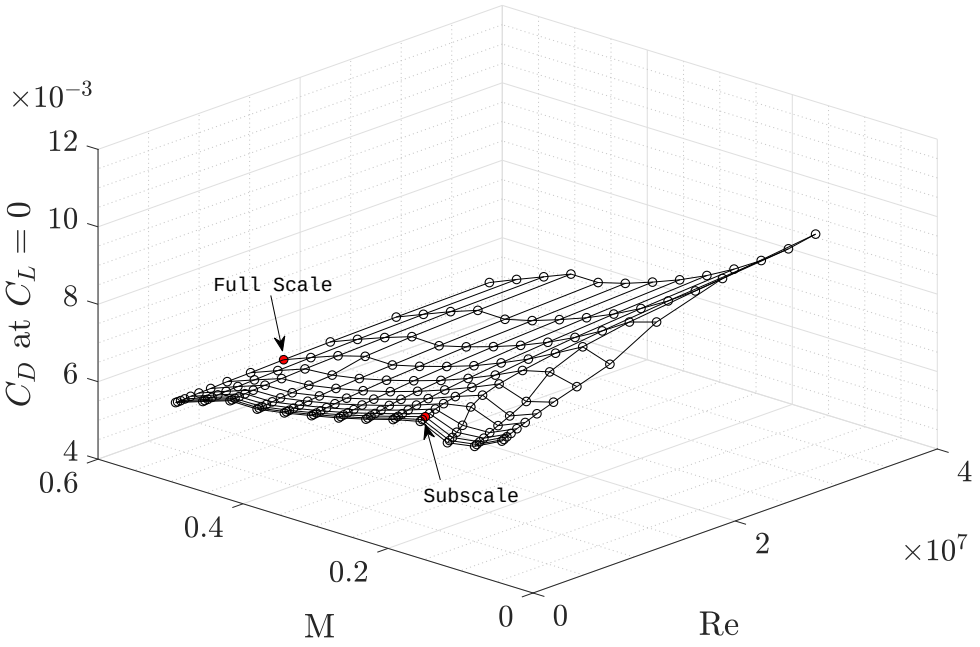

Figure A.4: C_D at $C_L = 0$ data.

This page is intentionally left blank.

APPENDIX B

Manufacturing Proof-of-Concept: xb-1

A prototype, known as xb-1, was developed and manufactured as a learning process in developing a flexible wing using 3-D PolyJet printing technology. One of the objectives is to evaluate the skin effect on a spar and skin configuration of the model. For this purpose, a GVT was carried out for spar only and spar with skin configuration. Hereafter, the spar only configuration is denoted as skin-off, while spar and skin configuration is denoted as skin-on configuration. Off-the-shelf IMUs were used to collect acceleration data during the GVT. It is worth noting that the length of the spar is 805 mm, while the length of the skin is 840 mm. The sensor positions for the skin-off test is presented in Figure B.1, while the sensor position for skin-on configuration is given in Figure B.2. Noted that only two of the IMUs were located in a comparable positions (IMU 2 and IMU 3 for skin-off is similarly located with IMU 1 and IMU 3 of the skin-on configuration). While IMU 4 were placed as near as possible to the tip by considering the physical limitation (size of the spar in the skin-off configuration, and the attachment of the skin for the skin-on configuration)

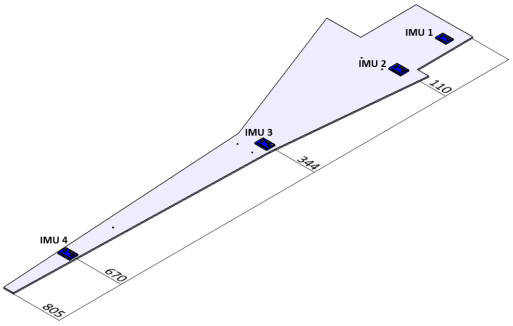

Figure B.1: IMU positions for skin-off configuration.

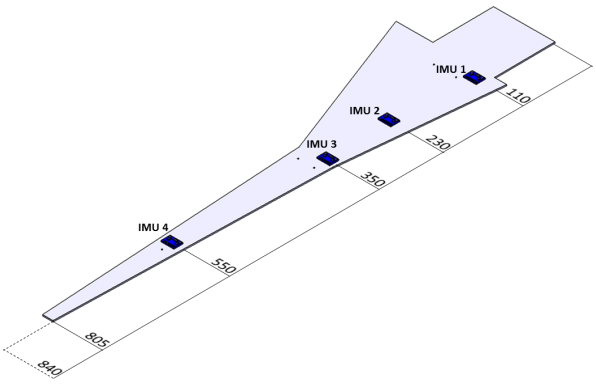

Figure B.2: IMU positions for skin-on configuration.

During the excitation, the spar was constrained at the rectangular shape of the spar (bolted to the shaker). A deterministic input using a sine sweep that covers the frequency range of 2 to 60 Hz, as well as random noise was used to excite the wing, from which

the structural characteristics of the wing configuration were extracted. The frequency response from each of the sensor during sinusoidal sweep test for both skin-on and skin-off configuration are given in Figure B.3 and B.4.

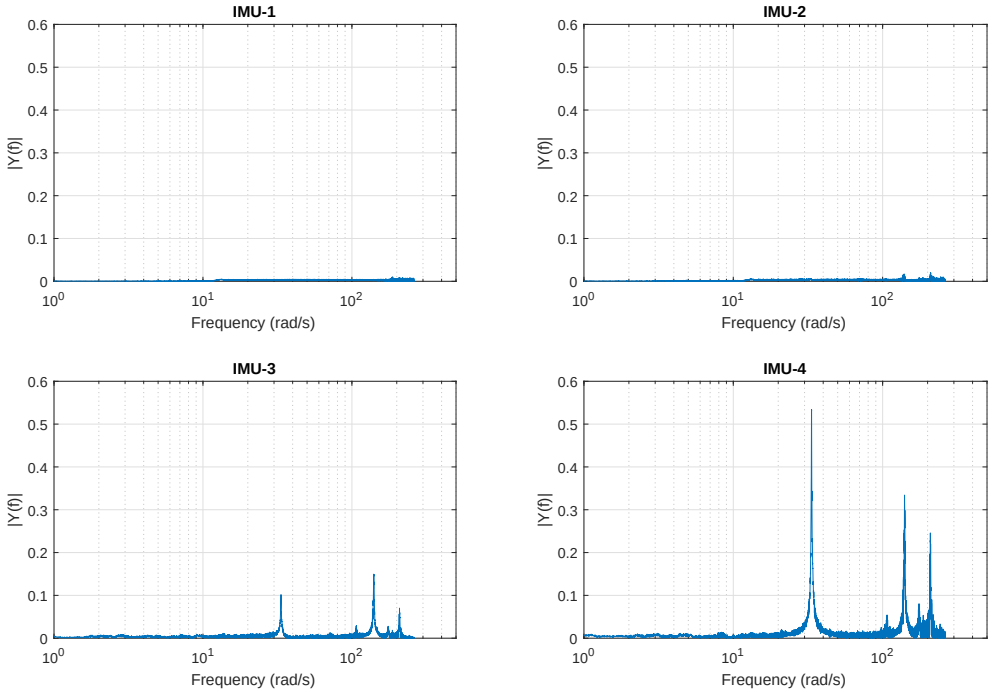

Figure B.3: Frequency response function for skin-off configuration.

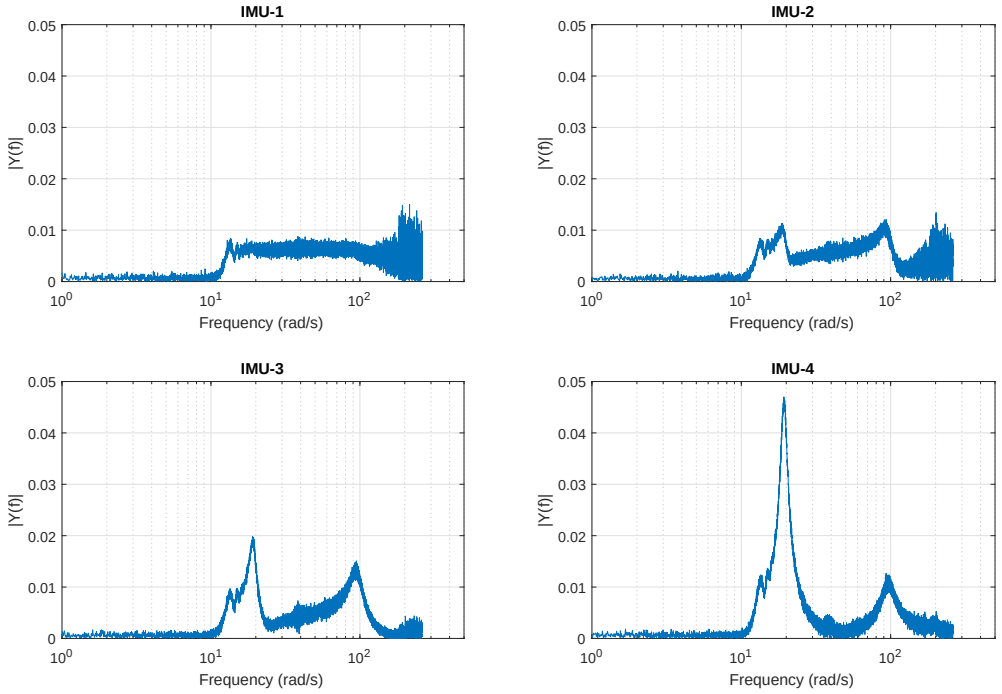

Figure B.4: Frequency response function for skin-on configuration.

The frequency response shows that the highest amplitude is obtained from IMU 4 that is

	skin-off	skin-on
Total Mass		
(gram)	316	687
Mode 1		
Frequency (Hz)	5.29	3.04
Damping (%)	0.86	4.31
Mode 2		
Frequency (Hz)	22.21	14.32
Damping (%)	0.66	10.97

Table B.1: Identification of the modal properties from GVT results.

	Prediction	GVT result	difference
mode 1	3.60	3.04	15.5%
mode 2	15.11	14.32	5.2%

Table B.2: Identified frequencies.

located close to the tip. Overall, the frequency response for skin-on configuration is lower than of the skin-off configuration, both in frequency and the amplitude. The skin-on configuration have a wider resonant peak and lower amplitude response compared to the skin-off configuration, indicating that the skin introduces more damping to the system. The frequency and damping was identified using subspace identification method [126] and given in Table B.1. However, due to the limited excitation frequency and limited measurement system, only the first two bending modes could be captured on the xb-1.

The premise of xb-1 work is based on the assumption that the skin does not add any stiffness to the wing, while introducing more mass to the system. The weight of the skin is doubled the weight of the spar. Using the simple relation of:

$$\omega = \sqrt{\frac{k}{m}} \tag{B.0.1}$$

considering two systems has similar stiffness, previous equation can be rearranged into:

$$k = \frac{\omega_1^2}{m_1} = \frac{\omega_2^2}{m_2} \tag{B.0.2}$$

or

$$\frac{\omega_1}{\omega_2} = \sqrt{\frac{m_2}{m_1}} \tag{B.0.3}$$

Considering ω_1 as the frequency response of the skin-off configuration, and ω_2 as the frequency of the skin-on configuration, the shift in frequency response is assume to be equal to $\sqrt{\frac{m_2}{m_1}} = \sqrt{\frac{687}{316}} = 1.47$. The frequency of the skin-on configuration is expected to be 1.47 smaller than the skin-off configuration.

A comparison of the predicted frequencies based on mass and identified frequency from the GVT are presented in Table B.2. Resulting in a less than 20% difference, it can be

concluded that the change of stiffness due to skin is minimal. This study shows that the use of PolyJet printing leads to less than 5% influence to the overall stiffness of the model[24]. Furthermore, the identified mode shape matrix is presented in Figure B.5 for skin-off configuration, and Figure B.6 for skin-on configuration.

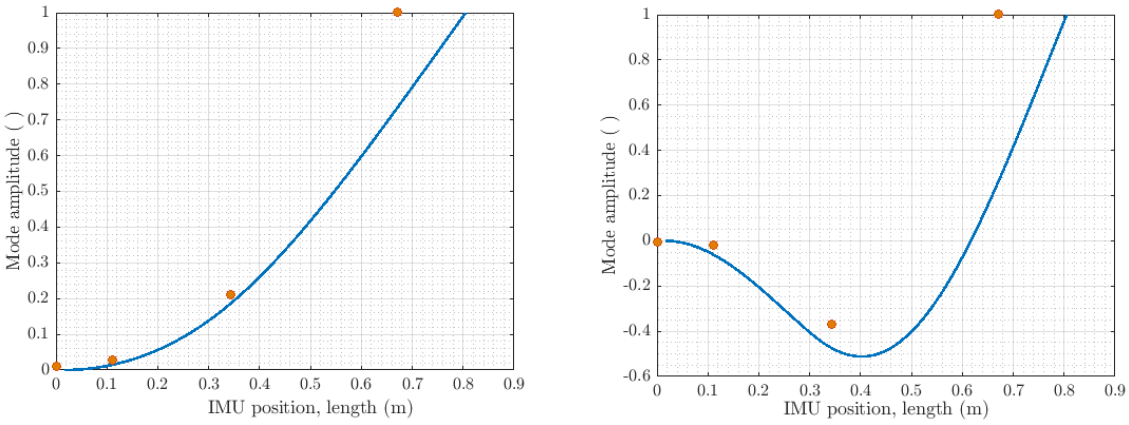

1st bending 2nd bending

Figure B.5: Identified mode shape for the skin-off configuration (•: identification results, -: theoretical).

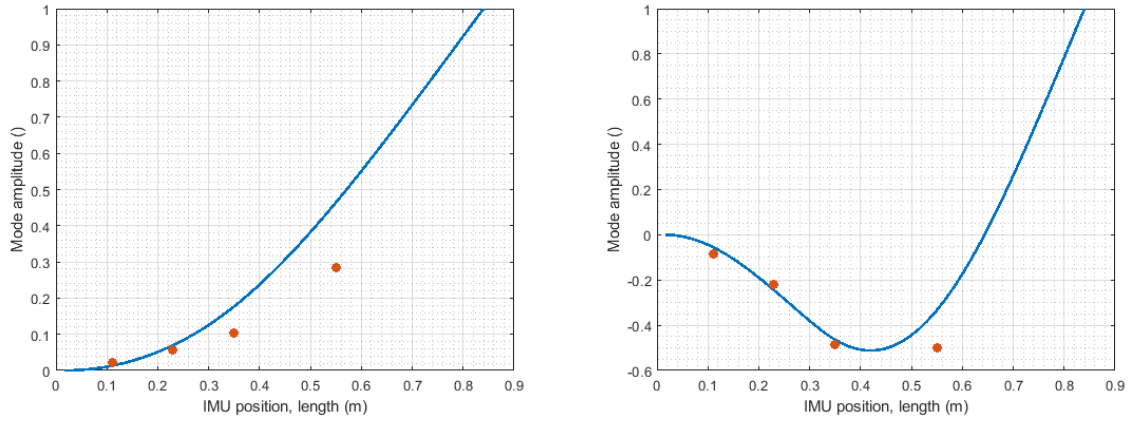

1st bending 2nd bending

Figure B.6: Identified mode shape for the skin-on configuration (•: identification results, -: theoretical).

APPENDIX C

Flowchart of Subscale Model Development

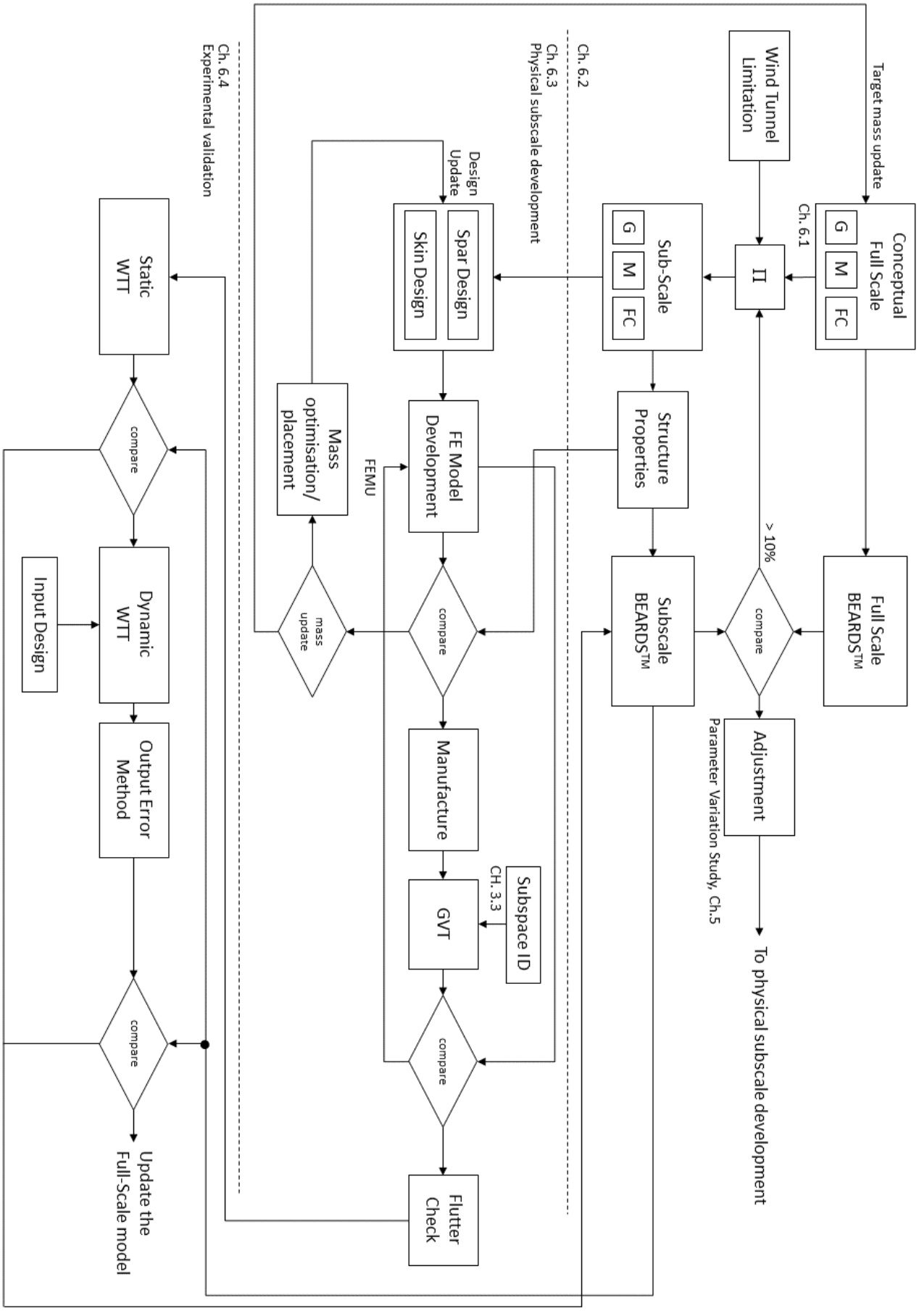

Figure C.1: Flowchart of the subscale model development